ANALYSIS OF HELICAL GEAR PERFORMANCE UNDER ELASTOHYDRODYNAMIC LUBRICATION

by

Hazim U. A. Jamali

Thesis submitted in candidature for the degree of
Doctor of Philosophy at Cardiff University

Institute of Mechanics and Advance Materials
Cardiff School of Engineering
Cardiff University

March 2015

Declaration

The work has not previously been accepted in substance for any degree and is not being concurrently submitted in candidature for any degree.

Signed ……………………....…… (Hazim Umran Alwan Jamali)

Date ……………………………

Statement 1

This thesis is the result of my own investigations, except where otherwise stated. Other sources are acknowledged by the provision of explicit references.

Signed ……………………....…… (Hazim Umran Alwan Jamali)

Date ……………………………

Statement 2

I hereby give consent for my thesis, if accepted, to be available for photocopying and for inter-library loan, and for the title and summary to be made available to outside organisations.

Signed ……………………....…… (Hazim Umran Alwan Jamali)

Date ……………………………

Summary

In this thesis an elastohydrodynamic lubrication (EHL) solution method has been developed for helical Gears. Helical gears mesh with each other and develop contact areas under load that are approximately elliptical in shape. The contact ellipses have aspect ratios which are large and lubricant entrainment takes place in the rolling / sliding direction which is along the minor axis of the contact ellipse.

The contact between helical gear teeth is therefore considered as a point contact EHL problem and the EHL analysis has been developed to include all aspects of the correct gear geometry. This includes the variation in radius of relative curvature at the contact over the meshing cycle, the introduction of tooth tip relief to prevent premature tooth engagement under load, and axial profile relief to prevent edge contact at the face boundaries of the teeth. The EHL solution is first obtained as a quasi-steady state analysis at different positions in the meshing cycle and then developed into a transient analysis for the whole meshing cycle. The software developed has been used to assess the effects of geometrical modifications such as tip relief and axial crowning on the EHL performance of a gear, and different forms of these profile modifications are studied. The analysis shows that the transient squeeze film effect becomes significant when the contact reaches the tip relief zone. Thinning of the film thickness occurs in this region and is associated with high values of pressure which depend on the form of tip relief considered.

A transient EHL analysis for helical gears having faceted tooth surfaces has also been developed. Such surface features arise from the manufacturing process and can have a significant effect on the predicted transient EHL behaviour. The EHL results have been found to depend significantly on the facet spacing and thus on the manufacturing process.

The important effect of surface roughness is also considered by developing a three dimensional line contact model to include real surface roughness information by considering a finite length of the nominal contact in the transverse direction of the tooth. This model is based on the use of the fast Fourier transform method to provide the repetition of the solution space along the nominal contact line between the helical teeth with the inclusion of cyclic boundary conditions at the transverse boundaries of the solution space. In helical gears the lay of tooth roughness (direction of finishing) is generally inclined to the direction in which rolling (entrainment) and sliding take place, and this is found to have a significant effect on both film thickness and pressure distribution.

Acknowledgment

First of all, I would like to praise and thank God for helping me to complete this thesis.

I am indebted to my supervisors, Prof. H.P. Evans and Prof. R.W. Snidle and Dr. K.J. Sharif for their encouragement, thoughtful advice and support throughout my study. I would particularly like to thank Prof. H.P. Evans for providing guidance and invaluable experience to develop my skills as a researcher and also for dealing with me as a colleague more than a student.

The work presented in this thesis would not have been possible without the financial support of the Iraqi Ministry of Higher Education and Scientific Research and University of Karbala.

I would also like to express my thanks to Dr. K.J. Sharif for providing the line contact solver used for comparisons in this work and also for helping us to settle down in Cardiff when we first came here.

Thanks are also due to all of my colleagues in the Tribology and Gearing group, in particular: Dr. Anton Manoylov for our useful discussions about the FFT method, Dr. Alastair Clarke for introducing me to the Profilometer and my friends Shaya Al Shahrany (for almost daily discussions about our projects) and Ali Al Saffar.

I must thank my friends Amjad Al Hamood, Haider Galil, and Ahmed Al Moadhen. We shared more than four years in Cardiff working on our PhD studies and together we overcame the mutual difficulties that we encountered.

I would like to thank my family particularly: my mother, the memory of my unforgettable father and my brother.

Finally, but by no means least, I would like to thank my dear wife for supporting me and spending most of her time in looking after our son and daughter throughout the duration of my studies.

Contents

Chapter 1: Introduction and background

Chapter 2: Gear contact geometry

Chapter 3: EHL point contact problem and solution methods

Chapter 4: Transient EHL analysis: Introduction of axial crowning

Chapter 5: Tip relief

Chapter 6: Transient EHL Analysis of Helical Gears Having Faceted Tooth Surfaces

Chapter 7: 3D Line Contact Model

Chapter 8: Conclusions and future work

Appendix

Nomenclature

Symbol	**Description**	**Units**
a	Hertz dimension in x direction	m
b	Hertz dimension y direction	m
c_r	Clearance at the face edge	m
c_t	Tip relief value at the tip radius	m
d	Surface deformation	m
E'	Effective elastic modulus	Nm^{-2}
E_1, E_2	Elastic modulus, surface 1 and 2	Nm^{-2}
F	Face width	m
f	Weighting function used in the differential deflection equation	m^{-1}
g	Weighting function used in the deflection equation	m
h	Film thickness	m
h_o	Distance of common approach	m
h_u	Undeformed geometry	m
N, M	Number of elements in the x and y direction	
n_f	Number of facets	n_f
p	Pressure	Pa
p_x , p_{tb} , p_{nb}	Axial, transverse and normal pitch	m
R_1' , R_2'	Radius of curvature, surface 1 and 2	m
r_{start}	Radius of relief starting point	m
r_{b1} , r_{b2}	Radius of base circle, pinion and wheel	m
r_{tip1} r_{tip2}	Tip radius, pinion and wheel	m
s_{min}	Position of the first contact point	m
s_{max}	Position of the last contact point	m
U_1, U_2	Velocity of surface 1 and 2 in the x direction	m.s^{-1}
u_s	Sliding velocity	
$\bar{v}$	Mean velocity in the y direction	m.s^{-1}
V_1 , V_2	Velocity of surface 1 and 2 in the y direction	m.s^{-1}
x	Co-ordinate in the entrainment direction	
y	Co-ordinate transverse to the entrainment direction	
z_c	Gap due to axial crowning	m
z_t	Gap due to tip relief	m
α	Pressure viscosity coefficient	Pa^{-1}
β	Parameter for tip relief	β
β_b	Base helix angle	Degree
γ	Density pressure coefficient	Pa^{-1}
η	Absolute viscosity	Pa.s

η_0	Absolute viscosity at reference pressure	Pa.s
ψ	Pressure angle	deg.
λ	Density pressure coefficient	Pa^{-1}
ρ	Density	kg m^{-3}
ρ_0	Density at reference pressure	kg m^{-3}
σ_x, σ_y	Flow factors, in the x and y directions	m.s
σ_s, σ_r	Flow factors, in the sliding and non-sliding direction	m.s
τ	Shear stress	N.m^{-2}
υ_1, υ_2	Poisson's ratio for surface 1 and 2	
ξ	Slide/roll ratio	
ω_1, ω_2	Angular velocity for the pinion and the wheel	s^{-1}

N.B. Other symbols are defined in the text when their use is local to the section concerned.

Chapter 1

Introduction and background

1.0 History of gears

This thesis is concerned with the generation of elastohydrodynamic lubrication (EHL) oil films between the teeth of gears. Gears are considered as one of the man's earliest mechanical devices. Early man used toothed wheels in addition to various other devices such as the inclined plane and the lever to increase the force which could be applied to an object. Dudley (1969) provided an interesting review of the history of gears and their uses through the ages. Gears were described in the early writings as common devices in everyday use rather than by viewing them as new inventions. The first known gearing device from early times is the south pointing chariot, 2600 BC. The ancient Chinese designed this chariot using a very complex differential gear train. In principle it was used as a guide while traveling through the desert because it points south continuously. In Iraq, it seems the Babylonians were using gear devices around 1000 BC in various applications such as water lifting machines and also in temple devices. In the Roman Empire (100BC-400AD) gears started to be used to provide continuous power, with water power being used to drive flour mills through gears, for example. An historically important mechanism was built in this era (82 BC) which has since become known as the Antikythera mechanism. It was found in a sunken ship near the Greek island of Antikythera. The Antikythera mechanism contains many gear trains and there were indications of tooth breakage and repair.

The use of gears has been increasing throughout thousands of years and much development has occurred in gear technology. The material used for gear has changed from being wood to include various metals and even plastics. New gear types have been invented such as spur, helical, bevel and worm gears compared with the simple toothed wheel devices of ancient times. Recently, the machine tool industry has developed highly sophisticated machines which have automated the manufacture and measurement of the gear teeth. Despite all these developments through the thousands of years, we still have gear troubles as did the Romans.

1.1 Gear use and advantages

The development of gear technology for making various types of gears gives the ability to transmit motion and power between rotating shafts regardless of whether they rotate about parallel axes, non-parallel axes, or intersecting axes. In comparison with other power transmission systems, gear systems can be used with high reliability to transmit high power with generally low space requirements. The gear system can also be completely enclosed which prevents any exposure to the surroundings (Maitra, 1994). These attributes and many others have made the gear wheel a vitally important element in most types of machines in use today.

Nowadays gears are being used in toys, home appliances, automobiles, naval vessels, industrial and other applications. In the aircraft field, gears are used to drive propellers, pumps and many other accessories. Gears are essential in helicopters to drive the main and tail rotors. Gears are manufactured in a relatively large size for some applications. Mill gears, for example, are made up to 11 metres in diameter as shown in Figure 1.1 (Dudley, 1984).

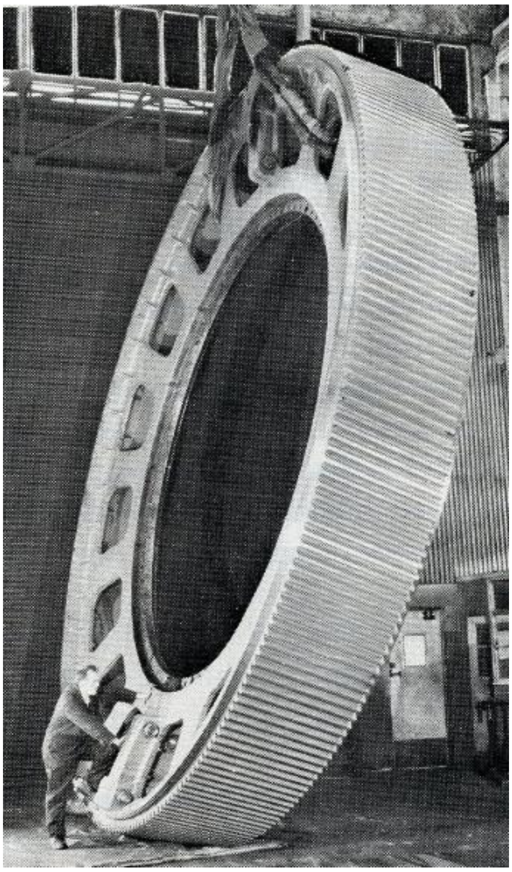

Figure 1.1: Large size gear for a mill application (Dudley, 1984)

1.1.1 Helical gears

The gear wheel shown in Figure 1.1 is a helical gear and helical gears resulted from development of spur gears to improve their performance. Spur gears transmit motion and power between parallel shafts through teeth that run parallel to the gear axes across the face width. The manufacturing cost of spur gears is comparatively low and, in general, they are commonly used in relatively low power and low rotational speed applications. The gear is described as helical when the teeth are not parallel to the axis but are twisted at an angle with the gear axis. This angle is usually called the helix angle and it gives the teeth a helix shape. In a pair of mating helical gears the helix angle must have the same value. In addition, they must have opposite helix hand. A typical helical gear pair is illustrated in Figure 1.2

Figure 1.2: A Pair of helical gears in contact (Litvin & Fuentes, 2004).

In a similar way to spur gears, helical gears are used in applications when the rotating shafts are parallel. They are also adapted to the more general case where the shafts are non-parallel or non-intersecting. In this case, they are called crossed helical gears (Maitra, 1994). In helical gears, the tooth profile is usually chosen to be involute in the section perpendicular to the axis of the gear. This section is described as the transverse section.

Spur gears tend to produce noticeable noise in operation. The noise is related to the intermittent nature of the tooth contact and consequently the transmission of the load. In spur gears the tooth contact starts and ends suddenly over the whole tooth width. In contrast, the contacting characteristics of a pair of helical gears are quite different from that in spur gears. The motion is transmitted gradually and more smoothly between the engaged helical teeth. The contact between a pair of helical gears starts at the tooth end, and as the engagement develops, the contact progresses throughout the tooth face width until it arrives at the other end of the tooth. This action is the essential cause of the gradual, even action of the tooth and the more uniform distribution of the load. The line of contact acts diagonally between the ends of the helical teeth. In addition, in a well-designed helical gear there are always at least two pairs of teeth in contact. These characteristics permit helical gears to have a significant increase in the load carrying capacity as compared with the corresponding spur gears drive, or alternatively, the gears may have longer life with the same spur gear load (Drago, 1988). The smooth and quiet operation of helical gears make them preferred in applications that require high speed drives.

The disadvantage of helical gears is that they produce an axial thrust in addition to the radial and tangential spur gears load (Drago, 1988). To overcome this problem, either appropriate thrust bearings are used, or the axial thrust can be neutralised by using double helical gears (Houghton, 1961). In the latter case, the “hand” of the teeth on one gear is opposite to the hand of the other gear teeth as shown in Figure 1.3. This arrangement makes the resulting axial thrusts equal and opposite, so they have the effect of cancelling each other and a thrust bearing is not needed (Dudley, 1984). Therefore, with the regard of cost considerations of using double helical gear drives, they may be used to realise the quiet running advantage of normal single helical gears without the side thrust problem.

Figure 1.3: Double helical gear (B. K. Gears Pvt. Ltd)

1.2 Gear modes of failure:

Gears like many other machine elements are considered to have failed when they no longer continue to carry out the purpose of their design with certain efficiency. This definition of failure covers a wide range of causes such as fatigue, impact, wear, etc. Fatigue is considered as one of the most frequent modes of failure in gear applications (Alban, 1985) .

From a tribological point of view, in which the surfaces of mating teeth are supposed to be separated by a very thin layer of lubricant, the major modes of tooth failure are likely to be classified as pitting, scuffing, and also to some extent, mild wear. These forms of failure are mainly related to the lubrication performance during the operation of the gears. The breakdown in the lubricant film thickness, for whatever reason, may lead to a catastrophic failure in some applications such as helicopters for example, and in such cases failure must be avoided at all costs. These lubrication-related modes of failure are briefly explained in the following sections.

1.2.1 Scuffing

Scuffing is essentially a wear mode of failure but the damage occurs very rapidly due to metal to metal contact resulting from the breakdown of the film thickness or loos of lubrication supply under severe conditions of relatively high sliding velocities and applied load. The contact between the surface asperities under these conditions involves a rapid increase in the surface temperatures associated with the failure of the lubricant to separate the surfaces. As a result welding and subsequent tearing of the surfaces occurs which completely changes the nature of the surface topography of the teeth. This sequence of events is accompanied by noticeable noise and vibration and a rapid increase in friction and can lead to a catastrophic failure involving tooth breakage. Scuffing is often seen near the tips and roots of the teeth as shown in Figure 1.4. In general those areas of the teeth have the worst combination of high sliding velocities and load conditions.

The example shown in Figure 1.4 has scuffing near the tip of the gear where sliding is high. The unscuffed area near the tip is consistent from tooth to tooth and probably corresponds to reduced loading due to misalignment or tooth crowning.

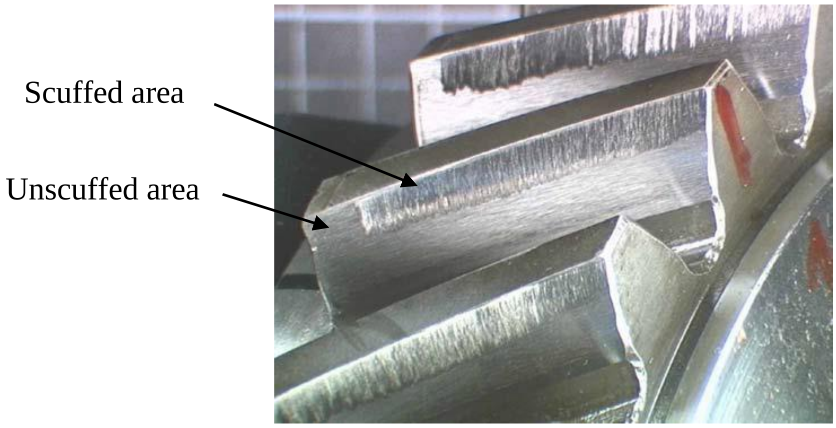

Figure 1.4: Scuffing failure of helical gear teeth at their tips. (Snidle & Evans, 2009)

The occurrence of scuffing may be promoted by any factor leading to overloading under high slide to roll ratio or the failure of the oil film separating the tooth surfaces. These effects may be the result of various causes, such as insufficient tip relief modification, thermal effects and the consequences of pitting of the teeth. Tooth surfaces need to be protected from this sort of failure and this can be achieved to a large extent by using special additives to improve lubricant properties under severe conditions of high pressure and temperature (EP additives). Another means of protection is by reducing the roughness of the surface by pre running of the gears at slowly increased increments of load and speed or by “superfinishing”.

1.2.2 Pitting

The appearance of pits (or micro-pits) in gear teeth is a well-known fatigue effect. The cause of these pits is of great interest for researchers at the present time because of damage occurring in wind turbine gearboxes. Pitting of tooth surfaces is related to the high contact stresses at the contacts between the teeth. Stresses higher than the nominal Hertzian values may be the result of factors such as geometrical changes in the tooth profiles, surface roughness and the consequent dramatic variation in the stresses over the contacting surfaces. These high local values of stress tend to initiate (or exacerbate existing) cracks which may propagate causing a removal of the material at those high stress areas. The initial, minor pitting may arrest when the gears operate for a considerable period of time. This is attributed to the surface asperities reducing with time which promotes the surface stresses to be become more uniform. Sometimes, however, pitting continues to progress rather than halting due to a high load. This progression leads to pits merging with each other which then results in comparatively larger size pits. This form of serious pitting is termed as spalling. It is difficult to predict whether the initial pitting will come to a halt or will continue to the serious progressive stage. The progressive form of pitting is likely to be found on the tooth dedendum but it may spread further to the pitch line area as shown in Figure 1.5.

As progressive pitting continues, it will likely lead to a gear failure. Pitting sometimes can be seen by the naked eye. The pit size in other cases is in the micrometre range and is called micro pitting.

It is worth mentioning that mild wear can continue to remove material at the rolling/sliding asperity encounters even when gears operate under conditions that may not be severe enough to introduce pitting or scuffing failure. This material removal can be attributed to many sources such as fatigue, corrosion, adhesion and others. However, with time mild wear can affect the gear performance due to the change caused to the tooth profiles.

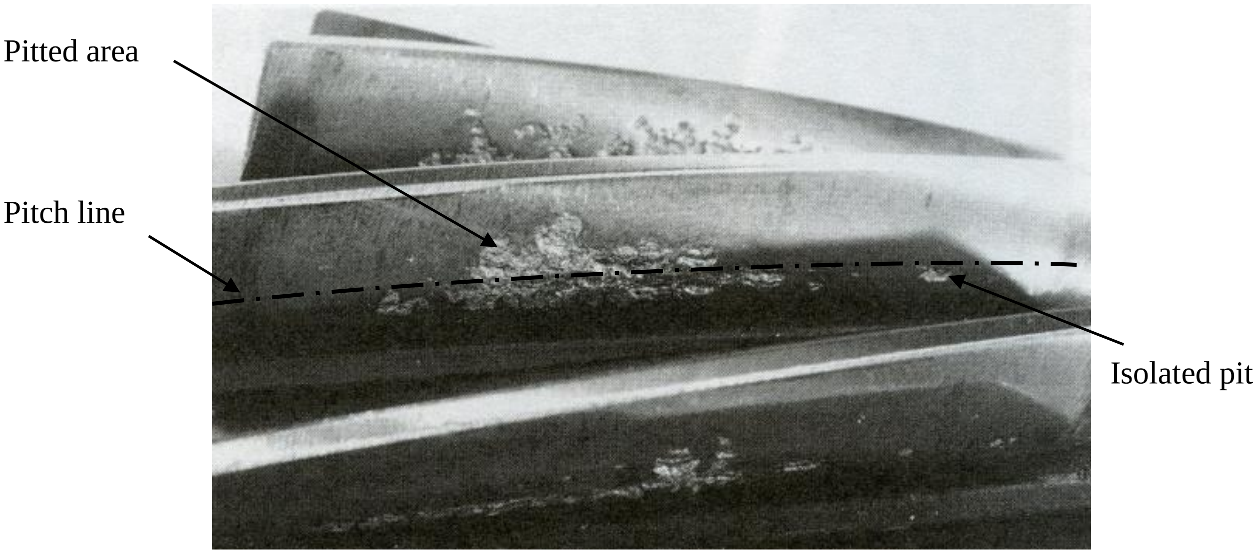

Figure 1.5: Pitting of helical gear teeth (Alban, 1985)

1.3 Engineering surfaces

All real surfaces that are used in engineering applications such as gears are in fact rough when they are examined on the microscopic scale. More expensive methods of surface preparation can only reduce the surface roughness to some extent, but cannot produce perfect smoothness. Roughness has significant consequences in many engineering applications involving concentrated contacts. One of its essential effects on the contact between two surfaces is on the actual dimensions of the real contact area which is smaller than expected. When such contact occurs, it starts at the tips of the highest asperities. As the load is increased the contact area will involve other asperities due to the deformation of the existing contacts as explained schematically in Figure 1.6.

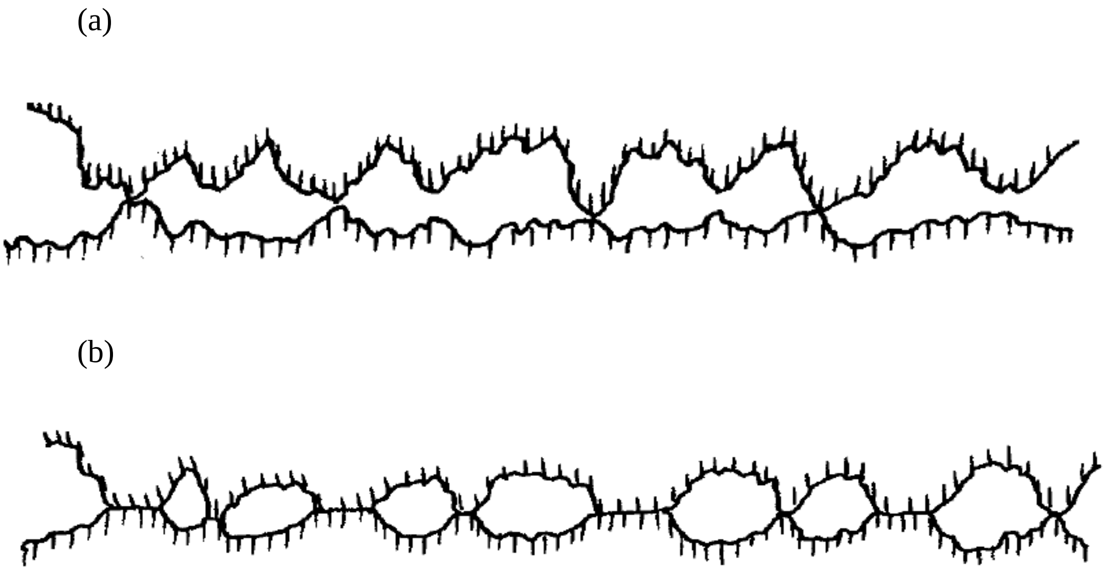

Figure 1.6: The contact of rough surfaces, (a) Under zero load and (b) Under load

Experimental results, and numerical simulations of contact, emphasize that the true load carrying area is much smaller than the apparent contact area and consequently the contact of rough surfaces will produce high contact pressures in comparison with the calculated nominal values based on the assumption of smooth surfaces. The surface topography is therefore very important in studying the actual contact behaviour under load due to the effects of local asperity shape on the asperity nature of deformation. The roughness effect can also have a significant impact on the lubricated contact problem. Examples of this occur in bearings and in the contact between gears teeth. Tribologists tend to evaluate the effectiveness of lubrication at contacts in terms of the ratio between the minimum lubricant film thickness which is calculated from the smooth surface assumption to the mean surface roughness. This ratio is known as the lambda ratio, Λ, which also gives an indication for fatigue life in some bearing applications. Reducing the gear tooth roughness by means of a surface finishing process such as lapping or polishing is found to be beneficial in increasing the resistance against the previously mentioned fatigue and wear modes of failure. In view of the importance of surface finish there is the need to measure, assess and control the roughness characteristics of gear surfaces in relation to their performance and durability. Gear surfaces in recent and most current applications are usually produced using various methods of finishing such as grinding, honing, etc. There are some directional characteristics associated with each finishing processes which probably have significant effects on the contact behaviour of surfaces. The surface roughness is generally classified into two main components described as waviness and roughness. Waviness describes the longer-wavelength features of a measured roughness profile which are usually removed by a high pass filter. These features, which typically have a “wavelength” in excess of a millimetre on gear teeth, do not affect the behaviour of the nominal Hertzian contact which would typically be less than a millimetre in gears. It is therefore the height and spatial characteristics of the shorter wavelength features that are of importance. In engineering practice various roughness parameters are calculated from profile data stored digitally. Digitally stored roughness profiles from gear tooth surfaces will be used in some of the lubricated contact simulations to be described in the following chapters of the thesis.

1.4 Tribology and elastohydrodynamic lubrication

Tribology as a term first appeared in 1966 in a report introduced by the UK Department of Education and Science (Jost, 1966). This report defined tribology as “The science and technology of interacting surfaces in relative motion and the practices related thereto”. This term originates from the Greek ward *tribos*, which means rubbing. The facts and concepts behind this relatively new definition of tribology can be traced back to the period of prehistory.

Dowson (1979) has comprehensively described the history and development of human activities related to tribology. Early man started to generate fire in the Palaeolithic period, around 200, 000 years ago. The idea of using friction between pieces of wood or stones to create fire can be considered as very early evidence of man’s application of frictional heating. Another example of an ancient application of tribology is the potter’s wheel which appeared about 5000 years ago in the Neolithic period and which relied on an early form of journal bearing.

In the study of the lubrication of loaded gear tooth contacts it is generally accepted that the mechanism responsible for the generation of an effective oil film is that of elastohydrodynamic lubrication (EHL). A large and growing body of literature has been concerned with EHL since the middle of the last century, and the term has come to be used to refer to a form of hydrodynamic lubrication in which the combined effects of elastic deformation and the tremendous increase of lubricant viscosity at high pressures combine to generate an effective film in rolling/sliding contacts such as those between rollers or gear teeth. Contacts of this type are described as “non-conforming” or of “low geometrical conformity” or “concentrated” and in the case of perfectly smooth surfaces the contact pressures and contact dimensions can be accurately calculated using the classic equations of Hertz under dry, elastic conditions. Typical examples of this type of lubrication are found in engineering applications such as gears, cams, roller and ball bearings. These machine elements operate under heavy load and can be classified as non-conforming contacts. In this regime the lubricant film thickness is generally of the order of a micron and the maximum contact pressures are typically about 1.0 GPa in gears and possibly up to 3.0 GPa in rolling element bearings. Despite this very thin layer of lubricant, it is probably sufficient to prevent metal to metal contact between the interacting surfaces provided that the surface finish is carefully controlled.

1.5 Development of the EHL analyses

Several studies such as Nijenbanning et al. (1994), Chittenden et al. (1985) and Hamrock & Dowson (1976) developed expressions to predict the minimum and central film thickness for the lubricated point contact between smooth surfaces operating in the EHL regime. And in today’s applications full understanding of the EHL contact behaviour between the surfaces plays a vital role in their design.

The EHL problem is defined by two basic equations: the hydrodynamic equation and the surface elastic deformation equation (as will be considered in Chapter 3). This pair of equations presents a highly non-linear system and thus has led researchers to develop ingenious numerical solution models during the last six decades to solve this difficult problem. EHL problems are usually solved using either a line contact or point contact approach depending on the shape of the contact area under load. Line contacts are present in roller bearings and spur and helical gears, and point contacts occur in ball bearings and certain types of crossed-axis gears.

The real contact in engineering applications is two dimensional in nature. However, early numerical studies in the EHL field mainly focused on the line contact problem where the contact may be considered one dimensional. Although this relative simplification of the EHL problem is valid for some applications, its study was related to the limitations of computational resources in the early days of digital computers. The development in the speed of calculations in the modern computer gives the ability to use a point contact (two-dimensional) approach. Different methods have been developed to provide reliable solutions to the EHL problem such as the *Forward* method, *Inverse* method, *Newton-Raphson* method, *Multigrid* method, *Coupled* method and the novel *differential deflection* method. Holmes (2002) provided an interesting description as well as clarifying the limitations of these methods.

The Forward method was used in several studies such as Ranger et al. (1975) and Evans & Snidle (1981). The inverse method was introduced by Dowson & Higginson (1959) in a line contact problem and was subsequently developed for point contacts by Evans & Snidle (1982). Houpert & Hamrock (1986) used a Newton-Raphson method for the line contact problem. Lubrecht et al. (1986) were the first to use a Multigrid method in EHL problems**.** Despite the widespread use of the multi grid method it is not desirable for mixed EHL problems when the surface roughness is of moderate or high frequency (Zhu, 2007).

The idea behind the more recent coupled method in contrast with the previous techniques is that it attacks the solution of the two basic equations (Reynolds and elastic equations) simultaneously. Elcoate (1996) and Elcoate et al. (1998) developed this method initially in a *fully-coupled* form to solve a line contact problem and showed it to be robust and reliable in dealing with high load contacts.

The coupled method was significantly developed when Evans & Hughes (2000) for the first time used an ingenious *differential form* for the formulation of the elastic equation. Hughes et al. (2000) solved the line contact EHL problem using this method and compared the result with the standard method for handling the deflection calculation. Two cases were examined, first where the surfaces were both smooth, and, second, the case in which a smooth surface was moving against a stationary rough surface. In both cases the results were obtained with an enormous reduction in the time of computing, when using the differential deflection method, compared to the fully-coupled approach. Elcoate et al. (2001) successfully used this method to solve the transient EHL line contact proplem for moving rough surfaces.

Holmes et al. (2003a) and (2003b) extended this novel method to solve transient EHL *point* contact proplems where the effect of surface roughness was also taken into account.

With the progressive developments in the EHL analyses of contacting surfaces, the incorporation of surface roughness effects has been given considerable attention over the last 40 years or so. Lee & Cheng (1973) reported one of the first studies to consider the effect of a single asperity on the EHL characteristics where a one dimensional Reynolds equation is used in the analysis.

The effects of roughness orientation was examined by Patir & Cheng (1978) where an average flow approach was developed. The levels of film thickness generated were found to be related to the roughness orientation. The film thickness was predicted to decrease as the direction of entrainment was altered from transverse, through isotropic, to longitudinal.

The directional effect of the surface roughness was investigated by Lubrecht et al. (1988) when sinusoidal longitudinal and transverse roughness features were incorporated in a circular EHL contact model. The results were compared with corresponding Patir & Cheng (1978) results. With this form of roughness feature they found that the effect is overestimated by the flow factor model.

Similar results was found by Kweh et al. (1989) who analysed an EHL elliptical contact when the surface roughness was 2D transverse and three dimensional sinusoidal in profile.

Kweh et al. (1992) considered surface roughness in an EHL analysis of elliptical contact when a smooth surface moves relative to a stationary rough surface. The roughness was also sinusoidal in profile and straight extruded in the direction perpendicular to the rolling/sliding direction. Two scales of amplitude and period for this transverse roughness wave were used. It was found that the amplitude of the larger scale roughness suffers the bigger proportional reduction in comparison with the smaller one. It should be noted that the lubricant in these early solutions was assumed to be Newtonian.

Overall, the important results of these studies and many others highlighted the need to include real roughness in the EHL analysis. Poon & Sayles (1994) developed an elastic-plastic model to simulate the contact between a smooth ball on a real rough surface as well as smooth and sinusoidal surfaces. The effect of fluid film was not considered in this analysis.

Ai & Cheng (1994) studied the transient effect in a line contact EHL analysis for the contact between surfaces having measured (i.e. “real”) surface roughness. It was found that the transient effect due to the surface roughness has noticeable influences on the EHL results.

Hu & Zhu (2000) developed a model for mixed EHL analysis. Three-dimensional real roughness was incorporated in this point contact analysis. The surface radii of relative curvature were equal in both directions which produced under load a circular contact area of less than 0.5 mm in radius. The limits for the EHL solution space were $-1.9a \leq x \leq 1.1a$ and $-1.5a \leq y \leq 1.5a$ where x and y represent the rolling/sliding and transverse directions respectively and a was the corresponding Hertzian radius of the contact area. A fine mesh of 257*257 nodes was used in this analysis in order to make the model sensitive to the roughness features. This model was questioned by a number of workers in the field because it discarded the pressure gradient terms in the Reynolds equation for small film thicknesses below 0.05 μm (Evans, 2015).

Tao et al. (2003) used real measured surface roughness in the line contact EHL analyses of gear teeth. Breakdown of film thickness due to the interaction of asperities was found which means the contact was under the mixed lubrication regime. In this regime of lubrication the applied load is not carried only by the lubricating film but also by the solid ("metal to metal") contact at the asperities.

Zhu & Wang (2013) used a mixed EHL model to study the effect of roughness orientation on film thickness levels in a line, circular and elliptical contact problems. Three forms of roughness were used which are longitudinal, transverse and isotropic. The orientation effect was found in general to be significant when the range of Λ ratio was between 0.05 and 1.

As the previous studies showed the roughness orientation has an important influence on the contact behaviour, the roughness lay direction and its relation to the scuffing failure for the ball on disc contact was studied by Li (2013) using a scuffing model developed by Li et al. (2013). It was found that the scuffing performance was substantially affected by the roughness lay direction where scuffing resistance was found to be inversely proportion to the difference between the angles of orientation of the lays on the two surfaces.

Because of the energy saving brought about by the use of low viscosity oils in engines, for example, there is a tendency for lubricated contacts to operate with thinner films. This requires a better understanding of the behaviour of EHL contacts which operate in the mixed lubrication regime. Recently Morales-Espejel (2013) traced in a review the development of solving the micro EHL problems during the last four decades. He found that despite the wide range of literature available in this field, the problems of mixed lubrication need more engineering and physics understanding in order to solve practical problems of thin film lubrication.

1.6 Profile modification of gear teeth

In addition to surface roughness, other surface features such as discontinuities in the profile of an otherwise smooth surface can be the source of lubrication and contact problems. In the manufacture of gear teeth, for example, modifications are usually made to the involute profile near the tips of the teeth (tip relief) in order to avoid severe contact during meshing under load. Walker (1940) determined the required tip relief modification to overcome the problem of tooth deflection in spur gear drives working under heavy load.

The resulting tooth profiles are not perfect involutes in the area of modification (Bonori et al. 2008). Such variation in the tooth profile geometry has consequences for the contact and EHL behaviour between the gear teeth.

Kugimiya (1966) studied the profile modification effect on helical gear dynamic properties. The levels of vibration were reduced using a suitable modification.

Simon (1989) carried out an investigation on the optimal tip relief and axial crowning modifications in spur and helical gears . For the tip relief, only a linear profile was used while linear and parabolic functions were examined for the crowning modification. The amount and length of modification (for both tip relief and crowning) were used as parameters in this study to evalute the load and stress distributions. The fluid film effect was not considered in this study. The results presented suggested that the stress distribution is related to the parametrs of modification to a considerable extent.

Kahraman & Blankenship (1999) carried out an interesting experimental study to investigate the effect of tip relief modification on the vibration characteristics of spur gears. Linear tip relief modification only was considered in this study. The results showed that this type of modification is not optimum for applications that require a gearing system to operate under a wide range of torque and suggested that alternate forms of modification may be helpful.

Wagaj & Kahraman (2002) considered the effect of profile modification forms on the durability of helical gears by examining the contact and bending stresses. The effect of an EHL fluid film was not considered in this study. The contact mechanics models used in this study considered both 2D and 3D profile modifications. These two kinds of modification are illustrated in Figure 1.7. This study showed that for helical gears the 2D modification (which is the most common type of gear tooth modification where tip relief and lead crowning are applied) is not optimum due to the directional difference between the contact lines and the profile modifications. This difference was overcome by using the second proposed form (3D modification). The stresses were first calculated for unmodified gear teeth then compared with the corresponding results using the two modification methods. The calculated stresses were increased by a smaller amount when using the 3D modification.

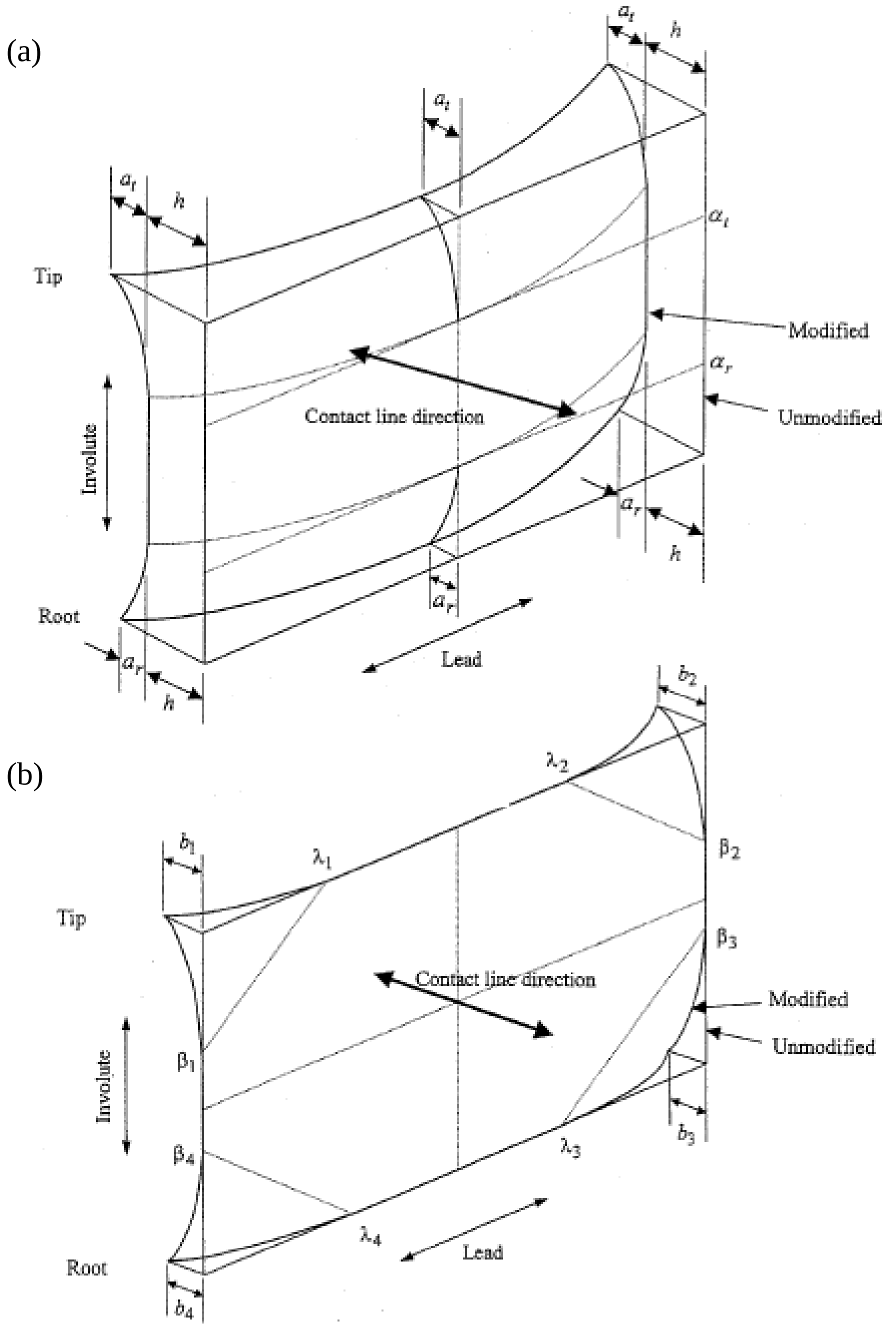

Figure 1.7: Modification of helical gear teeth, (a) 2D and (b) 3D.
(Wagaj & Kahraman 2002)

Despite the possibility of improving the durability of helical gears by using this 3D modification method, it is still not common due to the cost of production considerations (Kahraman et al. 2005). Kahraman et al. (2005) investigated the effect of profile modifications on helical gear wear and a design formula that explains the relation between the initial wear rate and the modification parameters was proposed.

Edge contact (i.e. at the transverse edge faces) between the tooth surfaces due to misalignment represents one of the major concerns in the design of helical gears. Designers of gear drives usually provide simple chamfers at the edges of the tooth, or more sophisticated crowning over the whole face width to avoid severe, and possibly damaging, contact. However, in practice edge contact still occurs in many cases. This is mainly because an accurate chamfer magnitude is not predetermined analytically as reported by Litvin et al. (2005) where the misalignment effect on the dry contact between helical gears having parallel axes was studied.

Sankar & Nataraj (2010) discussed a modified profile in their study on avoiding damage in helical gear teeth for the drives used in wind turbine generators. They used in addition to the tip relief modification a composite profile which consisted of epi-cycloid and involute parts. The resulting bending stresses in the gear teeth due to the power transmission between the gear drives were compared between the case when the new proposed profile was applied and the corresponding case where the classical involute profile was used. The composite profile was found more effective (showed lower levels of stress) in this specific application of helical gears as the wind turbine generators operate under severe conditions including high levels of fluctuation in the wind forces.

1.7 EHL analyses of gears.

The recent implementation of EHL in gear contact modelling started with spur gears as this type gives rise to a relatively simple contact (from the geometry point of view) and therefore can be modelled using a line contact model. Akbarzadeh & Khonsari (2008) presented steady state solutions for the EHL contact of spur gears. Thermal effects and surface roughness were taken into consideration in this study. The contact between the gears along the line of action was modelled as that between two cylinders having radii of curvature equivalent to those of the involute tooth profile.

Li & Kahraman (2010) provided a transient EHL analysis for the prediction of power losses in spur gears. The transient effect in the analyses of spur gear contacts was studied before that by Larsson (1997) when EHL results (pressure and film thickness) using a non-Newtonian fluid model were calculated throughout the meshing cycle of the gears. In this isothermal and smooth surfaces model solution it was found that the transient effect is most noticeable at the load transition positions ("change points"). The transient effect was also investigated when the surface velocities and radius of relative curvature varied during the meshing cycle, but this was found not to be as significant as the load effect at the load transitions.

The same transient effect on the EHL result at the change points was also found by Wang et al. (2004) when the thermal effect was taken into consideration in the analysis of the spur gear meshing cycle. The tooth surfaces were assumed to be smooth, and a Newtonian fluid model was used in this analysis.

A more advanced study for the EHL analysis of spur gear meshing cycle was presented by Li & Kahraman (2010) which focussed on transient effects in a non-Newtonian and mixed EHL model. The effect of profile modification was also investigated where a gentle tip relief and circular crown profile were considered. The comparison between steady state and corresponding transient EHL solutions was carried out for smooth surfaces. The surface roughness effect was studied in the transient case. The solution domain was fixed during the transient analysis which was $2.5\, a_{\max} \le x \le 1.5\, a_{\max}$ where $a_{\max}$ is the maximum half-Hertzian contact width during the meshing cycle. The results showed the significant difference between steady state and transient analyses of the gear meshing cycle (predominately due to the load variation) which emphasises the necessity of including the transient effect in the EHL analysis of gears. The consideration of surface roughness in the transient analysis had a significant effect on the prediction of the pressure distribution where pressure values of more than three times the corresponding smooth results were found. This high level of pressure was associated with breakdown of the film thickness at several locations.

More recently, analysis of EHL of the geometrically simpler spur gear type has also been reported by other workers. Wang et al. (2012) developed a transient EHL model in a study of the effects of impact loads during the meshing of spur gears. Dynamic loading of spur gear contacts under the EHL regime was also considered in a paper by Liu et al. (2013), which included a treatment of thermal effects.

Relatively little work is available in the literature about EHL analysis of helical gears particularly a full transient analyses of the meshing cycle. Simon (1988) investigated EHL analysis of helical gears using a point contact model with a consideration of thermal effects. This model considered only steady state analyses at a single position in the meshing cycle when the contact acts over the whole face width, and this did not give a complete picture of the variation of pressure distribution and film thickness during the whole meshing cycle.

Li et al. (2009) provided an advanced treatment by considering the helical gear to be represented as a number of thin slices of spur gears, with each individual slice modelled as a transient line contact EHL problem between two cylinders. The radius of each cylinder corresponded to the involute radius of curvature.

Ebrahimi Serest & Akbarzadeh (2013) presented a model to predict the EHL performance of helical gears taking into account both surface roughness and thermal effects. In this model, the helical gear was also treated as a series of narrow width spur gears.

Han et al. (2013) also used an equivalent EHL line contact approach for the contact of helical gear teeth, which included a consideration of roughness effects based on the simple model of load sharing by asperity contacts in mixed lubrication prepared by Johnson et al. (1972).

In considering the EHL behaviour associated with the edge contacts that occur where the nominal line of contact reaches the end faces of the gears or at the ends of relieved, crowned contacts, it is important to include the influence of *side leakage* of the lubricant because this will cause significant thinning of the lubricant film. Dealing with contact between modified profile teeth in helical gears as a line contact problem instead of point contact problem leads to the important side leakage effect being ignored.

1.8 3D line contact model

Surface roughness has great influence in the life of machine elements that involve power transmission through lubricated contact. The concentrated contacts at the asperities produce very high contact pressure which consequently increases the possibility of surface failure.

Previous studies mentioned in the above sections included well developed EHL point contact models which involved 3D rough surface analysis. Even though these models represent significant progress, there are limitations related to the size of the contact in both directions. From the surface roughness point of view such models may not be efficient enough to deal with relatively large contact areas. Gears are a typical example of such contacts where the contact length in one direction (along the face width) is considerably longer than the length in the nominally transverse direction. Using the point contact approach to model such contacts may limit the resolution and hence the accuracy along the larger length of the contact area. In addition, the classical EHL line contact approach may be far from accurate in modelling the 3D surface topography. These issues emphasize the advantage of developing a “3D Line contact” EHL model that has the ability to model a selected area of the contact region and include the real 3D surface roughness features without sacrificing the accuracy of the analysis.

In general, consideration of surface roughness in the analyses of contact problems requires fine computing grids in order to give realistic modelling for the surface features, which makes classical contact mechanics methods impractical in such analyses Polonsky & Keer (2000).

The calculation of surface elastic deformation is a fundamental issue in EHL analyses, particularly when fine grids and large numbers of grid points are used. Stanley & Kato (1997) used a numerical technique which involves the fast Fourier transform (FFT) method to obtain the surface deformation and contact pressure resulting from contact between an elastic half-space and a rigid plane. The FFT method which was first introduced by Cooly & Tukey (1965) is commonly used to speed up the process of convolution calculations as will be shown in chapter 7, and has been adopted in the present thesis.

Wang et al. (2003) compared discrete convolution and the fast Fourier transform method with other methods for the calculation of surface deformation. The method was found to be very efficient (from computing time point of view), particularly when a large number of grid points are used in the analyses of contact and EHL problems.

Chen et al. (2008) developed a 3D model to analyse the dry contact between flat surfaces with periodic surface roughness features. The fast Fourier transform method was used to calculate the discreet convolution that occurs in the numerical calculation of the surface elastic deformation. The model was modified to be applicable to the simulation line contact problems where the contact length is infinite in one direction and has a finite length in the other direction. In the latter case a mixed padding method was used in the FFT implementation which depends on duplicating the pressure distribution in the periodic direction (infinite length direction) and zero padding the pressure distribution in the other direction (finite and non-periodic length direction) as shown in Figure 1.8. The notation in this figure for the repeated domain in the periodic direction is duplicated padding while in the current work the notation is repeated domain or repeated solution space.

Ren et al. (2009) developed a novel 3D model which has the ability to analyse mixed lubrication for a finite length line contact problem with consideration of surface roughness.

In this analysis, the solution domain in the direction perpendicular (transverse) to the entrainment direction is cut to a finite length. The idea behind this model was based on considering the roughness feature as well as the pressure and film thickness distributions over this reduced space size as being repeated periodically in the transverse direction.

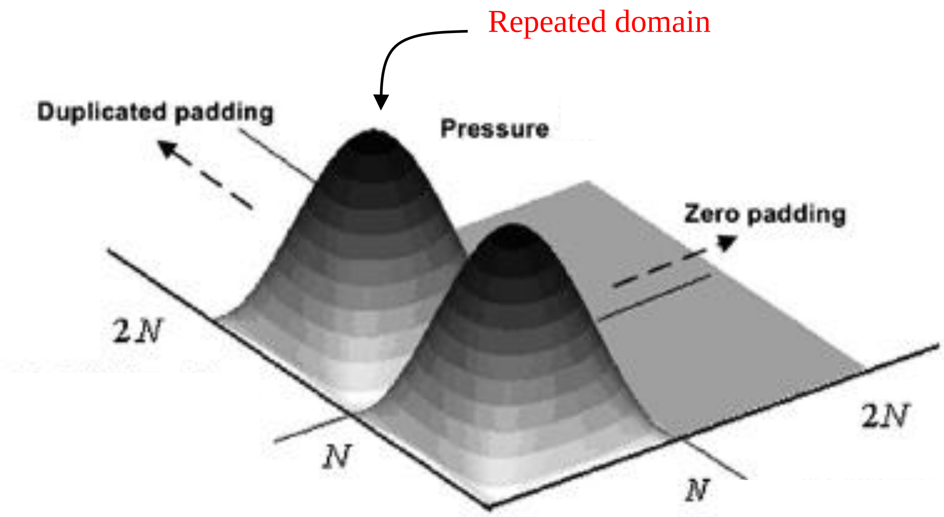

Figure 1.8: Mixed method for the solution of contact problems (Chen et al. 2008)

The elastic deformation of contacting surfaces was analysed using the same method by Liu et al. (2000) and a following development by Chen et al. (2008) where a discrete convolution and FFT were used based on the mixed padding method as mentioned previously. An example of a contact that can be analysed using the approach defined in this study is depicted in Figure 1.9. A simple roller and a flat plane together with the coordinate system are shown in Figure 1.9 (a). Figure 1.9 (b) illustrates how the contact length in one direction (y) is significantly larger than that in the other direction (x). The corresponding 3D line contact model is shown in Figure 1.10. The model has significant limitation as zero slope is assumed for the pressure with respect to the y direction at the boundaries of the solution space in the repeated direction. This assumption can only be correct if the roughness profile is extruded parallel to the y direction, or the solution domain has a groove at each of the repeated boundaries.

The 3D line contact model presented by Ren et al. (2009) was further developed by Zhu et al. (2009) to predict the pitting life of gears but retained the restriction of the no-flow condition at the transverse boundaries which is generally not the case for real 3D roughness conditions.

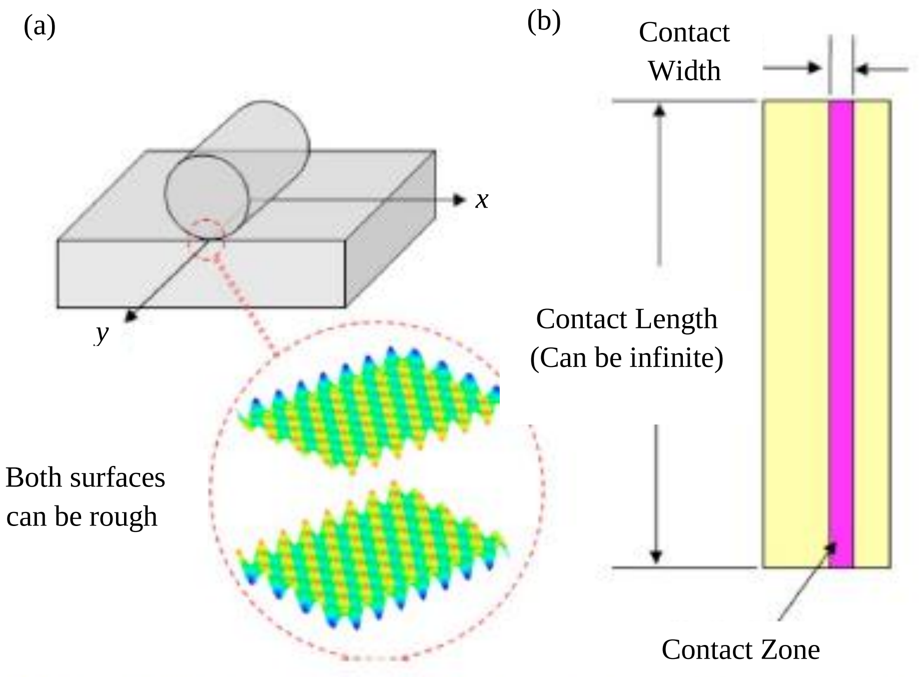

Figure 1.9: A contact can be analysed using the 3D line contact model. (a) A roller on a flat plate and (b) Contact zone dimensions (Ren et al. 2009)

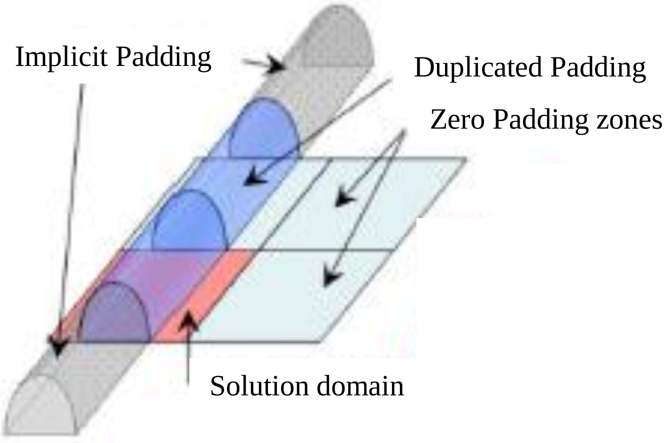

Figure 1.10: 3D line contact model for the contact shown in Figure 1.9 (Ren et al. 2009)

1.9 Software available as basis for research

At the onset of this research the author had access to existing EHL analysis software developed within the research group. This was in the form of a code to provide transient solution to the EHL point contact problem with non-Newtonian lubricant behaviour as an option choice. The code was developed in its simplest form by Holmes (2002), Holmes et al (2003a, 2003b) and developed for several particular engineering problems and lubricant formulations by Sharif et al (2001) and Sharif et al (2004).

In the current research new subroutines were developed and introduced to the EHL code to define the helical gear geometry and kinematic conditions occurring over the meshing cycle of the gear pair. This included the fundamental geometry as described in chapter 2, tooth crowning as described in chapter 4, various forms of tip relief as described in chapter 5 and faceting as described in chapter 6. These developments allowed the whole gear transient analyses reported in this thesis to be obtained.

For the consideration of surface roughness effects a new program was developed by significant adaptation of the transient EHL solver. This involved significant modifications to the fundamental algorithms carrying out the numerical analysis as reported in chapter 7.

1.10 Research objectives

The aims of the work reported in this thesis are concerned with the prediction of EHL film thickness and pressure at the tooth contacts of helical gears. These aims can be classified into three main categories:

- Carry out a full point contact transient EHL analysis for the helical gear meshing cycle and study the effects of including profile modifications on the results of this analysis. The tooth profile modifications considered involve different forms of tip relief and crowning in the axial direction.

- Study the effect of generating the tooth profile by a process that results in axial faceting on the transient EHL behaviour of helical gears.
- Develop a 3D line contact model based on a cyclic boundary condition concept in order to consider the rough surfaces EHL problem in gear contacts.

1.11 Thesis Organisation

This thesis consists of eight chapters, and the following is a brief description of the remaining chapters.

Chapter 2 addresses the contact geometry of helical gears where the total un-deformed gap between mating teeth is calculated, including the effect of profile modifications.

Chapter 3 discusses the EHL point contact problem and gives a brief description of the solution techniques used for the problem, including the Finite Element and Finite Difference methods.

Chapters 4 and 5 focus on the transient EHL solution for the meshing cycle of helical gears taking into account tooth profile modifications with the assumption of smooth surfaces. Chapter 4 deals with crowning modifications and Chapter 5 focuses on the effects of tip relief modifications considered.

Chapter 6 investigates the effect of axial faceting (due to the manufacturing process) of helical gear teeth on the transient EHL results, and compares the outcome with the corresponding smooth surface results given in Chapter 5.

Chapter 7 describes the development of a 3D line contact model for rough surfaces using cyclic boundary conditions.

Chapter 8 draws conclusions from the results obtained in the previous chapters, and also makes some suggestions for future work.

Chapter 2

Gear contact geometry

2.0 Introduction

The contacting characteristics of a pair of helical gears are different from that in spur gears. The motion is transmitted gradually and more smoothly between the mating gears. In a spur gear drive the contact occurs along a straight line which is parallel to the gear axis. The contact initiates suddenly over the full face width at the start of the tooth meshing cycle and also ends abruptly at the end.

In contrast, the contact between a pair of helical gears starts at the first tooth face end as a point. As the gears rotate, the contact extends from being point to a line of steadily increasing length which moves over the tooth flank extending in length until it reaches the second tooth face. The contact line length subsequently reduces and ends as a point at the second tooth face end. The line of contact acts diagonally between the face ends of the helical teeth. In addition, there are at least two pairs of teeth always in contact when using helical gear drives.

The nature of tooth meshing in helical gears is illustrated in Figure 2.1. Figure 2.1 (a) shows the contact conditions at an instant of the gear meshing cycle where two pairs of teeth are in contact, $z_1 z_1'$ and $z_2 z_2'$. Figure 2.1 (b) illustrates the contact at a further position in the meshing cycle where teeth pair $z_1 z_1'$ leaves the contact. Meanwhile the contact line of teeth pair $z_2 z_2'$ moves away from the lower gear tooth tip. This figure shows another pair of teeth coming into contact as shown in the figure on the right side.

Figure 2.2 depicts a comparison between helical and spur gear drives, which shows the directional difference of the line of contact in the two drives as well as the inclination of the line of contact between helical gear teeth relative to the gear axis as a result of the helix angle .

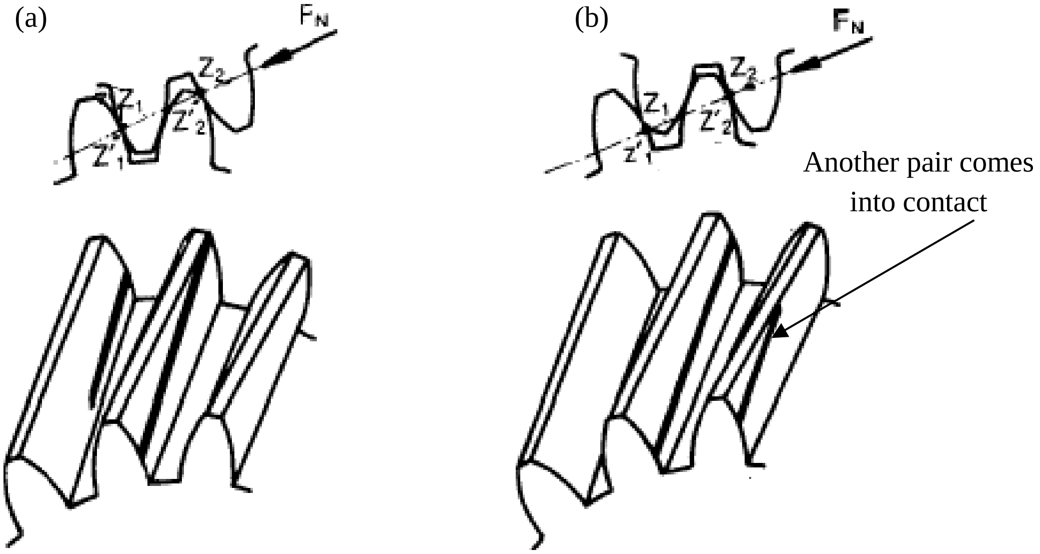

Another pair comes into contact

Figure 2.1: Nature of tooth engagement in helical gear drive (Maitra 1994).

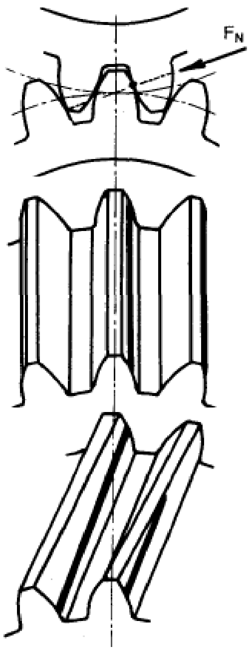

Figure 2.2: Comparison between spur and helical gear contact, transverse section (upper figure), spur gear (central) and helical gear (lower) (Maitra 1994).

In order to perform EHL analysis of contacting surfaces such as gears, which is the purpose of the current work, the contact geometry needs to be determined as a first step of such analysis. However, analysis of this kind of contact involves challenges. The major difficulty is related to the continuous changing of contact geometry and kinematic throughout the gear meshing cycle. These are mainly consequences of the nature of the involute gear tooth profile having a different radius of curvature at each profile point in addition to the movement of the point under consideration along the tooth profile. Therefore, before proceeding to determine the gear geometry, it is necessary to understand the way in which gears contact.

Figure 2.3 shows a schematic drawing of a transverse section of a pair of gears in contact. This drawing applies to both spur and helical gears. Any pair of meshing involute teeth develops contact along the straight line AB which is tangent to the gear base circles. This line is termed as the line of action and is inclined to the line perpendicular to the gear centres line O_1O_2 at an angle ψ termed the pressure angle.

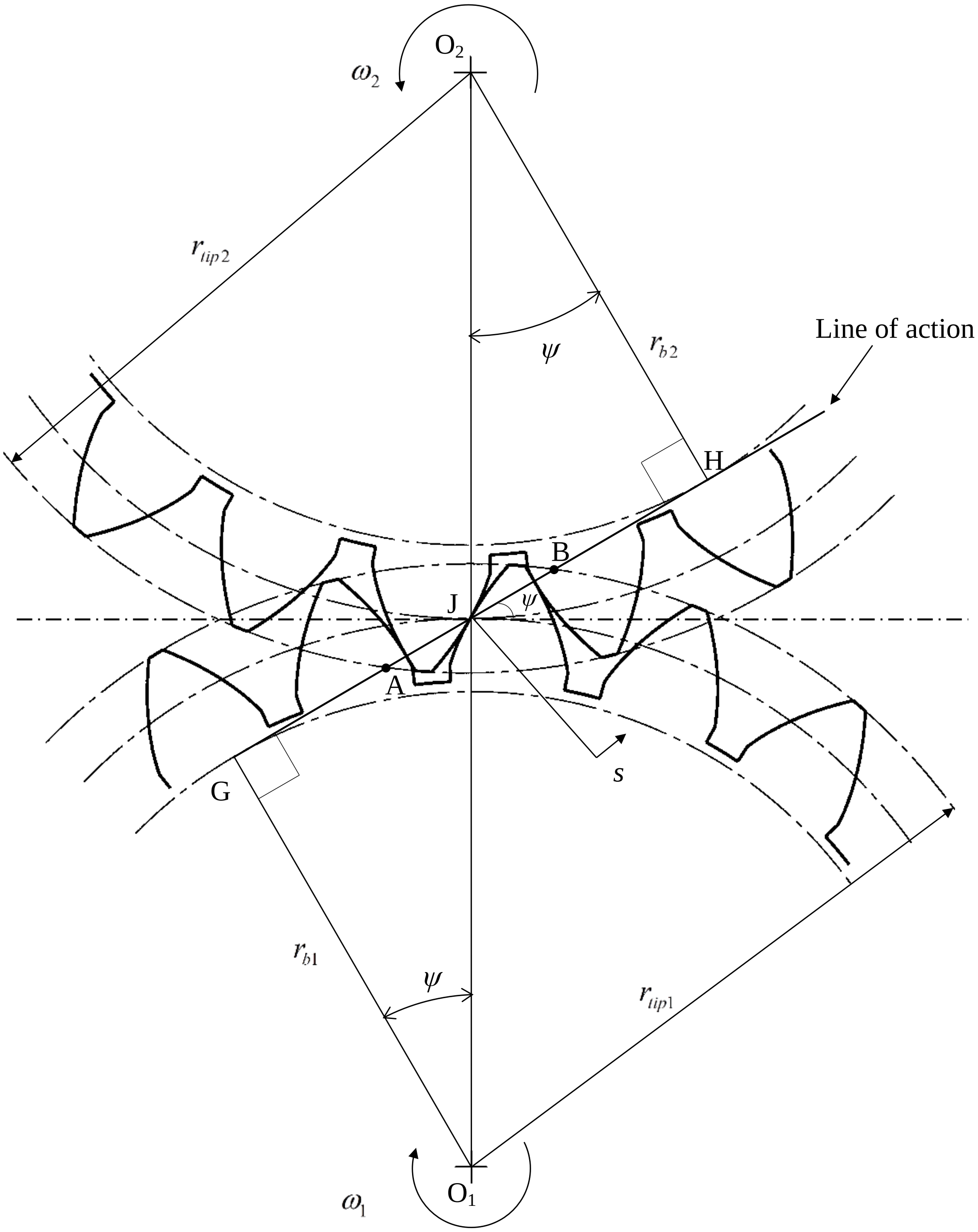

Figure 2.3: Involute gears in contact. Note that the root form in this figure is shown schematically as a rectangular recess.

2.1 Path of contact in the transverse plane

Points A and B in Figure 2.3 represent the first and last points of the path of contact respectively and correspond to the intersection of the line of action with the two tip circles of the gears. The position of these points can be determined in terms of distance, s, where s is the distance from the pitch line to the contact point considered measured along the line of action, taken as positive in the direction of motion of the contact. Denoting the positions of points A and B by s_{min} and s_{max} respectively, the length of the path of face contact is :

$$\mathrm{AB} = s_{\max} - s_{\min} \tag{2.1}$$

The minus sign is due to the negative value of s_{min} , These limits of the path of contact can be determined from the geometry of the triangles outlined in Figure 2.4 as follows:

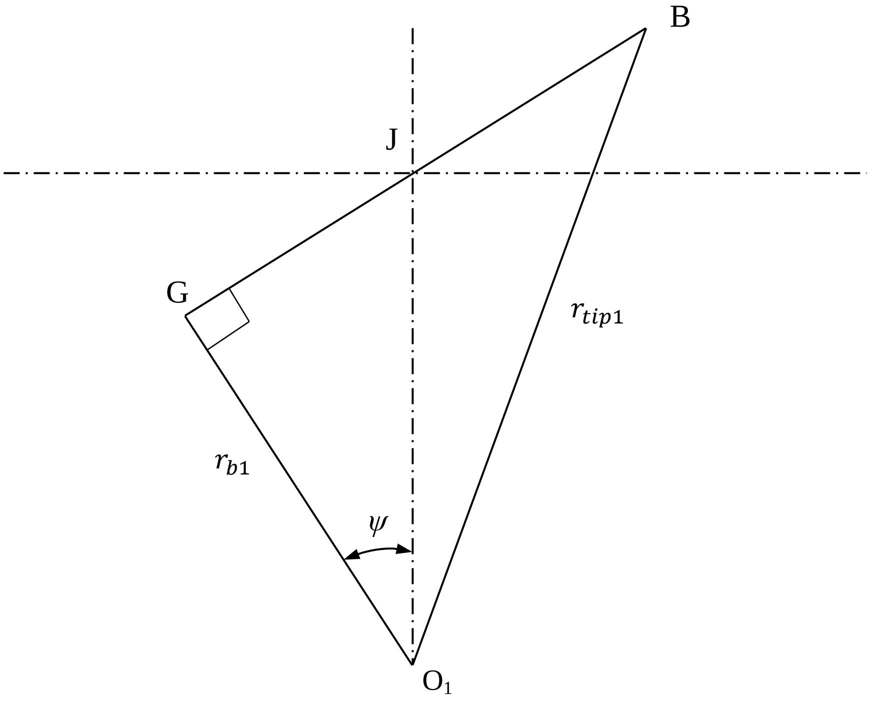

Figure 2.4: Schematic geometry for the pinion

Considering triangle O_1GJ the distance GJ is given by:

$$\mathrm{GJ} = r_{b1} \tan\psi$$

The distance GB can be obtained from the triangle O_1GB as:

$$\mathrm{GB} = \sqrt{r_{tip1}^2 - r_{b1}^2}$$

Therefore, the position of the last point of contact, s_{max} is determined from

$$s_{\max} = \mathrm{GB} - \mathrm{GJ}$$

$$s_{max} = \sqrt{r_{tip1}^2 - r_{b1}^2} - r_{b1} \tan\varphi \tag{2.2}$$

Similarly the position of the first point of contact, s_{min} is given by

$$s_{min} = r_{b2} \tan\varphi - \sqrt{r_{tip2}^2 - r_{b2}^2} \tag{2.3}$$

where, subscript 1 is used to define the pinion (which is the lower gear), and subscript 2 refers to the wheel, r_b is the radius of base circle and r_{tip} is the tip radius.

The velocity of the contact point as the contact progresses along the line of action between s_{min} and s_{max} is constant and is given by:

$$u_{contact} = r_{b1}\omega_1 = r_{b2}\omega_2$$

This equation can be used to determine the total time that is required to complete the meshing cycle of a pair of teeth in contact. The time for contact to occur at a given axial position is

$$t_{contact} = (s_{max} - s_{min}) / u_{contact}$$

and the time for a pair of teeth to complete their meshing cycle in a pair of helical gears is (see Figure 2.5)

$$t_{contact} = (s_{max} - s_{min} + F \tan \beta_b) / u_{contact} \tag{2.4}$$

2.2 Zone of contact in helical gears

The contact between any pair of teeth occurs within the zone ABCD that is shown in Figure 2.5. This rectangular zone is tangential to the base cylinders of the gears and is called the plane of contact. It is limited by the end faces at AB and DC, and the tip cylinders of the mating gears at DA and CB (Tuplin 1962).

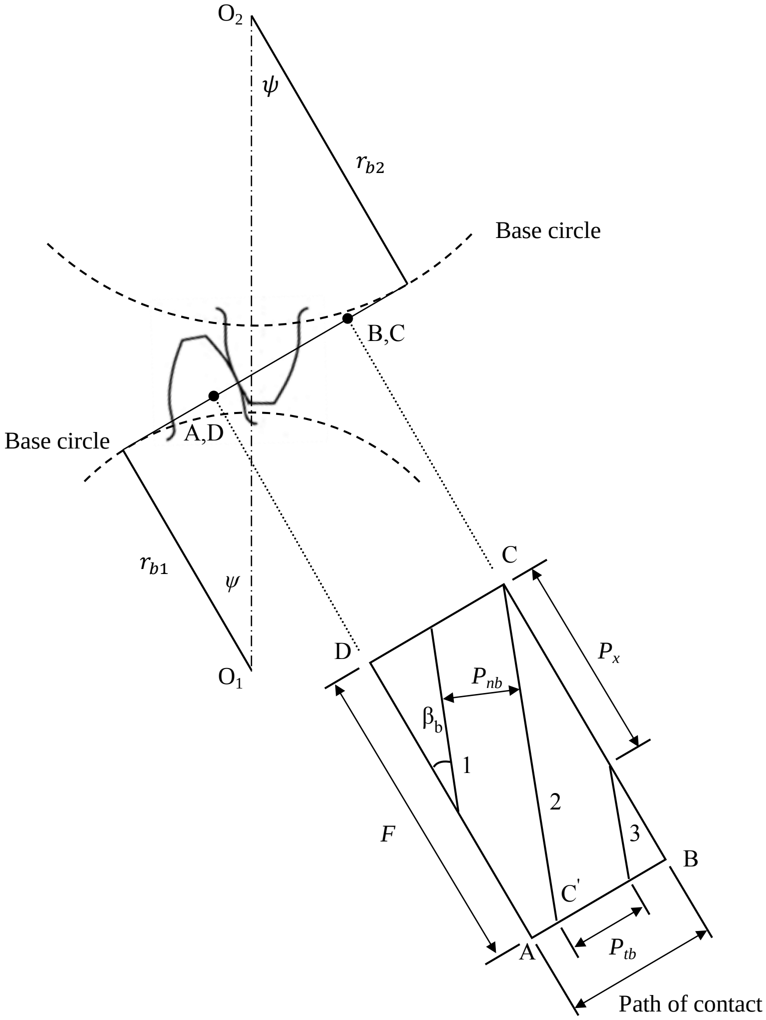

.

Figure 2.5: Zone of contact of a pair of helical gear teeth,
P_x: axial pitch, P_{tb}: transverse pitch , O_1O_2: center distance

The contact begins at point D which then extends to be a line inclined at the base helix angle β_b to the gear axis as shown by the typical contact lines 1, 2 and 3 in this figure. The contact is limited by the boundaries of the zone of contact, i.e. one or both of the side edges and the tip cylinder boundaries.

In the depicted tooth contacts, line 2 intersects CD at C at one end, and intersects AB at C′ at the other end. Other, simultaneous, contacts occur on parallel straight lines at normal spacing, P_{nb} . The number of these lines depends on the transverse contact ratio of the gears.

2.2.1 Length of line of contact

As mentioned previously the contact between a pair of teeth in spur gears is a straight line. The length of this line is equal to the face width of the tooth and this length remains constant at all positions in the meshing cycle. This line is parallel to the axes of the gears. On the other hand for a helical gear pair, due to the nature of the contact as illustrated in Figure 2.5, the length of the line of contact generally depends on the face width (F), base helix angle (β_b), and the position (s_i) in the meshing cycle, where s_i is defined as the s coordinate at which the line of contact intersects boundary AB of the plane of contact as seen in Figure 2.6.

In order to determine the length, L, of the line of contact in a general form for any pair of helical gears and at any position in the meshing cycle, three different cases need to be considered. The classification depends on the relation between the face width and the path of contact (distance AB that was given by equation (2.1)). These cases are $F \tan\beta_b <$ AB, $F \tan\beta_b =$ AB and when $F \tan\beta_b >$ AB. Figures 2.6 (a), (b) and (c) show the variation of the line of contact length with the position s_i on the line of action for the three cases, respectively. It can be shown from these figures that the required equations to calculate the contact line length for each case are as follows:

Case 1: $F\tan\beta_b <$ AB

$$L_i = \frac{F}{cos\,\beta_b} - \frac{s_{min} - s_i}{sin\,\beta_b} \qquad \text{for} \qquad s_{min} - F\,tan\,\beta_b \le s_i \le s_{min}$$

$$L_i = \frac{F}{cos\,\beta_b} = L_{max} \qquad \text{for} \qquad s_{min} \le s_i \le s_{max} - F\,tan\,\beta_b$$

$$L_i = \frac{s_{max} - s_i}{sin\,\beta_b} \qquad \text{for} \qquad s_{max} - F\,tan\,\beta_b \le s_i \le s_{max}$$

Case 2: $F\tan\beta_b =$ AB

$$L_i = \frac{F}{cos\,\beta_b} - \frac{s_{min} - s_i}{sin\,\beta_b} \qquad \text{for} \qquad s_{min} - F\,tan\,\beta_b \le s_i \le s_{min}$$

$$L_i = \frac{s_{max} - s_i}{sin\,\beta_b} \qquad \text{for} \qquad s_{min} \le s_i \le s_{maxx}$$

Case 3: $F\tan\beta_b >$ AB

$$L_i = \frac{F}{cos\,\beta_b} - \frac{s_{min} - s_i}{sin\,\beta_b} \qquad \text{for} \qquad s_{min} - F\,tan\,\beta_b \le s_i \le s_{max} - F\,tan\,\beta_b$$

$$L_i = \frac{s_{max} - s_{min}}{sin\,\beta_b} = L_{max} \qquad \text{for} \qquad s_{max} - F\,tan\,\beta_b \le s_i \le s_{min}$$

$$L_i = \frac{s_{max} - s_i}{sin\,\beta_b} \qquad \text{for} \qquad s_{min} \le s_i \le s_{maxx}$$

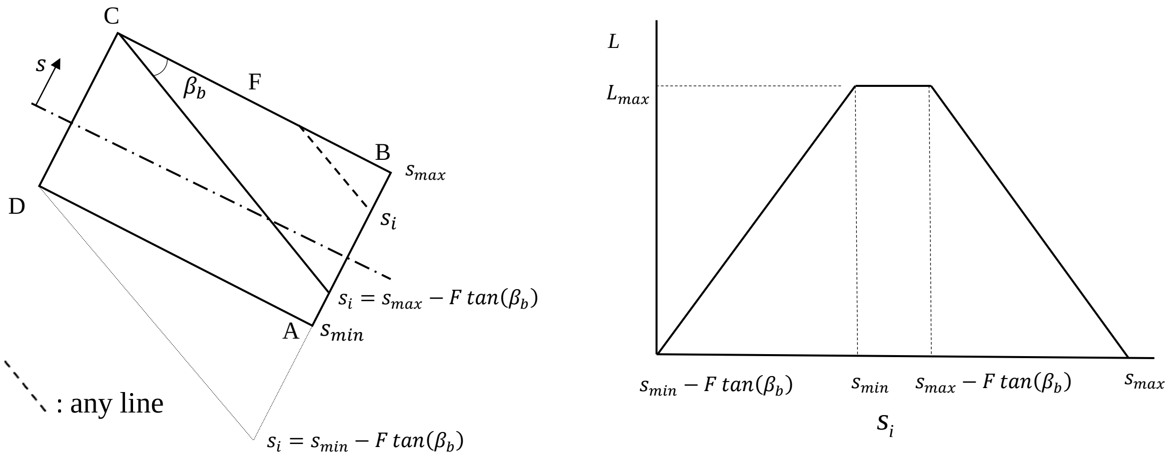

(a) : $F\,tan(\beta_b) < $ path of contact

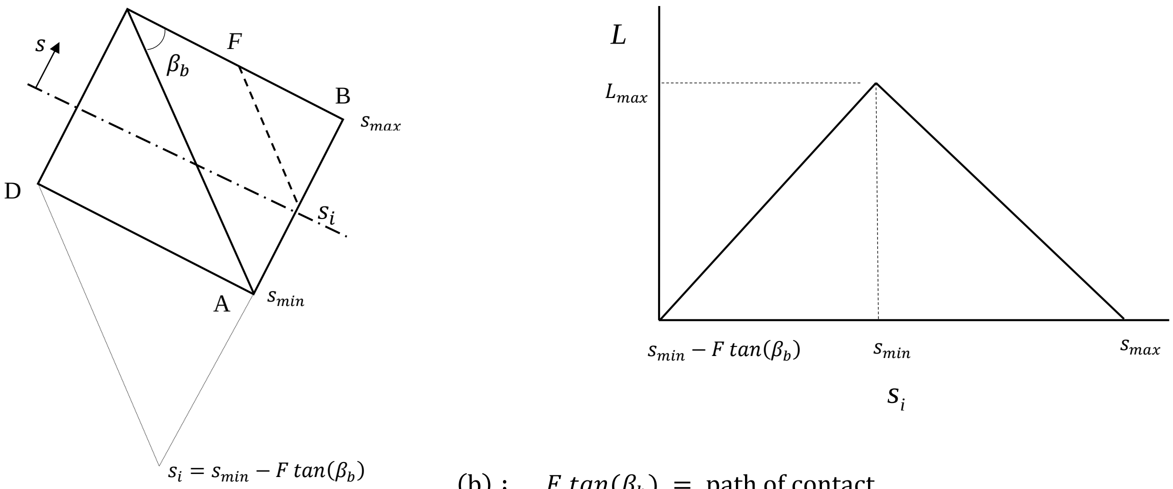

(b) : $F\,tan(\beta_b) = $ path of contact

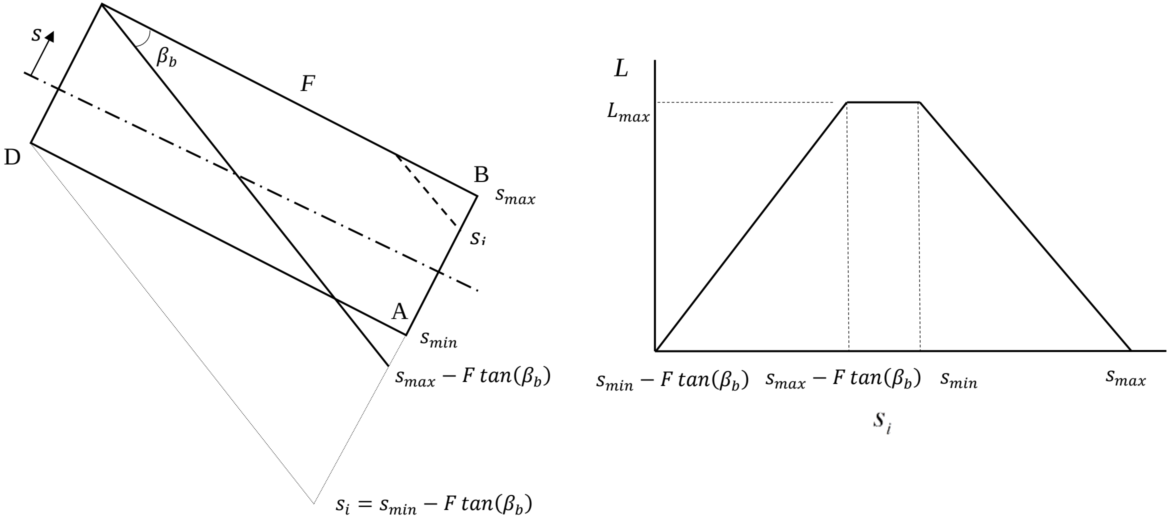

(c) : $F\,tan(\beta_b) > $ path of contact

Figure 2.6: Variation of the length of line of contact with the position s_i.

2.3 Contact geometry

In an ideal line contact, such as that between cylindrical rollers, the elastic contact is of uniform rectangular shape under load. In helical gears this nominal contact area becomes distorted in three ways. First, there is a variation in the radius of relative curvature in the normal plane along the contact line due to the curvature of the involute teeth changing from root to tip. Second, the introduction of tooth "tip relief" (used to prevent premature tooth engagement under load) can, depending on the form used, cause a local stress-raising discontinuity in the curvature of the tooth profile. Third, axial profile relief (used to prevent edge contact at the side faces of the gears under misalignment conditions) transforms the line contact into a nominal point contact.

The gap between the contacting surfaces in many machine components such as gears, bearings, cams, etc. can be represented or approximated by that between a plane and a parabola which presents good geometrical agreement in the close vicinity of the contact as shown in Figure 2.7. The gap between each surface and the contact plane as shown in Figure 2.7 (a) is determined by:

$$z_1' = x^2 / 2R_1' \tag{2.5}$$

$$z_2' = x^2 / 2R_2' \tag{2.6}$$

The total gap between the surfaces, h_u, is given by:

$$h_u = z_1' + z_2' = \frac{x^2}{2R_1'} + \frac{x^2}{2R_2'} = \frac{x^2}{2R'}$$

where R' is the equivalent radius of relative curvature for both surfaces as shown in Figure 2.7 (b) which is given by

$$\frac{1}{R'} = \frac{1}{R'_1} + \frac{1}{R'_2}$$

In the spur gear case, the contact may be approximated by two rollers as shown in Figure 2.8. The radii of these rollers are equal to the local involute radii of curvature (i.e. the tangential distance between the contact point and the base circle). Thus, the radii of curvature at any point of contact can be determined by:

$$R'_1 = r_{b1}\, tan\,\psi + s \qquad (2.7)$$

$$R'_2 = r_{b2}\, tan\,\psi - s \qquad (2.8)$$

The total gap can then be evaluated by substituting these radii in equations (2.5) and (2.6) respectively.

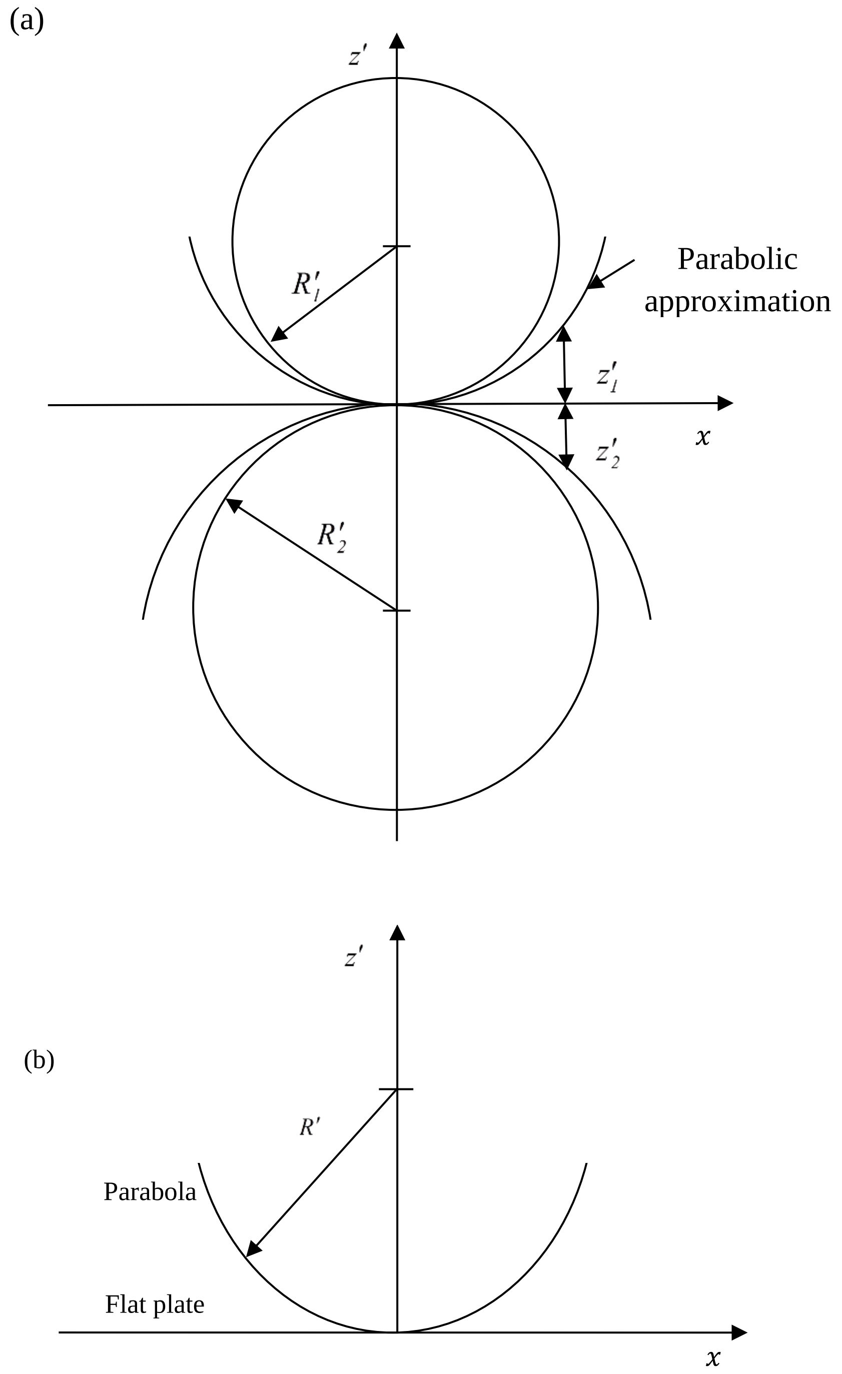

Figure 2.7: Geometry and coordinate system, (a) curvature of both surfaces, (b) equivalent system

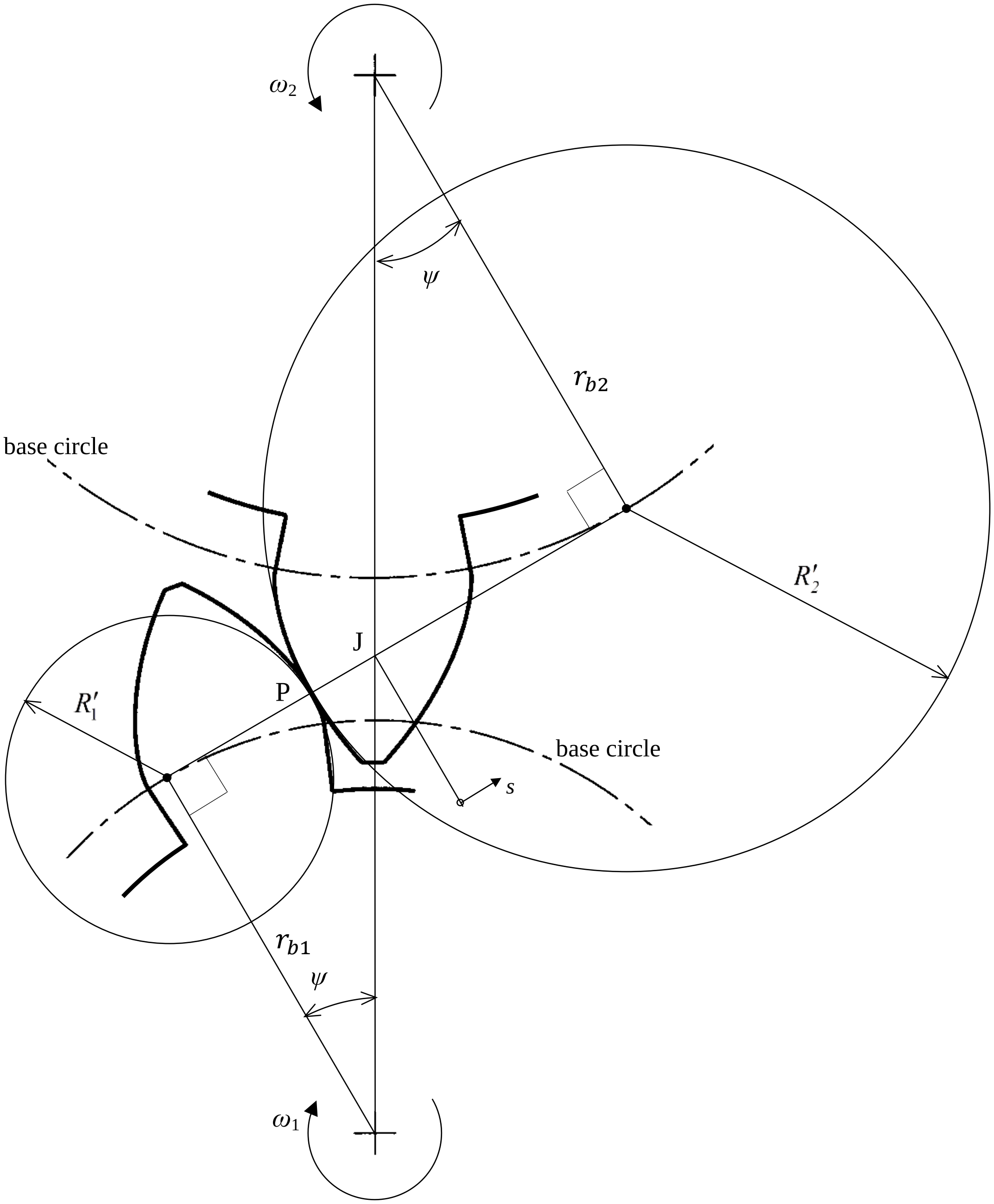

Figure 2.8: Involute gear teeth showing equivalent rollers of radius R_1' and R_2' at the contact P.

Unlike the spur gear geometry, in a helical gear pair each point on the line of contact has a different radius of relative curvature.

By using the spur gear contact approximation the contact between a pair of helical gear teeth can be also modelled with some modifications. Figure 2.9 shows a line of contact EE' for a helical gear which moves in the plane of contact. Point O is fixed at the middle of the face width. The common normal to the contacting helical gears teeth is Oz and the common tangent plane at the line of contact is $\mathrm{O}xy$.

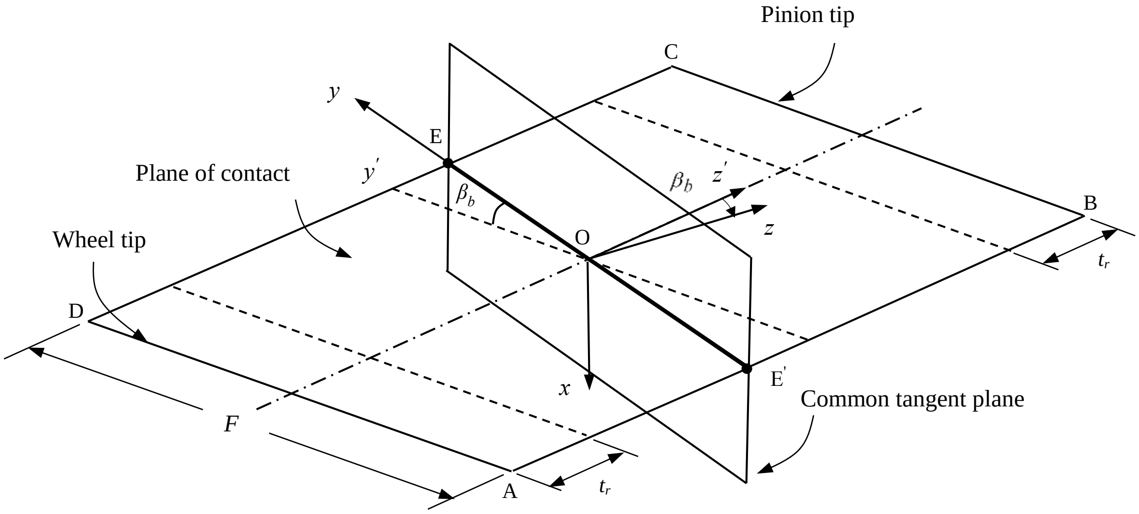

Figure 2.9: Surface of action and contact line tangent plane, t_r: tip relief zone

The required gap for the contact between the pair of spur gears is least in the transverse direction $\mathrm{O}z'$. In helical gears the generation of a lubricant film between the contacting teeth depends on the gap between them in the normal direction, Oz, and also depends on the motion of the surfaces relative to the contact line. The relative motion between the tooth surfaces and the contact line takes place in the Ox direction.

Figure 2.10 (a) shows tangent, normal and transverse planes at a specified point, P on the line of contact. In order to determine the gap for the first surface at this point , suppose point $P_1(x, y, z)$ is the point of intersection between curve 1 which has a radius of R_1 and curve 2 which has a radius R_1' as illustrated in Figure 2.10 (b) , where :

R_1 : radius of curvature in the normal direction at point P.

R_1' : radius of curvature in the transverse direction at another point P_1' on the line of contact.

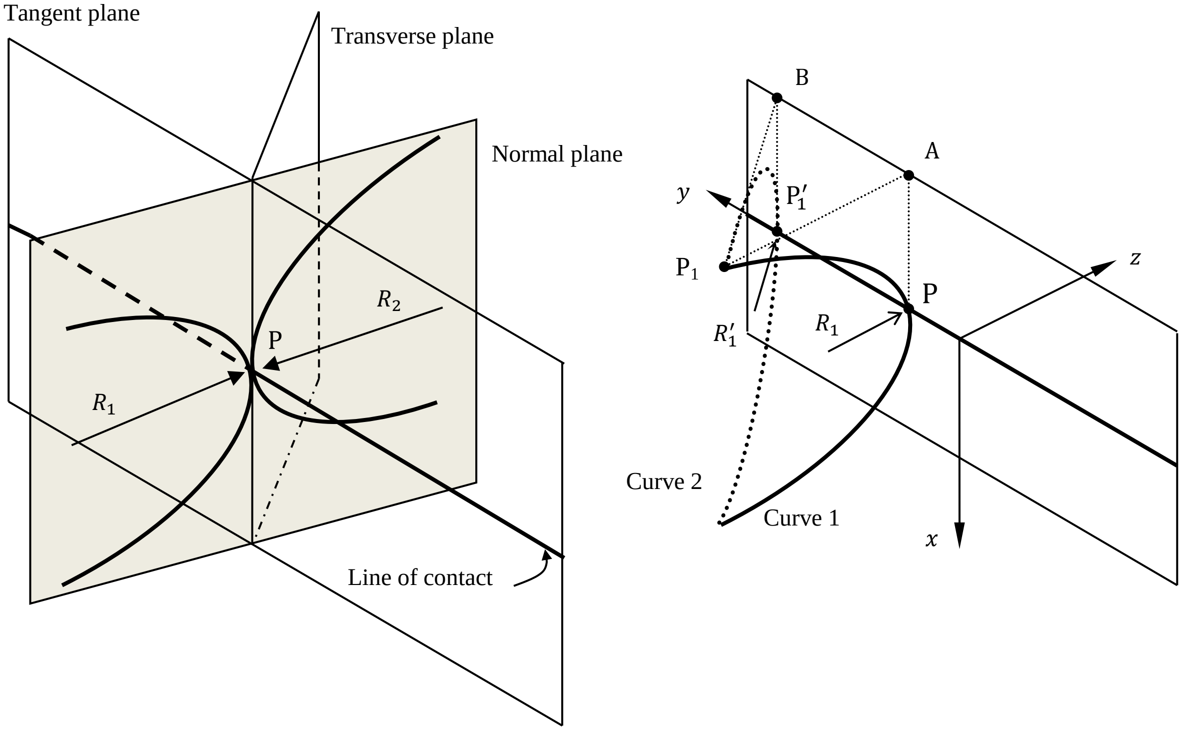

a- Tangent ,normal and transverse planes at point P

b- The gap at point P_1 determined by the curvature R_1' at point P_1' in the transverse plane

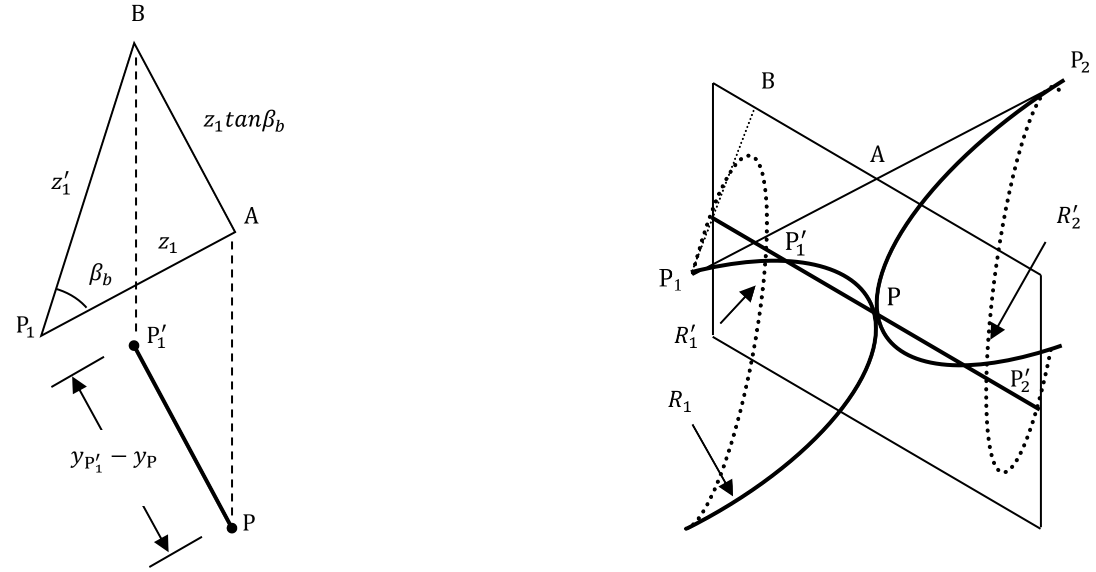

c- Relation between the transverse (z') and normal (z) gaps at point P_1

d- Both surfaces

Figure 2.10: Contact geometry of helical gears teeth

The distances between the points shown in Figure 2.10 (b) are clarified in Figure 2.10 (c). In this figure the gap in the transverse direction at point P_1 is equal to the distance P_1B and can be obtained using equation (2.5) as

$$P_1B = z_1' = \frac{x^2}{2R_1'\left(y_{P_1'}\right)} \tag{2.9}$$

As mentioned previously the normal direction is inclined by an angle β_b to the transverse direction. Therefore, the corresponding gap at this point in the normal direction is the distance P_1A, where:

$$P_1A = z_1 = z_1' \cos\beta_b \tag{2.10}$$

Substituting equation (2.9) into equation (2.10) gives:

$$z_1 = \frac{x^2 \cos\beta_b}{2R_1'\left(y_{P_1'}\right)}$$

which gives the relation between z_1 and x.

It can be seen from Figure 2.10 (c) that:

$$y_{P_1'} = y_P + z_1 \tan\beta_b$$

For each point on curve 1 there is a corresponding curve 2 from which the gap in the transverse direction can be determined.

Therefore, the radius of curvature R_1' depends on the x, y and z coordinates of the point on curve 1. Generally, at any point on curve 1, the contact geometry is given by:

$$z_1(x,y) = \frac{x^2 \cos\beta_b}{2R_1'\left(y + z_1 \tan\beta_b\right)} \tag{2.11}$$

For a given (x,y) position in order to evaluate z_1 this equation needs to be applied recursively with the radius of curvature obtained by modifying its argument $R'_1(y+z_1\,tan\,\beta_b)$ with successive z_1 values until converged. The radius of curvature R'_1 is obtained from the spur gear geometry in terms of the contact position s, which is known in terms of y and z_1 as discussed below. A similar equation can be obtained for the second surface. Taking into consideration that $y_{\mathrm{P}'_2}$ is given by:

$$y_{\mathrm{P}'_2} = y_{\mathrm{P}} - z_2 \tan\beta_b$$

the gap z_2 on the other side of the contact is given by:

$$z_2(x,y) = \frac{x^2\,cos\,\beta_b}{2R'_2(y - z_2\,tan\,\beta_b)} \tag{2.12}$$

The total undeformed gap h_u in the normal direction is the combination of the two distances z_1 and z_2 (i.e. $h_u = z_1 + z_2$).

It is worth noting that for helical gears the distance s varies with the position y along the line of contact as shown in Figure 2.11, where a single line of contact is illustrated. Therefore, s can be given by:

$$s = s_i + \left(y + \frac{F}{2\cos\beta_b} \right)\sin\beta_b \tag{2.13}$$

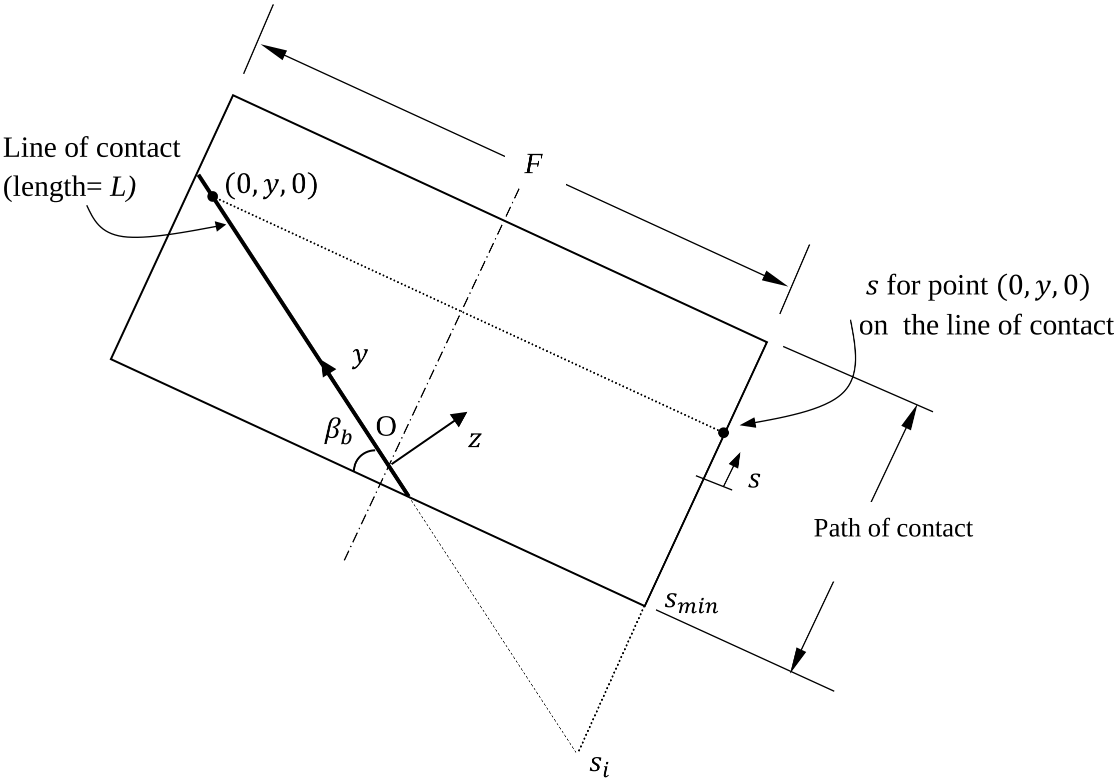

Figure 2.11: Variation of s with the position on the line of contact, y.

Thus, the radii of curvature at a given s position on the line of contact can be obtained by subsuming equation (2.13) into equation (2.7) and (2.8).

2.4 Tip relief

The implementation of tip relief leads to a decrease in the length of the path of contact as shown in Figure 2.12 (a). Point B represents the last point of contact along the line of action when no modification is made to the tooth profile, while point Q will be the last engagement point if tip relief is applied. Therefore, the length of the path of contact is reduced by an amount equal to the distance QB due to tip relief of the pinion teeth. This can be determined from the triangles shown in Figure 2.12 (b) as follows:

$$\mathrm{GQ} = \sqrt{r_{start1}^2 - r_{b1}^2}$$

$$\mathrm{GB} = \sqrt{r_{tip1}^2 - r_{b1}^2}$$

$$\mathrm{QB} = \mathrm{GB} - \mathrm{GQ}$$

$$z_p = \sqrt{r_{tip1}^2 - r_{b1}^2} - \sqrt{r_{start1}^2 - r_{b1}^2} \tag{2.14}$$

where,

z_p : equal the distance QB

r_{start}: radius of relief starting point.

Similarly, as shown in Figure 2.12 (c) due to tip relief of the wheel teeth the path of involute contact is also reduced by z_w, where,

$$z_w = \sqrt{r_{tip2}^2 - r_{b2}^2} - \sqrt{r_{start2}^2 - r_{b2}^2} \tag{2.15}$$

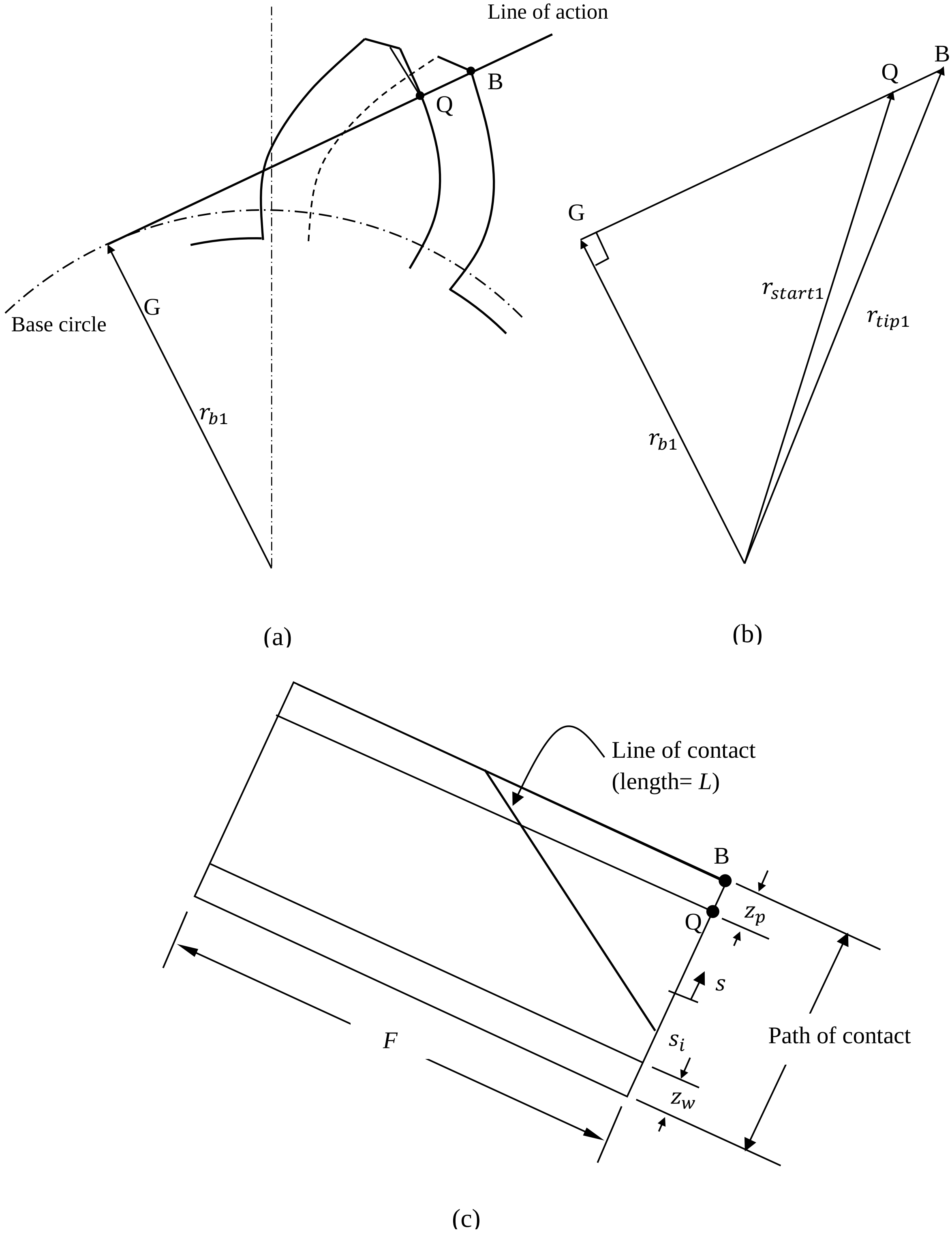

Figure 2.12: Tip relief of the gear teeth

2.4.1 Undeformed geometry due to tip relief

The undeformed gap due to the profile modification needs to be determined in order to obtain the total gap between any pair of teeth in contact as a part of the EHL analysis. Figure 2.13 shows point P on a pinion tooth for which the amount of relief needs to be determined. The x-axis is tangent to the involute profile at the contact point, and point P is in the negative x-direction. It can be shown by considering triangle OPT that:

$$r(x,y)=\sqrt{(r_{b1}-x)^2+(r_{b1}\,tan\psi+s-z_1')^2} \tag{2.16}$$

where,

r : distance from the center of the pinion base circle to point p.

z_1' : gap between the involute profile and x-axis in the transverse direction.

The amount of relief, z_t, is a function of the radius r according to the manufacturing setting as will be shown in chapter 5.

Similarly, for the wheel tooth:

$$r(x,y)=\sqrt{(r_{b2}+x)^2+(r_{b2}\,tan\psi-s-z_2')^2} \tag{2.17}$$

In contrast to the pinion the x-axis is negative towards the root of the wheel which gives a different sign for x in equation (2.17). It is worth mentioning that these equations are applicable at any transverse section on the contact line as s is y dependent as explained previously.

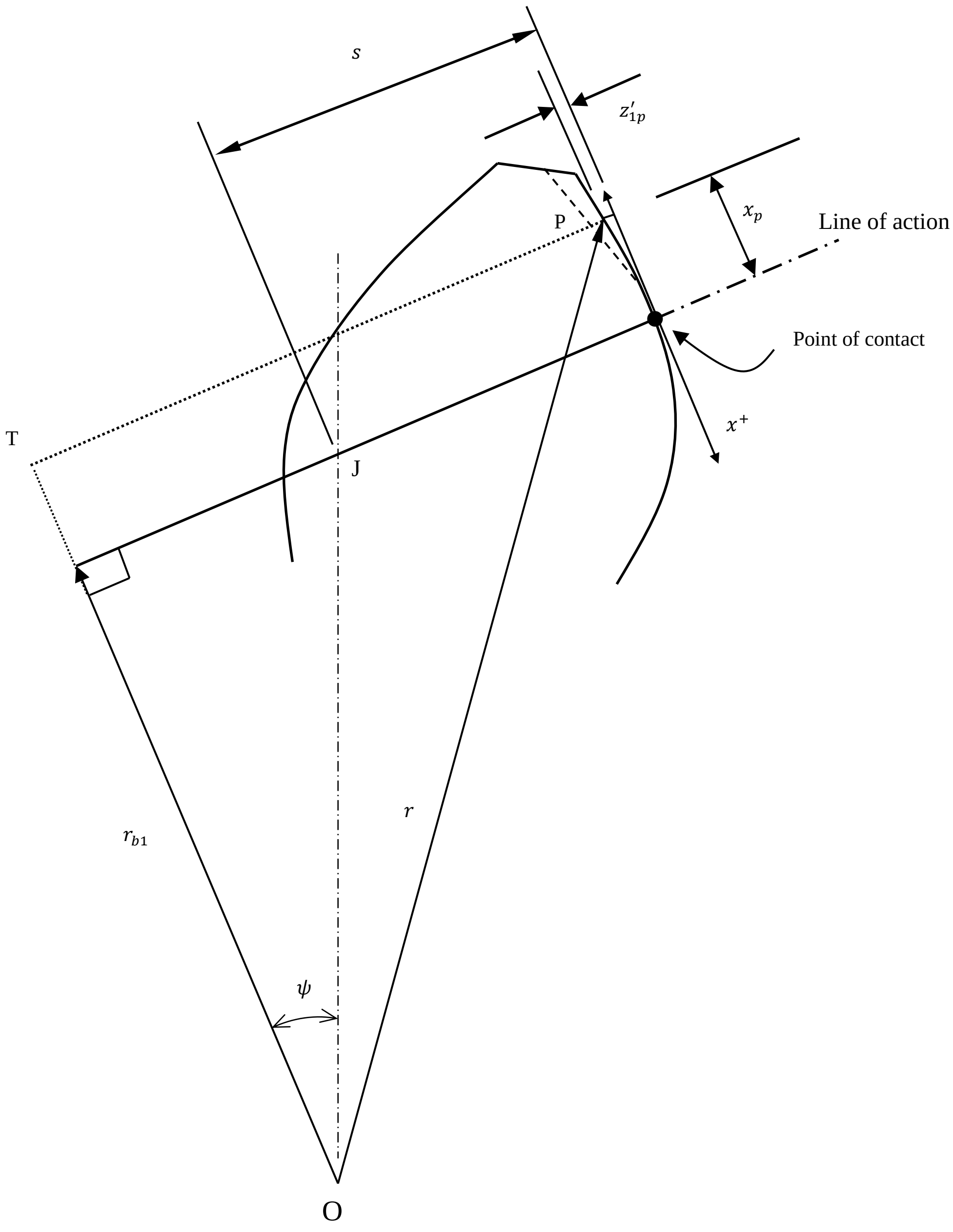

Figure 2.13: Undeformed geometry due to tip relief of the pinion

2.5 Crowning of the gear teeth

Heavy end of tooth contacts at the side edges of the gears, which result from lack of parallelism between the gear axes due to mounting errors or shaft deflections under load, can be alleviated by axial crowning of the teeth. Axial crowning is expressed in terms of a radius that provides a transverse clearance c_r for each tooth at the side edges when contact occurs at the centre of the gear under zero load. The gap due to this modification, $z_c(x,y)$, will be considered in detail in chapter 4.

2.6 Total undeformed geometry

At a given x and y position, the distances $z_1(x,y)$, $z_2(x,y)$, $z_t(x,y)$ and $z_c(x,y)$ can be combined to give the total gap between any two teeth in contact measured normal to the tangent plane as:

$$h_u(x,y) = z_1(x,y) + z_2(x,y) + z_t(x,y) + z_c(x,y) \tag{2.18}$$

As the contact position changes throughout the meshing cycle from point D to point B in Figure 2.5, the time varying total gap, $h_u(x,y)$ needs to be identified in advance before solving the equations that describe the EHL problem for the gears.

Chapter 3

EHL point contact problem and solution methods

3.0 Introduction

The EHL problem is described by two basic equations which are the elastic deformation equation and the hydrodynamic equation. This chapter gives a brief description of these equations for the point contact problem together with some related equations, and also considers the discretization of these equations using both the finite element method (FEM), and the finite difference method (FD). More details about the discretization analysis can be found in Holmes (2002) where a full description for a point contact software developed by Cardiff Tribology Group is also available. The basic transient EHL point contact solver that described in this chapter was made available to the author as a starting point for this research as described in section 1.9

3.1 The hydrodynamic equation

The hydrodynamic equation is the well-known Reynolds equation which has the following form for the 2D problem:

$$\frac{\partial}{\partial x}\left(\sigma_x \frac{\partial p}{\partial x}\right)+\frac{\partial}{\partial y}\left(\sigma_y \frac{\partial p}{\partial y}\right)-\frac{\partial}{\partial x}\left(\rho \bar{u} h\right)-\frac{\partial}{\partial y}\left(\rho \bar{v} h\right)-\frac{\partial}{\partial t}\left(\rho h\right)=0 \tag{3.1}$$

where

$\bar{u}=\left(U_1+U_2\right)/2$ and $\bar{v}=\left(V_1+V_2\right)/2$.

For Newtonian oil behaviour the flow factors are

$$\sigma_x=\sigma_y=\frac{\rho h^3}{12\eta} \tag{3.1a}$$

Non-Newtonian behaviour is considered in detail in section 3.9.

3.2 The Elastic deformation equation

The total gap between two contacting surfaces can be approximated by that between an equivalent paraboloid and a plane as explained in section 2.3 (chapter 2). Figure 3.1 illustrates schematically a section at the centre of the contact between these surfaces under load along the entrainment direction, *x*, from which the film thickness equation can be written as

$$h(x,y) = h_u(x,y) + d(x,y) + h_o \tag{3.2}$$

where $h_u(x,y)$ is the undeformed gap between the two surfaces, $d(x,y)$ is the surface elastic deformation and h_o is a constant that represents the distance of common approach. The calculation of the undeformed gap between helical gears teeth was shown in detail in Chapter 2. The surface elastic deformation is evaluated using the equation for the deflection of a semi-infinite body subjected to a surface pressure loading, $p(x,y)$ as given by Timoshenko and Goodier (1951), for example.

$$d(x_1, y_1) = \frac{2}{\pi E'} \iint_A \frac{p(x,y)}{\sqrt{(x-x_1)^2 + (y-y_1)^2}}\, dxdy \tag{3.3}$$

where x_1, y_1 represent the coordinates of the point where the deflection is calculated and

$$\frac{2}{E'} = \frac{1-\upsilon_1^2}{E_1} + \frac{1-\upsilon_2^2}{E_2}$$

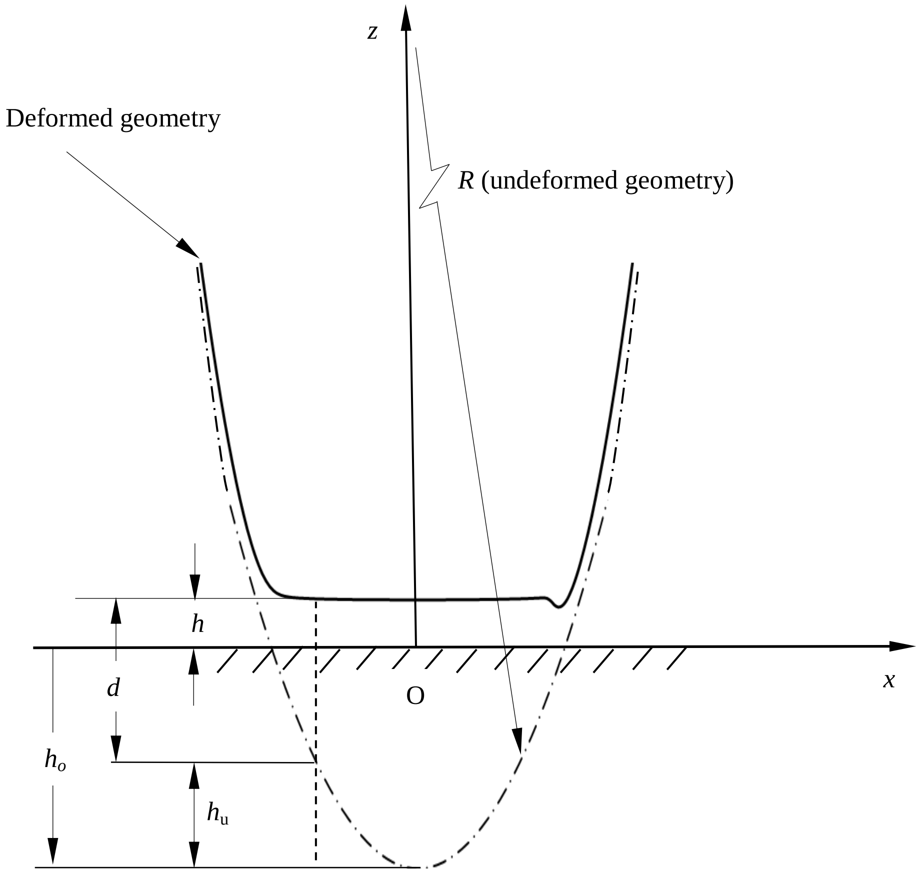

Figure 3.1: Section at the centre of the contact in the entrainment direction. h_o is a negative value

3.3 The pressure –viscosity equation

An empirical equation for the relation between the viscosity as given in equation (3.1) (the Reynolds equation) and the pressure value was given by Roelands (1966) and is adopted in the current work (isothermal analysis) in the form (Clarke et al. 2006)

$$\eta = \eta_0 \, exp\left\{ln\left(\eta_0/\kappa\right)\left[\left(1+\chi p\right)^Z - 1\right]\right\} \tag{3.4}$$

where

$\kappa = 63.15 \times 10^{-6}$ Pa.s,

$\chi = 5.1$ GPa^{-1} Pa.s and

$$Z = \frac{\alpha_0}{\chi \ln(\eta_0 / \kappa)}$$

3.4 The pressure-density equation

In addition to the viscosity, the density in equation (3.1) is also pressure dependent and is assumed to be given by the Dowson and Higginson (1966) formula

$$\rho = \rho(p) = \rho_0 \left(\frac{1 + \gamma p}{1 + \lambda p} \right) \tag{3.5}$$

The values for the pressure coefficients γ and λ in the current work are

$\gamma = 2.266$ GPa^{-1}

$\lambda = 1.683$ GPa^{-1}

3.5 Evaluation of the surface elastic deflection

As can be seen in equation (3.2) the evaluation of surface deflection is required in order to calculate the film thickness in the lubricated contact. This can be achieved by solving equation (3.3) which is a convolution integration of pressure.

This integral can be evaluated numerically for any general pressure distribution such as that which occurs in the contact between rough surfaces. As a result of numerical discretization, this integral can be transformed to a summation of influence coefficients multiplied by the pressure value at all points of the solution domain, which can be written (Evans & Hughes 2000) as

$$d(x_i, y_j) = \frac{2}{\pi E'} \sum_{k=1}^{N} \sum_{l=1}^{M} g_{k-i,l-j}\ p_{k,l} \tag{3.6}$$

The method of evaluating the influence coefficients is given by Kong (2001).

3.6 The differential deflection method

In this method the deflection equation (3.6) is expressed in a differential form as given by Evans & Hughes (2000). Using this technique leads to localisation of the pressure effect on the deflection calculation in comparison with the conventional method described by equation (3.6). Evans & Hughes (2000) show detailed steps for the implementation of this method where the differential form of the deflection is given by

$$\nabla^2 d \equiv \frac{\partial^2 d}{\partial x^2} + \frac{\partial^2 d}{\partial y^2}$$

which may also be written in the following form

$$\nabla^2 d(x_i, y_j) = \frac{2}{\pi E'} \sum_{all\,k, all\,l} f_{k-i,l-j}\ p_{k,l} \tag{3.7}$$

where $f_{i,j}$ are the differential influence coefficients, and closed forms for these coefficients are available in Evans & Hughes (2000). The advantage of using the differential deflection method can be seen by comparing the g and f coefficients as shown in Figure 3.2. This figure shows how the f coefficients decay rapidly in a short distance from the point where the deflection value is required $(x/a = 0)$.

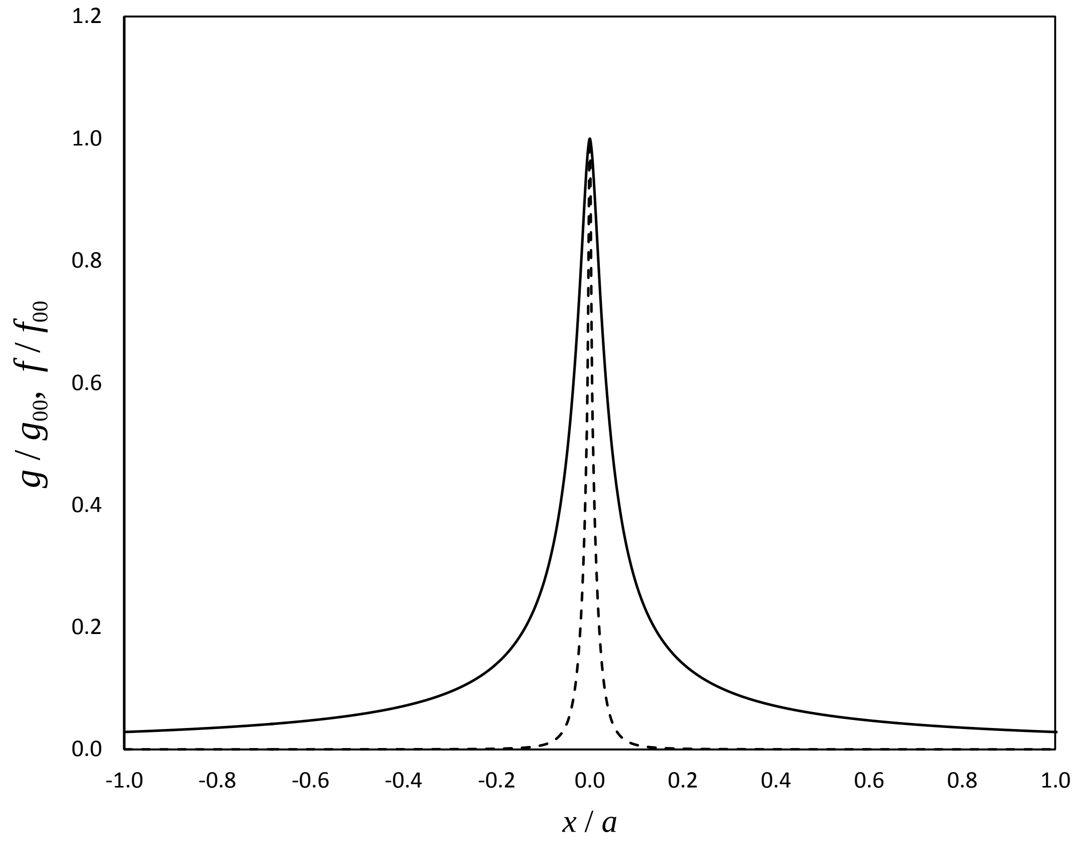

Figure 3.2: Comparison between normalized *f* (dashed) and *g* (solid) coefficients.

This localised effect of the *f* coefficients has proved to be very useful in avoiding the time consuming evaluation of equation (3.6) which is in the case of the conventional calculation requires $(NM)^2$ operations in a 2D problem. This advantage is taken into consideration in evaluation of the Laplacian in the point contact software as the region of calculation (solution space) is divided to two parts with respect to each point in the solution space. These are described as the “close” and “far” contribution parts. The contribution of the far points to the deflection of the point of interest ($x/a = 0$ in Figure 3.2) is calculated over relatively course mesh points and an interpolation method is used to find the contribution values between these points for the other points of the far part. The close part is a square area which involves the points where the influence coefficients dominate the contribution to the Laplacian of deflection at the point of interest.

3.7 Discretization methods

In this section a brief description to the solution of the steady state point contact EHL problem using both FEM and FD methods is given.

3.7.1 Discretization of the hydrodynamic equation using FD method

The Poiseuille flow term in the Reynolds equation is discretised using the central difference method while the wedge term is discretized using either a first order accurate backward difference, a second order accurate backward difference, or a central difference scheme.

The discretization is carried out using a rectangular control volume centred about each node. The dimensions of this control volume are $\Delta x, \Delta y$. Figure 3.3 shows a single control volume used to represent the Poiseuille term at node position *i*,*j*.

Using the illustration given in this figure the Poiseuille term, which involves the flow due to the pressure gradients in the *x* and *y* direction, can then be given by

$$\frac{\partial}{\partial x}\left(\sigma_x \frac{\partial p}{\partial x}\right)+\frac{\partial}{\partial y}\left(\sigma_y \frac{\partial p}{\partial y}\right)==\frac{\sigma_a\left(\frac{\partial p}{\partial x}\right)_a-\sigma_b\left(\frac{\partial p}{\partial x}\right)_b}{\Delta x}+\frac{\sigma_c\left(\frac{\partial p}{\partial y}\right)_c-\sigma_d\left(\frac{\partial p}{\partial y}\right)_d}{\Delta y} \qquad (3.8)$$

Where mean values for the flow factors are considered at the boundaries of the control volume which can be given by

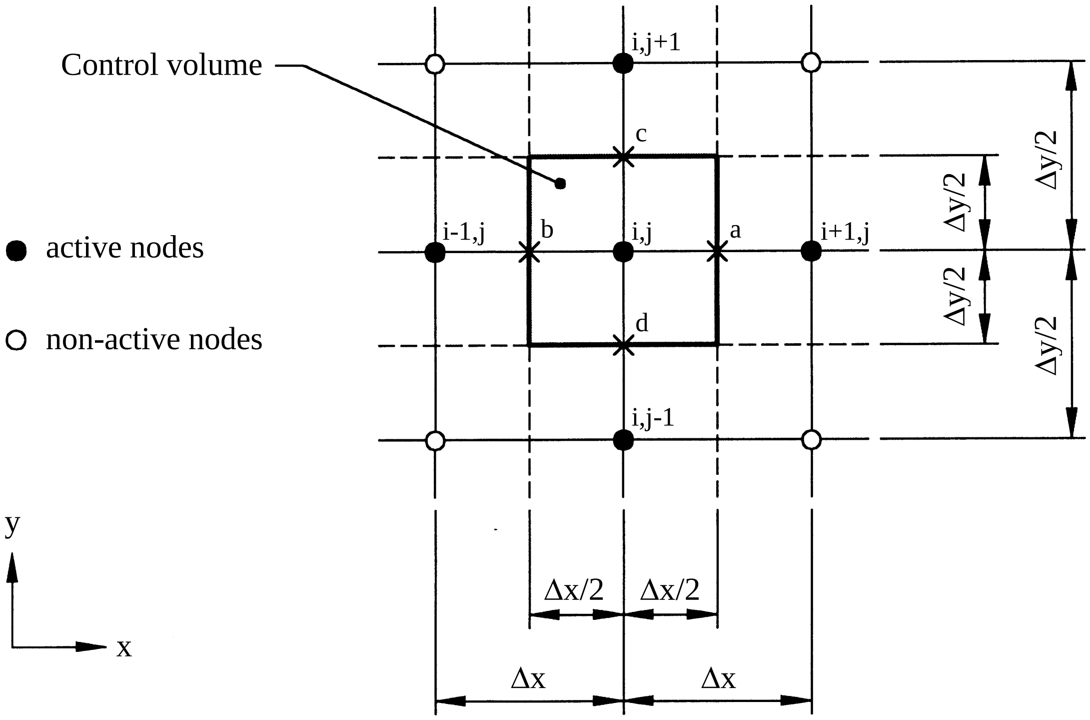

Figure 3.3: A control volume representation of the Poiseuille flow term shown a portion of the finite difference mesh taken from Holmes (2002)

$$\left.\begin{aligned}\sigma_a &= \left(\sigma_{i+1,j} + \sigma_{i,j}\right)/2\\ \sigma_b &= \left(\sigma_{i,j} + \sigma_{i-1,j}\right)/2\\ \sigma_c &= \left(\sigma_{i,j+1} + \sigma_{i,j}\right)/2\\ \sigma_d &= \left(\sigma_{i,j} + \sigma_{i,j-1}\right)/2\end{aligned}\right\} \tag{3.9}$$

The central difference approximation for the pressure gradient (in the *x* and *y* direction) in equation (3.8) gives

$$\left.\begin{aligned}
{\frac{\partial p}{\partial x}}_a &= \left(p_{i+1,j} - p_{i,j}\right)/\Delta x \\
{\frac{\partial p}{\partial x}}_b &= \left(p_{i,j} - p_{i-1,j}\right)/\Delta x \\
{\frac{\partial p}{\partial y}}_c &= \left(p_{i,j+1} - p_{i,j}\right)/\Delta y \\
{\frac{\partial p}{\partial y}}_d &= \left(p_{i,j} - p_{i,j\text{-}1}\right)/\Delta y
\end{aligned}\right\} \tag{3.10}$$

The wedge term in the Reynolds equation is

$$-\bar{u}\left(\rho\frac{\partial h}{\partial x} + h\frac{\partial \rho}{\partial p}\frac{\partial p}{\partial x}\right) - \bar{v}\left(\rho\frac{\partial h}{\partial y} + h\frac{\partial \rho}{\partial p}\frac{\partial p}{\partial y}\right)$$

The central difference approximation of this term may be expressed as

$$-\bar{u}h\frac{\partial \rho}{\partial p}\left(\frac{p_{i+1,j} - p_{i-1,j}}{2\Delta x}\right) - \bar{u}\rho\left(\frac{h_{i+1,j} - h_{i-1,j}}{2\Delta x}\right) - \bar{v}h\frac{\partial \rho}{\partial p}\left(\frac{p_{i,j+1} - p_{i,j\text{-}1}}{2\Delta y}\right) - \bar{v}\rho\left(\frac{h_{i,j+1} - h_{i,j\text{-}1}}{2\Delta y}\right) \tag{3.11}$$

where the values of ρ, $h(\partial\rho/\partial p), \bar{u}, \bar{v}$ in this equation are taken at the node where the hydrodynamic equation is applied. Substituting equations (3.10) and (3.11) in equation (3.1) gives

$$\begin{aligned}
&\sigma_a\left(\frac{p_{i+1,j} - p_{i,j}}{\Delta x^2}\right) - \sigma_b\left(\frac{p_{i,j} - p_{i-1,j}}{\Delta x^2}\right) - \bar{u}h\frac{\partial \rho}{\partial p}\left(\frac{p_{i+1,j} - p_{i-1,j}}{2\Delta x}\right) - \bar{u}\rho\left(\frac{h_{i+1,j} - h_{i-1,j}}{2\Delta x}\right) \\
&+ \sigma_c\left(\frac{p_{i,j+1} - p_{i,j}}{\Delta y^2}\right) - \sigma_d\left(\frac{p_{i,j} - p_{i,j\text{-}1}}{\Delta y^2}\right) - \bar{v}h\frac{\partial \rho}{\partial p}\left(\frac{p_{i,j+1} - p_{i,j\text{-}1}}{2\Delta y}\right) - \bar{v}\rho\left(\frac{h_{i,j+1} - h_{i,j\text{-}1}}{2\Delta y}\right) = 0
\end{aligned}$$

which can be simplified after collecting the common factors to be in the following form

$$
\begin{aligned}
& p_{i,j}\left(-\frac{\sigma_a}{\Delta x^2}-\frac{\sigma_b}{\Delta x^2}-\frac{\sigma_c}{\Delta y^2}-\frac{\sigma_d}{\Delta y^2}\right)+p_{i+1,j}\left(\frac{\sigma_a}{\Delta x^2}-\frac{\bar{u}h}{2\Delta x}\frac{\partial\rho}{\partial p}\right)+p_{i\text{-}1,j}\left(\frac{\sigma_b}{\Delta x^2}+\frac{\bar{u}h}{2\Delta x}\frac{\partial\rho}{\partial p}\right)\\
&+p_{i,j+1}\left(\frac{\sigma_c}{\Delta y^2}-\frac{\bar{v}h}{2\Delta y}\frac{\partial\rho}{\partial p}\right)+p_{i,j-1}\left(\frac{\sigma_d}{\Delta y^2}+\frac{\bar{v}h}{2\Delta y}\frac{\partial\rho}{\partial p}\right)+h_{i+1,j}\left(-\frac{\bar{u}\rho}{2\Delta x}\right)+h_{i\text{-}1,j}\left(\frac{\bar{u}\rho}{2\Delta x}\right)\\
&+h_{i,j+1}\left(-\frac{\bar{v}\rho}{2\Delta y}\right)+h_{i,j\text{-}1}\left(\frac{\bar{v}\rho}{2\Delta y}\right)=0
\end{aligned}
\tag{3.12}
$$

The wedge term can also be discretised using any of the methods mentioned above using the same general procedure for the central difference method.

3.7.2 Discretization of the hydrodynamic equation using FEM method

The discretization of the hydrodynamic equation by the FEM method involves the use of the Galerkin method. In this approach, the same approximation is used for both the weight functions and trial solution (Fish and Belytschko, 2012). Applying this method to equation (3.1) gives

$$
\begin{aligned}
& \int N_i\frac{\partial}{\partial x}\left(\sigma_x\frac{\partial p}{\partial x}\right)dxdy-\bar{u}\int N_i\left(\rho\frac{\partial h}{\partial x}+h\frac{\partial\rho}{\partial p}\frac{\partial p}{\partial x}\right)dxdy\\
&+\int N_i\frac{\partial}{\partial y}\left(\sigma_y\frac{\partial p}{\partial y}\right)dxdy-\bar{v}\int N_i\left(\rho\frac{\partial h}{\partial y}+h\frac{\partial\rho}{\partial p}\frac{\partial p}{\partial y}\right)dxdy=0
\end{aligned}
\tag{3.13}
$$

where N_i are standard shape functions.

The software considers a four nodes linear quadrilateral element, and the integrals given by equation (3.13) are carried out over this element using two point Gauss integration. Figure 3.4 shows the element adopted together with the Gauss points.

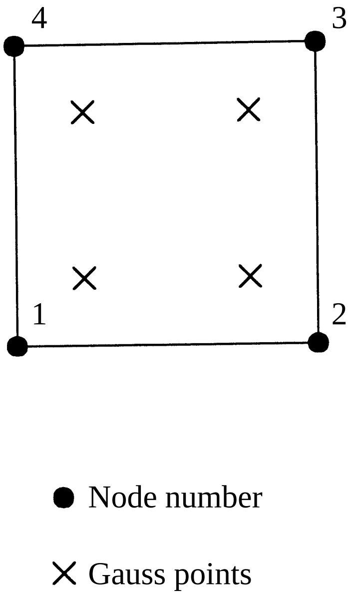

Figure 3.4: The four nodes linear finite element

A detailed description of the discretisation method can be found in Holmes (2002). Following integration by parts for the Poiseuille flow transforming and the weak formulation (which is equivalent to the governing equation and the boundary conditions), equation (3.13) becomes

$$\begin{aligned}&\int\left(\frac{\partial N_i}{\partial x}\tilde{\sigma}_x\sum_{j=1}^{4}\frac{\partial N_j}{\partial x}p_j\right)dxdy+\int N_i\tilde{\bar{u}}\left(\tilde{\rho}\sum_{j=1}^{4}\frac{\partial N_j}{\partial x}h_j+\tilde{h}\frac{\partial\tilde{\rho}}{\partial p}\sum_{j=1}^{4}\frac{\partial N_j}{\partial x}p_j\right)dxdy\\&+\int\left(\frac{\partial N_i}{\partial y}\tilde{\sigma}_y\sum_{j=1}^{4}\frac{\partial N_j}{\partial y}p_j\right)dxdy+\int N_i\tilde{\bar{v}}\left(\tilde{\rho}\sum_{j=1}^{4}\frac{\partial N_j}{\partial y}h_j+\tilde{h}\frac{\partial\tilde{\rho}}{\partial p}\sum_{j=1}^{4}\frac{\partial N_j}{\partial y}p_j\right)dxdy=0\end{aligned}\qquad(3.14)$$

where

$$\tilde{\sigma}_x=\sum_{k=1}^{4}N_k\sigma_{x\,k}\qquad\tilde{\sigma}_y=\sum_{k=1}^{4}N_k\sigma_{y\,k}\qquad\tilde{\rho}=\sum_{k=1}^{4}N_k\rho_k\qquad\tilde{h}=\sum_{k=1}^{4}N_k h_k$$

$$\tilde{\bar{u}}=\sum_{k=1}^{4}N_k\bar{u}_k\qquad\tilde{\bar{v}}=\sum_{k=1}^{4}N_k\bar{v}_k\qquad\frac{\partial\tilde{\rho}}{\partial p}=\sum_{k=1}^{4}N_k\,\frac{\partial\rho}{\partial p}_k$$

These average terms are evaluated over the element at the Gauss points.

Performing the integration over an element results in a contribution from the film thickness and pressure at each of its four nodes. Each node (except the boundary nodes) has a contribution from four adjacent elements as shown in Figure 3.5. The coefficients of pressure and film thickness at each node which involves all these contributions are obtained by an assembling procedure.

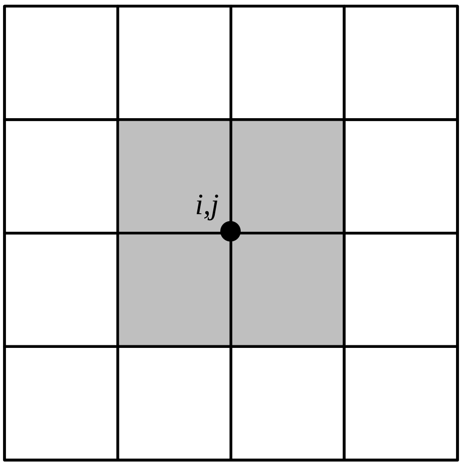

Figure 3.5: The node *i,j* has contributions from the four adjacent elements (shaded)

3.7.3 Elastic deformation equation

The elastic equation can be written in the following form after substituting equation (3.6) in equation (3.2)

$$h = h_u + \frac{2}{\pi E'} \sum_{all\,k, all\,l} g_{k-i,l-j}\; p_{k,l} + h_o \tag{3.15}$$

The differential form of this equation is

$$\nabla^2 h = \nabla^2 h_u + \frac{2}{\pi E'} \sum_{all\,k, all\,l} f_{k-i,l-j}\; p_{k,l} \tag{3.16}$$

where

$$\nabla^2 h = \frac{\partial^2 h}{\partial x^2} + \frac{\partial^2 h}{\partial y^2}$$

The undeformed gap in this equation (h_u) involves all surface modifications of the gear teeth as explained in Chapter 2.

Discretising the derivative terms in this equation using the central difference method gives

$$\left(\frac{h_{i+1,j} + h_{i-1,j} - 2h_{i,j}}{\Delta x^2}\right) + \left(\frac{h_{i,j+1} + h_{i,j-1} - 2h_{i,j}}{\Delta y^2}\right) = \nabla^2 h_u + \frac{2}{\pi E'} \sum_{all\,k,all\,l} f_{k-i,l-j}\; p_{k,l} \qquad (3.17)$$

The second term of the right hand side of equation (3.17) is split into two parts in the solution process in addition to the point of interest (*i,j*). These are the '*near'* part which considers the contributions of the eight neighbouring nodes for the point of interest and the remaining are denoted as '*other*' contributions.

$$\frac{2}{\pi E'} \sum_{all\,k,all\,l} f_{k-i,l-j}\; p_{k,l} = \frac{2}{\pi E'} f_{0,0}\; p_{i,j} + \frac{2}{\pi E'} \sum_{near} f_{k-i,l-j}\; p_{k,l} + \frac{2}{\pi E'} \sum_{other} f_{k-i,l-j}\; p_{k,l} \qquad (3.18)$$

Equation (3.17) can be rearranged by using equation (3.18) and setting the pressure and film thickness at point *i,j* on one side of the equation and moving all the other terms to the other side.

$$\begin{aligned} p_{i,j}\left(\frac{2}{\pi E'} f_{0,0}\right) + 2h_{i,j}\left(\frac{1}{\Delta x^2} + \frac{1}{\Delta y^2}\right) &= \left(\frac{h_{i+1,j} + h_{i-1,j}}{\Delta x^2}\right) + \left(\frac{h_{i,j+1} + h_{i,j-1}}{\Delta y^2}\right) - \nabla^2 h_u \\ &\quad - \frac{2}{\pi E'} \sum_{near} f_{k-i,l-j}\; p_{k,l} - \frac{2}{\pi E'} \sum_{other} f_{k-i,l-j}\; p_{k,l} \end{aligned} \qquad (3.19)$$

letting:

$C_{i,j} = \left(\frac{2}{\pi E'} f_{0,0} \right)$, $\quad D_{i,j} = 2\left(\frac{1}{\Delta x^2} + \frac{1}{\Delta y^2} \right)$ and

$$E_{i,j} = \left(\frac{h_{i+1,j} + h_{i-1,j}}{\Delta x^2} \right) + \left(\frac{h_{i,j+1} + h_{i,j-1}}{\Delta y^2} \right) - \nabla^2 h_u - \frac{2}{\pi E'} \sum_{near} f_{k-i,l-j}\, p_{k,l} - \frac{2}{\pi E'} \sum_{other} f_{k-i,l-j}\, p_{k,l}$$

After these steps the elastic equation becomes

$$C_{i,j}\, p_{i,j} + D_{i,j} h_{i,j} = E_{i,j} \tag{3.20}$$

where $E_{i,j}$ contains the near pressure contributions which are embedded in the calculation and the other contribution which is evaluated for the current outer loop results of pressure.

Also the Reynolds equation can be expressed in the following general form

$$\sum_{k=0}^{k=n_c} A_k\, p_k \Big|_{i,j} + \sum_{k=0}^{k=n_c} B_k h_k \Big|_{i,j} = R_{i,j} \tag{3.21}$$

where:

A_k are the Reynolds coefficients of pressure.

B_k are the Reynolds coefficients of film thickness.

n_c is the number of coefficients involved in the formulation.

$R_{i,j}$ is the right hand side, that has a zero value for steady state conditions

3.8 Transient Analyses

The software also has the ability to take the squeeze film term in the hydrodynamic equation into consideration. Equation (3.21) can be written in the following form to include the squeeze term

$$A_{i,j}p_{i,j} + B_{i,j}h_{i,j} - \left.\frac{\partial(\rho h)}{\partial t}\right|_{i,j} = R'_{i,j} \tag{3.22}$$

where

$$R'_{i,j} = R_{i,j} - \sum_{all\ other\ k} A_k p_k\Big|_{i,j} - \sum_{all\ other\ k} B_k h_k\Big|_{i,j}$$

In the software two methods were used to discretise the squeeze term which are the second order backward difference and the Crank-Nicolson methods. The backward difference method is illustrated in the next section and the Crank-Nicolson method is illustrated in Holmes (2002) and Chapra & Canale (2002)

3.8.1 Backward difference method

This method was detailed by Venner & Lubrecht (1994). By using the second order backward difference, the time dependent term in the Reynolds equation can be discretized to be in the following form

$$\frac{\partial(\rho h)}{\partial t} = \frac{1.5(\rho h)^{q+1} - 2(\rho h)^{q} + 0.5(\rho h)^{q-1}}{\Delta t} \tag{3.23}$$

where q in this equation represents the time step. The density and film thickness values at time step q and $q-1$ are used to calculate the film thickness at time step $q+1$.

Using this method in combination with the central difference formulation of equation (3.12) as an example, the Reynolds equation can be written in the following form, where the left hand side gives the relation between variables *p* and *h* at time step q+1:

$$
\begin{aligned}
& p_{i,j}\left(-\frac{\sigma_a}{\Delta x^2}-\frac{\sigma_b}{\Delta x^2}-\frac{\sigma_c}{\Delta y^2}-\frac{\sigma_d}{\Delta y^2}\right)+p_{i+1,j}\left(\frac{\sigma_a}{\Delta x^2}-\frac{\bar{u}h}{2\Delta x}\frac{\partial\rho}{\partial p}\right)+p_{i\text{-}1,j}\left(\frac{\sigma_b}{\Delta x^2}+\frac{\bar{u}h}{2\Delta x}\frac{\partial\rho}{\partial p}\right) \\
& +p_{i,j+1}\left(\frac{\sigma_c}{\Delta y^2}-\frac{\bar{v}h}{2\Delta y}\frac{\partial\rho}{\partial p}\right)+p_{i,j-1}\left(\frac{\sigma_d}{\Delta y^2}+\frac{\bar{v}h}{2\Delta y}\frac{\partial\rho}{\partial p}\right)+h_{i+1,j}\left(-\frac{\bar{u}\rho}{2\Delta x}\right)+h_{i\text{-}1,j}\left(\frac{\bar{u}\rho}{2\Delta x}\right) \\
& +h_{i,j+1}\left(-\frac{\bar{v}\rho}{2\Delta y}\right)+h_{i,j\text{-}1}\left(\frac{\bar{v}\rho}{2\Delta y}\right)+h_{i,j}\left(-1.5\frac{\rho}{\Delta t}\right)=\frac{2(\rho h)^q-0.5(\rho h)^{q-1}}{\Delta t}=R_{i,j}
\end{aligned}
$$

(3.24)

where

$$R_{i,j}=\frac{2(\rho h)^q-0.5(\rho h)^{q-1}}{\Delta t}$$

It can be seen in equation (3.24) there is an additional $-1.5\frac{\rho^{\,q+1}}{\Delta t}$ contribution added to the central film thickness weighting due to the time dependent term, and the influence of previous time steps appears in the non-zero right hand side, $R_{i,j}$.

3.9 Effect of Non-Newtonian oil behaviour

The assumption of Newtonian oil behaviour overestimates the effective viscosity values at high pressure levels which affects the EHL results. As sliding between the surfaces of contacting teeth occurs due to the difference between their velocities, the lubricant experiences extremely high rates of shear. The prediction of the lubricant behaviour in such cases requires inclusion of a non-Newtonian rheological model, and in this study the relation between the shear strain rate and the shear stress is taken to be the form

$$\frac{\partial u}{\partial z}=F(\tau) \tag{3.25}$$

where $F(\tau)$ is a non-linear function.

Several formulas have been proposed in the literature for the non-linear relation between the shear strain rate and the shear stress. Johnson and Tevaarwerk (1977) proposed the following relation based on the results of elastohydrodynamic friction testing under controlled sample temperatures:

$$F(\tau) = \frac{\tau_0}{\eta} sinh\left(\frac{\tau}{\tau_0}\right) \tag{3.26}$$

where τ_0 is the non-Newtonian parameter. This relationship is adopted in the current study.

Equation (3.25) is used for a one dimensional problem and in two dimensional cases it becomes (Sharif et al, 2001)

$$\frac{\partial u}{\partial z} = \frac{\tau_s}{\tau_e} F(\tau_e) \tag{3.27}$$

$$\frac{\partial v}{\partial z} = \frac{\tau_r}{\tau_e} F(\tau_e) \tag{3.28}$$

where s is the sliding direction, r is the perpendicular (non-sliding) direction and

$$\tau_e = \sqrt{\tau_s{}^2 + \tau_r{}^2}$$

This generalisation is based on the assumption that the resultant shear stress is parallel to the resultant strain rate and related to it according to equation (3.25). Note that suffix *s* is used in this section to denote the sliding direction and should not be confused with the more general use of *s* in the notation section.

The shear stress components can be related to the pressure gradient by considering the equilibrium of a fluid element leading to the relations

$$\frac{\partial \tau_s}{\partial z} = \frac{\partial p}{\partial s} \tag{3.29}$$

$$\frac{\partial \tau_r}{\partial z} = \frac{\partial p}{\partial r} \tag{3.30}$$

and since it is assumed that pressure does not vary in the z direction, these relations can be integrated to give

$$\tau_s(z) = \tau_{sm} + \frac{\partial p}{\partial s} z \tag{3.29a}$$

$$\tau_r(z) = \tau_{rm} + \frac{\partial p}{\partial r} z \tag{3.30a}$$

where

z : distance measured from the film thickness mid plane.

τ_{sm} and τ_{rm} are the mid-film shear stress components.

Integrating equations (3.27) and (3.28) across the thickness of the film, and applying non-slip boundary conditions gives

$$0 = -u_s + \int_{-h/2}^{h/2} \frac{\tau_s}{\tau_e} F(\tau_e) dz \tag{3.31}$$

$$0 = \int_{-h/2}^{h/2} \frac{\tau_r}{\tau_e} F(\tau_e) dz \tag{3.32}$$

The values of τ_{sm} and τ_{rm} are obtained by solving these equations numerically to determine the shear stress values $\tau_s(z)$ and $\tau_r(z)$ which satisfy the kinematic requirements. τ_{sm} and τ_{rm} are a function of $\eta(p)$, $\frac{\partial p}{\partial s}$, $\frac{\partial p}{\partial r}$ and h and vary throughout the lubricant film.

Sharif et al (2001) explain in detail how the non-Newtonian effect (involving the above equations) can be incorporated in the formulation of the Reynolds equation when they analysed the EHL behaviour of worm gears, which presents a general kinematic problem.

Considering of the flow between the surfaces, the mass flow rate in each direction is

$$Q_s = \int_{-h/2}^{h/2} \rho u(z) dz$$

$$Q_r = \int_{-h/2}^{h/2} \rho v(z) dz$$

Integrating these equations by parts assuming ρ does not vary across the film gives

$$Q_s = \rho \bar{u} h - \int_{-h/2}^{h/2} \rho z \frac{\partial u}{\partial z} dz \tag{3.33}$$

$$Q_r = \rho \bar{v} h - \int_{-h/2}^{h/2} \rho z \frac{\partial v}{\partial z} dz \tag{3.34}$$

Substitution of equation (3.27) in (3.33) and (3.28) in (3.34) gives

$$Q_s = \rho \bar{u} h - \int_{-h/2}^{h/2} \rho z \frac{\tau_s}{\tau_e} F(\tau_e) dz \tag{3.35}$$

$$Q_r = \rho \bar{v} h - \int_{-h/2}^{h/2} \rho z \frac{\tau_r}{\tau_e} F(\tau_e) dz \tag{3.36}$$

Morris (2000) showed that, when the formulation of flow equations is made in the sliding and non-sliding directions, the second term in each of these equations (the integral term) is proportional to the pressure gradient in that particular direction. Therefore, equations (3.35) and (3.36) can be written in the forms

$$Q_s = \rho \bar{u} h - \sigma_s \frac{\partial p}{\partial s} \tag{3.37}$$

$$Q_r = \rho \bar{u} h - \sigma_r \frac{\partial p}{\partial r} \tag{3.38}$$

Equating equation (3.35) with (3.37) and equation (3.36) with (3.38) gives

$$\sigma_s = \frac{\int_{-h/2}^{h/2} \rho z \left(\frac{\tau_s}{\tau_e} \right) F(\tau_e) dz}{\frac{\partial p}{\partial s}} \tag{3.39}$$

$$\sigma_r = \frac{\int_{-h/2}^{h/2} \rho z \left(\frac{\tau_r}{\tau_e} \right) F(\tau_e) dz}{\frac{\partial p}{\partial r}} \tag{3.40}$$

where τ_s and τ_r are given by equation (3.29a) and (3.30a) respectively.

These equations imply that the flow factors in the sliding and non-sliding directions are different when the effect of non-linearity of the relation between shear stress and shear strain rate is taken into consideration. This is not the case in the Newtonian situation where the flow factors are equal in both directions as previously given by equation (3.1a).

For the EHL of helical gears considered in this thesis, the surface velocities in the *y* direction are zero. Therefore, sliding occurs in the *x*-direction throughout the film and the flow factors in the *x* and *y* directions become:

$$\sigma_x = \frac{\int_{-h/2}^{h/2} \rho z \left(\frac{\tau_x}{\tau_e} \right) F(\tau_e) dz}{\frac{\partial p}{\partial x}} \tag{3.41}$$

$$\sigma_y = \frac{\int_{-h/2}^{h/2} \rho z \left(\frac{\tau_y}{\tau_e} \right) F(\tau_e) dz}{\frac{\partial p}{\partial y}} \tag{3.42}$$

where:

$$\tau_e = \sqrt{{\tau_x}^2 + {\tau_y}^2} \tag{3.43}$$

A routine for determining the flow factors given by equations (3.41) and (3.42) at each mesh point as developed by Morris (2000) was incorporated in the software. As the software is built in a general form to deal with both Newtonian and non-Newtonian oil behaviour, the general form of the Reynolds equation given by equation (3.1) remains as it is.

3.10 Solution techniques

Using the methods of formulation described in the previous sections, the Reynolds and elastic equations can be written in the form:

$$\left. \begin{aligned} A_{i,j} p_{i,j} + B_{i,j} h_{i,j} &= R'_{i,j} \\ C_{i,j} p_{i,j} + D_{i,j} h_{i,j} &= E_{i,j} \end{aligned} \right\} \tag{3.44}$$

Both equations are clearly formulated in terms of pressure and film thickness at the point *i,j*. These two equations need to be solved simultaneously (which is the idea behind the coupled method). The software provides two methods to solve this pair of equations which are Gauss Seidel and alternate direction implicit (ADI) methods**.** The ADI method solves the 2D problem as a series of 1D problems where each row is firstly solved in one direction of the solution domain and then each column is solved. More detail about this method can be found in Kreyszig (1999). However it has been found that in the EHL problem the second stage of the ADI process (column solution) is unnecessary and the solution is best obtained by repeated row solution (Holmes, 2002). This is because transverse flow is not very influential in the transient problem and the entrainment direction flow balance dominates the calculation.

In solving the pair of equations (3.44) simultaneously, the new values of $p_{i,j}$ and $h_{i,j}$ can be calculated from

$$\left.\begin{aligned} p_{i,j}^{new} &= \frac{R'_{i,j}D_{i,j} - E_{i,j}B_{i,j}}{A_{i,j}D_{i,j} - B_{i,j}C_{i,j}} \\ h_{i,j}^{new} &= \frac{E_{i,j} - C_{i,j}\,p_{i,j}^{new}}{D_{i,j}} \end{aligned}\right\} \tag{3.45}$$

The results of these equations are used to update the pressure and film thickness until convergence is obtained.

This procedure is used to solve for the points inside the solution space and boundary conditions are applied at the boundaries of the solution space. The pressure values are set to zero at the boundaries and the deflection in the elastic equation is calculated using equation (3.6) based on the current pressure approximation to determine the value of the film thickness on the boundary.

To calculate the film thickness at the boundary, the constant h_o in equation (3.2) needs to be determined. This can be achieved by using an empirical equation given by

Chittenden et al. (1985) which gives the value of the central film thickness. At the centre of the contact the value of the undeformed geometry is zero. Therefore equation (3.2) becomes

$$h_c = d_c + h_o \tag{3.46}$$

where d_c is the surface deflection at the centre of the contact resulting from a Hertzian pressure distribution. Therefore the constant h_o can be calculated by rearranging equation (3.46) to be

$$h_o = h_c - d_c \tag{3.47}$$

This process gives the initial estimated value for h_o to allow the steady state EHL solution method to commence. The value of h_o is continuously adjusted in the solution algorithm to ensure that the converged result provides the specified load.

3.11 EHL results using FEM and FD method

Figure 3.6 shows a comparison between FEM and FD (central difference) methods for the EHL analysis of a helical gear contact at a particular position in the meshing cycle. Figure 3.6 (a) shows the film thickness (left) and pressure (right) results using the FEM method and Figure 3.6 (b) shows the corresponding FD results. The required data that were used to obtain these results are given in Chapter 4. No significant difference can be seen in this figure between the results obtained using the two different methods. Further sectional comparisons at the centre of the contact for the results shown in Figure 3.6 are shown in Figure 3.7. Figure 3.7 (a) shows the section results in the entrainment direction, *x*, and Figure 3.7 (b) shows the comparison in the *y* direction at $x = 0$. The results of the two methods coincide very closely.

It is worth mentioning that the solution to the EHL problem for the helical gears was first approached using the FD method as it is easier to understand in comparison with the FEM method. Then for the purpose of comparison the necessary understanding for the FEM method was developed. This method was found to be more stable numerically and therefore adopted as the default approach.

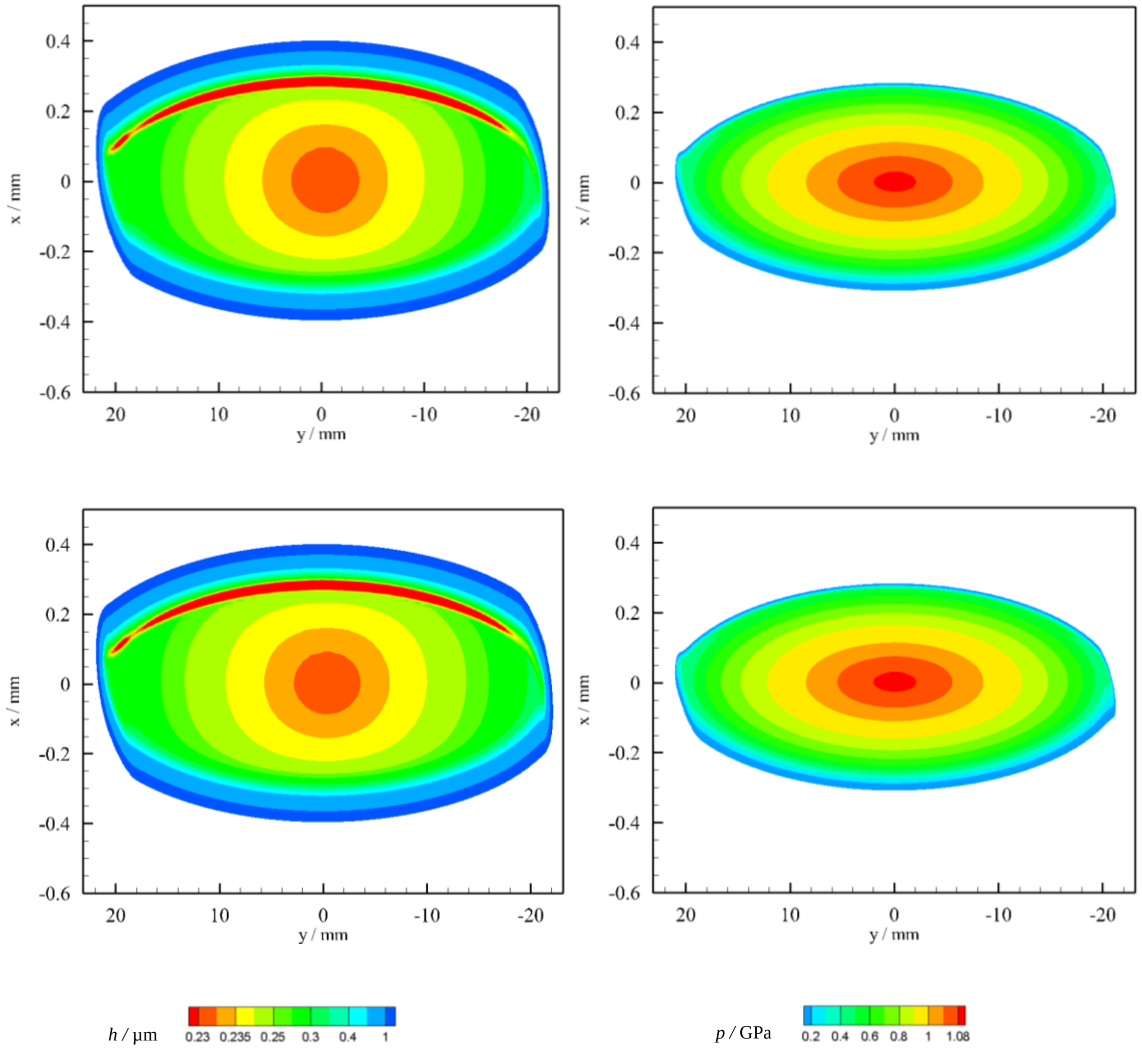

Figure 3.6: Comparison between FEM (upper) and FD (lower) EHL results at a position in the meshing cycle of helical gear. Left: film thickness; right: pressure

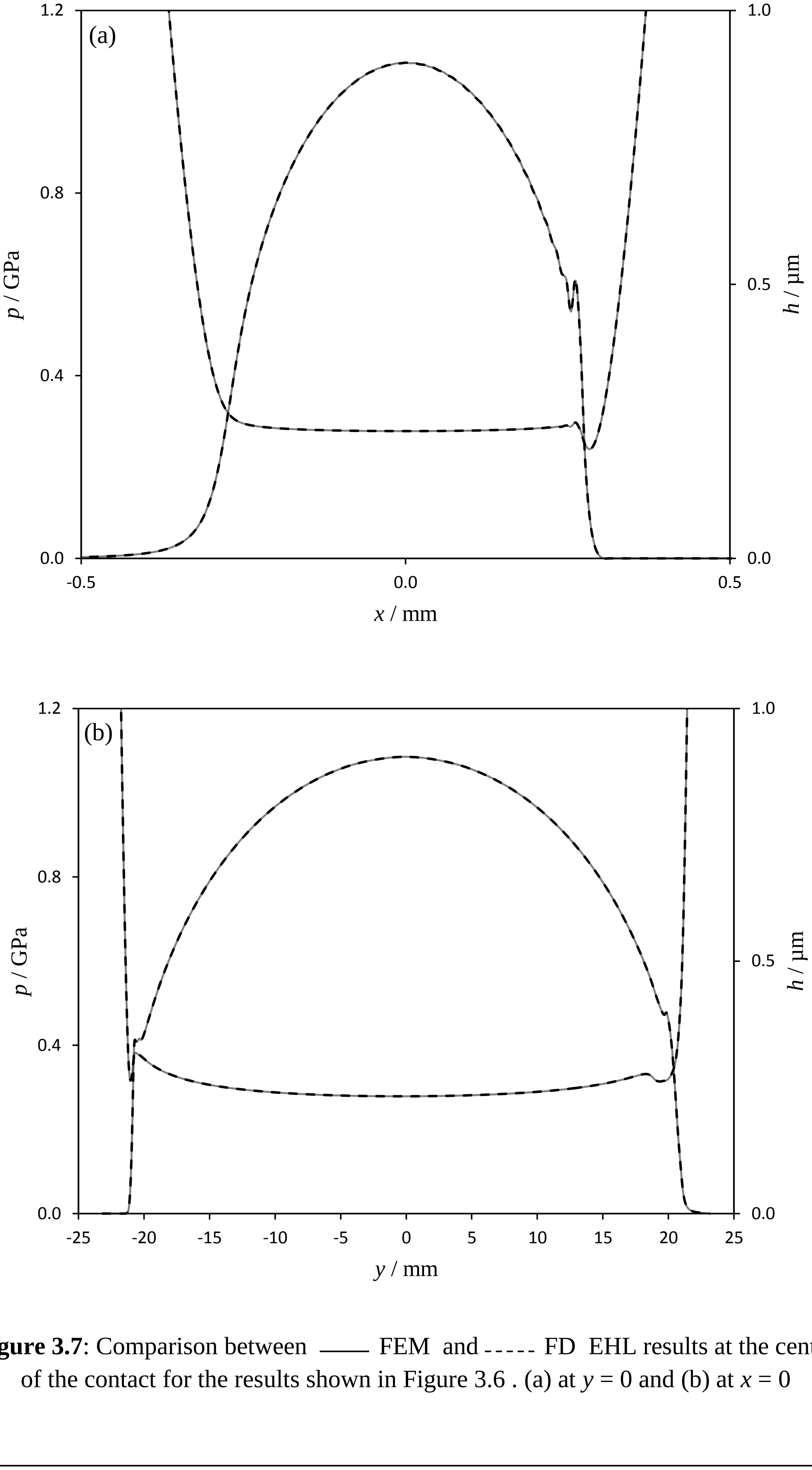

Figure 3.7: Comparison between —— FEM and - - - - - FD EHL results at the centre of the contact for the results shown in Figure 3.6 . (a) at $y = 0$ and (b) at $x = 0$

Chapter 4

Transient EHL analysis: Introduction of axial crowning

4.0 Introduction

The results shown in this chapter cover a full transient EHL analysis for a complete meshing cycle of the helical gears considered. Software has been written in a general form to solve the EHL contact problem for a pair of helical gears, whatever the contact ratio. Two pairs of helical gears are considered as test cases which have significant differences in their gear ratios and consequently different dimensions. The first pair (design A), which has a 33:34 gear ratio, is from a test rig used for micropitting tests at Newcastle University (Zhang & Shaw, 2011) for which transient mixed lubrication line contact analyses were carried out by Evans et al. (2012) and Evans et al. (2013) to examine near-surface fatigue effects in the context of micropitting. As the gear ratio of set A is close to unity the resulting entrainment velocity at all positions in the meshing cycle is almost constant. The second pair considered (design B) has a 33:99 gear ratio which gives a greater variation of entrainment velocity during the meshing cycle. A pinion torque and pinion rotational speed of 1.06 kNm and ω_1= 235.62 rad/sec (2250 rpm) respectively, are assumed for both designs. The EHL analysis was isothermal and the following lubricant parameters were assumed (Mobil Jet 2) (Mobil, 1979): ambient pressure viscosity η_0 = 0.00625 Pa.s; pressure-viscosity coefficient α = 13.3 GPa^{-1}; and non-Newtonian shear thinning parameter τ_0 = 10 MPa. Further details of the gears are given in Table 4.1. The tip relief and tooth crowning values given in the table were the default values used in this study and were applied for all cases except those for which specified differences are given.

Table 4.1: Dimensions and parameters of gear pairs A and B

	Design A	Design B
Normal module / mm	4.5	4.5
Pinion tooth number	33	33
Wheel teeth number	34	99
Pressure angle / deg	20.0	20.0
Reference helix angle / deg	19.60	19.60
Pinion tip diameter / mm	166.61	166.61
Wheel tip diameter / mm	171.39	481.83
Centre distance / mm	160.00	315.22
Face width / mm	44.0	44.0
Tip relief value at the tip radius / µm	70	70
Tip relief radial distance / mm	2	2
Crown at the face edges / µm	8	8

4.1 Length of line of contact and the corresponding transmitted load.

In a spur gear drive, as the contact area during the meshing cycle is not significantly changed, the most significant variation in the transmitted load comes from the sudden change in the number of lines of contact at the change point positions in the meshing cycle and the consequent effects on the tooth deflections. For helical gears, the transmitted load will vary (in additional to other factors) due to the continuous changing of the tooth contact area during the meshing cycle as the change of the number of line of contacts is taking place very smoothly. This can be seen in Figure 4.1 which shows the variation of length of a single line of contact, the transmitted load and the total length of lines of contact throughout the meshing cycle in the absence of crowning and tip relief. Figure 4.1 (a) shows these variations for design A, and those for design B are shown in Figure 4.1 (b). The number of lines of contact (number of pairs of teeth in contact at any instant) changes during the meshing cycle of a pair of helical gears. For the gear ratio of design A and B the number of contact lines varies between two and three throughout meshing cycle (the other two (or one) contact lines are not shown in these figures). These figures show how a single line of contact in both designs starts at a point and gradually changes to be a line of increasing, then constant and then decreasing length, and finally ending as a point. It may be noticed in Figure 4.1 that there is no significant change in the total length of the lines of contact and consequently the load carried by a single line of contact is almost insensitive to the effect of change points.

On the other hand, the introduction of tip relief reduces the theoretical contact line length which consequently decreases the total contact line length at any instant. Figures 4.2 (a) and (b) show the corresponding variations together with the transmitted load when tip relief is taken into consideration. The decrease in the nominal contact line length is clear in these figures where the total length is reduced by 41.18 % and 41.6 % for design A and B respectively. However, the contact may extend into the tip relief region depending on the form of tip relief in use.

In this study it was assumed that each contact line carried load in proportion to its nominal length as a working approximation. The actual load distribution depends on the tooth flexure and modelling this effect requires a complex 3D FEM with many teeth included in the model and a fine mesh at the loaded flanks. However, dependence of EHL film thickness on load is week (see equation 4.6) and if the flexure load variation is known, it is possible to introduce a flexure misalignment of contact lines to account for it in the EHL analysis. Such a task is not realistic for the current study which assumes that the load is numerically uniformly distributed along the contact line as a first approximation.

This means that the proportion of the total load carried by a contact is assumed to be given by the instantaneous length of the contact line divided by the corresponding total contact length for all tooth pairs in contact. For gear pairs A and B specified in Table 4.1 the total length of tooth contacts varied by 4.3% and 4.8% respectively at the change points, so the load per unit length of a given contact varied only by this relatively small amount. The maximum transmitted load is 14.4 kN which occurs when the contact acts over the whole face width at $s_i = -7.5$ mm.

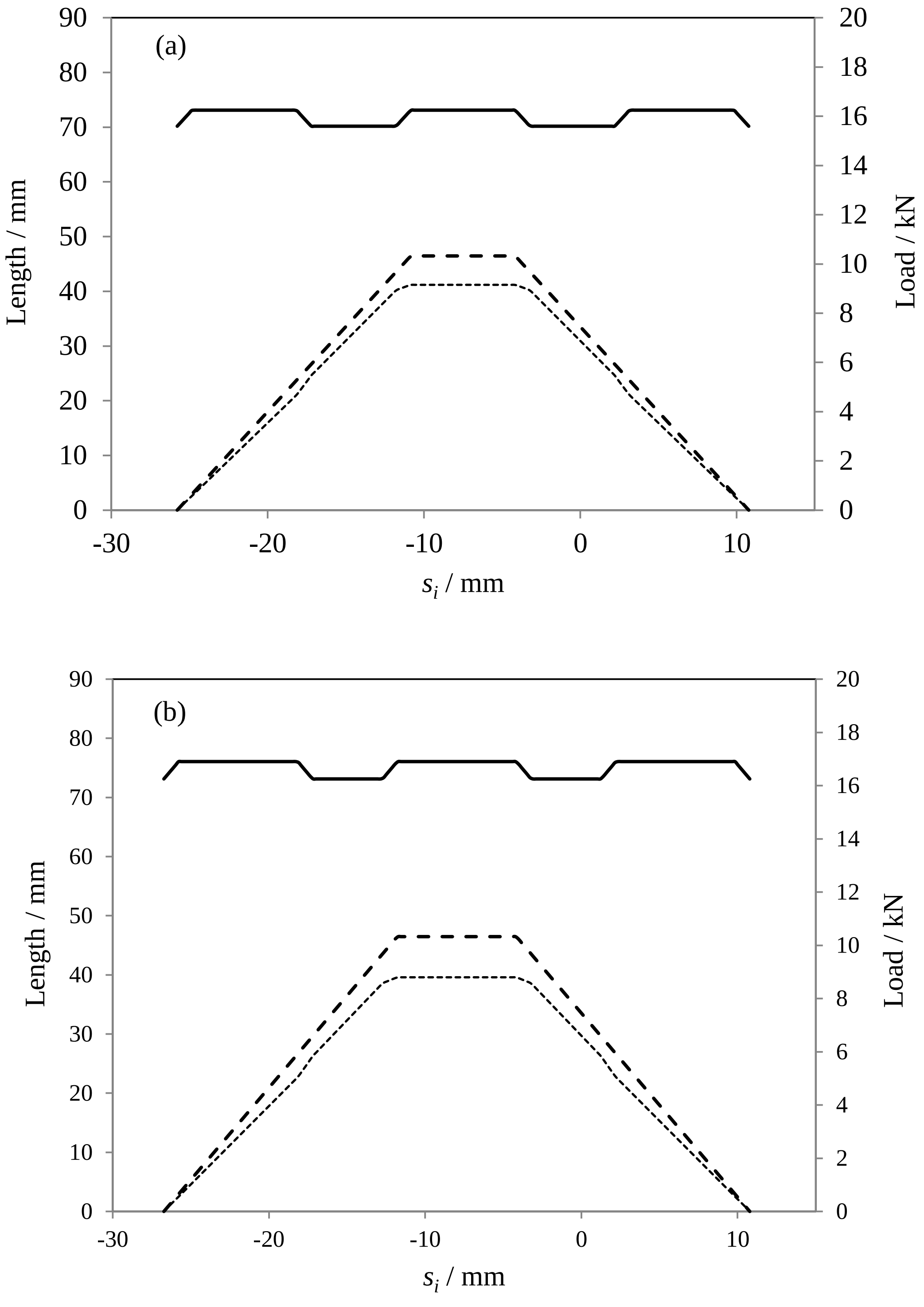

Figure 4.1: Variation of contact line length – – – and contact line load ------- for a single contact line over its meshing cycle without tip relief. Also shown is the variation in total length of the contact lines of the tooth pairs in contact ——.
(a) Design A; (b) Design B

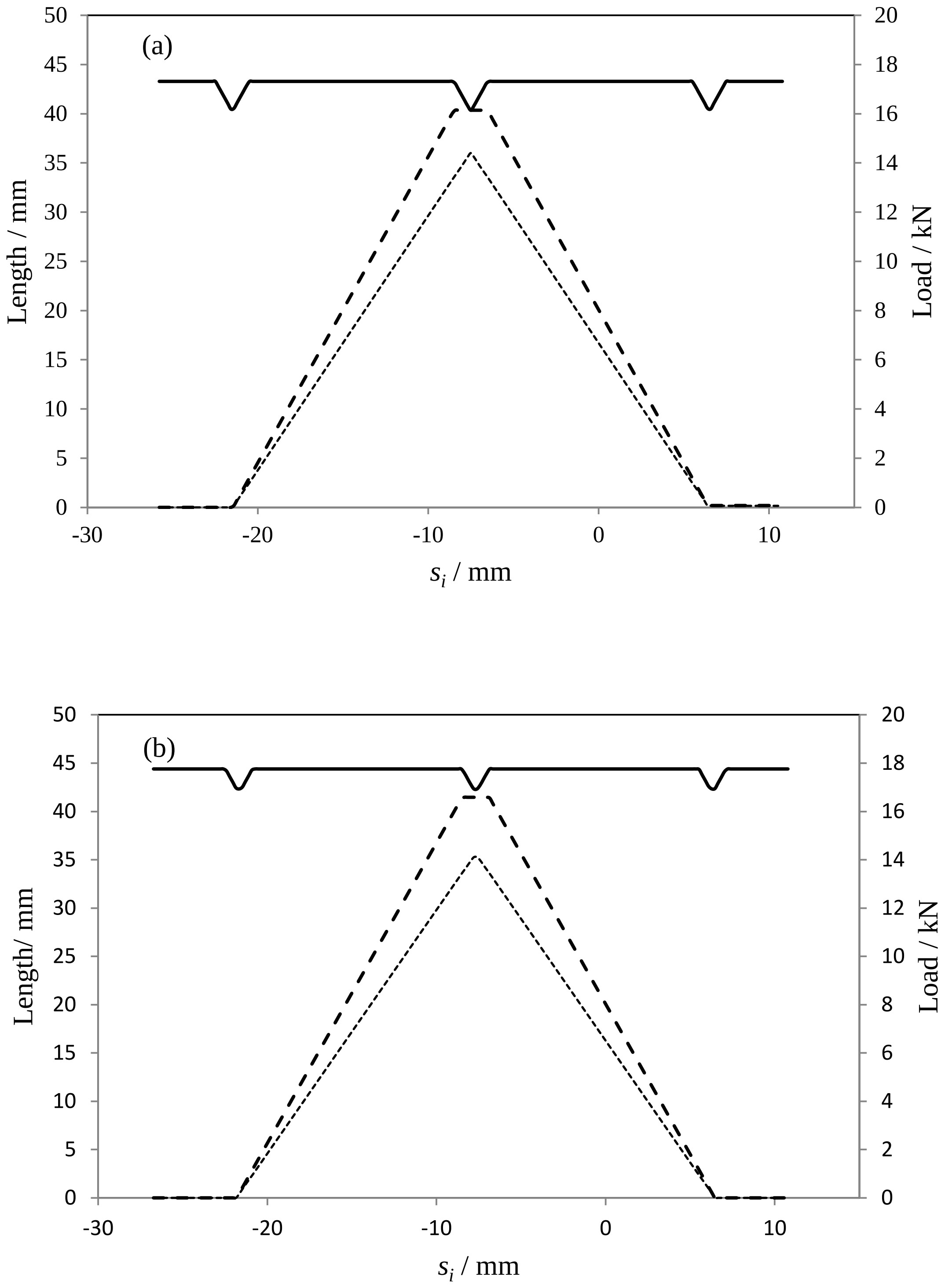

Figure 4.2: Variation of contact line length – – – and contact line load ------- for a single contact line over its meshing cycle with tip relief. Also shown is the variation in total length of the contact lines of the tooth pairs in contact ——.
(a) Design A; (b) Design B

4.2 Radius of curvature and surfaces velocities

Figure 4.3 shows the variation of the radius of relative curvature, entrainment velocity, and slide/roll ratio over the meshing cycles for the two designs. It can be seen that the first contact for designs A and B occurs at $s = -10.8$ mm and $s = -11.8$ mm, respectively, and in both designs the contact ends at $s = 10.8$ mm. In design B, the path of contact is therefore 4.4% longer than that for design A. It can be seen from Figure 4.3 (a) that there is a significant difference in the radii of relative curvature over the meshing cycle between the two pairs. The radius in design A (dashed line) is almost symmetric as the two gears have slightly different dimensions. In design B the radius of relative curvature increases as *s* increases.

For the kinematic behavior of the gears, the entrainment velocity takes place in the rolling/sliding direction between the teeth, which is parallel to the minor axis of the contact ellipse. Since the time varying radii of curvature are changed over the instantaneous line of contact, the surface velocities are also varying and are given by:

$$u_1(y,t) = R_1'(s(y,t))\omega_1 \qquad (4.1)$$

$$u_2(y,t) = R_2'(s(y,t))\omega_2 \qquad (4.2)$$

The mean entrainment at the first position in the meshing cycle is 5.8 m/s for design B which varies by 25% over the meshing cycle, whereas it is almost constant at 6.7 m/s for design A as shown in Figure 4.3 (b). The figure also shows the slide-roll ratio variation over the meshing cycle for the two designs.

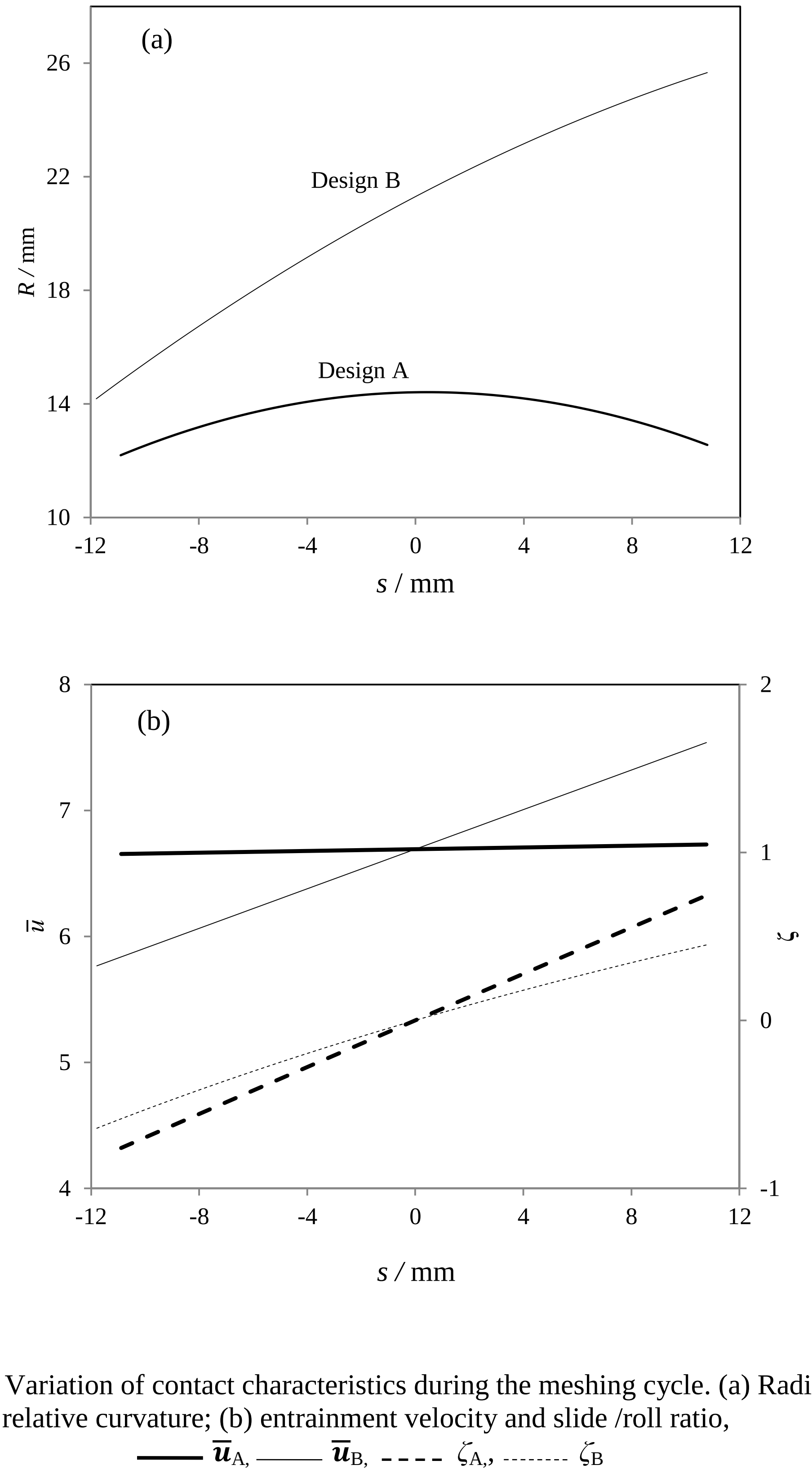

Figure 4.3: Variation of contact characteristics during the meshing cycle. (a) Radius of relative curvature; (b) entrainment velocity and slide /roll ratio,
━━━ $\bar{\boldsymbol{u}}_{A}$, ——— $\bar{\boldsymbol{u}}_{B}$, – – – – ζ_{A},, -------- ζ_{B}

In the spur gear case, the radius of relative curvature, surface velocities, mean entrainment velocity and slide/roll ratio are all constant over an individual contact position specified by an *s* position in the meshing cycle. This is not the case in helical gears contact as the contact lines are inclined to the gear axis at the base helix angle. The contact line at a corresponding position in the meshing cycle acts over a range of *s* and consequently all these values change over this range. The sliding velocity, $(u_s = u_1 - u_2)$ for example is changing between negative, zero and positive values over an individual contact area as shown in Figure 4.4. It is worth noting that this does not reflect a change in direction of motion, rather it is a question of which of the two surfaces is moving faster relative to the contact line. This figure shows the variation along the major axis of the contact ellipse for a pinion input speed of 235.62 rad/s for design A. This variation also takes place at other positions in the meshing cycle wherever a contact line intersects the pitch line while in a spur gear, this sliding velocity is either negative or zero or positive at any position in the meshing cycle.

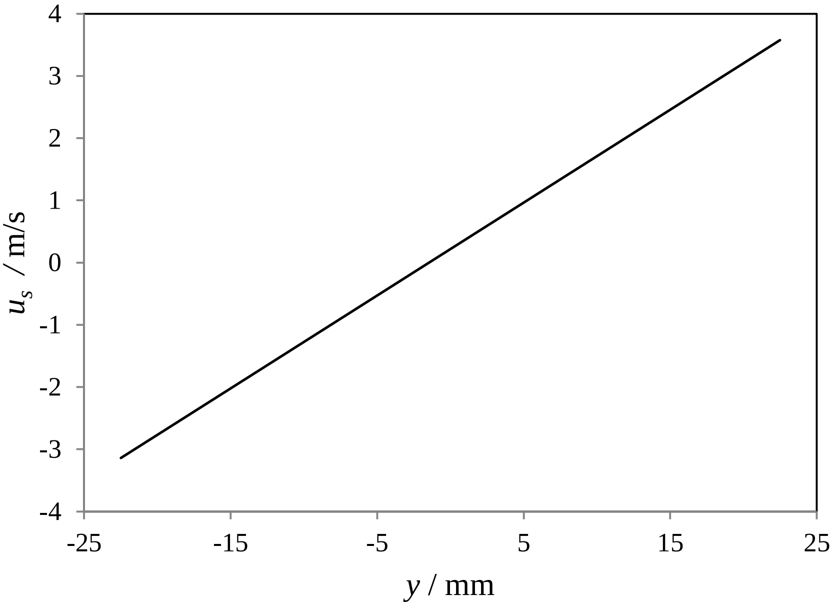

Figure 4.4: Variation of sliding velocities over an individual contact line for design A

4.3 Profile and surface modifications

Two forms of tooth geometry modifications are usually applied in practice. In order to avoid bending deformation overlap of the loaded teeth (Park and Yoo, 2004) (also called “pre-engagement”) and reduce the static transmission error under load (Kahraman & Blankenship, 1999) (Tuplin, 1962) (Bonori et al., 2008) it is desirable to modify the involute tooth form by removing some material from the tooth flanks near their tips. In addition to increasing gear durability this modification also improves gear dynamic response and reduces noise (Bahk and Parker, 2013). This modification is termed “tip relief” which is important to avoid the damaging premature contact that would otherwise begin on the top corner edge of the driven tooth due to tooth flexure under load.

The second area of potential stress concentration and film thinning occurs at the side edges of the teeth, which is exacerbated by any small degree of out-of-parallel misalignment between the gears. In order to minimise this problem the teeth may be “crowned” (Kahraman et al., 2005) (a modification in which the chordal thickness of the teeth is diminished by a small amount from a maximum at the middle of the gear to a minimum at the side edges). In principle crowning changes the contacts from “line” to “point” form, but in practice the contact area becomes an elongated area approximately elliptical in shape under load. By careful choice of the degree of crowning it is possible to prevent heavy contact at the side edges of the teeth under all conditions of loading and misalignment due to mounting errors or shaft deflections under load.

All four gears described in Table 4.1 have the same amount of profile relief at their tips which is a maximum value of 70 μm over a radial distance $r_{tip} - r_{start} = 2$ mm. In order to provide axial profile relief (crowning) the zero load clearance, c_r, is chosen to be 8 μm at the face edges of the teeth. This gives a maximum contact length of 0.93*w* in the at the operating load when the whole face width is crowned and there is no tip relief, where *w* is the maximum contact line length (in the *y*-direction) over the meshing cycle. The form of tip relief adopted in this chapter is parabolic as discussed in chapter 5 (see Figure 5.1) and other forms are considered in detail.

4.3.1 Form of crowning

In this section the effect of different forms of axial crowning is investigated by adopting a general form of modification as shown in Figure 4.5 (a). It is assumed that crowning modification is started at a distance F_o measured from the centre of the face width in both directions. The modification is started with zero slope at the starting points relative to the gear axis direction. The amount of modification, z_c, depends on the parameter F_o and the position, y, along the contact line which can be given by:

$$z_c = \left(\frac{y\cos\beta_b - F_o}{F/2 - F_o} \right)^2 c_r \cos\beta_b \qquad \text{for} \qquad y > \frac{F_o}{\cos\beta_b} \tag{4.3}$$

$$z_c = \left(\frac{y\cos\beta_b + F_o}{F/2 - F_o} \right)^2 c_r \cos\beta_b \qquad \text{for} \qquad y < \frac{-F_o}{\cos\beta_b} \tag{4.4}$$

$$z_c = 0 \qquad \text{for} \qquad \frac{-F_o}{\cos\beta_b} \le y \le \frac{F_o}{\cos\beta_b}$$

The form of the modification for a given value of c_r is controlled by parameter F_o. For example setting F_o equal to zero in any of equations (4.3) and (4.4) will give

$$z_c(x,y)) = \left(\frac{y\cos\beta_b}{F/2}\right)^2 c_r\cos\beta_b$$

This equation represents a fully parabolic form as shown in Figure 4.5 (b). Figure 4.5 (c) shows the 3D total gap between the two teeth surfaces when $F_o = 0.25F$ and when the contact acts over the whole face width for design B.

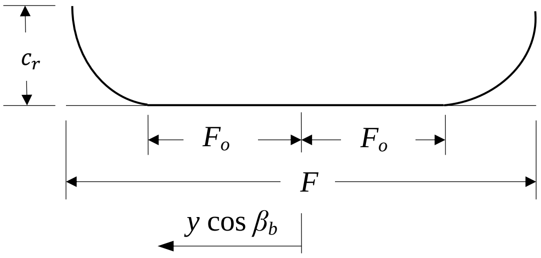

(a)

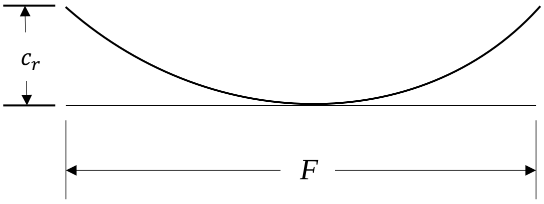

(b)

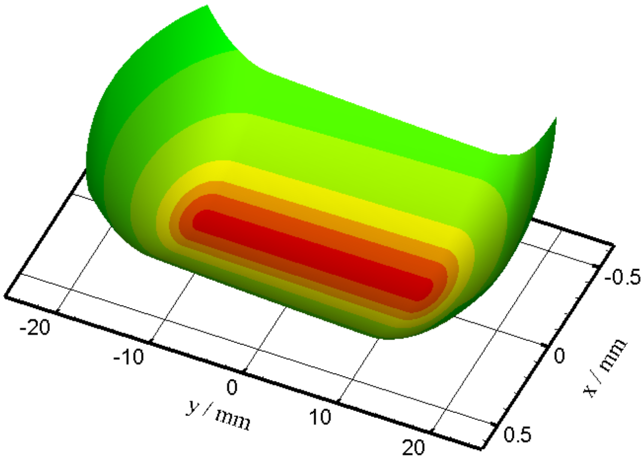

(c)

Figure 4.5: Form of crowning. (a) General form; (b) $F_o = 0$; (c) $F_o = 0.25F$

4.4 EHL results

The solution space for the EHL analysis is the common tangent plane between the teeth in the vicinity of the instantaneous contact line. This is discretised with a mesh spacing $\Delta x = a/40$ in the rolling/sliding direction and $\Delta y = w/857$ in the contact line direction. Here a is the contact semi-width in the x direction at the maximum load and w is the maximum contact line length (in the y-direction) over the meshing cycle, as defined previously.

The transient EHL analysis was carried out for a contact line from a nominal start position where its length is $0.16w$, to a nominal end position where its length falls below $0.16w$. The transient EHL solution was obtained using range of time steps between 300 and 2300 time steps. For the meshing cycle it was found that the transient results are almost identical when the number of time steps is greater than 400. The time step adopted for the analyses divided the meshing cycle into 575 time steps for convenience as the analysed meshing cycle length was 23 mm so that 25 time steps correspond to 1 mm distance. The initial condition was determined from a steady-state EHL analysis at the geometric, kinematic and load conditions of the first time step.

The total gap between the tooth surfaces, which is the basis for the EHL model, is a combination of relative curvature at the point considered plus the profile modification effects.

As the curvature and the contact length change with the progression through the meshing cycle, the undeformed-gap shape varies consequently. Figure 4.6 shows three positions in the meshing cycle for which detailed comparisons for both designs will be shown in chapter 4 and 5. These are at time steps 75, 300 and 500 and correspond to positions where the contact (i) is mainly within the addendum of the wheel, (ii) occurs over the whole face width, and (iii) is mainly within the addendum of the pinion.

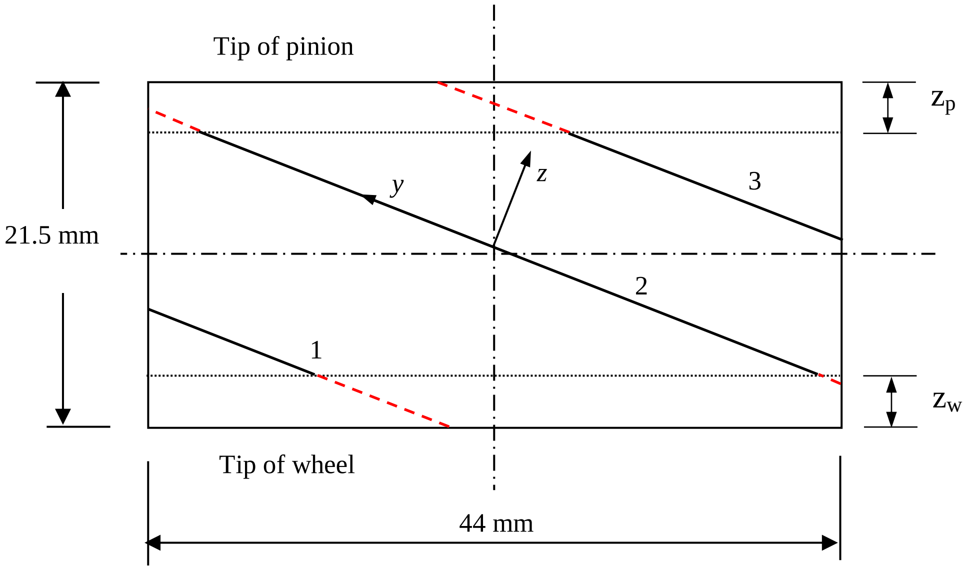

Figure 4.6: Contact position at the three time steps considered, (1): Timestep 75, (2): Timestep 300 and (3): Timestep 500, for the gears specified in table 4.1. Pinion tip relief zone z_p =4.3 mm, wheel tip relief zone z_w = 4.4 mm

The undeformed gap between the two surfaces at these three positions with the corresponding 3D EHL pressure distribution for design A and B are shown in Figure 4.7 and Figure 4.8 respectively. A full parabolic crown was used in both cases where F_o in equations (4.3) and (4.4) is equal to zero. As $y = 0$ at the centre of the face width in the coordinate system adopted, the contact line for the first selected position is in the positive y half of the plane of contact, the contact line for the second position is in both halves of the plane of contact, and the last position is mainly in the negative y half of the plane of contact.

Pressure spikes are produced at the first and third contact positions and are associated with tip relief modification. The contact at position 2 for both designs is essentially elliptic and covers the majority of the y axis range (most of the face width). The contact at this position is effectively dominated by the crowning of the gear teeth in contact rather than tip relief. This attributes to the position of tip relief with respect to the centre of the contact.

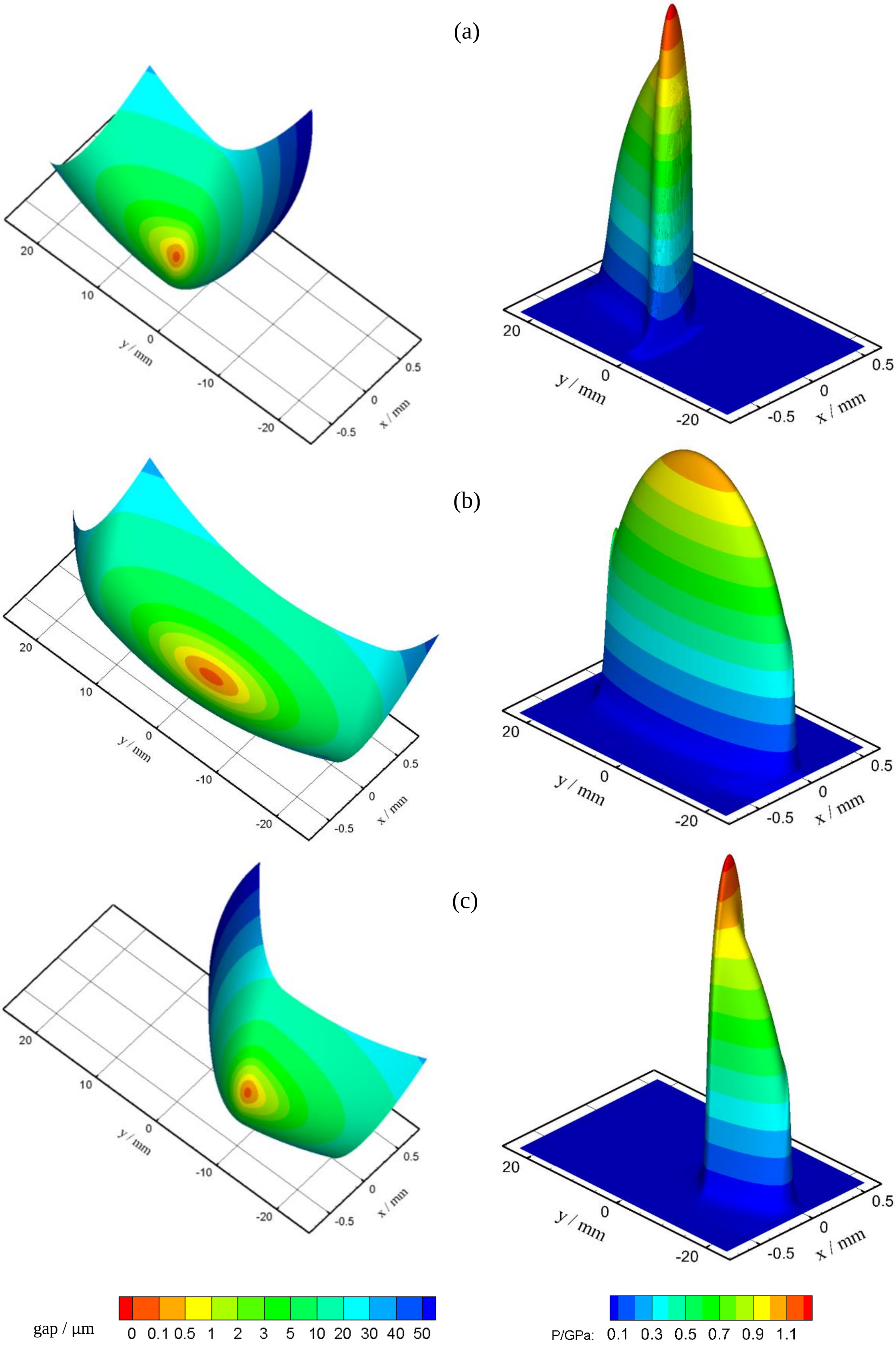

Figure 4.7: Undeformed gap and the corresponding 3D pressure at three positions in the meshing cycle for design A. (a) timestep 75, (b) time step 300 and (c) time step 500.

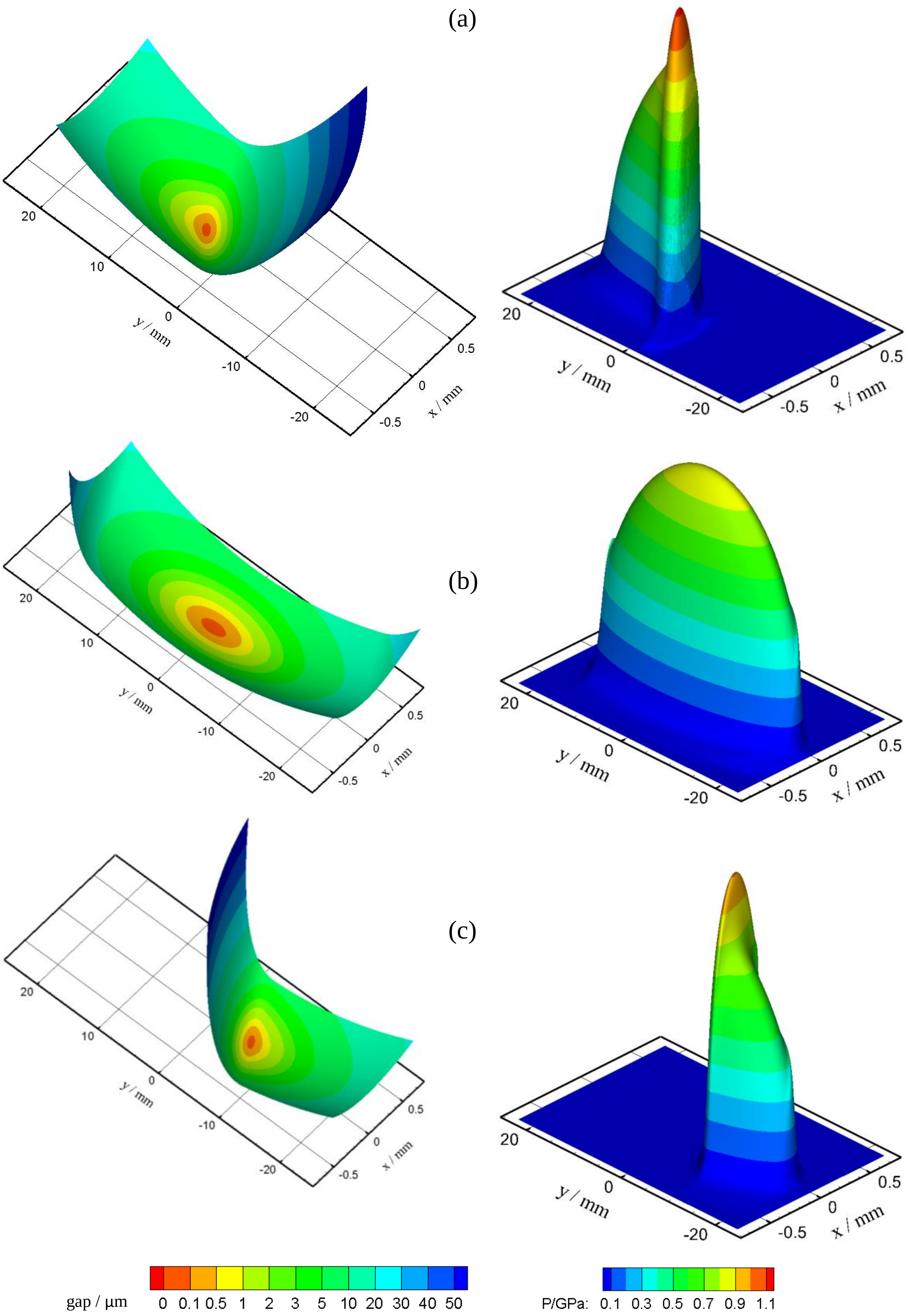

Figure 4.8: Undeformed gap and the corresponding 3D pressure at three positions in the meshing cycle for design B. (a) timestep 75, (b) time step 300 and (c) time step 500.

4.5 Load convergence:

The load carried by an EHL contact can be calculated by integration of the generated pressure over the solution domain. This is given by

$$Load_{EHL} = \iint\limits_{Area} p\,dxdy \tag{4.5}$$

Load convergence is maintained at each time step during the EHL solution of the gear meshing cycle. This process ensures that the load result from the EHL solution is within ± 0.5 percent of the assumed input load for each time step. Variations of the load by this amount has almost no consequent effect on the maximum pressure or minimum film thickness values as given by the well-known equations for elliptical EHL contacts (Hamrock and Dowson 1977)

$$H_{min} = 3.63U^{0.68}G^{0.49}W^{-0.073}\left(1-e^{-0.68\kappa}\right) \tag{4.6}$$

where W and H_{min} in this equation represent the (non-dimensional) load applied on the contacted surfaces and the minimum film thickness, respectively.

Obtaining the specified EHL load can be achieved by adjusting the separation between the two surfaces. The pressure and consequently the load can be increased by reducing the separation in the solution processes and vice versa until convergence is obtained.

Figures 4.9 (a) and 4.9 (b) show comparisons between the input load and the load results from ensuring that equation (4.5) is satisfied throughout the meshing cycle of design A and B respectively to the tolerance described above. The EHL load is presented with a dashed line which can be seen to coincide with the input load almost exactly for both designs. Full parabolic forms for both crowning and tip relief modification are used in these comparisons. Similar results were also found for all other forms of profile and crowning modifications

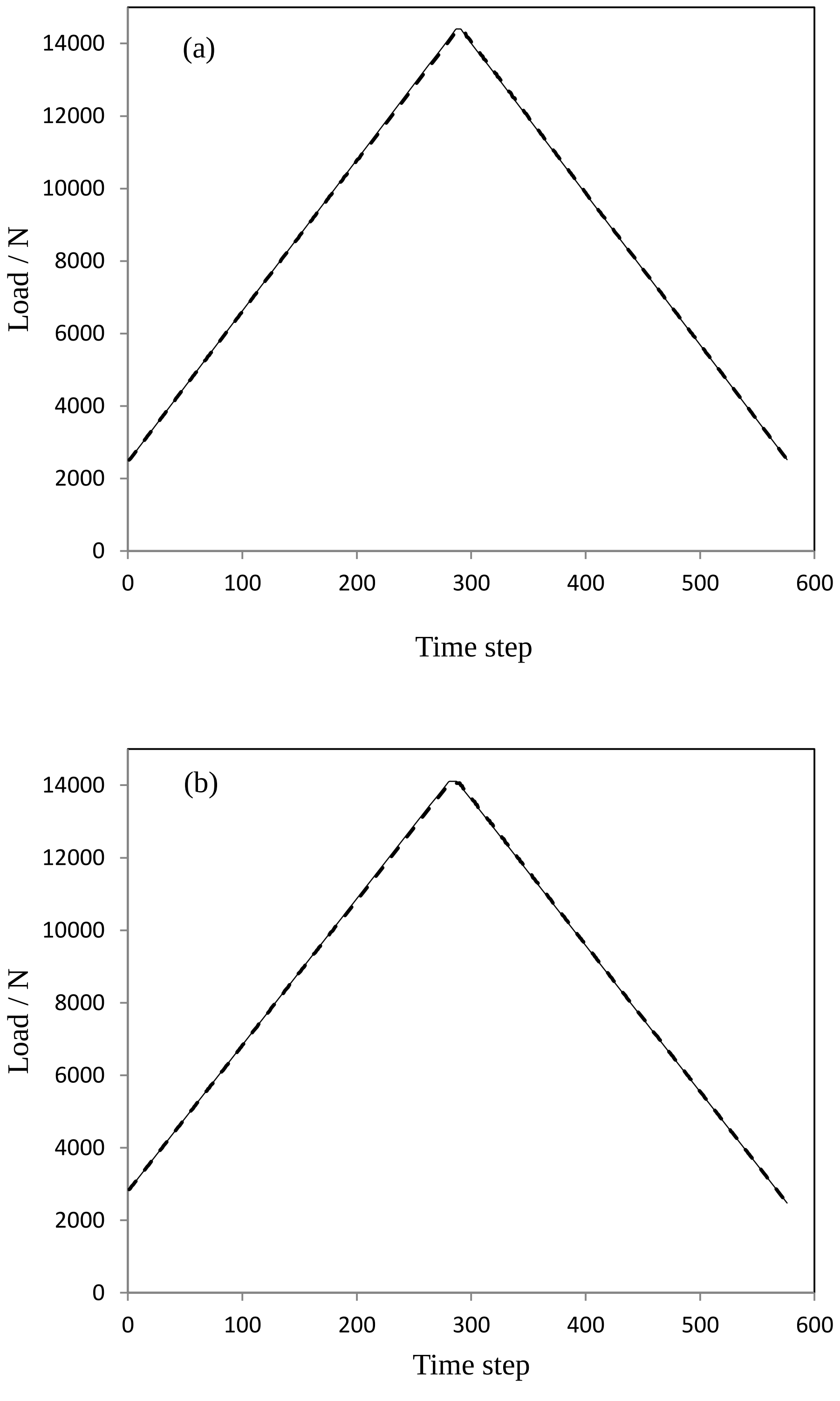

Figure 4.9: Load convergence during the meshing cycle, ------ the EHL load obtained and ______ the specified input load. (a) Design A; (b) design B

4.6 Results for different forms of crowning

Figure 4.10 shows the behaviour of the maximum pressure and minimum film thickness during the meshing cycle for design A for five forms of crowning where $F_o = 0$, 0.1*F*, 0.25*F*, 0.4*F* and 0.45*F*. With the parabolic form of tip relief that was used in this comparison, the maximum pressure and the minimum film thickness behaviour obtained varies significantly with the form of crowning. The case of full parabolic crowning which corresponds to $F_o = 0$, gives the highest calculated EHL pressure of 1.25 GPa.

For the case of $F_o = 0$ the maximum pressure occurs at one end or other of the contact line where tip relief is achieve over approximately time step ranges 0 to 210 and 360 to 575. From time step 210 to 360 the maximum pressure occurs at the centre of the contact and behaves differently. This features is typical of all the maximum pressure results considered in this thesis that are presented in this way.

The magnitude of the maximum pressure experienced decreases as F_o is increased. This is essentially related to the increase of the contact area length along the *y* direction which reduces the concentration of the load at a single point at the start of tip relief modification. However, when $F_o = 0.45F$, despite the noticeable reduction in the maximum pressure trends at the first and last 200 time steps, pressure spikes appear at the middle of the meshing cycle as shown in Figure 4.10 (a). This is associated with a reduction in the film thickness levels which is 0.14 μm in comparison with 0.21 μm when $F_o = 0$ at time step 300 as shown in Figure 4.10 (b). The case of $F_o = 0.25F$ gives the best combination of maximum pressure and minimum film thickness trends during the meshing cycle. With this form of crowning the maximum pressure varies between 0.98 GPa and 1.17 GPa during the meshing cycle. The corresponding minimum film thickness varies between 0.16 μm and 0.22 μm.

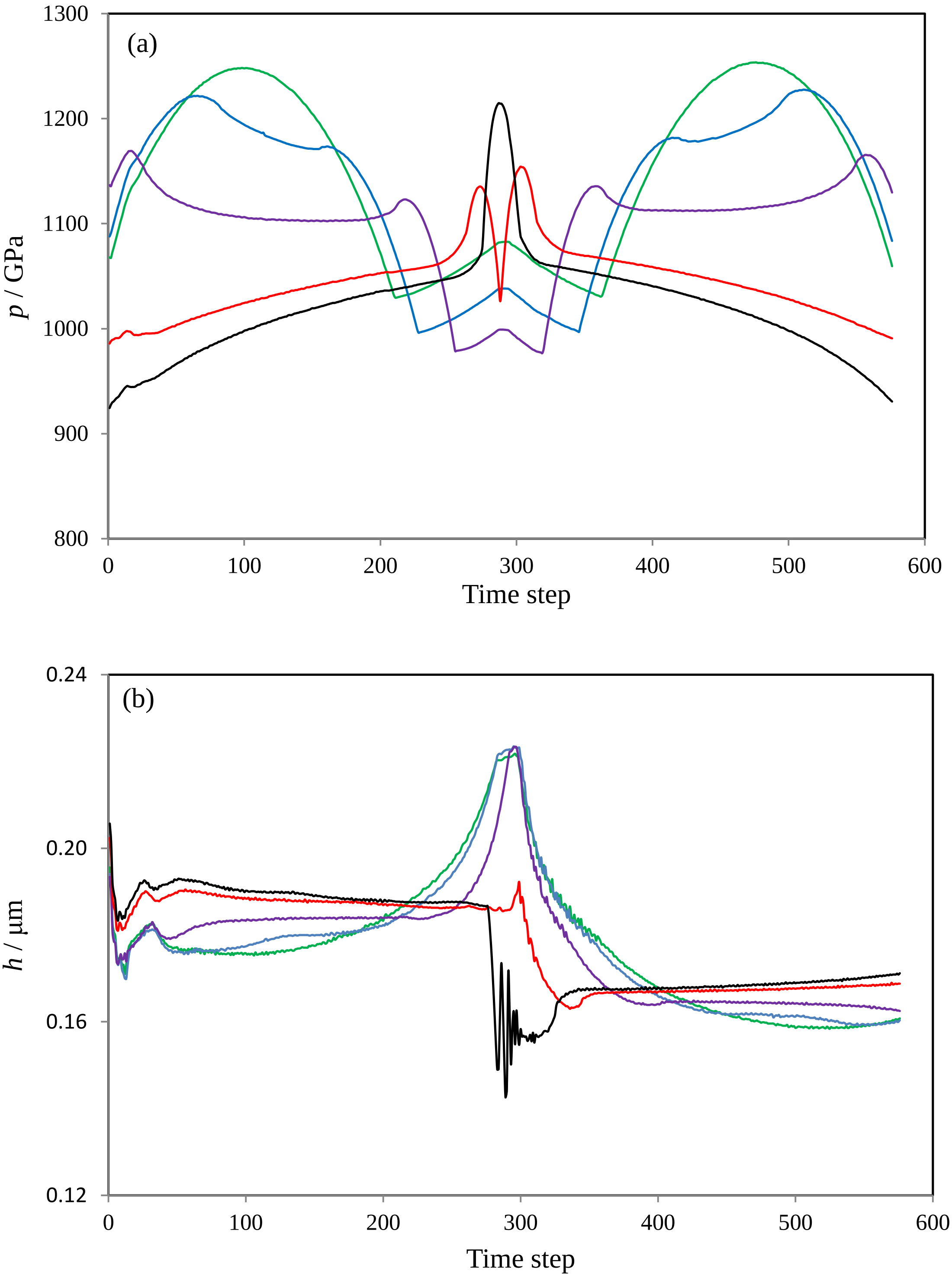

Figure 4.10: Variation of maximum pressure (upper) and minimum film thickness during the meshing cycle for design A for five forms of crowning, green: $F_o = 0$, blue: $F_o = 0.1F$, purple: $F_o = 0.25F$, red: $F_o = 0.4F$ and black: $F_o = 0.45F$, with parabolic tip relief.

The effects of choosing different forms of crowning are more clearly apparent in Figure 4.11 which shows 3D isometric plots of the transient EHL analyses pressure distribution at time step 300 for the five forms of crowning, together with the corresponding 2D film thickness contours for the results shown in Figure 4.10. Figure 4.11 (a) shows a typical point contact EHL result which corresponds to $F_o = 0$. With $F_o = 0$ axial crowning relieves the contact progressively along the contact line. As F_o increases, for contact lines that reach the tip relief zone before the crowning becomes active the contact is limited by the tip relief imposed. This is clear in the cases where $F_o = 0.4F$ and $F_o = 0.45F$ which are shown Figure 4.11 (d) and (e) respectively. In these cases the end of contact line stress concentration effect appears on both sides of the contact but it is more aggressive (has the effect of thinning the film thickness) on the left side of the contours (positive *y*). This is because at this particular time step the start point of tip relief on the tooth profile is closer to the starting position of crowning on the positive *y* part of the contact area in comparison to the negative *y* (right side of the contact).

With the exception of the case of $F_o = 0$, two peak pressure areas can be seen in this figure which are associated with the introduction of crowning modification on both sides of the contact. Thinning of the film thickness occurs at the start of crowning modification due to the side leakage which takes place in the *y* direction, which leads to the occurrence of these pressure spikes. This can be clearly seen in Figure 4.12 which shows transient pressure and film thickness distributions along the *y* direction at time step 300 for the five forms of crowning for design A. A similar comparison at this position in the meshing cycle was made for design B. In general, the same trend was found as shown in Figure 4.13 with some differences in the compared values as design B has different tooth curvature and surface velocities in comparison with design A.

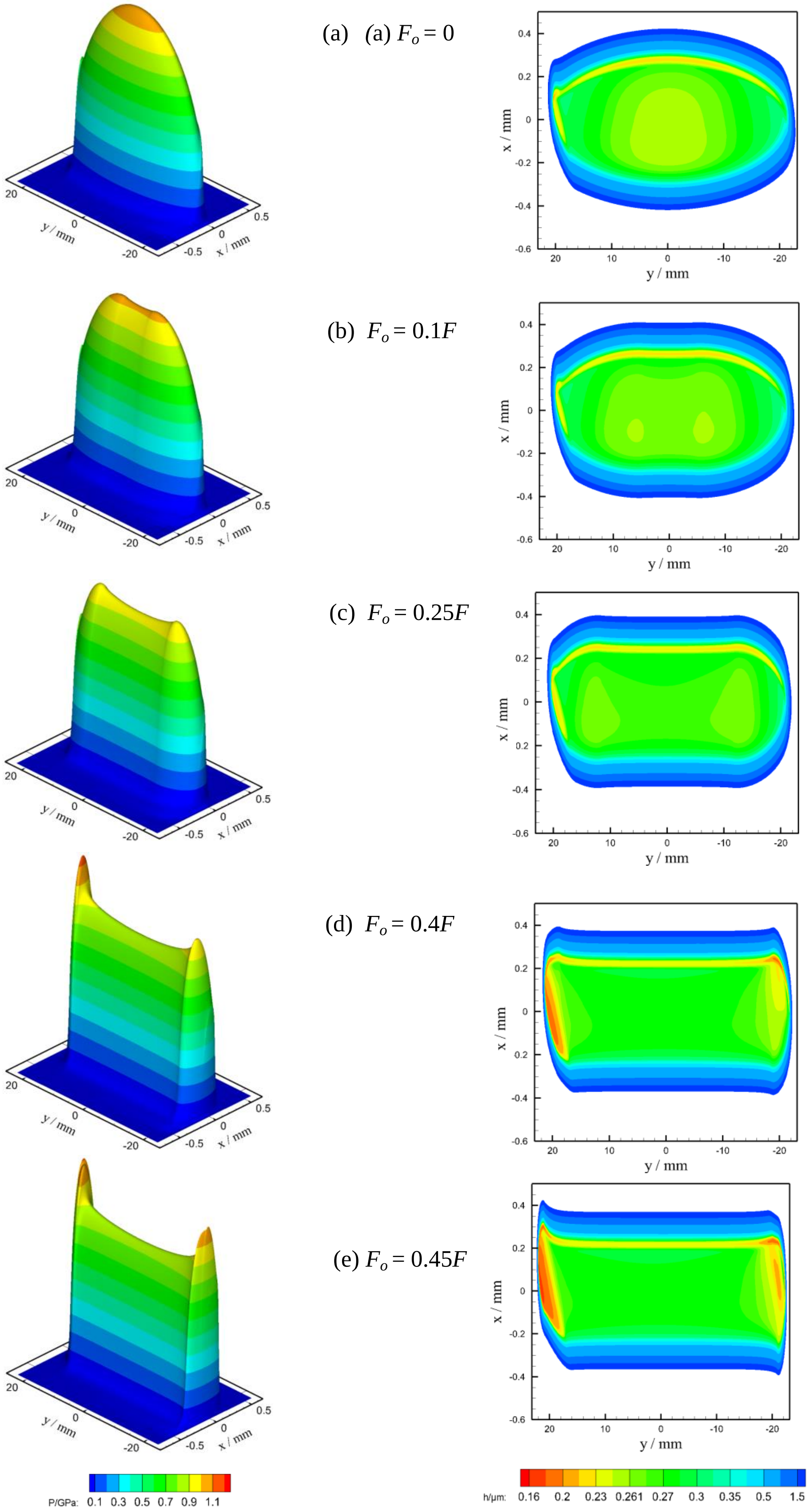

(a) (a) $F_o = 0$

(b) $F_o = 0.1F$

(c) $F_o = 0.25F$

(d) $F_o = 0.4F$

(e) $F_o = 0.45F$

Figure 4.11: Pressure distribution (left) and film thickness (right) at time step 300 for five forms of crowning

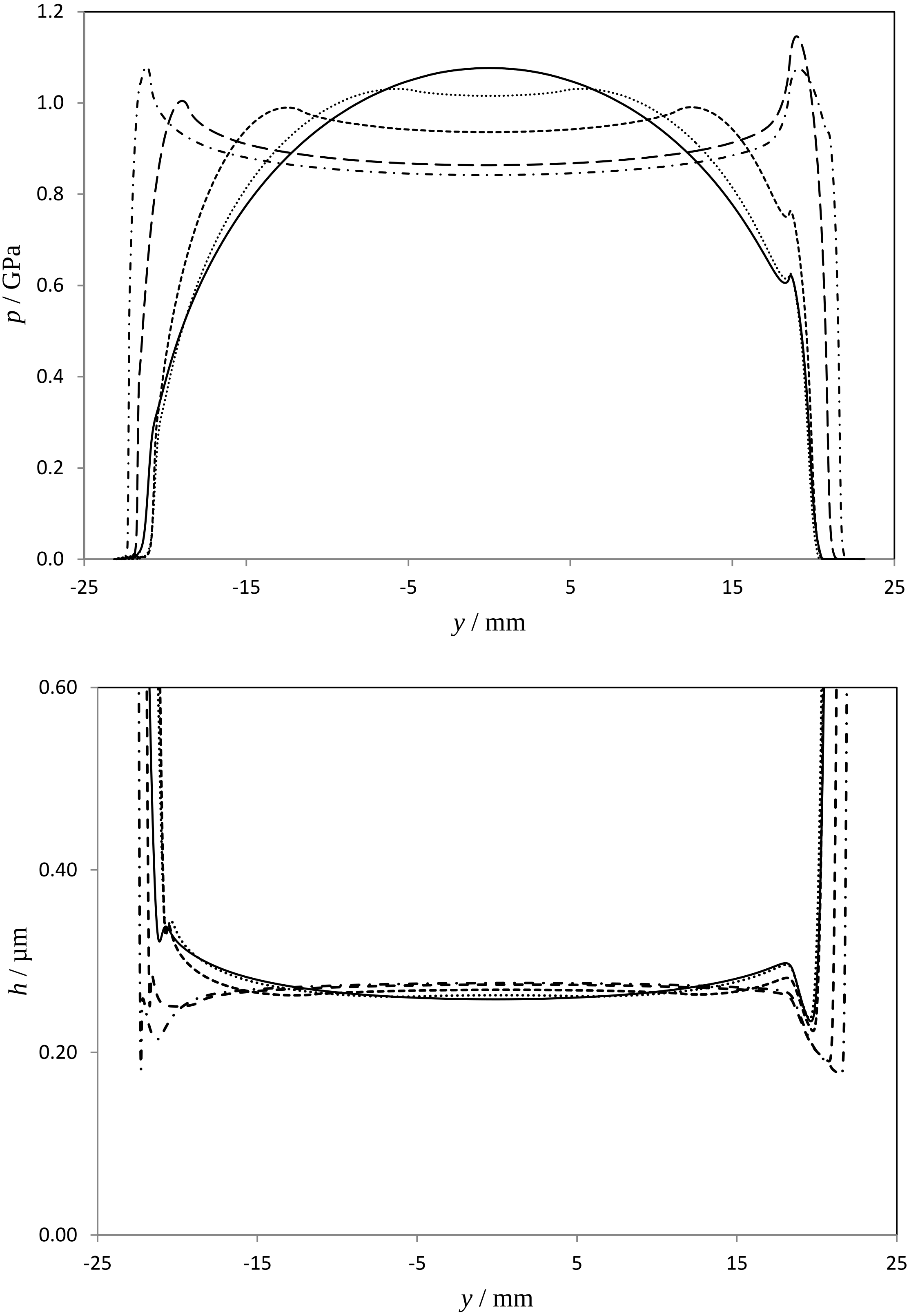

Figure 4.12: Pressure and film thickness distribution along y direction at x = 0 at time step 300 for design A, ——— $F_o = 0$, ... $F_o = 0.1F$, ------ $F_o = 0.25F$, — — $F_o = 0.4F$ and - · - · - , $F_o = 0.45F$.

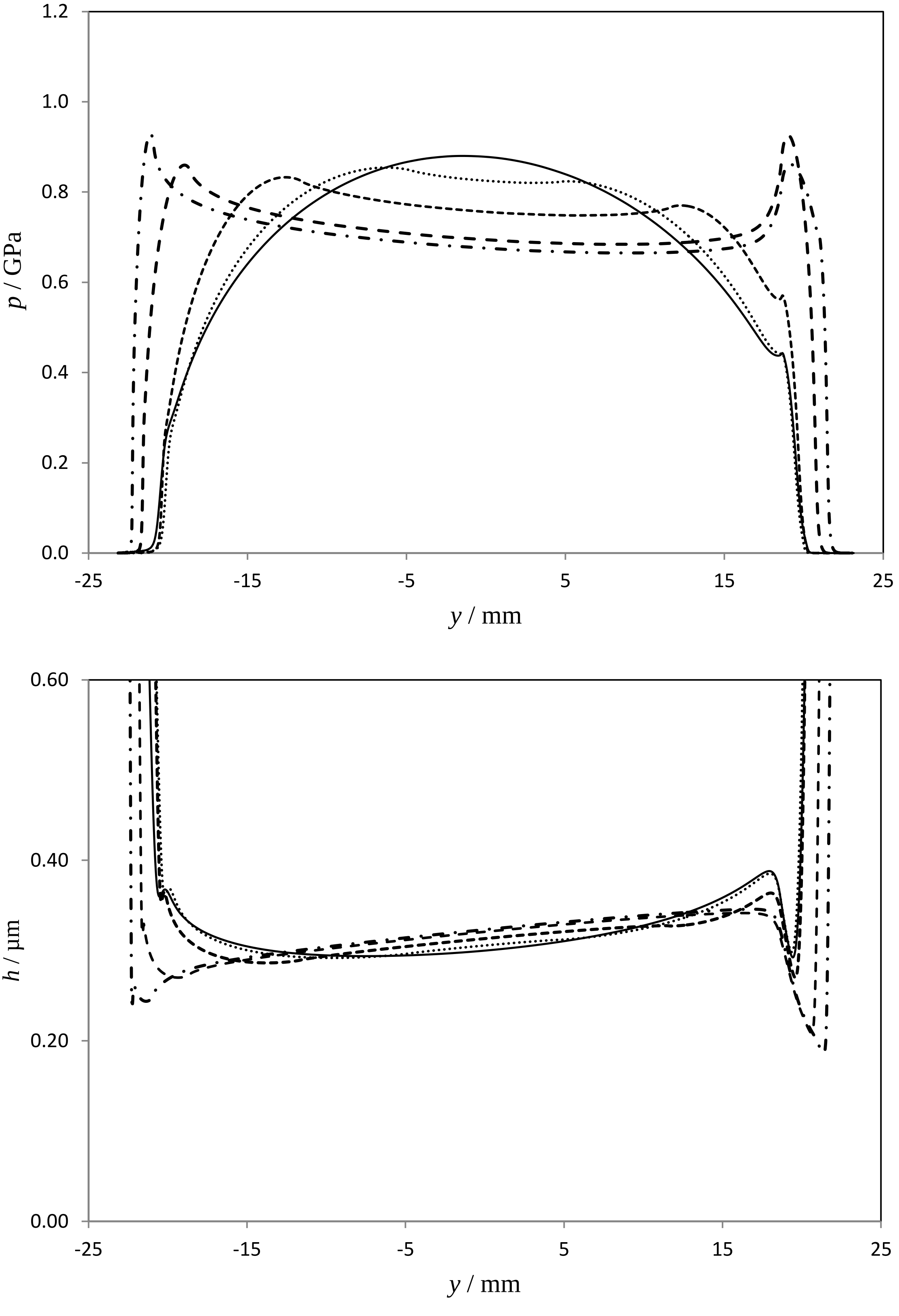

Figure 4.13: Pressure and film thickness distribution along y direction at $x = 0$ at time step 300 for design B, ——— $F_o = 0$, ... $F_o = 0.1F$, - - - - - $F_o = 0.25F$, — — · $F_o = 0.4F$ and – · – · , $F_o = 0.45F$.

Figures 4.14, 4.15, 4.16, 4.17 and 4.18 show the 3D pressure distribution and the corresponding film thickness contours for design A at three positions in the meshing cycle for the cases $F_o = 0$, 0.1F, 0.25F, 0.4F, 0.45F respectively. These are the positions shown in Figure 4.6 which are at time steps 75, 300 and 500 respectively. The case of timestep 300 which was shown in Figure 4.11 is repeated in these figures for the purpose of comparison. Figures 4.14 and 4.15 show single pressure spikes at time steps 75 and 500 which are related to the tip relief effect as the crowning effect when $F_o = 0$ and 0.1F is out of the contact region at this position in the meshing cycle. The other figures (4.16, 4.17 and 4.18) show two pressure spikes at time steps 75 and 500. The first pressure spike is associated with the introduction of crowning as stated previously, while the second one results from tip relief modification. The film thickness contours also show the reduction in the film thickness levels at the tip relief zone.

It is worth noting that although the contact and the pressure spikes elevate the pressure noticeably, the maximum pressures at these locations are not significantly greater than the central pressures seen for the case where $F_o = 0$.

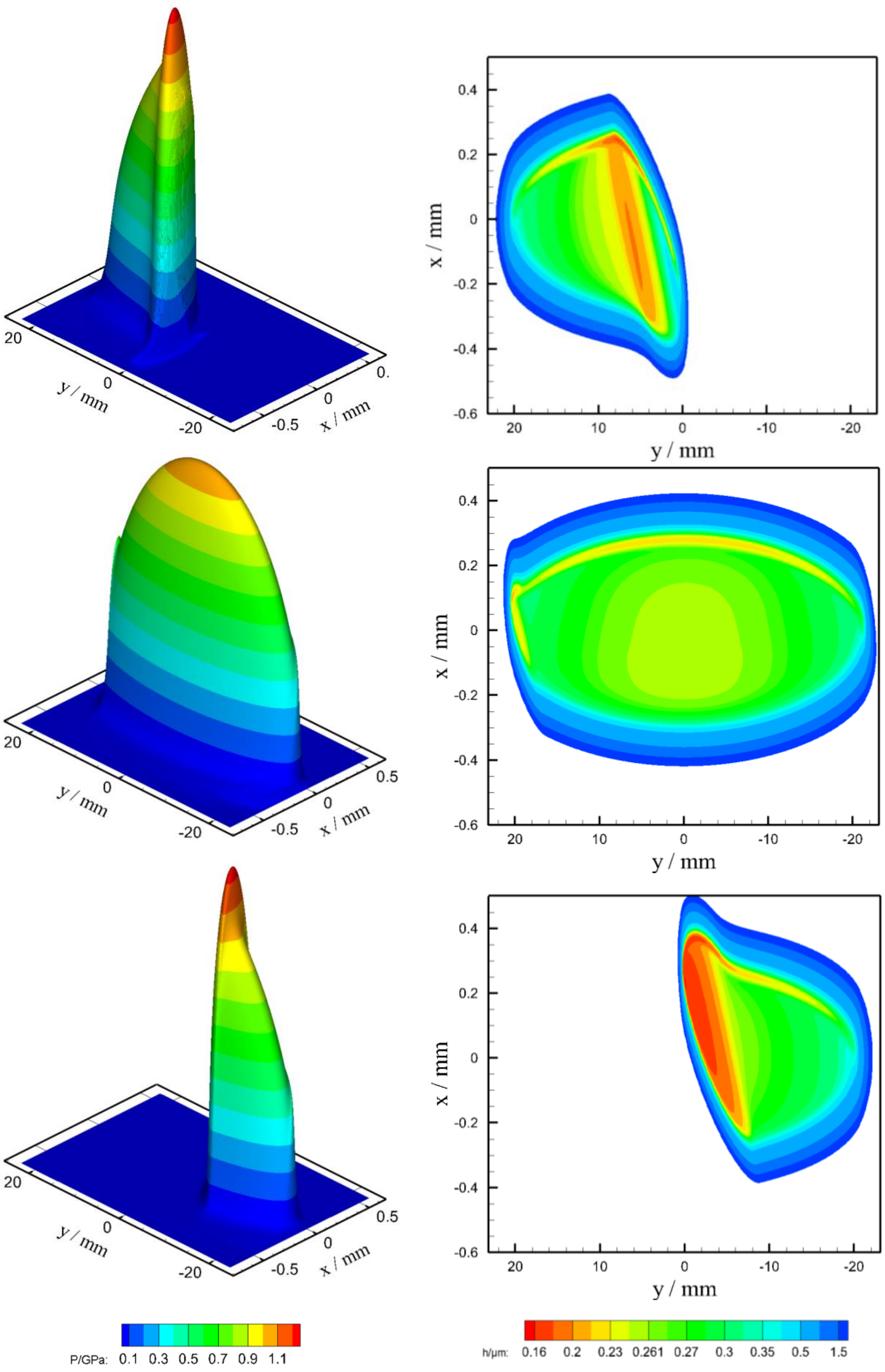

Figure 4.14: 3D pressure distributions and film thickness contours for design A with $F_o = 0$ at the three timesteps considered, timestep 75 (upper figures), timestep 300 (central), timestep 500 (lower).

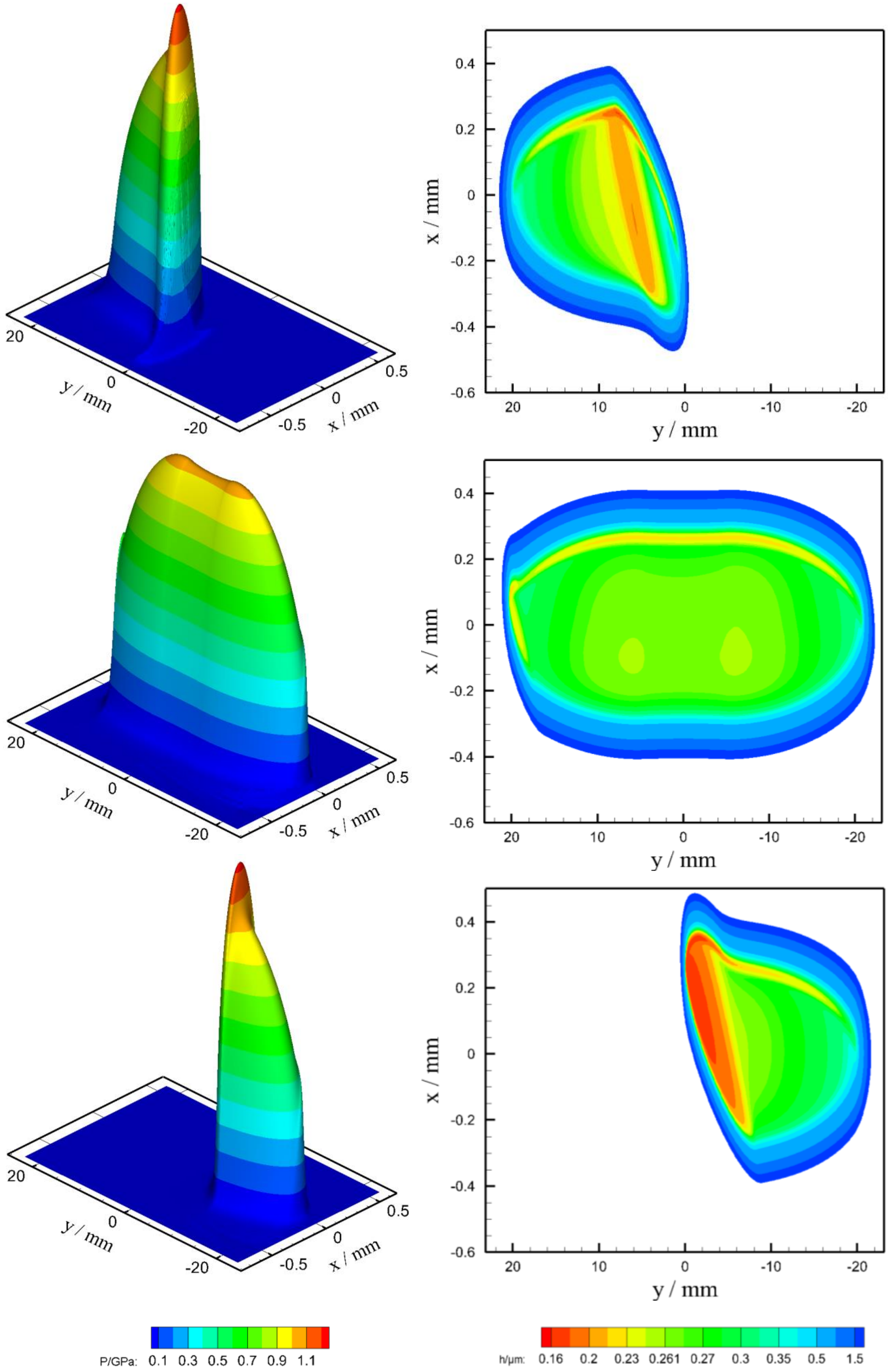

Figure 4.15: 3D pressure distributions and film thickness contours for design A with $F_o = 0.1F$ at the three timesteps considered, timestep 75 (upper figures), timestep 300 (central), timestep 500 (lower).

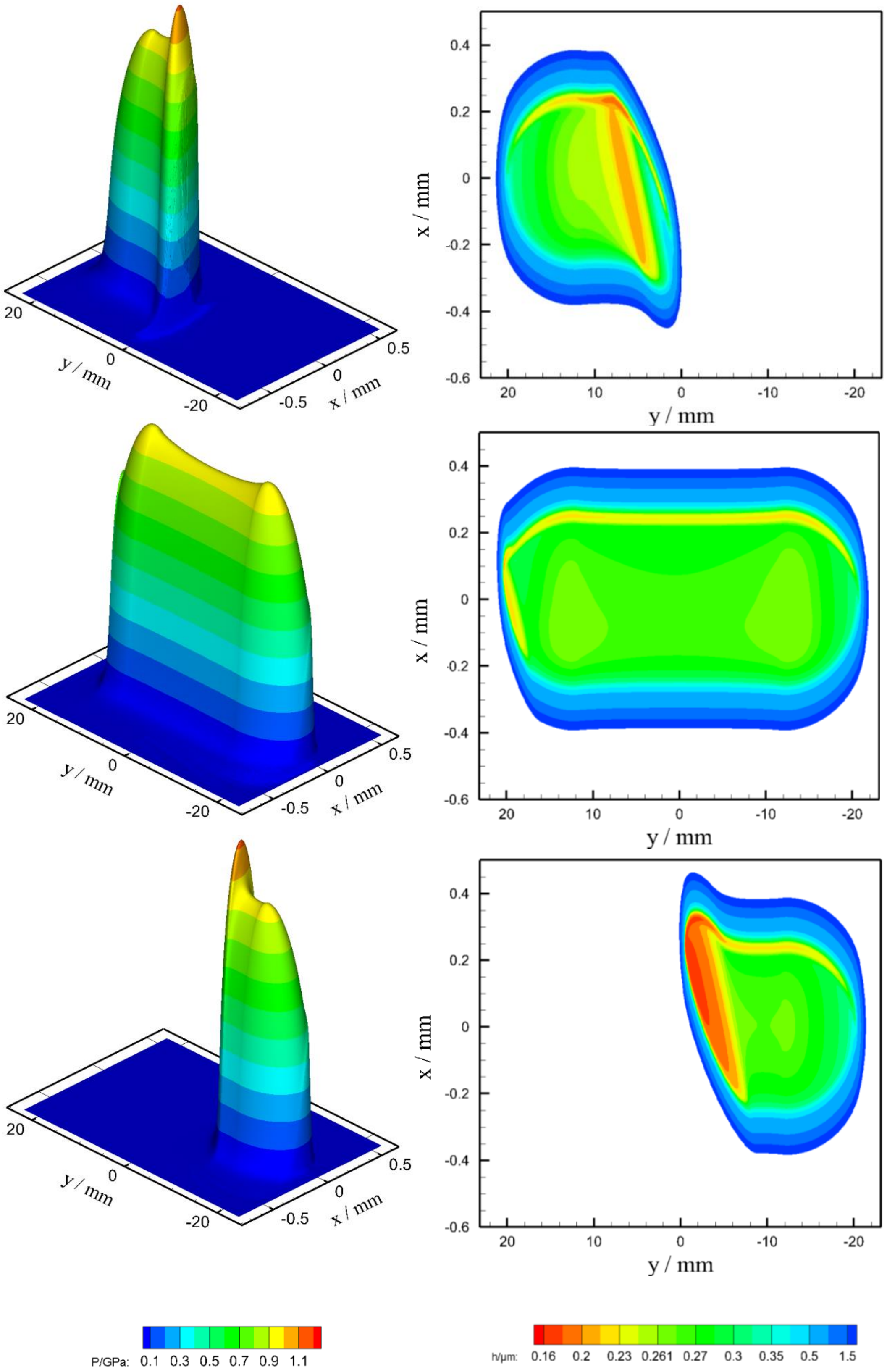

Figure 4.16: 3D pressure distributions and film thickness contours for design A with $F_o = 0.25F$ at the three timesteps considered, timestep 75 (upper figures), timestep 300 (central), timestep 500 (lower).

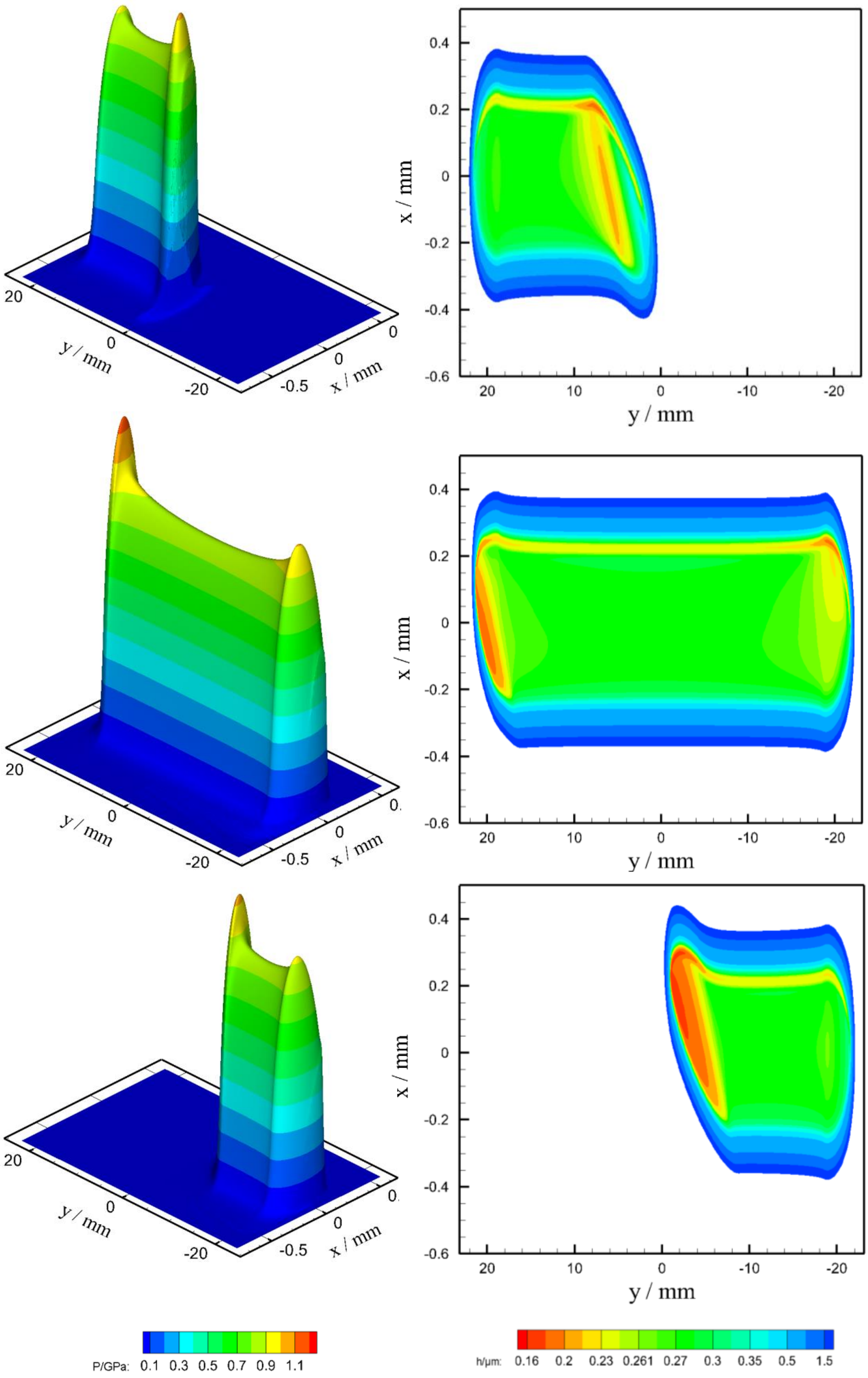

Figure 4.17: 3D pressure distributions and film thickness contours for design A with $F_o = 0.4F$ at the three timesteps considered, timestep 75 (upper figures), timestep 300 (central), timestep 500 (lower).

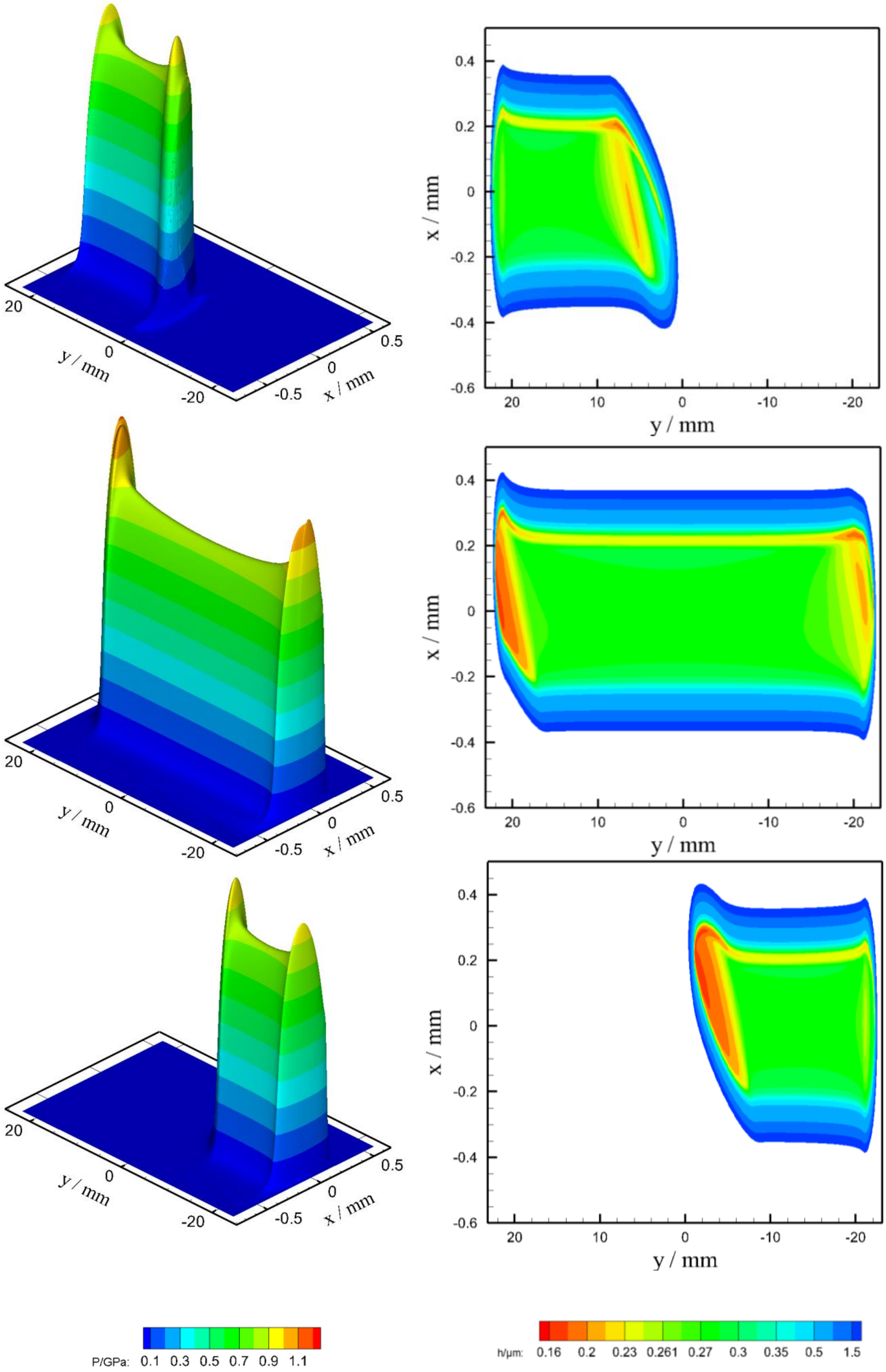

Figure 4.18: 3D pressure distributions and film thickness contours for design A with $F_o = 0.45F$ at the three timesteps considered, timestep 75 (upper figures), timestep 300 (central), timestep 500 (lower).

Chapter 5

Tip relief

5.0 Introduction

In this chapter the effect of tip relief on the EHL performance of helical gears has been investigated by adopting different forms for the relief geometry for the two gear pair designs considered in chapter 4. The tip relief profiles are applied to the involute profile over the radial range

$$r_{start} < r < r_{tip} \tag{5.1}$$

where r is the radius measured from the gear axis as given by equation (2.16).

The forms of tip relief used in this chapter can be categorized into two main cases which are:

a- Combinations of linear and parabolic profiles.

b- Power law profile.

In this chapter the axial crowning is expressed in the full parabolic form where $F_0 = 0$ in equations (4.3) and (4.4). The transverse clearance c_r for each tooth at the side edges is 8 μm when the contact occurs at the centre of the tooth under zero load.

5.1 Linear and parabolic profiles

The modification in this case consists of a combination of linear and parabolic profiles which join at $r = r_{ce}$ with equal slope as shown in Figure 5.1.

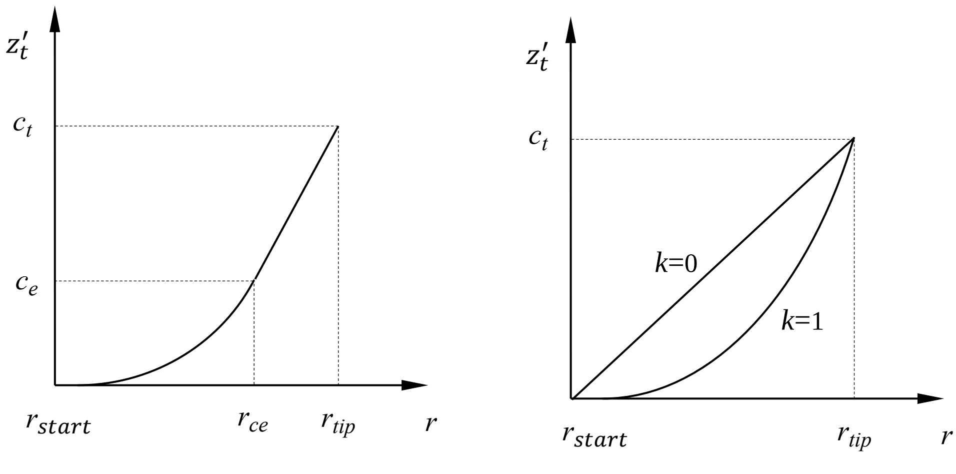

(a) (b)

Figure 5.1: Illustration of tip relief geometry showing parabolic and linear sections

The amount of surface removal, z_t', depends on parameters c_e, c_t, r_{start}, r_{tip} and r_{ce} as shown in Figure 5.1 (a). The parabolic modification starts with zero slope (relative to the involute profile) at radius r_{start} and transition to the linear profile occurs at radius r_{ce} where

$$r_{ce} = r_{start} + k(r_{tip} - r_{start}) \tag{5.2}$$

The nature of the modification for a given value of c_t is controlled by parameter k. A simple linear tip relief profile corresponds to k = 0, and the fully parabolic form with tooth slope continuity at $r = r_{start}$ is given by k = 1 as shown in Figure 5.1 (b). For intermediate values of k the transition between a parabolic profile and linear profile occurs with no change of slope.

The gap due to tip relief can be determined by considering the equations for the straight line and the parabolic curve as shown in Figure 5.1 (a). It can be easily shown that the equation for the linear part is

$$z_t'(x,y) = c_e + \frac{c_t - c_e}{r_{tip} - r_{ce}}\left(r(x,y) - r_{ce}\right) \tag{5.3}$$

and for the parabolic part

$$z_t'(x,y) = \left(\frac{r(x,y) - r_{start}}{r_{ce} - r_{start}}\right)^2 c_e \tag{5.4}$$

The amount of relief at the end of the curve, c_e can be determined by equating the slope at the end point of the parabolic curve and the start point of the straight line as

$$c_e = \frac{r_{ce} - r_{start}}{2r_{tip} - r_{ce} - r_{start}} c_t \tag{5.5}$$

The gap in the normal direction is

$$z_t(x,y) = z_t'(x,y) cos\, \beta_b$$

5.2 Features of the gap along *y* axis

During the first part of the meshing cycle the effective contact line is limited by the tip relief profile applied to the wheel tooth, and during the latter part it is limited by the tip relief profile applied to the pinion tooth. Figures 5.2, 5.3 and 5.4 illustrate the zero load gap between the tooth surfaces along the contact line at three meshing cycle positions for design A and B when *k*=0, *k*=0.5 and *k*=1 respectively. In each figure the upper and lower parts show the gap for design A and B respectively. Mesh positions 1, 2 and 3 are at time steps 75, 300 and 500, respectively. The zero load gaps are offset by 2 or 4 μm for clarity.

Figure 5.2 (a) shows the gap for design A when the tip relief profile is linear (k=0). For position 2 in this figure, it is clear that the gap is given by the axial crown with the pinion tip relief becoming apparent for $y > 18.5$ mm and for $y < -21.5$ mm . For position 1 the contact is essentially limited by the wheel tip relief at $y < 6.4$ mm, and for position 3 it is limited by the pinion tip relief for $y > -6.3$ mm. For positions 1 and 3 the combination of the axial crown and the active tooth relief leads to contacts that are curtailed at the onset of tip relief position where a significant stress concentration emerges in the calculations. Generally, the same feature can be seen in the corresponding gaps of design B which is shown in Figure 5.2 (b).

The severe change in the slope of the profile that is shown in Figure 5.2 for both designs due to the linear modification is overcome by adding a transition parabolic curve over a specified radial distance. The remaining part of modification is linear which meets with the parabolic curve at equal slope. The case when the modification corresponds to k=0.5 in equation (5.2) is shown in Figure 5.3 for both designs. The modification is further improved by using a full parabolic curve (k =1) as shown in Figure 5.4.

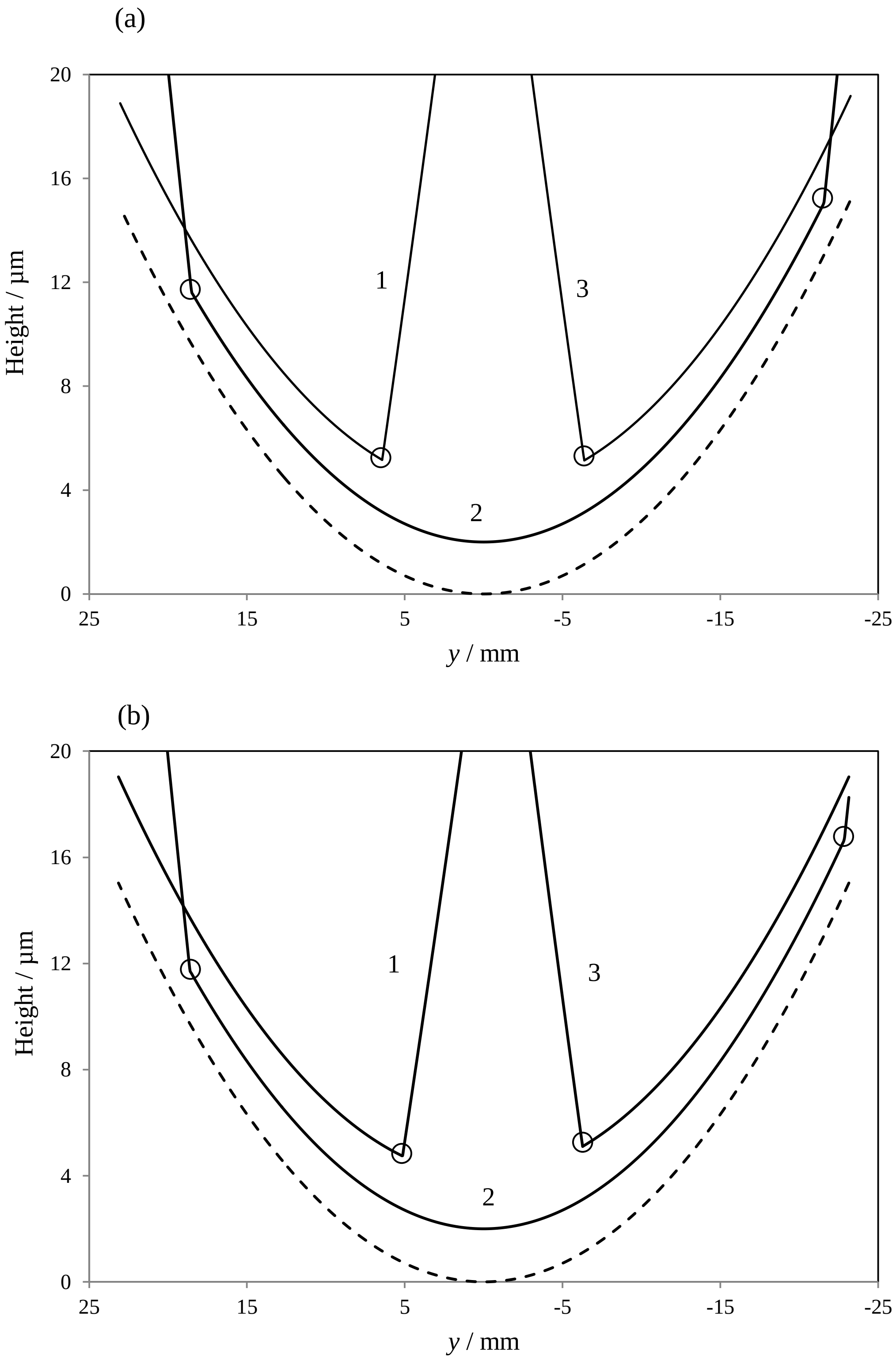

Figure 5.2: Gap between gear surfaces (offset) along contact line at positions 1, 2 and 3 in the meshing cycle for linear tip relief modification, $k = 0$. Axial crown is shown broken and symbol ○ indicates starts of tip relief for each contact line. (a) Design A; (b): Design B

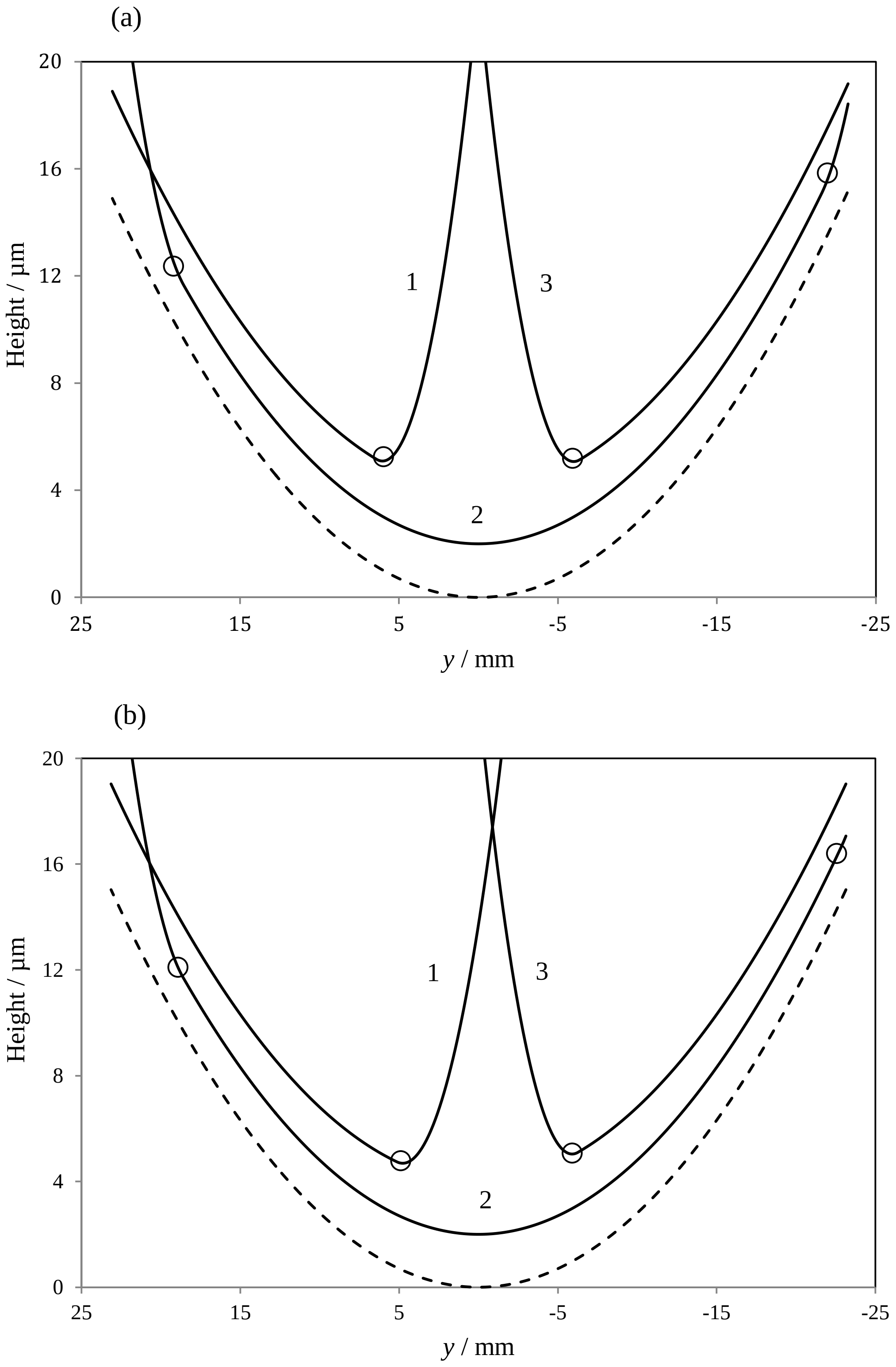

Figure 5.3: Gap between gear surfaces (offset) along contact line at positions 1, 2 and 3 in the meshing cycle for mixed relief modification, *k* =0.5 . Axial crown is shown broken and symbol ○ indicates starts of tip relief for each contact line.
(a) Design A; (b): Design B

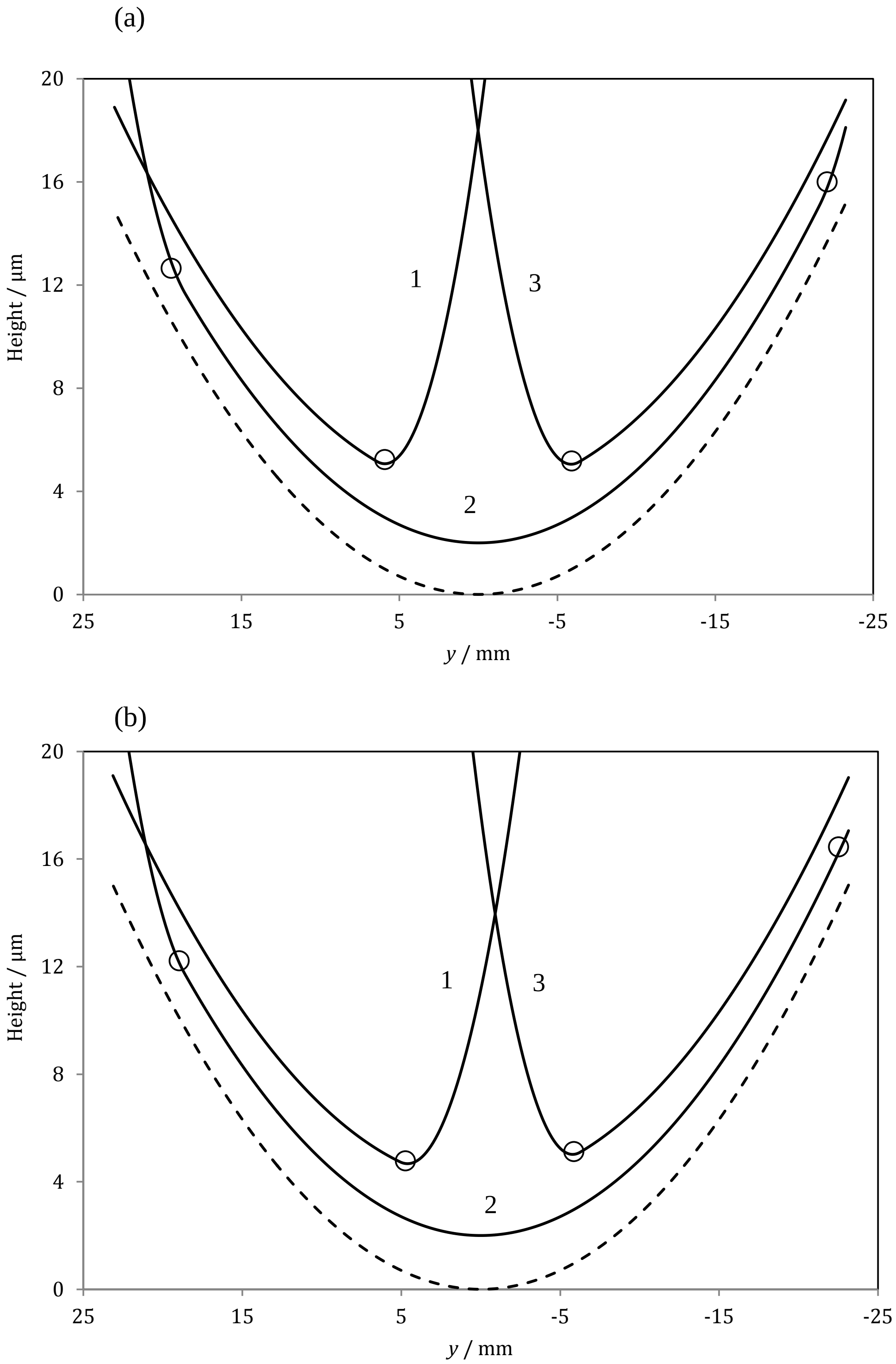

Figure 5.4: Gap between gear surfaces (offset) along contact line at positions 1, 2 and 3 in the meshing cycle for full parabolic tip relief modification, $k = 1$. Axial crown is shown broken and symbol ○ indicates starts of tip relief for each contact line. (a) Design A; (b): Design B

5.3 Results of parametric study

All four gears in this chapter have the same amount of profile relief at their tips which is 70 μm over a radial distance $r_{tip} - r_{start}$ = 2 mm. This is the design specification for the test gears of case A where a linear tip relief profile is utilised. The detailed results of the transient EHL analyses presented correspond to the full parabolic tip relief profile i.e. k = 1, and the effects of variation of k from unity to zero are also investigated. As far as this kinematic analysis is concerned (where tooth bending is not taken into account) it was found that the contact did not generate significant pressure beyond the radius where tip relief is applied, and this was taken into account by using the effective contact line length in the load specification.

Figure 5.5 compares the behaviour of the maximum pressure and the minimum film thickness during the meshing cycle for the two designs for the case where k = 1. The two designs generally give the same trend for both the maximum pressure and minimum film thickness with some lack of symmetry in the maximum pressure of design B towards the middle of the meshing cycle. This is related to the significant change in radius of relative curvature over the meshing cycle as discussed in relation to Figure 4.3 (a).

Between time steps 204 and 370 for design A and between time steps 180 and 370 for design B the contact line is effectively limited at both ends by the side faces of the gears and at other times one end of the contact line is limited by the tip relief profile of either the wheel or the pinion. With this form of tip relief the maximum calculated EHL pressure varies between 1.02 GPa and 1.25 GPa for design A, and between 0.82 GPa and 1.12 GPa for design B. This can be attributed to the differences in the radii of relative curvature between the two designs throughout the meshing cycles. The tooth profile in design B has a larger radius of relative curvature at all contact positions which gives a larger contact area, and as a result a smaller Hertzian pressure. The corresponding minimum film thickness varies between 0.16 μm and 0.22 μm for design A and between 0.16 μm and 0.25 μm for design B. The maximum pressure occurs where the contact lines is terminated by tip relief over time step ranges 0 to 210 and 360 to 575 as explained in section 4.6 .The maximum pressure in both designs approaches its highest value at time steps close to 100 and 500. These are the two contact lines that intersect the tip relief boundary at the centre of the face width.

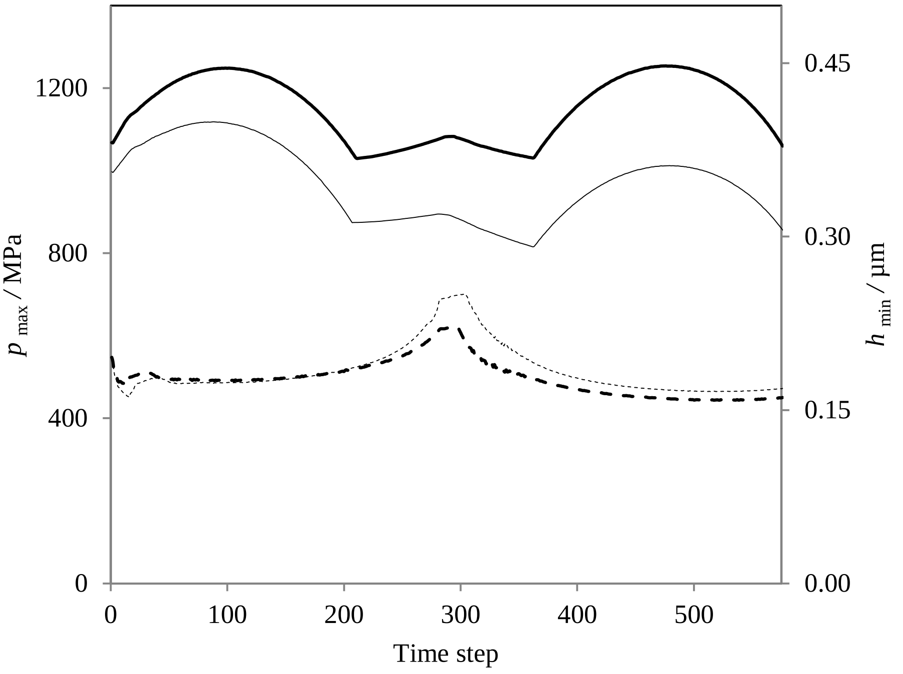

Figure 5.5: Variation of maximum contact pressure (solid lines) and minimum oil film thickness (broken lines) during the meshing cycle for the case of full parabolic tip relief modification, k = 1. Heavy lines: Design A; light lines: Design B.

Figure 5.6 shows the maximum pressure obtained during the meshing cycle when the tip relief profile adopted is linear. The gears are operating at a nominal maximum Hertzian pressure of about 1 GPa and it can be seen that during full contact width operation this is representative of the maximum pressure experienced. However, during the parts of the meshing cycle where the tip relief profile limits the length of the contact, very high pressures of up to 3.5 GPa are experienced and the fluid film is not able completely to separate the surfaces.

The high pressure levels are due to the stress concentration caused by the tip relief profile. This severe effect of the tip relief profile can be reduced by including a parabolic transition between the involute profile and the linear tip relief so that the slope of the tooth flank remains continuous, as will be shown later in this chapter.

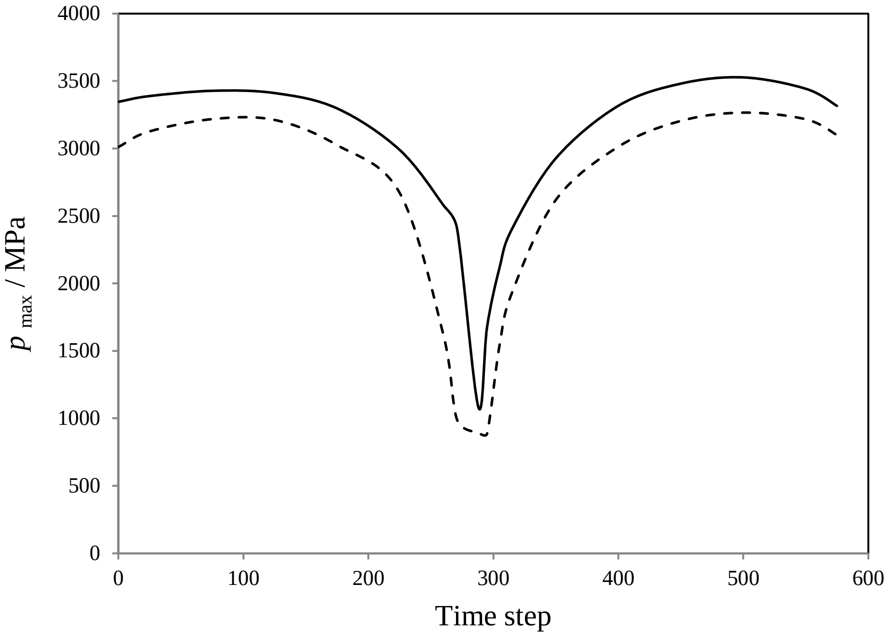

Figure 5.6: Maximum pressure obtained in each time step for the case of linear tip relief profile $k = 0$, design A (solid lines) and design B (broken lines).

Figures 5.7 and 5.8 illustrate comparisons between transient results and the corresponding steady state results at time steps 75, 300 and 500 for both designs. These positions were defined in section 4.4 and illustrated in Figure 4.6. Note that the scales of the *x* and *y* axes are very different in these figures to allow the film thickness and pressure contours to be compared. The real aspect ratio of the contact shown in Figure 5.7 (ii), for example, is 65:1. The results for case (2) in the two figures are very similar for both the steady state and transient cases and correspond to that seen in high aspect ratio transverse elliptical contacts. A characteristic horseshoe shaped restriction is seen in the film thickness contours plot at the exit to the Hertzian zone and the pressure distribution is essentially Hertzian. Transient effects are limited to the left hand limit of the contact where the tip relief profile is active. For this case the results do not show a visible stress concentration effect at the tip relief contact line limit (at $y \approx 20$ mm) because the load is relieved naturally by the axial crowning. For this case the centre of contact for design A is at $y = 0$ while for design B it shifts away from $y = 0$. This is due to the significant variation in the radius of relative curvature that occurs over the contact area in design B.

The contact area dimensions at the positions shown in cases (1) and (3) of these figures are noticeably different. In these cases the position of the minimum film thickness and maximum pressure is controlled by the tip relief zone which appears at the right of the figures in case (1), and on the left in case (3). The comparisons between transient and equivalent steady state analyses show considerable similarity over much of the contact but there are clear differences in film thickness behaviour in the areas where the contact is limited by the tip relief zone. These are the result of transient changes due to movement of the local geometry discontinuity as the tip relief zone moves along the contact line, and the results show that this transient effect is detrimental leading to thinner oil films in comparison with the equivalent steady state analyses. The differences in pressure at these locations are less marked, however. The area of similarity between the steady state and corresponding transient result at each of the three positions for design A is marked by a red arrow as shown in Figure 5.7.

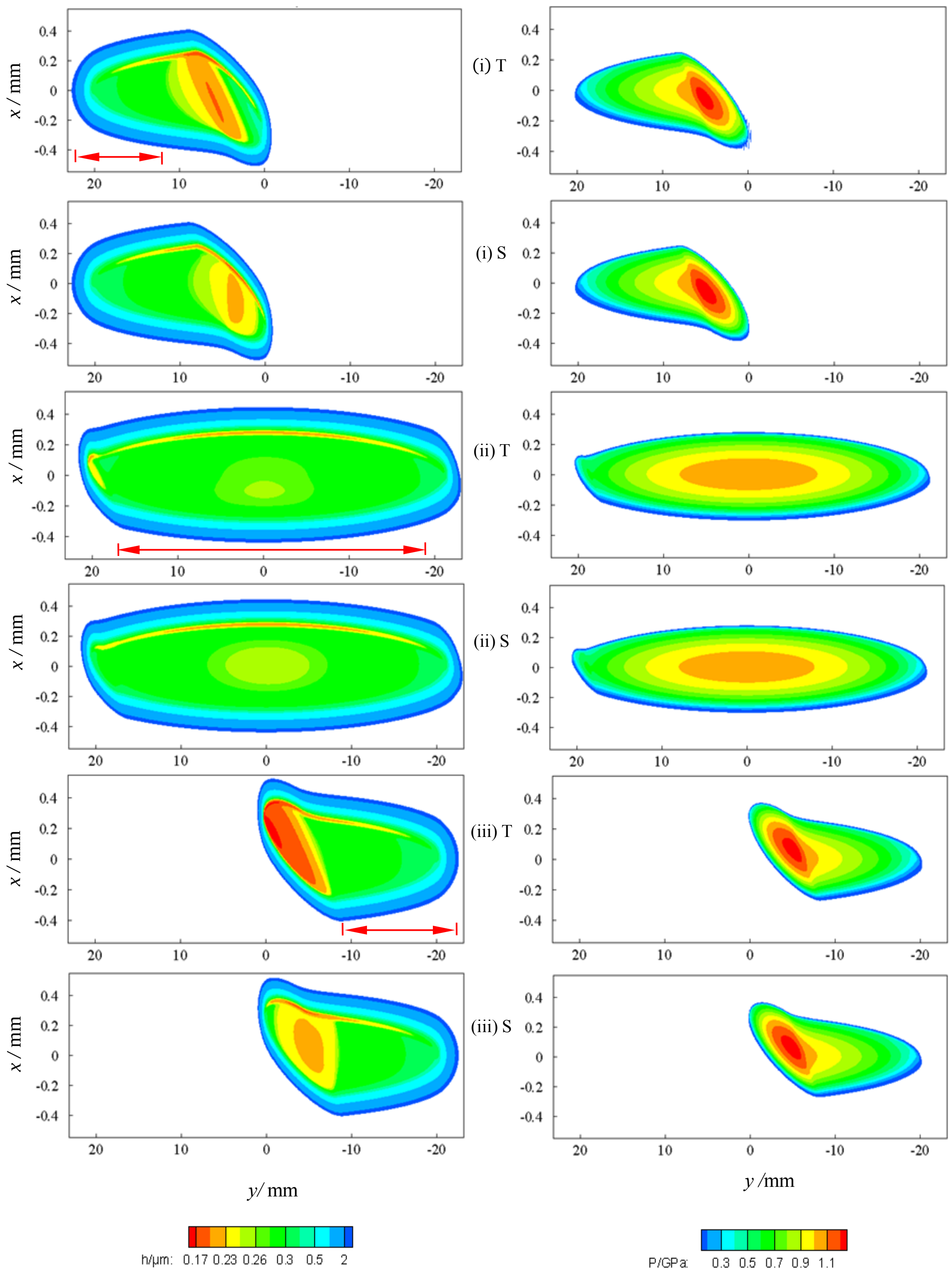

Figure 5.7: Comparison of EHL results for design A at: (i) time step 75; (ii) time step 300; (iii) time step 500 for transient (T) and steady-state (S) conditions. Left hand contour plots show film thickness, and right hand contour plots show pressure. The red arrows define the areas of similarity between steady state and transient results

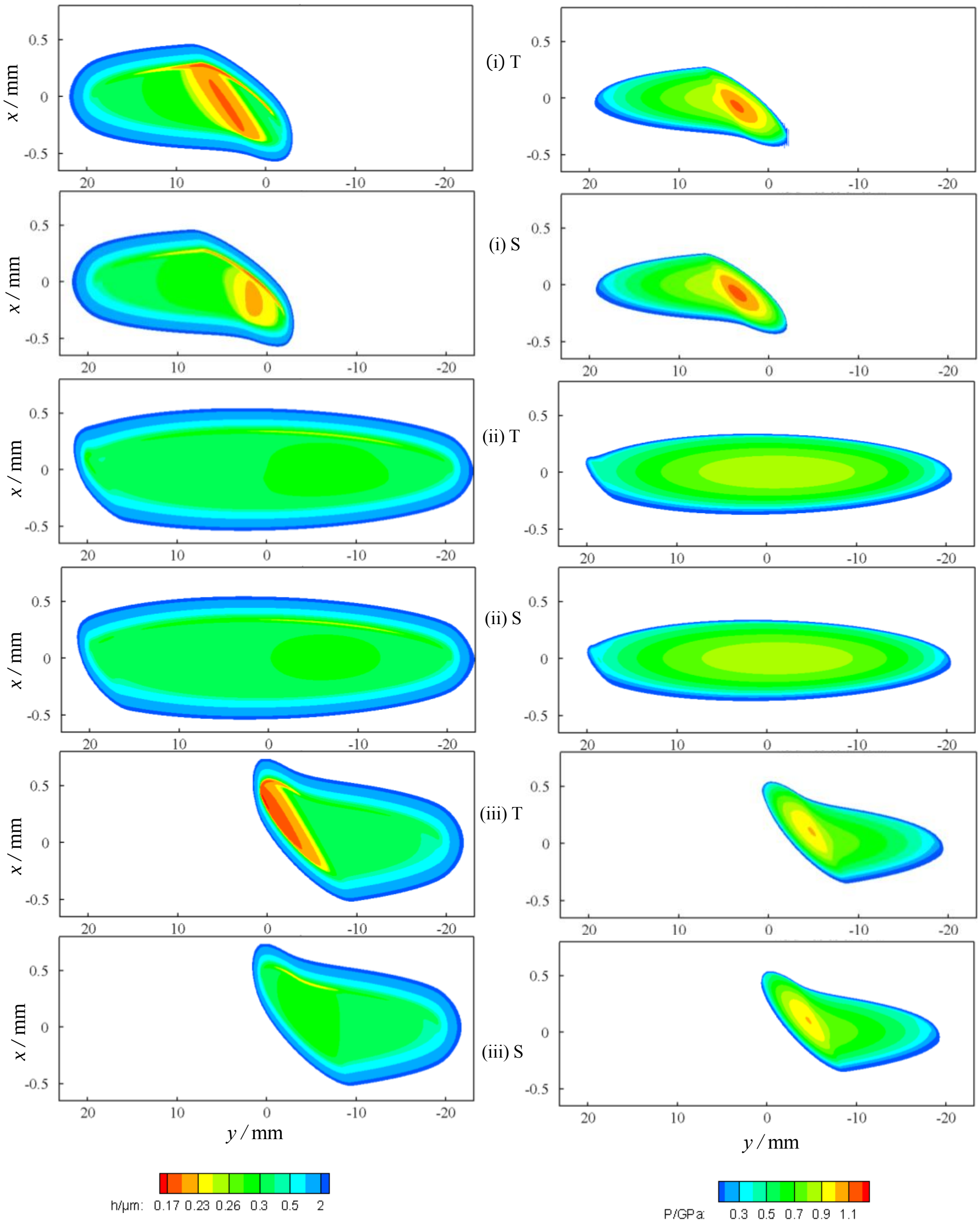

Figure 5.8: Comparison of EHL results for design B at: (i) time step 75; (ii) time step 300; (iii) time step 500 for transient (T) and steady-state (S) conditions. Left hand contour plots show film thickness, and right hand contour plots show pressure.

Figures 5.9, 5.10 and 5.11 show further detailed sectional comparisons between steady state and transient results for design A at time steps 75, 300 and 500 respectively. The sections shown are in the entrainment *x*-direction at a selection of *y* positions. Comparison of the sections shows that for parts of the contact area that are not close to the tip relief zone the results obtained using a steady state analysis are very similar to those obtained from the transient analysis.

At time step 75 a substantial part of the contact line lies in the tip relief zone which produces a significant difference in the behaviour of the film thickness in the transient case. This is clear, for example, from the results at *y* = 2 and 5 mm in Figure 5.9.

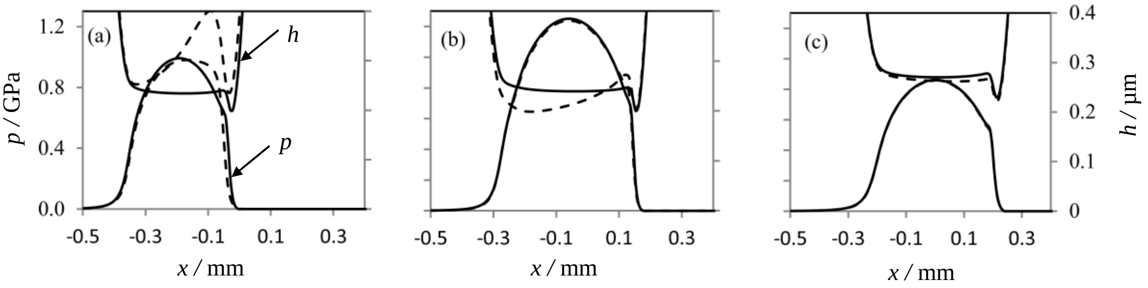

Figure 5.9: Comparison of sections of film thickness and pressure in the x-direction at timestep 75 for design A between transient (dashed) and steady state (solid) results. (a) *y* = 2, (b) *y* = 5, and (c) *y* = 12 mm.

At time step 300 a significant proportion of the contact is outside the tip relief zone and there is no significant difference between the two results (steady state and transient) as can be seen from the sections at *y* = −19, −10, 0 and 16 mm in Figure 5.10. The transient effect at the tip relief position is apparent at the sections with *y* =19 and 19.8 mm where the differences between transient and steady state film thickness can be clearly seen.

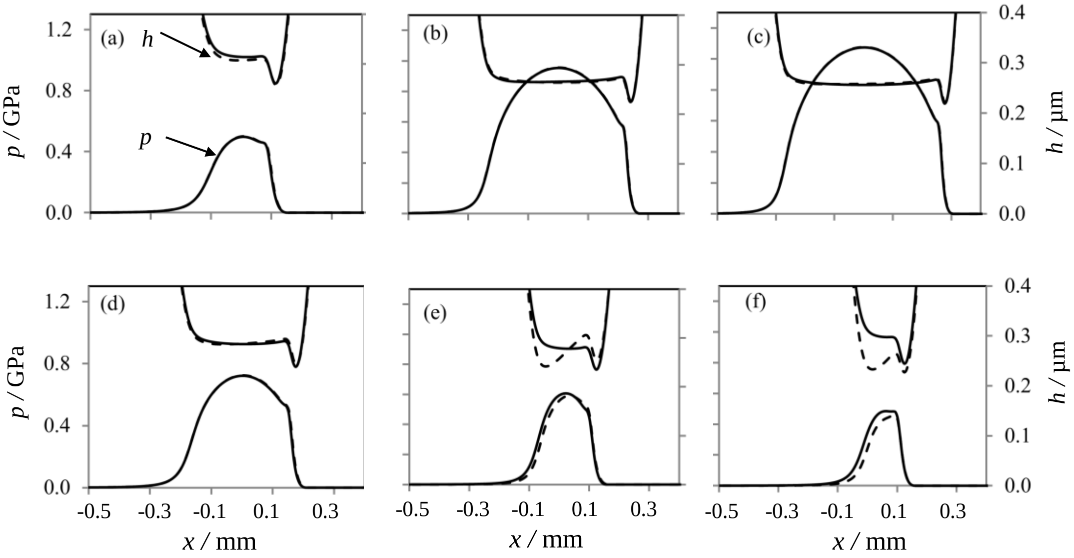

Figure 5.10: Comparison of sections of film thickness and pressure in the x-direction at time step 300 for design A between transient (dashed) and steady state (solid) results. (a) y = -19, (b) y = -10, (c) y = 0, (d) y = 16, (e) y = 19, and (f) y = 19.8 mm.

The contact behaviour at time step 500 is similar to that found at time step 75 where a substantial part of the contact line lies in the tip relief zone. The transient effect on the film thickness behaviour is also clear at this time step. This is clear, for example, from the results at $y = -2$ and -5 mm in Figure 5.11.

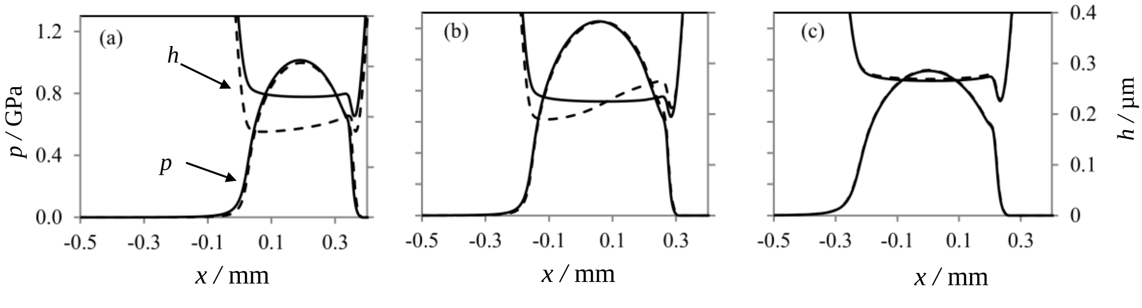

Figure 5.11: Comparison of sections of film thickness and pressure in the x-direction at time step 500 for design A between transient (dashed) and steady state (solid) results. (a) y = -2, (b) y = -5, and (c) y = -10 mm.

In all of the contacts there is a zone where the transient EHL result is essentially the same as the steady state result for the geometry and kinematics at that position. This is also found in the results of design B which are illustrated in Figures 5.12, 5.13 and 5.14 for the three mesh positions. These figures show sections of pressure and film thickness in the rolling/sliding direction. The figures show the steady state 3D results as solid lines and the transient results as broken lines. The equivalent 2D line contact result is shown as a dash-dot curve in Figure 5.13 for the sections where the transient and 3D steady state results are very similar at time step 300.

The sections shown in Figures 5.12 (a) and 5.12 (b) show considerable differences between the transient and steady state analyses in the vicinity of the tip relief profile modification. The pressure sections are almost identical but the film thickness shows that the squeeze film terms in the Reynolds equation are active causing significant differences in the lubricant films. For Figure 5.12 (c), which is typical of the rest of the contact line, the transient and steady state results are very similar showing that the squeeze film term is not influential away from the tip relief position.

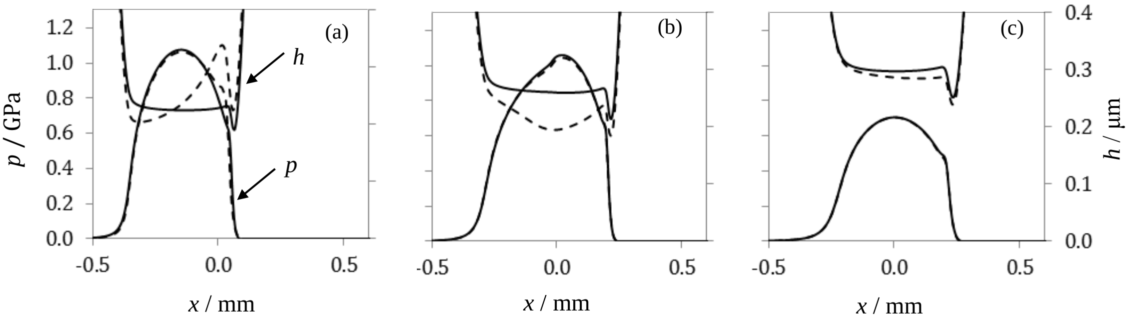

Figure 5.12: Comparison of sections of film thickness and pressure in the x-direction at time step 75 for design B between transient (dashed) and steady state (solid) results. (a) y = 2, (b) y = 5, and (c) y = 12 mm.

Figure 5.13 shows sectional comparisons of film thickness and pressure in the x direction for design B at time step 300. These sections present results for steady state and transient point contact analyses, together with the equivalent steady state line contact analysis. In order to carry out the equivalent steady state line contact analysis at a specified y position along the line of contact, the radius of relative curvature in x direction and the surface velocities were calculated at this y position, and the required load was determined by integrating the steady state point contact pressure in the x-direction at this y position. It is clear that despite the geometry and kinematic differences between the gears in design B, the steady state point contact and the equivalent steady state line contact analyses give good agreement with the transient point contact results at this time step over much of the contact area. This correspondence can be seen for the sections at $y = -18, -10, 0$ and 10 mm with differences due to transient effects starting to appear at $y = 17$ mm. The comparison at $y = 18$ mm (tip relief zone) is only made between steady state and transient point contact results, as the undeformed geometry is changing rapidly in the y direction at this position, and therefore cannot be represented by a one dimensional line contact approximation.

The contact at this time step (300) acts over the whole face width, which produces a relatively long contact ellipse with a small zone of tip relief at the left of the contact as shown in Figure 5.8 (ii). The transient tip relief effect is more noticeable at the other positions in the meshing cycle where tip relief is actively curtailing the effective length of the contact line, whereas at time step 300, which is near the middle of the meshing cycle, the tip relief becomes a modifying factor on the effect of the axial crown rather than the cause of the contact line termination. The general behaviour of film thickness (and the pressure) at this time step is similar to that in design A.

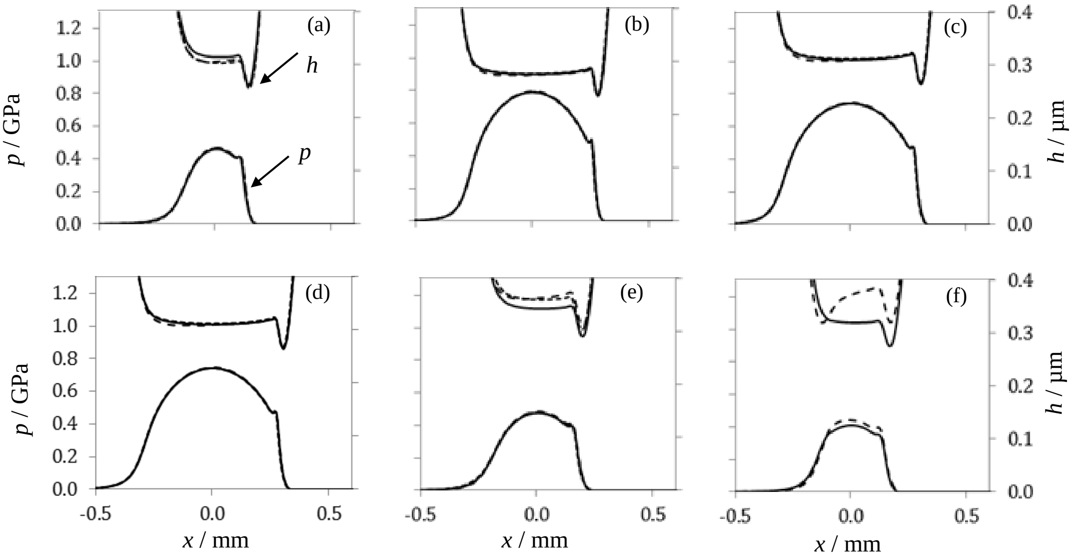

Figure 5.13: Comparison of sections of film thickness and pressure in the x-direction at time step 300 for design B between transient point contact (dashed), steady state point contact results (solid). (a) $y = -18$, (b) $y = -10$, (c) $y = 0$, (d) $y = 10$, (e) $y = 17$, and (f) $y = 18$ mm. The equivalent steady state line contact results are included in figures (a) to (e) and are indistinguishable from the steady state point contact except for minor differences in case (e).

Figure 5.14 shows results that are similar to those for Figure 5.8 in that steady state behaviour is apparent in Figure 5.14 (c), which is representative of most of the contact line, with significant transient effects in Figures 5.14 (a) and 5.14 (b) which are in the vicinity of the tip relief profile modification. Again, the pressure sections are almost identical, with significant film thickness differences due to squeeze effects.

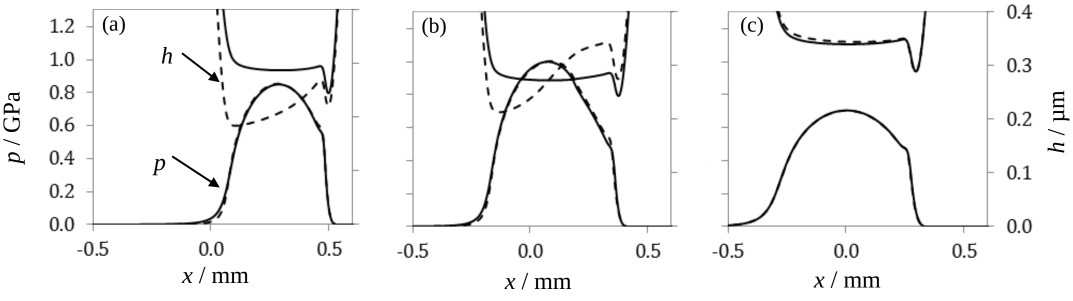

Figure 5.14: Comparison of sections of film thickness and pressure in the x-direction at time step 500 for design B between transient (dashed) and steady state (solid) results. (a) y = -2, (b) y = -5, and (c) y = -10 mm.

5.4 Effect of *k*

The intensity of the pressure spikes occurring at the tip relief boundaries increases as *k* is reduced, which reduces the extent of the parabolic blending zone. The transition to the linear tip relief curve becomes progressively more abrupt, and in the limit, corresponding to an entirely linear relief profile ($k = 0$), the surface profile has a slope discontinuity in the form of a cusp at the onset of the tip relief position.

These effects are clearly apparent in Figures 5.15 and 5.16 which show 3D isometric plots of the transient EHL analysis pressure distribution at time step 500 for six values of parameter *k* for the two designs. Figure 5.15 shows the results for design A, and the isometric pressure plots show the contact area which is limited in the direction of *y* increasing (on the left) by the pinion tip relief. The case where $k = 1$ is that illustrated in Figures 5.5 and 5.7, and appears at the bottom right. For $k = 1$ the peak pressure is 1.25 GPa, but as *k* is reduced there is a systematic increase in the peak pressure. This becomes an intense, localised pressure spike for the case where $k = 0.1$, with a maximum value of about 2 GPa. As *k* is further reduced the peak calculated elastic pressure reaches a predicted value of 3.5 GPa for the linear profile relief case of $k = 0$.

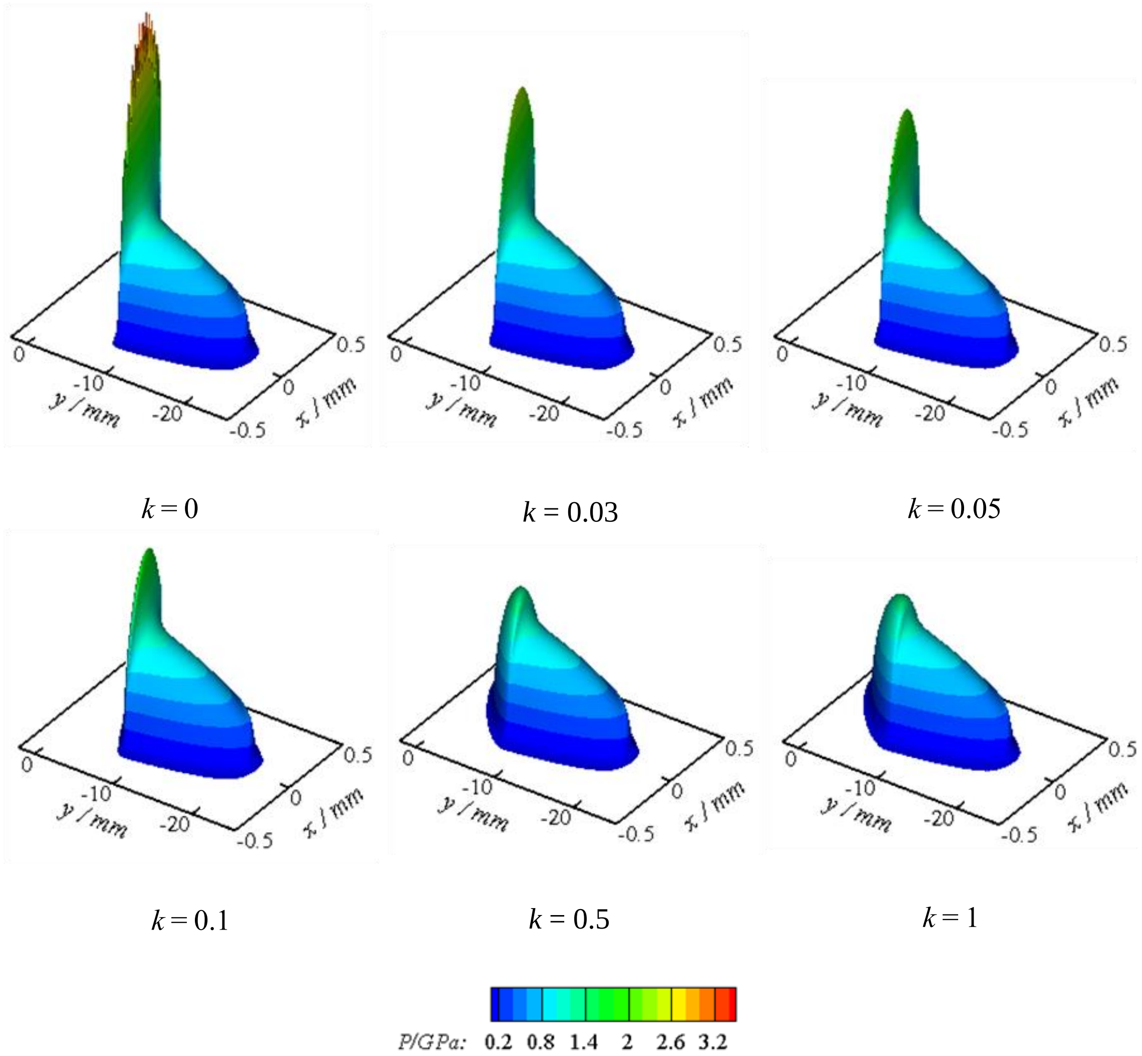

k = 0 *k* = 0.03 *k* = 0.05

k = 0.1 *k* = 0.5 *k* = 1

Figure 5.15: Contact pressure surfaces corresponding to six different patterns of the tip relief profile for design A.

Figure 5.16 shows the corresponding results for the case of design B, and it is clear that the pressure distributions and spikes for the two designs follow a very similar pattern.

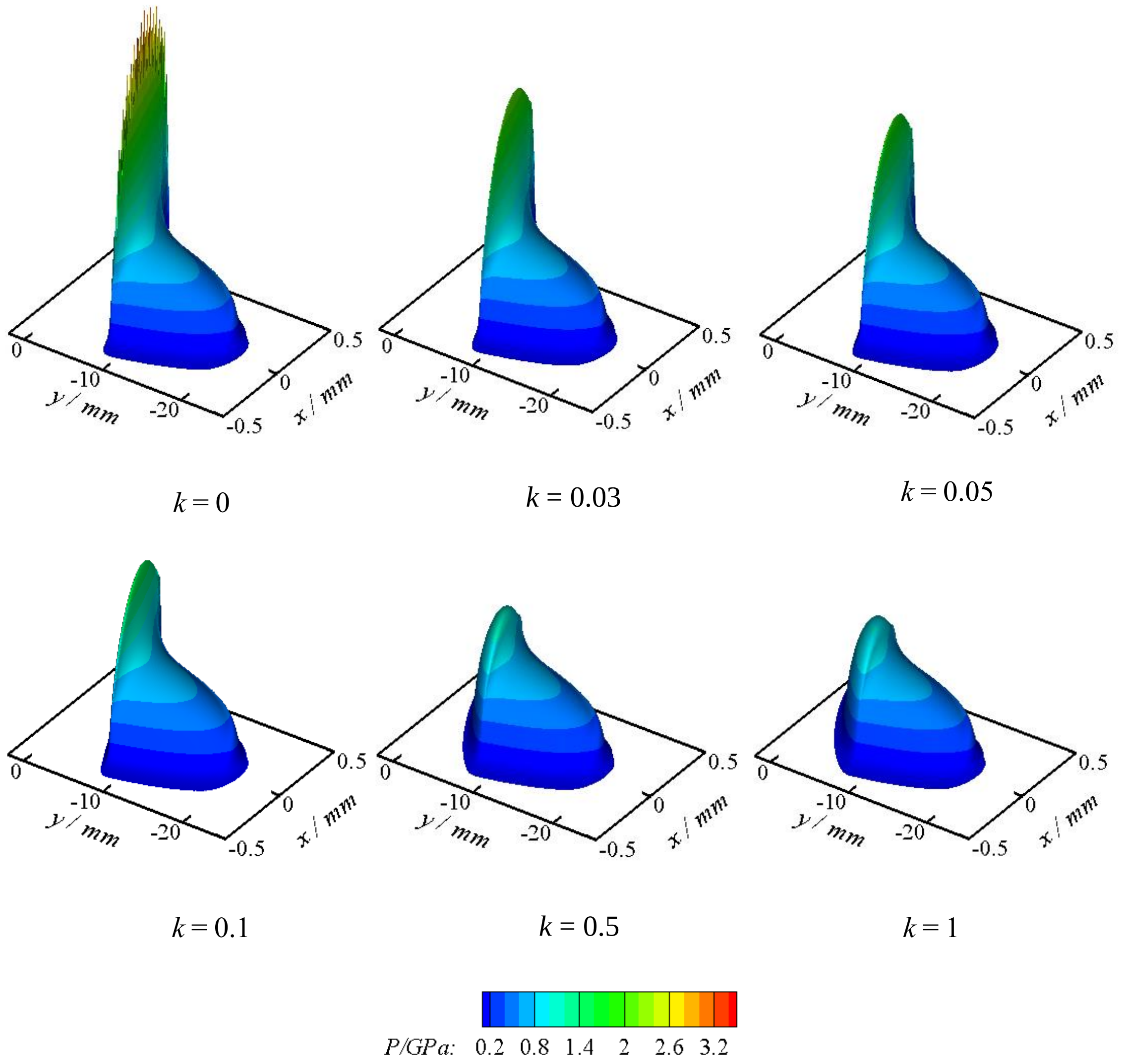

$k = 0$ $k = 0.03$ $k = 0.05$

$k = 0.1$ $k = 0.5$ $k = 1$

Figure 5.16: Contact pressure surfaces corresponding to six different patterns of the tip relief profile for design B.

The apparent oscillatory form of the pressure spike for the case k = 0 in both Figures 5.15 and 5.16 is caused by variation in the discretised second derivative of the surface geometry at the transition position between the crowned involute surface and the tip relief zone on the computing mesh.

Figure 5.17 shows the projection of lines of equal tip relief on to the tangent plane. The start of tip relief is the heavy line on the right of the plot which makes an angle of 8.5° to the y axis. The other lines have small systematic differences in their orientation.

When the computational mesh crosses the tip relief boundary line, the numerically calculated second derivatives vary in a mildly oscillatory fashion along the grid lines, achieving a maximum value when the tip relief boundary meets the grid line at a mesh point. This factor causes the observed oscillations in the peak pressure curve for $k = 0$.

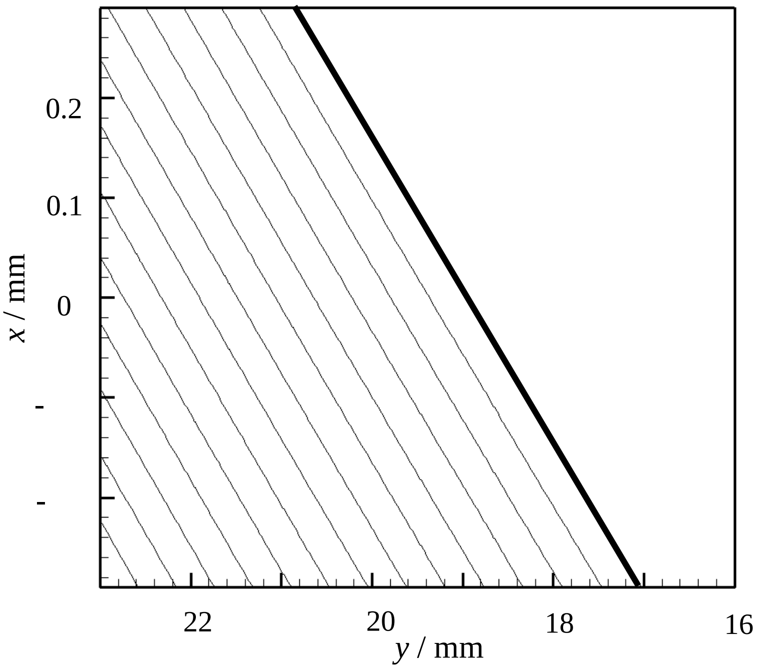

Figure 5.17: Inclination of the tip relief boundaries with the contact line direction at time step 300. Blank area to the right of the figure is the out of the tip relief zone

Figure 5.18 shows the variation of peak pressure and minimum film thickness over the meshing cycle as a function of k for designs A and B. It shows the same behaviour for the two designs with minor differences in the compared values. In both cases it can be seen that the pressure spike intensity varies by a factor of three, depending on the length of the transition between the involute and the linear relief. The variation in minimum film thickness is small as k is first reduced from unity, but has fallen by a factor of three for a k value of 0.1. For k values below 0.02 the transient EHL film is unable to separate the surfaces at the transition position which has become a slope discontinuity in the contact line profile of the contacting teeth. Edge contacts of this sort occur at the start of the tip relief position for all positive values of y, and at the end of tip relief position for negative values of *y*. So it is clear that the Λ values quoted for the gear (ratio of smooth surface film thickness to composite surface roughness) will not represent the real intensity of surface roughness effects at these locations. It is clear from a detailed consideration of these results that the case of a linear tip relief ($k = 0$), which introduces a definite discontinuity in the slope of the tooth profile in the form of a cusp, causes severe conditions at the edge of the contact resulting in extreme pressures and a failure of the lubricant film to separate the surfaces. The high level of similarity shown between the results for designs A and B in Figures 5.15, 5.16 and 5.18 suggests strongly that this behaviour is a consequence of the tooth relief profile and that the stress concentration inherent in the abrupt profile modification is not mitigated by the presence of an EHL lubricant film.

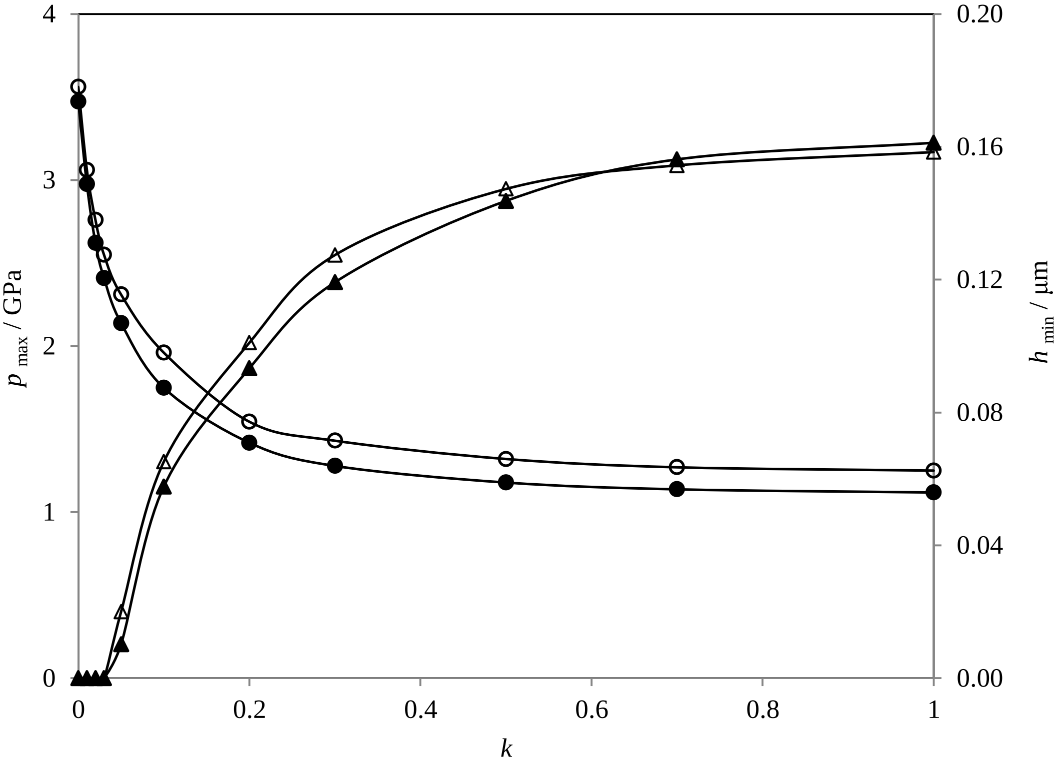

Figure 5.18. Variation of minimum lubricant film thickness and maximum contact pressure with the tip relief parameter *k* for designs A and B, —△— $h_{\min A}$, —▲— $h_{\min B}$, —○— $p_{\max A}$ and —●— $p_{\max B}$.

5.5 Effect of surface velocity

Figure 5.19 shows the effect of speed on the transient maximum pressure and minimum film thickness over the meshing cycle for the case of design A with *k* = 1. Four different entrainment speeds were used, $\bar{u}$, $2\bar{u}$, $5\bar{u}$ and $10\bar{u}$, where $\bar{u}$ corresponds to the pinion speed of 235.6 rad/s used for the results considered previously. The figure shows that operating at higher speed increases minimum film thickness levels almost exactly as $\bar{u}^{\,0.68}$, which coincides with the relation given in (Hamrock and Dowson 1977)

$$H_{min} = 3.63U^{0.68}G^{0.49}W^{-0.073}\left(1-e^{-0.68\kappa}\right)$$

Scaling the film thickness curves by this factor makes them coincide almost exactly as shown in Figure 5.20. However, the maximum pressure predicted is almost insensitive to speed which again supports the view that the pressure spike associated with the tip relief boundary is driven by elastic contact mechanics rather than elastohydrodynamic considerations.

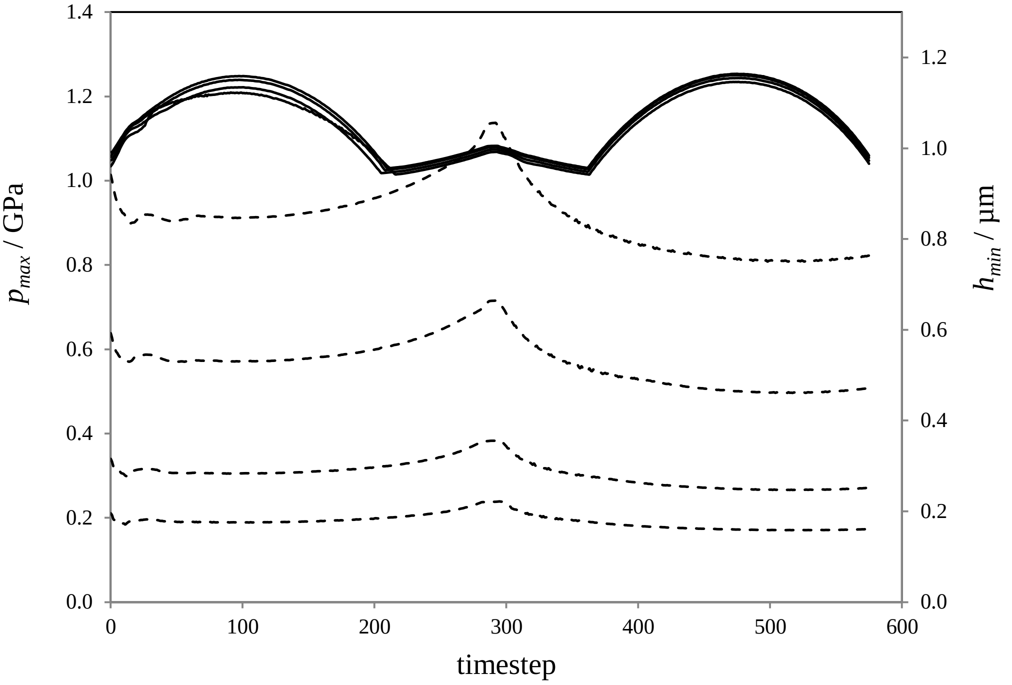

Figure 5.19: Variation of maximum pressure (solid) and minimum film thickness (dashed) throughout the meshing cycle for four entrainment velocities. Minimum film thickness curves shown in ascending order from $\bar{u}$ (lowest), $2\bar{u}$, $5\bar{u}$ and $10\bar{u}$ (highest), respectively. Maximum pressure almost insensitive to the velocity variation.

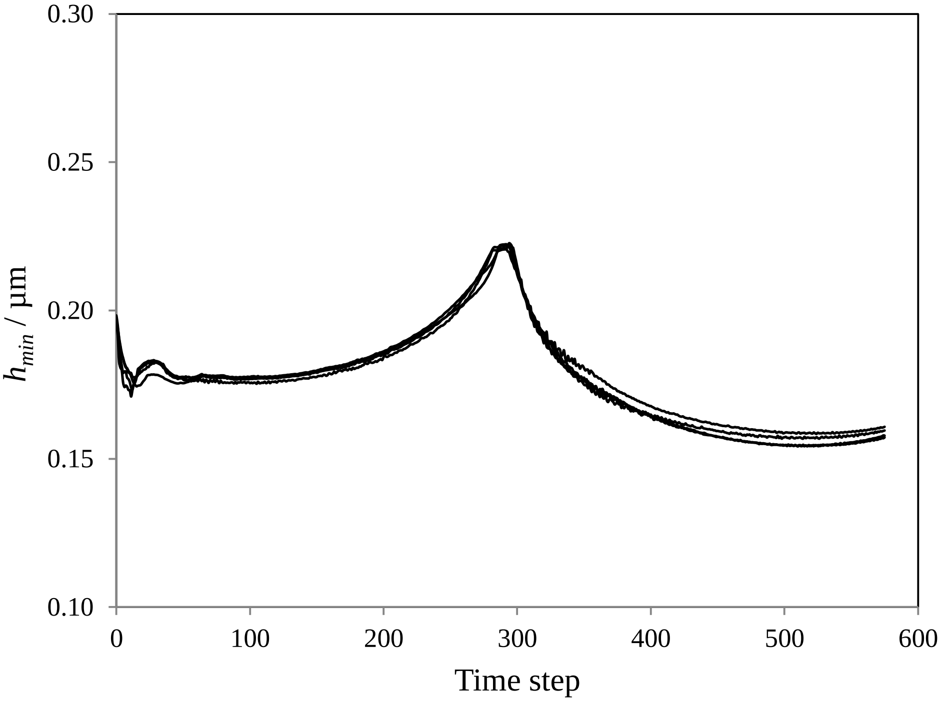

Figure 5.20: Scaling of minimum film thickness for four entrainment speeds ($\bar{u}$, $2\bar{u}$, $5\bar{u}$ and $10\bar{u}$) to a factor of 0.68

5.6 Results for optimised power law

In this section further investigation on the form of tip relief is reported. The form of tip relief considered in section 5.1 which describes linear, parabolic and a combination of linear and parabolic forms is now modified to a more general power law form as follows.

$$z_t' = c_t \left\{ \left(r - r_{start} \right) / \left(r_{tip} - r_{start} \right) \right\}^{\beta} \qquad (5.6)$$

where r, r_{start}, r_{tip} and c_t are as defined in section 5.1. The value of parameter β is varied between 1 and 4, where β =1 corresponds to the linear profile, and all values of β greater than 1 have zero slope at $r = r_{start}$ so the profile modification is tangential to the involute at the start of tip relief .

Figure 5.21 illustrates the zero load gap between the tooth surfaces along the contact line at three meshing cycle positions for design A and B when β = 3. The upper and lower parts show the gap for design A and B respectively. Mesh positions 1, 2 and 3 are at time steps 75, 300 and 500, respectively. The zero load gaps are offset by 2 or 4 μm for clarity.

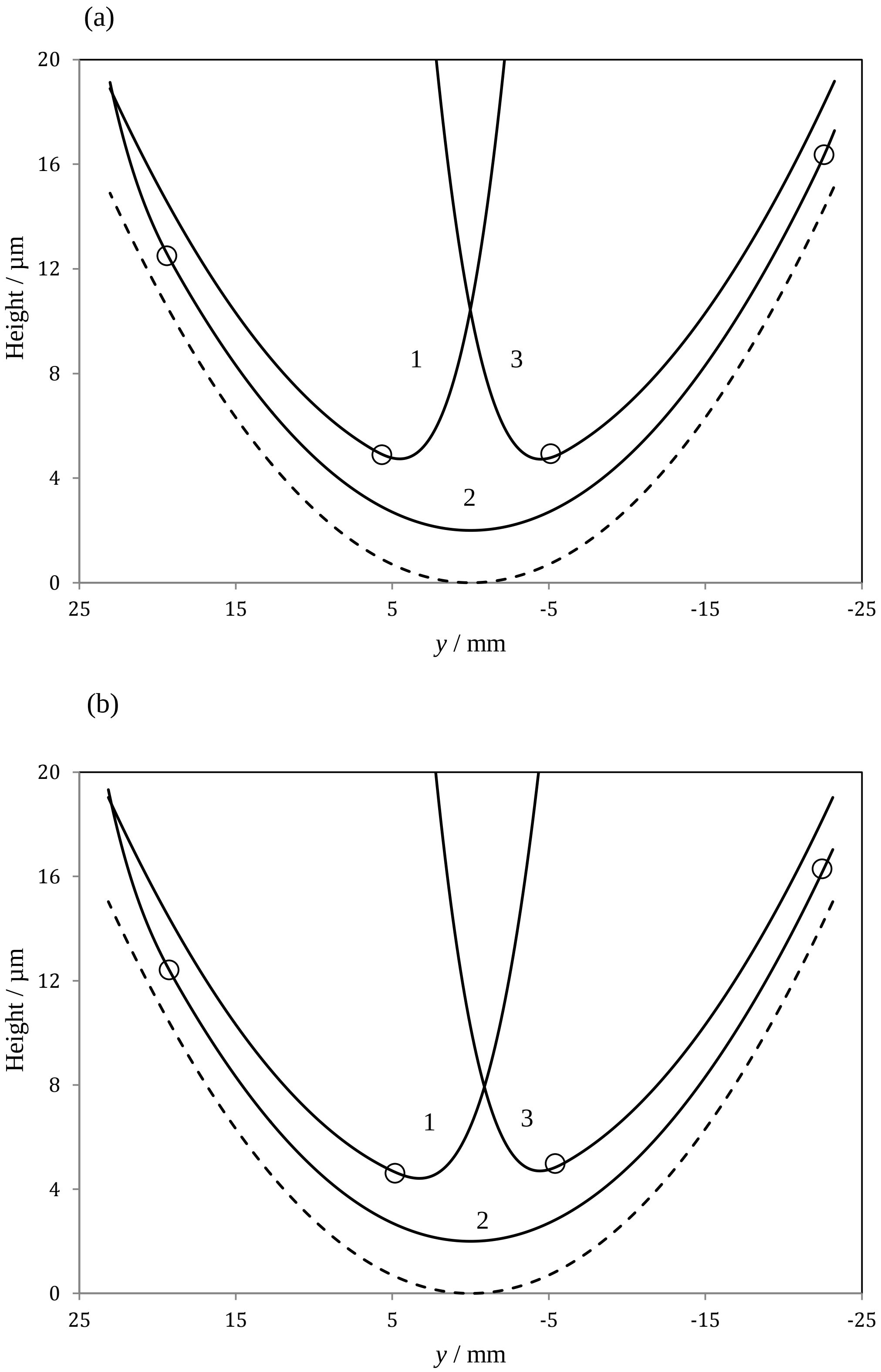

Figure 5.21 Gap between gear surfaces (offset) along contact line at positions 1, 2 and 3 in the meshing cycle for power law modification, $\beta = 3$. Axial crown is shown broken and symbol ○ indicates starts of tip relief for each contact line. (a) Design A; (b): Design B

Figure 5.22 shows the variation of maximum pressure and minimum film thickness over the meshing cycle for designs A and B for values of β = 2, 3 and 4. The results for design A shown in Figure 5.22 (a) show that the maximum pressures are reduced by a factor of three or more when compared to the result for β = 1 shown in Figure 5.6. The value of β can be seen to have a significant effect on the peak pressures and also on the minimum film thickness experienced in the contact. The pressures are further reduced for the higher β values, but these are minor further changes. Similar behaviour is also found in the corresponding results of design B as shown in Figure 5.22 (b).

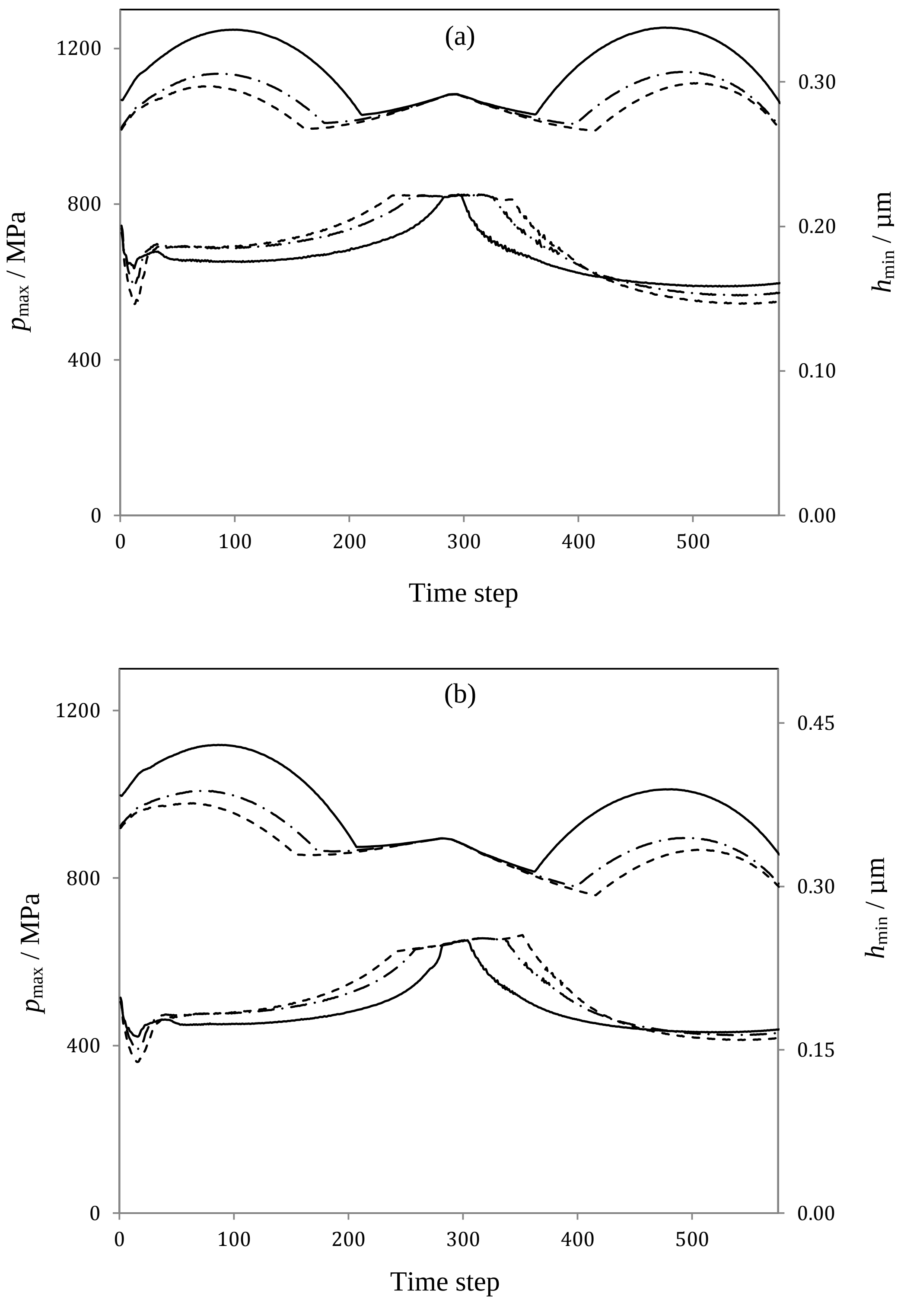

Figure 5.22: Maximum pressure (upper curves) and minimum film thickness (lower curves) over the meshing cycle, —— β =2, -·-·- β =3 and - - - - β =4. The corresponding results for the linear case (β=1) is shown in Figure 5.6.
(a) design A, (b) design B

Figure 5.23 shows film thickness and pressure contours at time step 75 for the range of powers β specified for the analyses. These results are for design B. For the linear profile β = 1 the maximum pressure contour is 3.2 GPa and the minimum film thickness contour is zero, indicating that the lubricant film is unable to separate the surfaces. This extreme behaviour is not seen with the cases where β = 2, 3 and 4 where the minimum film thickness contours are around 0.185 μm, and the maximum pressure contour values are 1.1, 1.0 and 0.96 GPa, respectively. This figure illustrates how the linear modification reduces the length of the contact area in the *y* direction in comparison with the other cases when β = 2, 3 and 4. The linear case (β = 1) produces a pressure of 0.1 GPa at $y \approx 0$ while the 0.1 GPa contour can be seen at $y \approx -5$ mm for the β = 4 case.

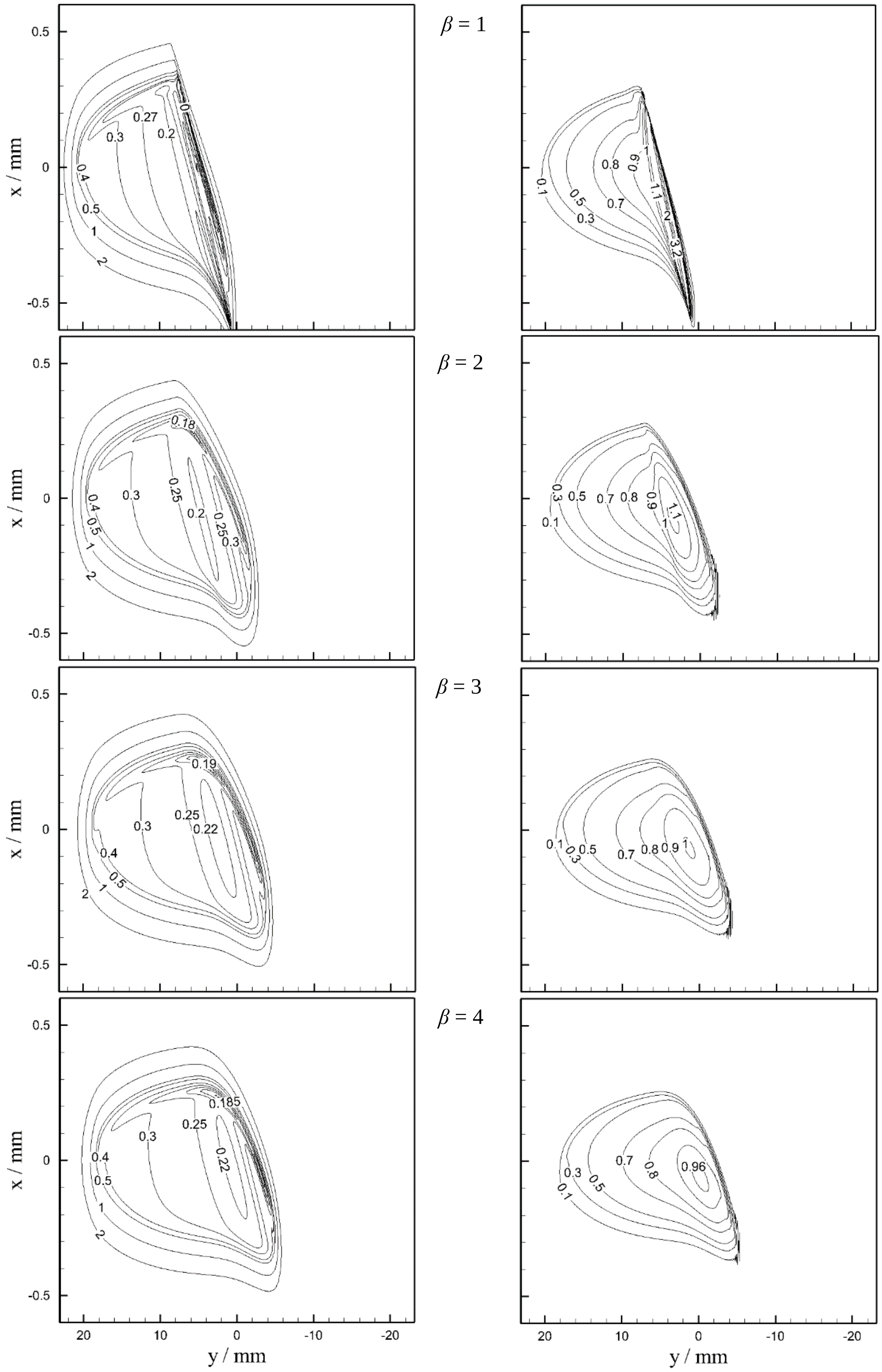

Figure 5.23: Film thickness contours / μm (left) and pressure contours / GPa (right) at time step 75 for the four values of β.

Further investigations on the effect of β on the contact behaviour were also performed. Figure 5.24 shows the contact line pressures for each time step assembled into a contour plot for each of the tip relief profile forms considered for designs A and B. In both designs for the $\beta = 1$ case intense closed contours for 3, 2 and 1 GPa appear at the top and bottom of the pressure map. The y axis is aligned with the contact line and the peak pressure contour indicates that the highest pressures occur at the start of tip relief positions, on the wheel at the bottom left of the contour plot, and on the pinion at the top right. For the higher values of β these contours become much less intense and the peak contact line pressure levels approach those occurring at the peak load, full face width contact lines.

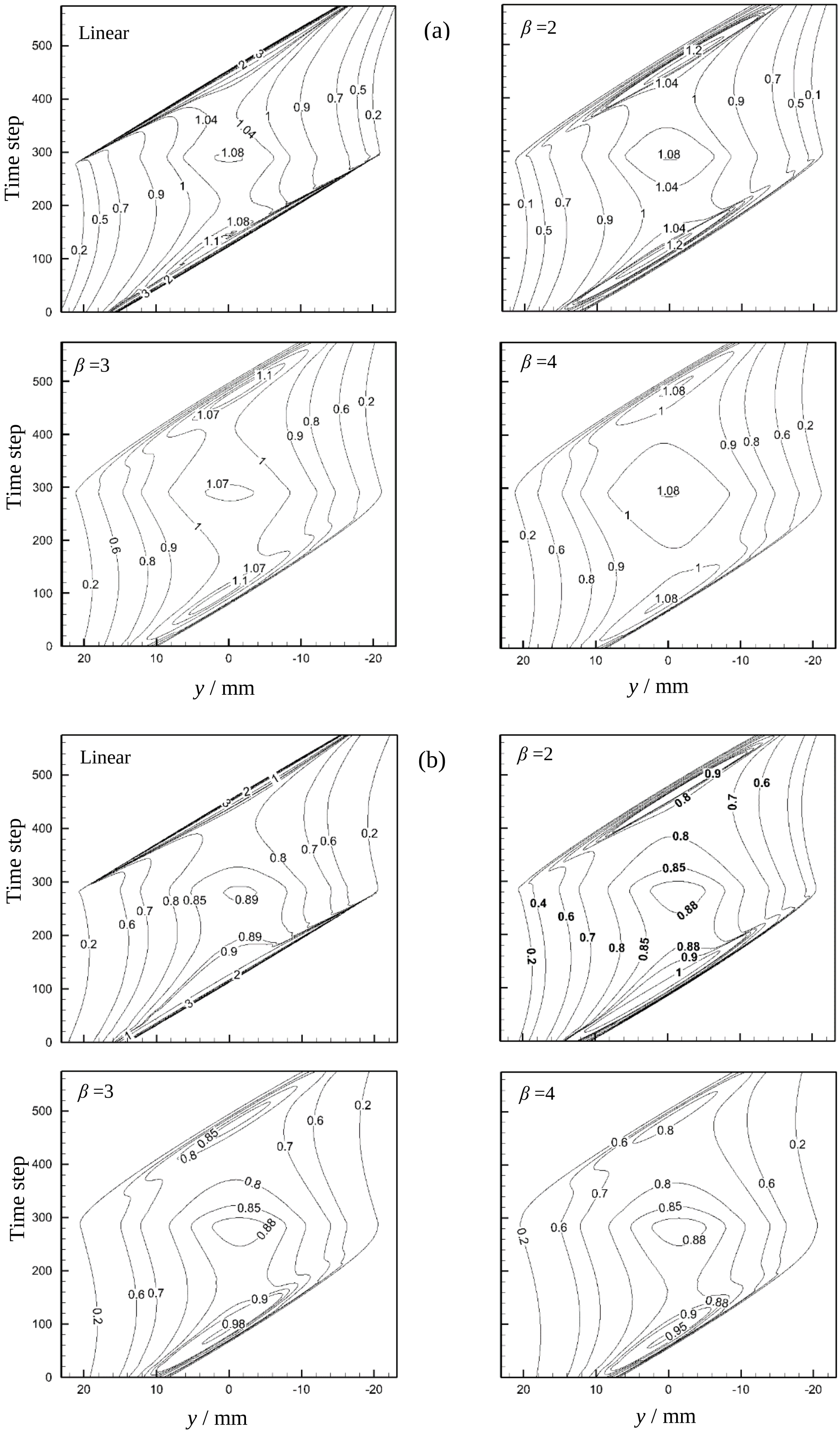

Figure 5.24: Contours of contact line pressure / GPa for the four values of β.
(a) design A and (b) design B

5.7 Discussion

Linear tip relief is the common form of modification due to manufacturing considerations. This form has been shown in this chapter to have very large stress concentrations due to the significant slope discontinuity at the start of modification. The suggested form of modification which consists of a parabolic blending curve in order to maintain slope continuity at the start of modification showed significant improvement in the EHL results. The lengths of the parabolic curve which correspond to $k > 0.3$ remove the stress concentrations in the cases considered. Smaller values of k also improve the result to some extent and the case of $k = 0.1$ for example reduces the maximum pressure from 3.5 GPa to 2 GPa approximately (see Figure 5.18). Comparison between the results of different power law modifications illustrates that the parabolic curve is the ideal form and the other higher power law modifications do not lead to significant improvement in the results. This results demonstrates that the continuous change of slope is the important requirement.

In this study the effects of bending of the teeth under load are ignored, and it is assumed that the share of the total tooth load carried by individual simultaneous contacts is proportional to their length at any instant. However, it is clear that the effect of tooth bending will lead to a different distribution of the load on the contacts. Furthermore, the bending effect will cause contact lines to extend into the tip relief zone under heavy loading conditions. These effects can potentially be included in the EHL analysis based on the results of full 3D finite element analysis of helical gears in contact as discussed in section 4.1, and this will be pursued in future work.

Chapter 6

Transient EHL Analysis of Helical Gears Having Faceted Tooth Surfaces

6.0 Introduction

When the final finish of helical gears is achieved using the generation grinding process the cutter passes axially over the tooth flank in a series of offset passes. This can result in axial faceting where the tooth profile consists of a number of facets rather than being a perfectly smooth curve. The number of facets will corresponds to the number of passes used which will be part of the grinding specification. For the module considered in this work between 20 and 40 facets are likely to be created. This chapter begins with a derivation of closed form equations for the resulting gap between the faceted profiles during the engagement between gear teeth and then investigates the effect of these axial facets, as well as their numbers, on the transient EHL results for helical gears. Detailed comparisons are also made with corresponding smooth surface results given in chapter 5

6.1 Undeformed geometry

The length of the active tooth profile in contact during a complete meshing cycle is equal to the distance $s_{max} - s_{min}$ along the line of action as explained in section 2.1. This distance is divided into a number of complete facets, n_f. Therefore, the arc length of each facet is:

$$arc = \frac{s_{max} - s_{min}}{n_f} \qquad (6.1)$$

The gap between the two teeth in contact needs to be determined as a part of the EHL analysis of contacting surfaces. The procedure adopted in Chapter 2 (section 2.3) to calculate the gap between two helical teeth in contact having involute profiles will be modified in this chapter to calculate the undeformed geometry of faceted surfaces. Figure 2-10 (c) (Chapter 2) shows how the gaps between gear teeth in the normal and transverse directions are related to each other. The same way of determining z_1 (and z_1') as described in section 2.3 is used here to determine in which transverse section the required normal gap is. Depending on this transverse section, the gap for the facetted surface can be determined as will be shown later. The gap in the normal direction of the faceted profile can then be easily determined by taking the effect of the helix into account.

To illustrate this, Figure 6.1 shows a parabolic approximation of a transverse section of an involute tooth profile together with the proposed faceted profile as an alternative to the smooth surface. The x axis is the tangent to the profile at the contact point C ($x_C = 0$) between the two mating teeth at a position $s_C(y)$ in the meshing cycle. Point P represents a point on the tooth profile where $x \neq 0$ and point P_F is the corresponding point on the faceted profile at the same x position (x_P) of point P. Points B_1 and B_2 are the boundaries of the facet that contains point P.

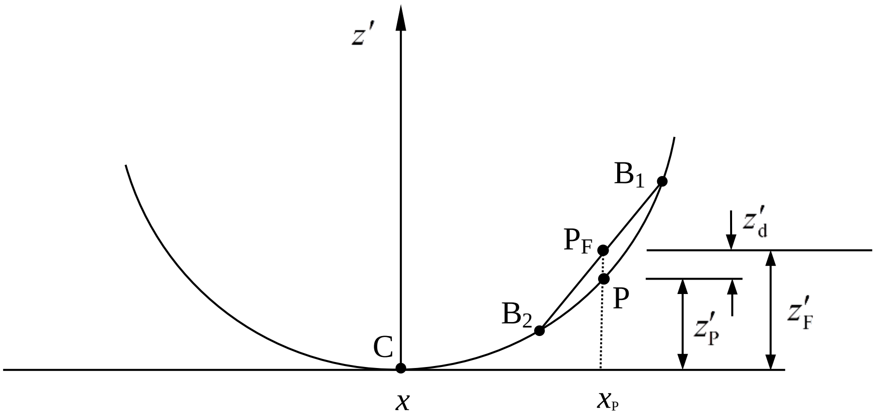

Figure 6.1: Section in the x direction illustrates the gap between the tangent plane and the facet profile. Only one facet step is shown in this figure.

The total gap at point P_F between the faceted profile and the *x* axis in the transverse direction is the distance z'_{F} which varies according to the *x* position of point P. This gap is given by

$$z'_{\mathrm{F}} = z'_{\mathrm{P}} + z'_{\mathrm{d}} \tag{6.2}$$

where z'_{P} is the distance between the parabolic curve and the *x* axis, and z'_{d} is the deviation from the parabolic curve (both in the transverse direction).

The solution space for the EHL analysis is the tangent plane *xy* (see Chapter 2, Figure 2.9). The distance z'_{P} (and its value in the normal direction) can be calculated at each point in this solution space as explained in Chapter 2 (section 2.3). In the case of a facetted profile the total gap at a given x_{P} in this *xy* plane which includes the distances z'_{P} and z'_{d} can be determined using the method explained below.

The radial distances in the transverse direction between any point on the involute profile (such as point P) and the gear axes can be determined using equations 2.16 and 2.17 in chapter 2. These two equations were derived by considering Figure 2.13. The figure and these equations are repeated here for clarity.

$$r_1(x,y) = \sqrt{(r_{b1} - x)^2 + (R'_1 - z'_1)^2} \tag{6.3-a}$$

$$r_2(x,y) = \sqrt{(r_{b2} + x)^2 + (R'_2 - z'_2)^2} \tag{6.3-b}$$

where 1 and 2 represent pinion and wheel respectively and R'_1 and R'_2 are the radii of curvature of the surfaces at point C in the transverse direction which are given by

$$R'_1 = r_{b1} \tan\psi + s_{\mathrm{C}}(y)$$

$$R'_2 = r_{b2} \tan\psi - s_{\mathrm{C}}(y)$$

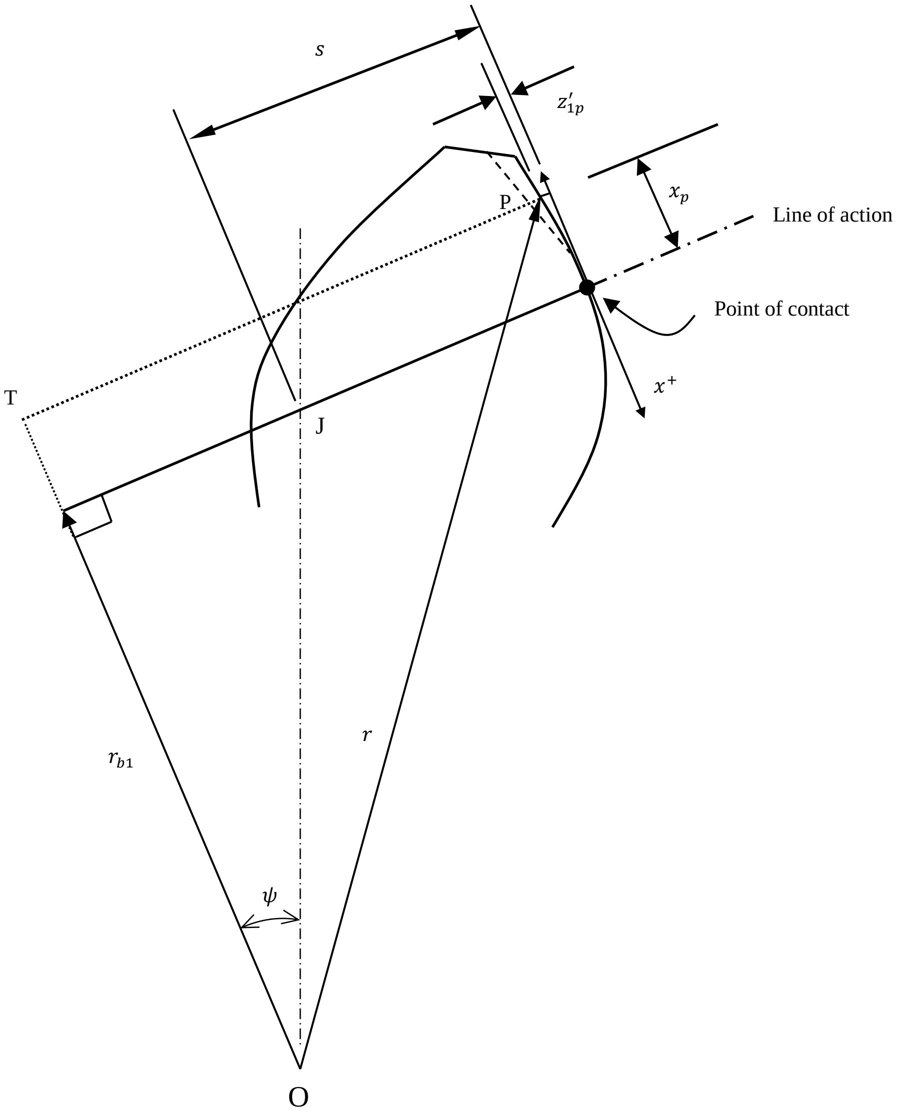

Figure 2.13: Undeformed geometry due to tip relief of the pinion, repeated here for clarity and convenience

The gaps in the transverse direction are

$$z'_1 = \frac{x^2}{2R'_1} \tag{6.4-a}$$

$$z'_2 = \frac{x^2}{2R'_2} \tag{6.4-b}$$

In order to find the total gap at point P, it is required to identify the following

1- Its position on the tooth profile.

2- At what facet it lies.

3- The *s* values at the boundaries (B_1 and B_2 in Figure 6.1) of this facet.

The position of point P on the tooth profile can be determined in terms of *s*. For a given *x* position, equation (6.3-a) gives the distance r_1. If the tooth in Figure 2.13 rotates clockwise until point P lies on the line of action as shown in Figure 6.2, s_P can be determined by considering the two triangles OET and OEP as

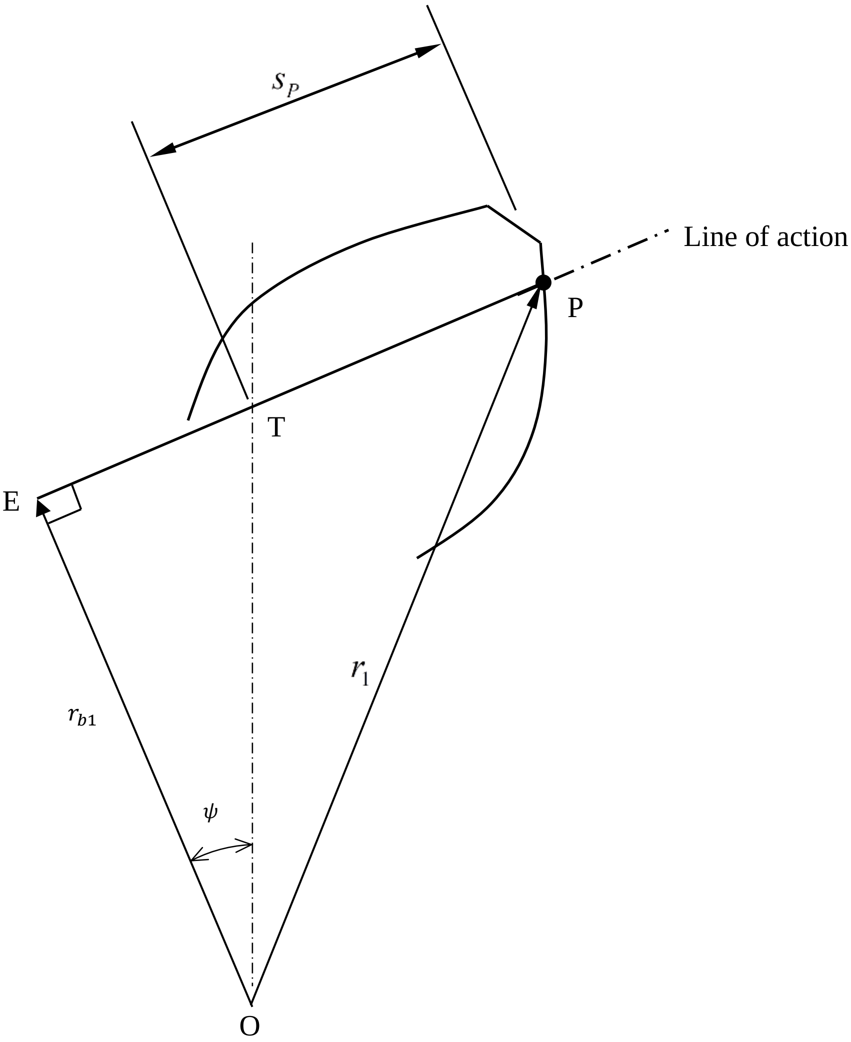

Figure 6.2: Determination of *s* position of point P

$$s_{\mathrm{P}} = \sqrt{r_1^2 - r_{b1}^2} - r_{b1}\tan\psi \tag{6.5}$$

As the profile is divided into a number of facet steps as given by equation (6.1), the step position of point P can be obtained from

$$k_{\mathrm{P}} = \mathrm{int}\left(\frac{s_{\mathrm{P}} - s_{\min}}{arc}\right) \tag{6.6}$$

where function *int* is the integer part of the argument.

Therefore, the *s* values of the boundaries of the facet defined by equation (6.6) can be calculated from

$$s_{\mathrm{B1}} = s_{\min} + k_{\mathrm{P}}arc \tag{6.7-a}$$

$$s_{\mathrm{B2}} = s_{\mathrm{B1}} + arc \tag{6.7-b}$$

Using equation (6.7-a), the radius at B$_1$, r_{B1}, with respect to the gear axis can also be determined by rotating the tooth shown in Figure 2.13 until B$_1$ lies on the line of action which is given by:

$$r_{\mathrm{B1}} = \sqrt{r_{b1}^2 + (r_{b1}\tan\psi + s_{\mathrm{B1}})^2} \tag{6.8}$$

Similarly for the second boundary B$_2$ with use of equation (6.6-b) gives

$$r_{\mathrm{B2}} = \sqrt{r_{b1}^2 + (r_{b1}\tan\psi + s_{\mathrm{B2}})^2}$$

(6.9)

Equation (6.3-a) can be used to evaluate the *x* position of B$_1$ and B$_2$. Substituting equations (6.4-a) in (6.3-a) gives

$$r_{B1} = \sqrt{(r_{b1} - x_{B1})^2 + (R_1' - \frac{x_{B1}{}^2}{2R_1'})^2} \tag{6.10}$$

Equation (6.10) can be written, after some simplification, in the following form

$$a_4 x_{B1}^4 + a_1 x_{B1} + a_0 = 0 \tag{6.11}$$

where, $a_4 = \dfrac{1}{4R_1'^2}$, $a_1 = -2r_{b1}$, $a_0 = R_1'^2 + r_{b1}^2 - r_{B1}^2$ and the radial distance r_{B1} is given by equation (6.8).

A similar equation can be derived for point B$_2$ using the previous procedure for point B$_1$ which is

$$a_4 x_{B2}^4 + a_1 x_{B2} + a_0 = 0 \tag{6.12}$$

And the constants are defined by

$$a_4 = \frac{1}{4R_1'^2},\ a_1 = -2r_{b1} \ \text{ and } \ a_0 = R_1'^2 + r_{b1}^2 - r_{B2}^2$$

Equations (6.11) and (6.12) are fourth order equations and solution of each equation gives one physically realistic real root. These equations can be solved by making the expression x_{Bi} as

$$x_{Bi} = \left(-a_0 - a_4 x_{Bi}^4\right) / a_1 \qquad i = 1 \text{ or } 2.$$

and using this recursively to converge to the root of interest.

The gap at the boundaries B$_1$ and B$_2$ can be calculated using the solution of equations (6.11) and (6.12) as

$$z'_{B1} = \frac{x_{B1}^2}{2R'_1}$$

$$z'_{B2} = \frac{x_{B2}^2}{2R'_1}$$

Figure 6.3 illustrates these distances at the parabolic approximation of the involute profile. Using a linear interpolation between the heights at points P_F, B_1, and B_2 the total gap that includes the facet effect at x_P can be determined by:

$$z'_F = z'_{B1} + (z'_{B2} - z'_{B1})\frac{x_P - x_{B1}}{x_{B2} - x_{B1}}$$

This equation gives the gap in the transverse direction. Therefore the gap in the normal direction, z_F can be calculated by taking the effect of the helix angle into account as

$$z_F = z'_F \cos B_b$$

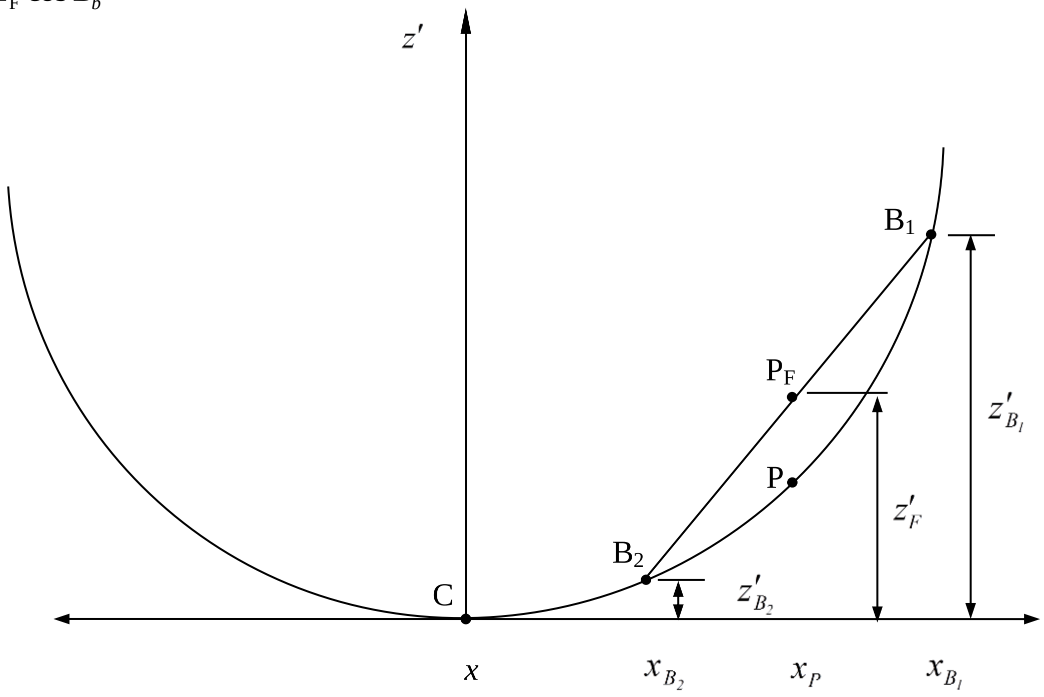

Figure 6.3: Relation between the gap at the point of interest, P, and the gaps at the facet boundaries

A similar procedure can be used to determine the gap between the tooth profile of the wheel and the tangent plane which gives the same form of equations (6.11) and (6.12) but with the following constants for the gap at B_1

$$a_4 = \frac{1}{4R_2'^2}\,,\ a_1 = 2r_{b2}\ \text{ and }\ a_0 = R_2'^2 + r_{b2}^2 - r_{w\mathrm{B}1}^2$$

and the following for the gap at B_2

$$a_4 = \frac{1}{4R_2'^2}\,,\ a_1 = 2r_{b2}\ \text{ and }\ a_0 = R_2'^2 + r_{b2}^2 - r_{w\mathrm{B}2}^2$$

where $r_{w\mathrm{B}1}$ and $r_{w\mathrm{B}2}$ are the radial distances from the centre of the wheel to point B_1 and B_2 respectively.

This procedure is repeated for all points in the solution space (*xy* plane) and as a result the 3D gap between the contacting teeth (with faceted profiles) at any position in the meshing cycle is available for the transient EHL analysis. Examples of this 3D gap near the middle of the meshing cycle between the pinion teeth and the tangent plane when $n_f = 20$, 40 and $n_f = 100$ are shown in Figure 6.4.

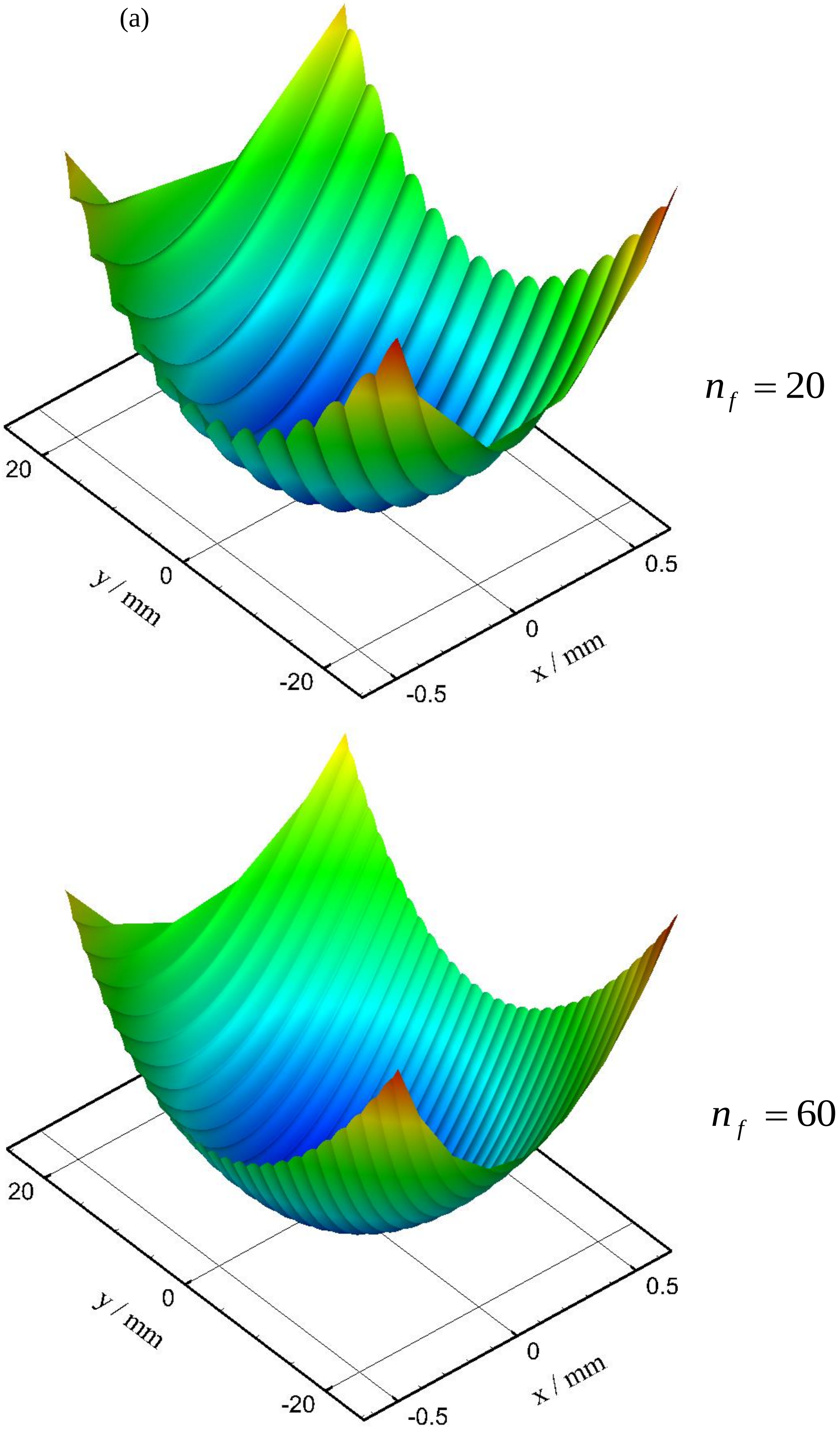

Figure 6.4 (continue)

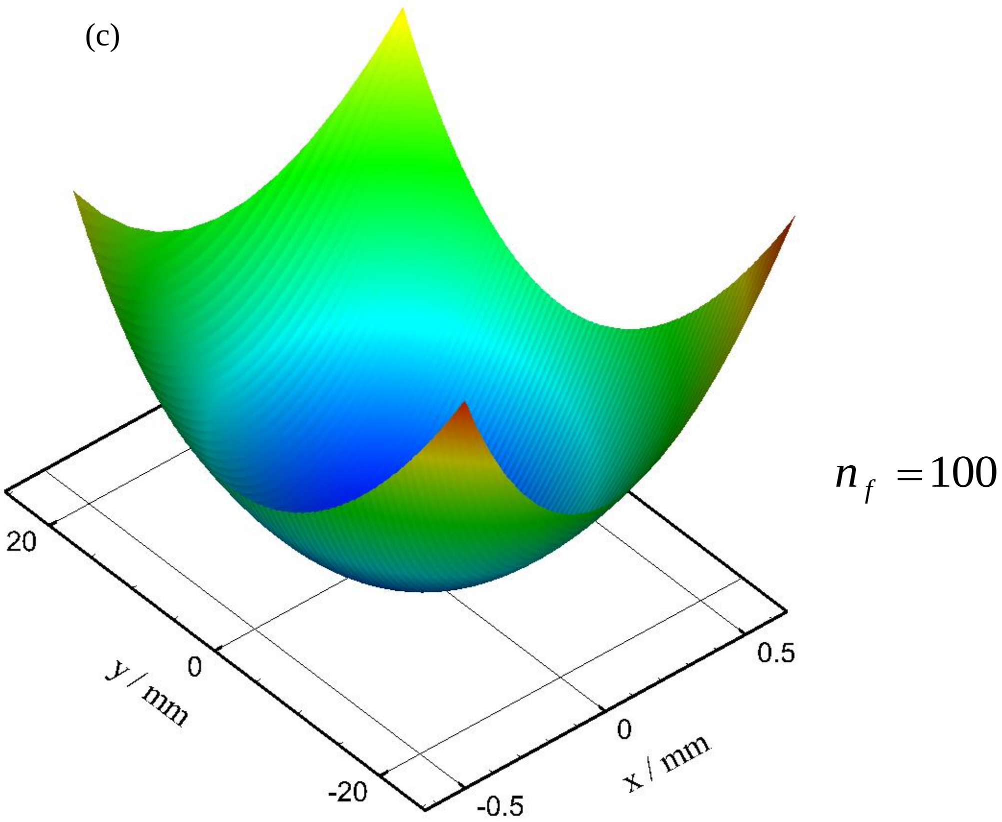

Figure 6.4:): Gap between pinion teeth and the tangent plane, (a) $n_f = 20$, (b) $n_f = 60$ and (c) $n_f = 100$

6.1.1 Smooth surface and the corresponding faceted profiles.

Figure 6.5 compares the faceted profile with the perfect smooth profile where corresponding gaps for their profiles with respect to the tangent plane are shown. The results shown in this figure are at a position in the meshing cycle where the contact between the teeth acts over the whole face width. This position corresponds to time step 300 as defined by position 2 in Figure 4.6 (chapter 4). Three cases of n_f = 40, 60 and 100 are shown in this figure where the section at the centre of the contact ($y = 0$) is shown for the profile of the pinion tooth in each figure. Figure 6.5 (a) shows the case when n_f = 40, and it is clear that in this case the faceted profile deviates considerably from the smooth profile. The effective profile in the EHL analysis that lies within the area of contact is in the range of $-a \le x \le a$ as shown in this figure by the distance 2*a*. There are severe changes of slope within these limits of the faceted profile which can be expected to act as stress raisers, and may have the effect of thinning the lubricant film. The divergence from the smooth profiles is reduced as the number of steps is increased. This behaviour is clear in Figures 6.5 (b) and (c) where n_f = 60 and 100 cases are presented respectively. At the scale of drawing, the faceted profile in Figure 6.5 (c) seems very close to the corresponding smooth one. However, the faceted profile still diverges to some extent from the corresponding smooth profile.

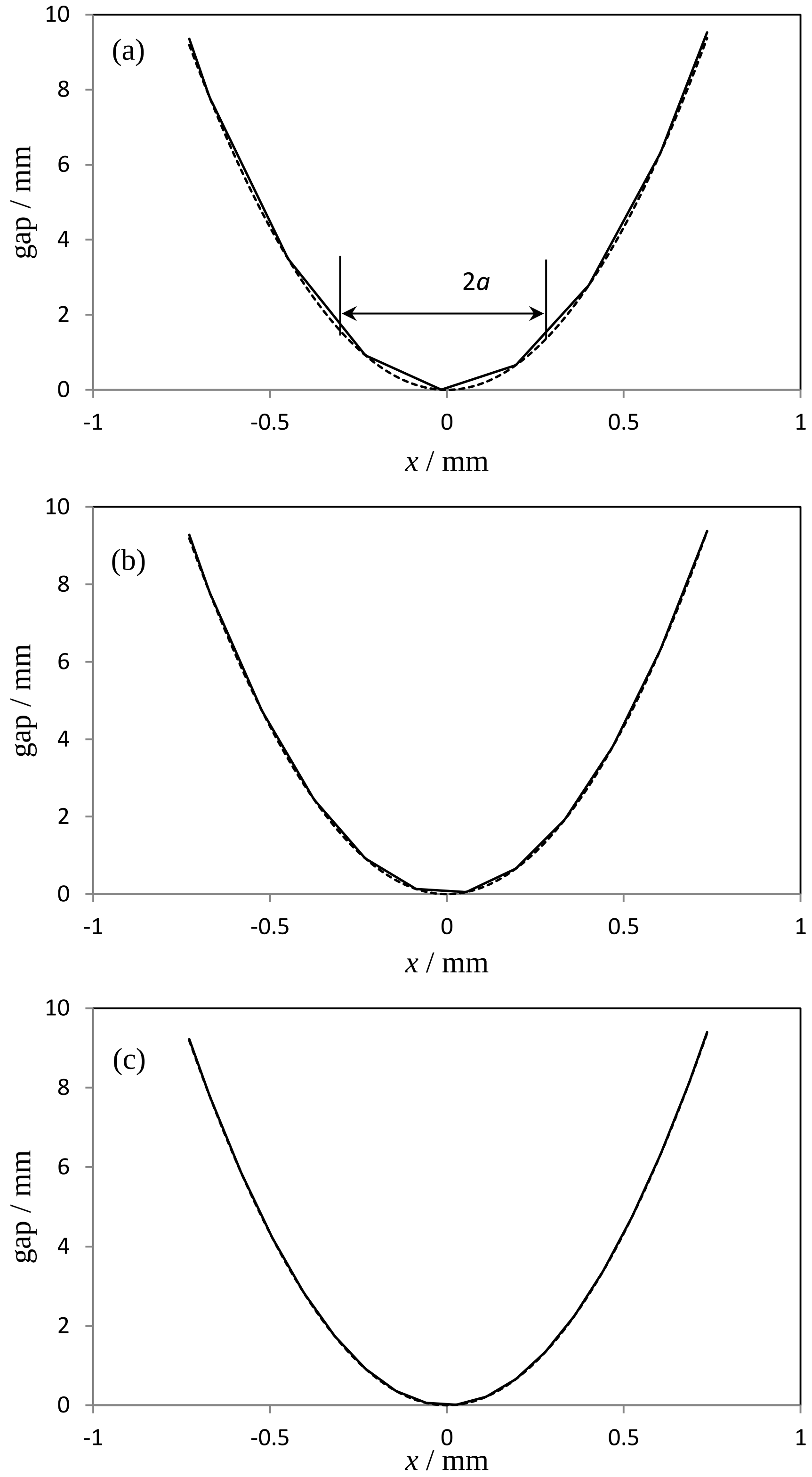

Figure 6.5: Gap in the *x* direction between the tangent plane and the tooth profile at y = 0 when (a) $n_f = 40$, (b) $n_f = 60$ and (c) $n_f = 100$; smooth (dashed) and faceted profiles (solid)

6.2 EHL results

Results are shown for two faceted profiles (pinion and wheel profiles) with the same n_f which are compared with those for perfect smooth profiles. This investigation was undertaken to find the minimum required n_f number that will produce film thickness and pressure distributions that are close to the corresponding results for smooth surfaces. In general six cases are examined where the tooth profiles are generated using n_f = 20, 30, 40, 60, 80 and 100.

Similar procedures for the EHL analyses of the helical gear meshing cycle that was discussed in chapters 4 and 5 were adopted in obtaining the results presented in this chapter. The only difference is related to the undeformed geometry. The transient gap between the smooth surfaces of the contacting teeth is replaced by the gap between the faceted profiles as calculated in section 6.1.

6.2.1 Effect of mesh density

In this section the effect of mesh resolution on the EHL results of helical gears having faceted tooth surfaces is investigated. Two cases are examined where the tooth profile has $n_f = 20$ and $n_f = 100$. Each case is analysed using three different mesh densities which are (*a*/20, *b*/200), (*a*/40, *b*/400) and (*a*/80, *b*/800). These resolutions give a corresponding total number of nodes in the solution space of (92*427), (182*857) and (362*1717), respectively. The results of this investigation are shown in Figure 6.6 where Figures 6.6 (a) and 6.6 (b) correspond to cases $n_f = 20$ and $n_f = 100$, respectively. In all cases changing the mesh density (twice doubling in both directions) does not significantly affect the general behaviour of the results (particularly the pressure distribution). The case $n_f = 100$ shows very little effect of mesh density.

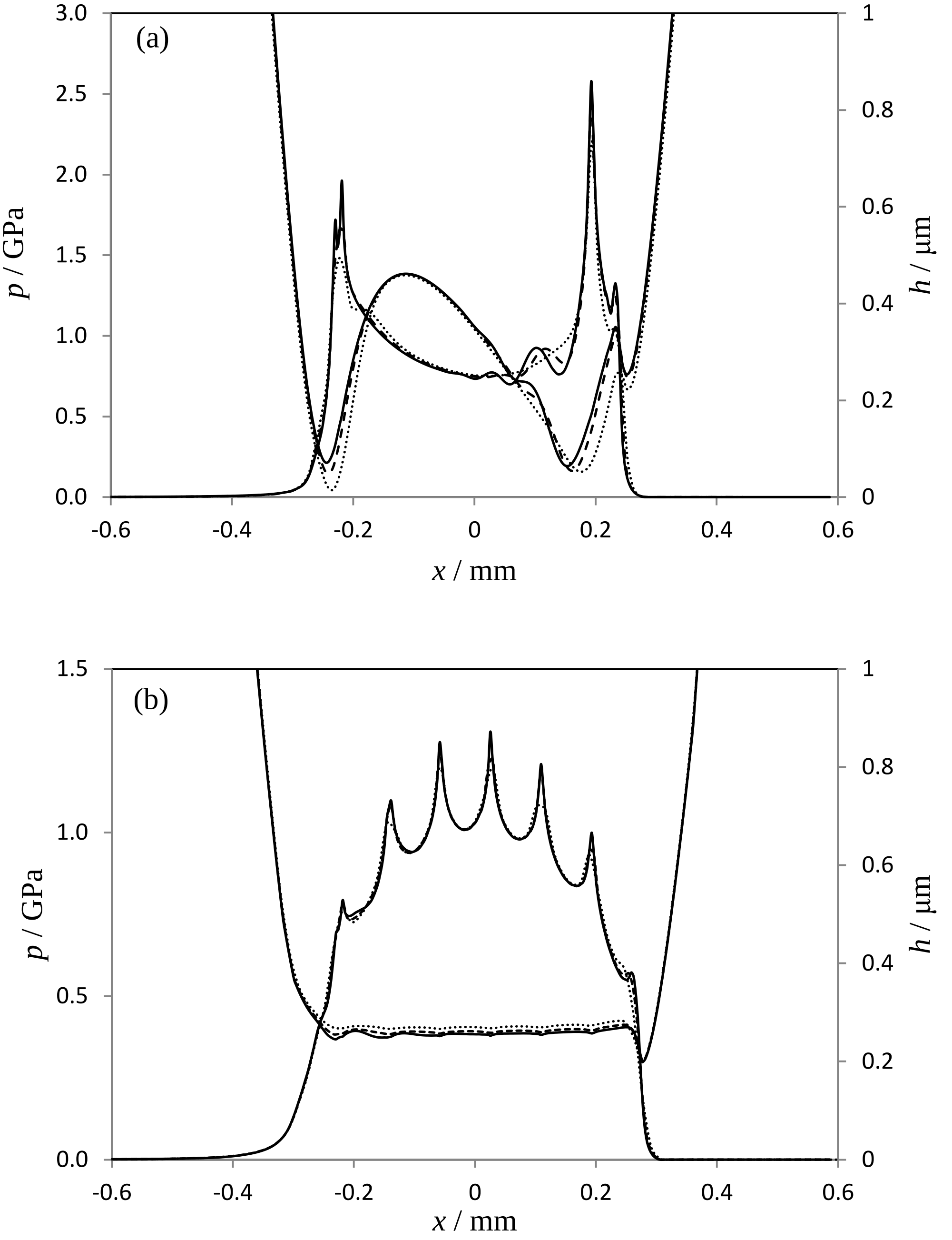

Figure 6.6: Effect of mesh density on the EHL results at the centre of contact ($y = 0$) at time step 300; ……. (92*427), - - - - (182*857) and ——— (362*1717). (a) $n_f = 20$ and (b) $n_f = 100$

6.2.2 EHL solution for the gear meshing cycle

Figure 6.7 compares the transient EHL results for the gear meshing cycle for the smooth and faceted profiles. The results for the faceted profiles (pinion and wheel profiles) are for n_f = 20, 30, 40, 60, 80 and 100. Figure 6.7 (a) shows the variation of maximum pressure throughout the meshing cycle and Figure 6.7 (b) shows the corresponding minimum film thickness. The maximum pressure in the smooth surfaces case varies between 1.02 and 1.25 GPa. Meanwhile, the film thickness varies between 0.16 and 0.22 μm. In the corresponding faceted profiles, the case of n_f = 20 produces the highest range of maximum pressure during the meshing cycle. In this case the maximum pressure varies between 2.44 and 3.16 GPa. These results are expected as the faceted profile has sharp discontinuities in the profile slope with n_f = 20. Also in this case metal to metal contact is predicted in significant parts of the meshing cycle. The maximum pressure in the case of n_f = 30 decreases to a value of 2.27 GPa. Although this represents a reduction of about 28% with respect to the case of n_f = 20, the level of the minimum film thickness is relatively low, and a breakdown of the film thickness occurs at some positions in the meshing cycle. In the case of n_f = 40 the maximum pressure varies between 1.6 and 1.9 GPa and the EHL mechanism succeeds in totally separating the two surfaces during the whole meshing cycle. The range of minimum film thickness variation is between 0.11 and 0.16 μm. Both these ranges of variation for the case of n_f = 40 represent a good improvement in the EHL response to the faceted profiles. The improvement is continued as the value of n_f is increased as shown for the cases n_f = 60, 80 and 100. In the last case (n_f =100) the maximum pressure varies between 1.18 and 1.42 GPa. The upper limit differs from the smooth surfaces results by only 13.6% .

The corresponding film thickness varies between 0.14 and 0.2 μm where the lower limit is 12.5% less than the corresponding smooth surface results.

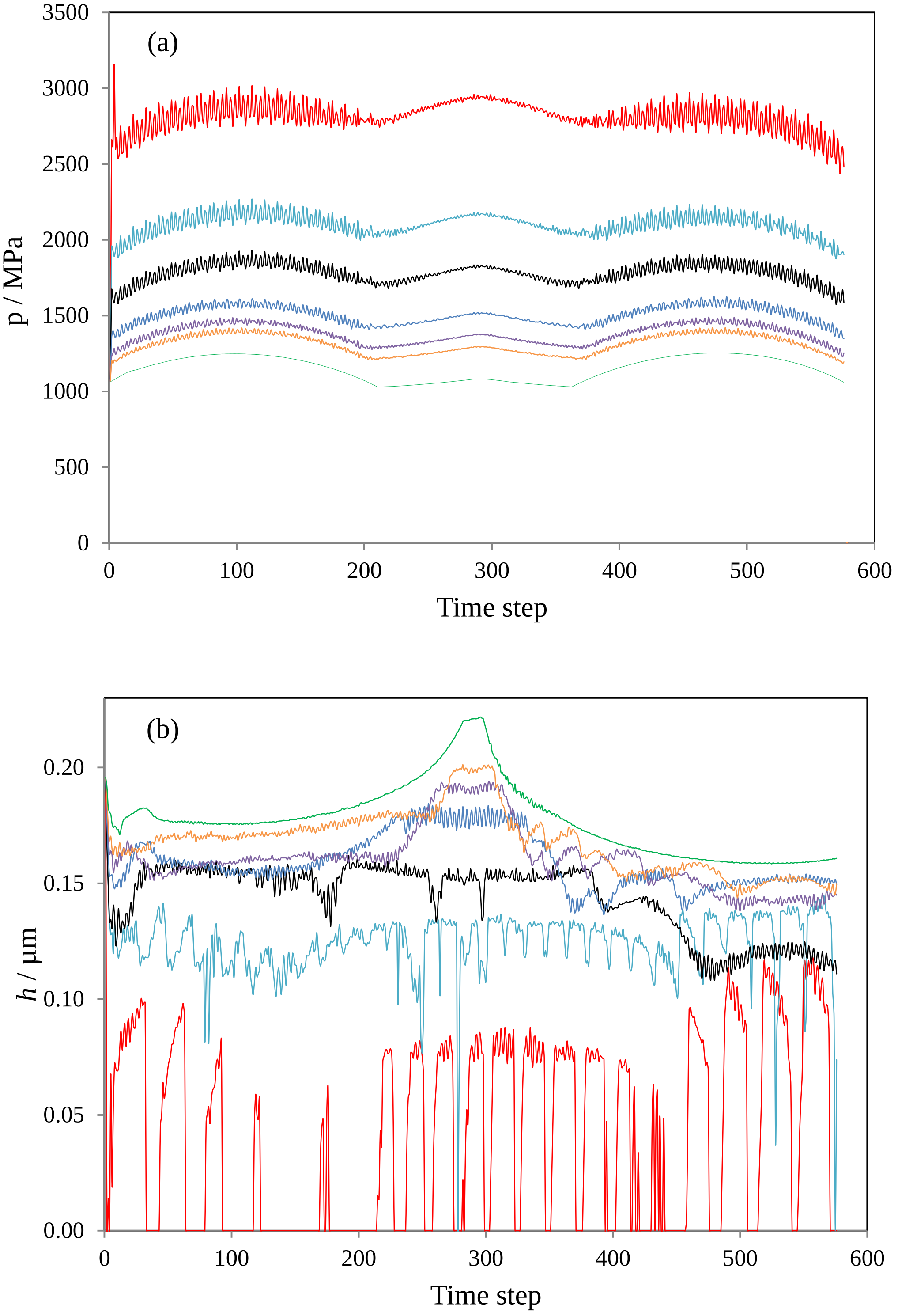

Figure 6.7: Variation of (a) maximum contact pressure and (b) minimum oil film thickness during the meshing cycle; green: smooth profile, orange: $n_f = 100$, purple: $n_f = 80$, blue: $n_f = 60$, black: $n_f = 40$, aqua: $n_f = 30$ and red: $n_f = 20$

Detailed results for the contact between faceted surfaces (both pinion and wheel have faceted profile) are presented in Figures 6.8 to 6.18. Three positions in the meshing cycle are selected which are at time steps 75, 300 and 500. As explained in the previous chapters these positions are examples where the contact is mainly within the pinion dedendum at time step 75, over the whole face width at time step 300 and within the addendum of the pinion at time step 500. In these figures the faceted profiles are generated using n_f = 20, 40, 60, 80 and 100. The *y*-axis represents the contact line direction and the *x*-axis is the rolling/sliding direction.

Figure 6.8 shows the pressure distribution for the six cases at time step 75. It can be seen in this figure how the pressure distribution tends towards the smooth surface results as n_f is increased from 20 to 100. Figure 6.9 shows the film thickness contours corresponding to the cases shown in Figure 6.8. The effect of the facets is very clear in these figures particularly at the lower n_f number where a sequence of parallel, low film thickness areas is apparent. The case of n_f = 20 is the most extreme case in terms of both pressure distribution and film thickness, which reflects the nature of the profile which contains severe changes of slope

Comparisons of pressure and film thickness sections in the entrainment direction are shown in Figure 6.10 at position y =12 mm. The case of n_f = 20 is clearly significantly different to the smooth surface result, and the differences decline with increasing facet number. Case n_f = 100 is the closest to the smooth surface result, nevertheless the pressure is clearly disturbed by the faceting. For this test case 40 or more facets results in small perturbations rather than significant ones.

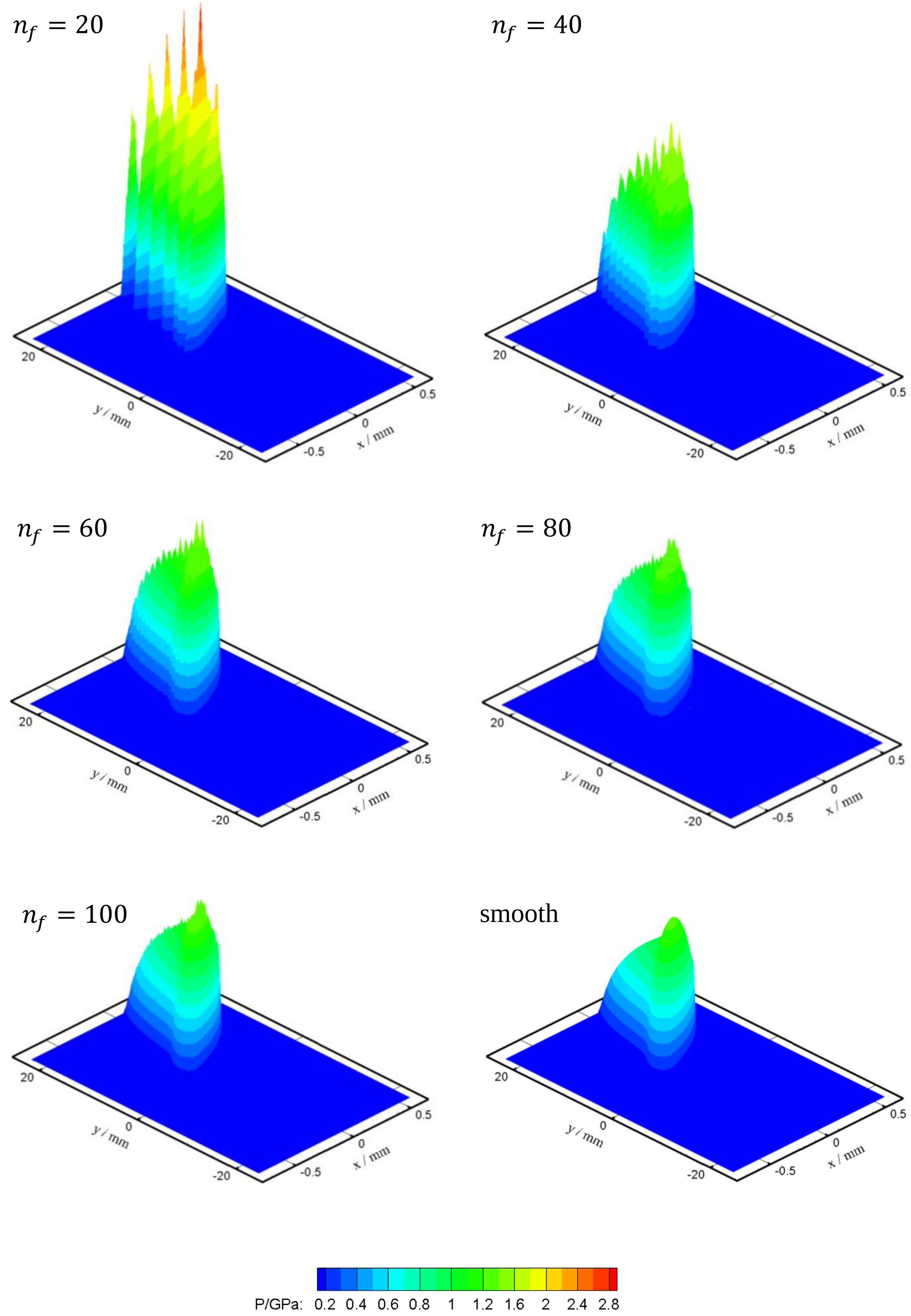

Figure 6.8: Contact pressure surfaces corresponding to six different patterns of tooth profile at time step 75

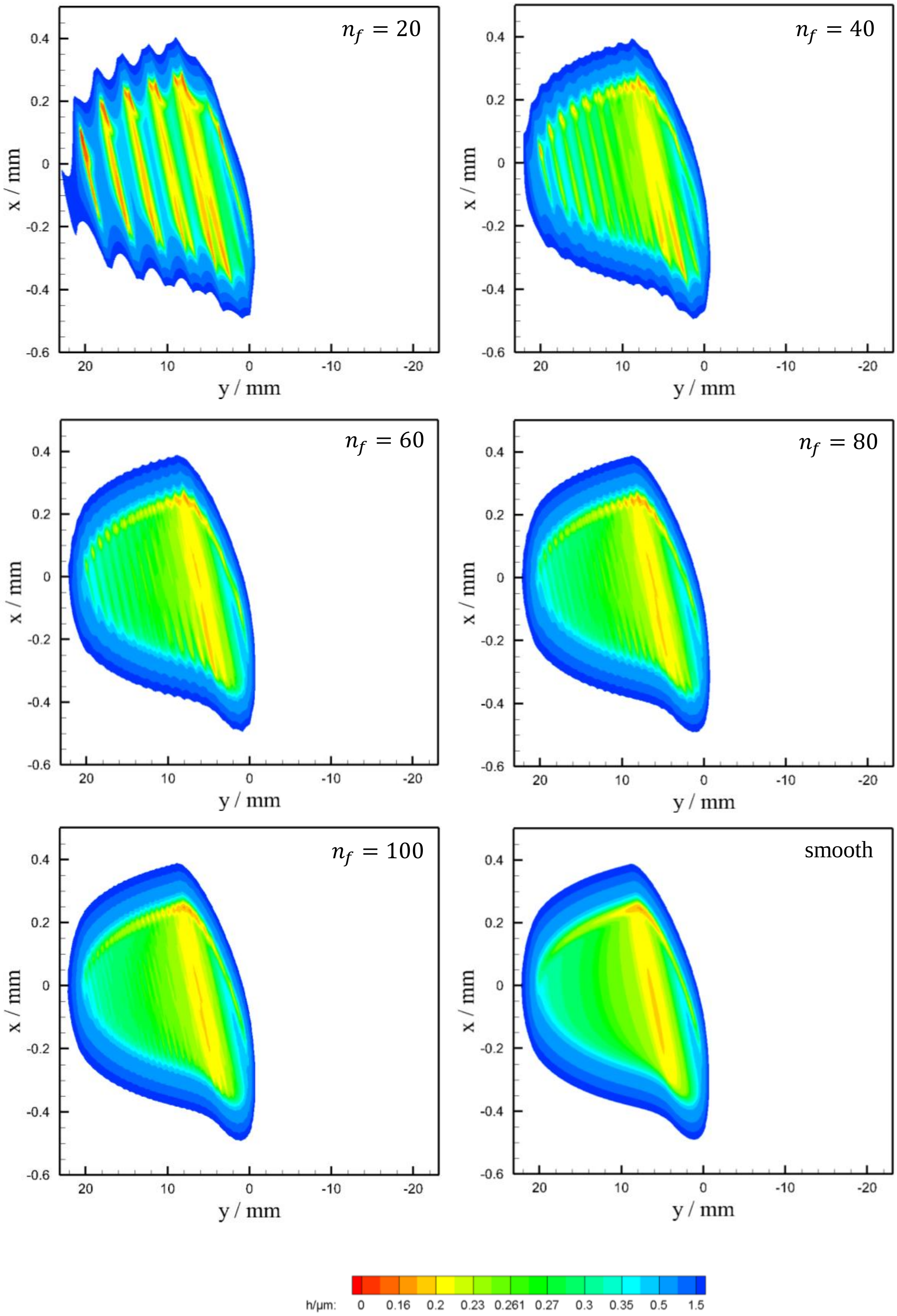

Figure 6.9: Film thickness contours corresponding to six different patterns of tooth profile at time step 75

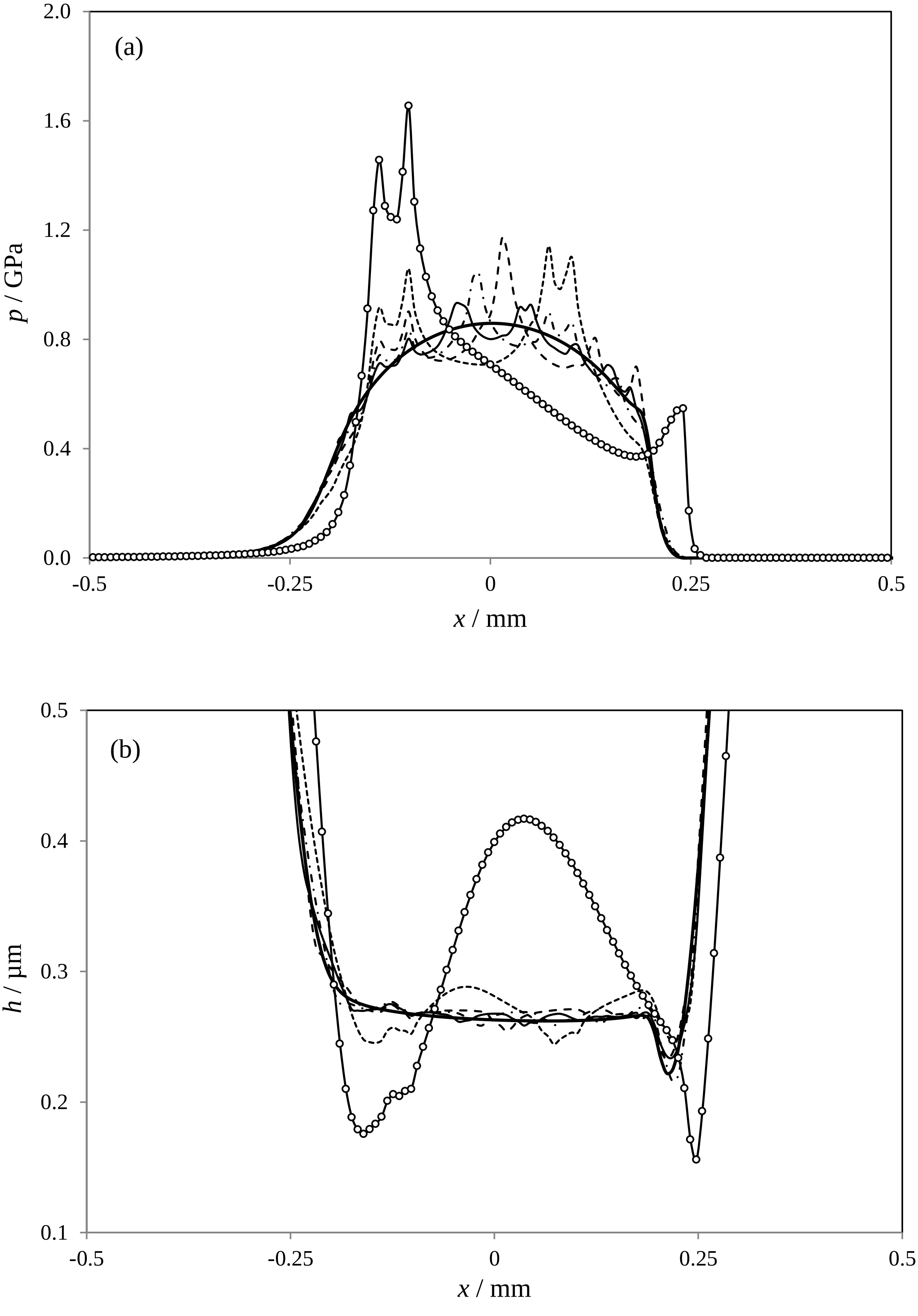

Figure 6.10: Sections at time step 75 of (a) pressure and (b) film thickness at position y = 12 mm; —— smooth profiles, —— n_f = 100, -·-·- n_f = 80, - - - n_f = 60, ……. n_f = 40 and -o- n_f = 20

Detailed results at time step 300 are given in Figures 6.11 to 6.15. Figure 6.11 illustrates the effects of increasing the number of facets on the 3D pressure distributions. As n_f is increased from 20 to 100 the pressure distribution becomes close to typical results of an elliptical contact which is the case for the smooth surface results. The cases of n_f = 80 and 100 are essentially very similar. The corresponding film thickness contours at this time step (300) are shown in Figure 6.12. The case of n_f = 20 shows a behaviour typical of an individual contact at the facet boundaries. This can also be seen in the previous figure where the 3D pressure distribution for n_f = 20 is not continuous and is separated into 13 pressure spikes as the profiles are generated using a relatively course steps distribution. The thinning of film thickness at the steps boundaries decreases with the increase of n_f and the film contours for the cases n_f = 60, 80 and 100 are in general similar to the smooth surfaces results. The effect of tip relief can be seen in the left sides of these contours, and this was discussed in detail in chapter 5.

Further comparisons for the result at this time step at three y (line of contact) positions are also made using faceted and smooth profiles. These are at $y = +19$, 0 and $y = -19$ mm which are shown in Figures 6.13, 6.14 and 6.15 respectively. In each figure the pressure distributions are shown in the upper part and the film thickness comparison is shown in the lower part. The results presented in these figures show similar behaviour to the results at time step 75 where the case of n_f = 20 gives the biggest pressure spikes and the lowest film thickness levels. The results for other cases also become closer to the smooth case results as n_f is increased.

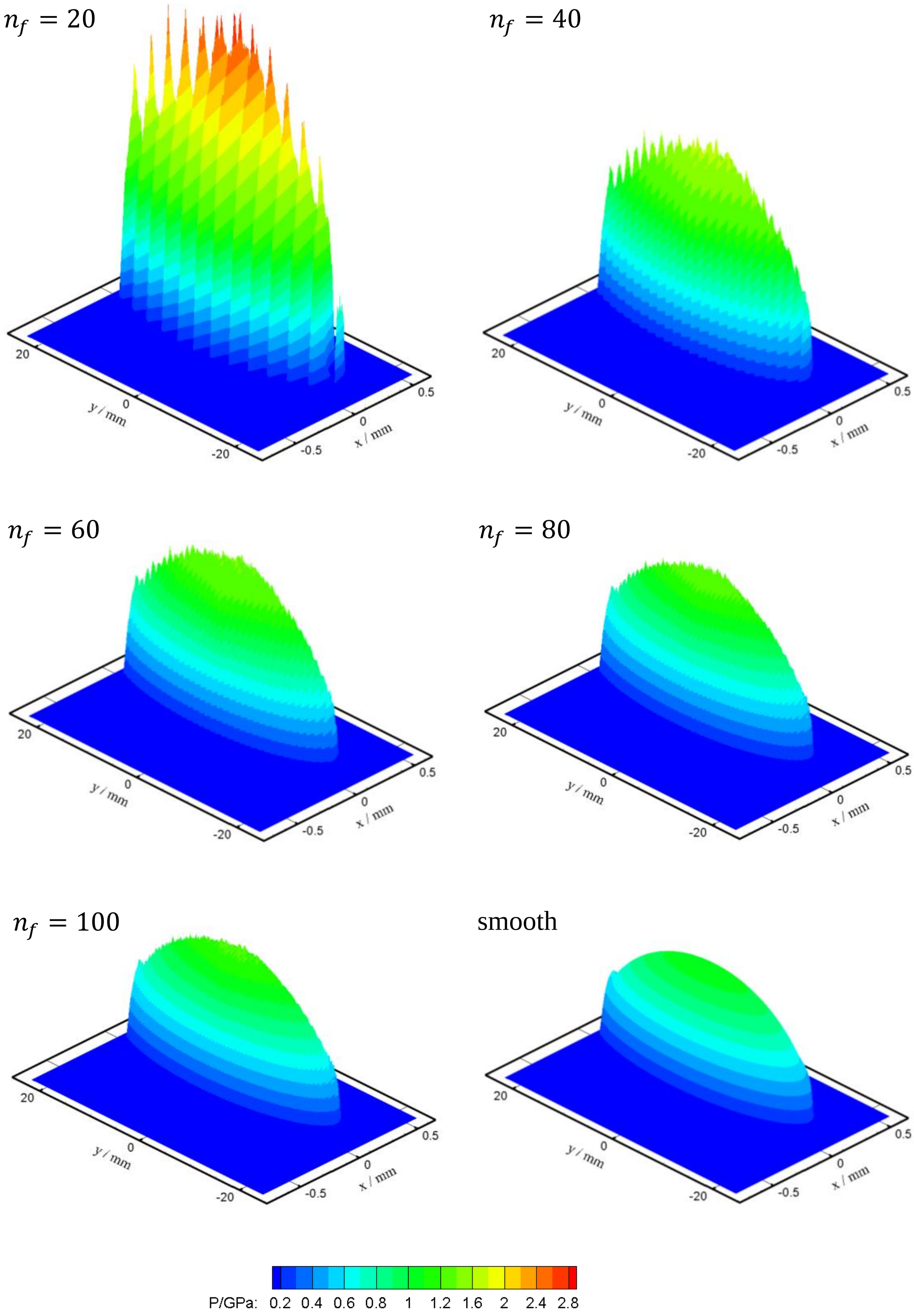

Figure 6.11: Contact pressure surfaces corresponding to six different patterns of tooth profile at time step 300

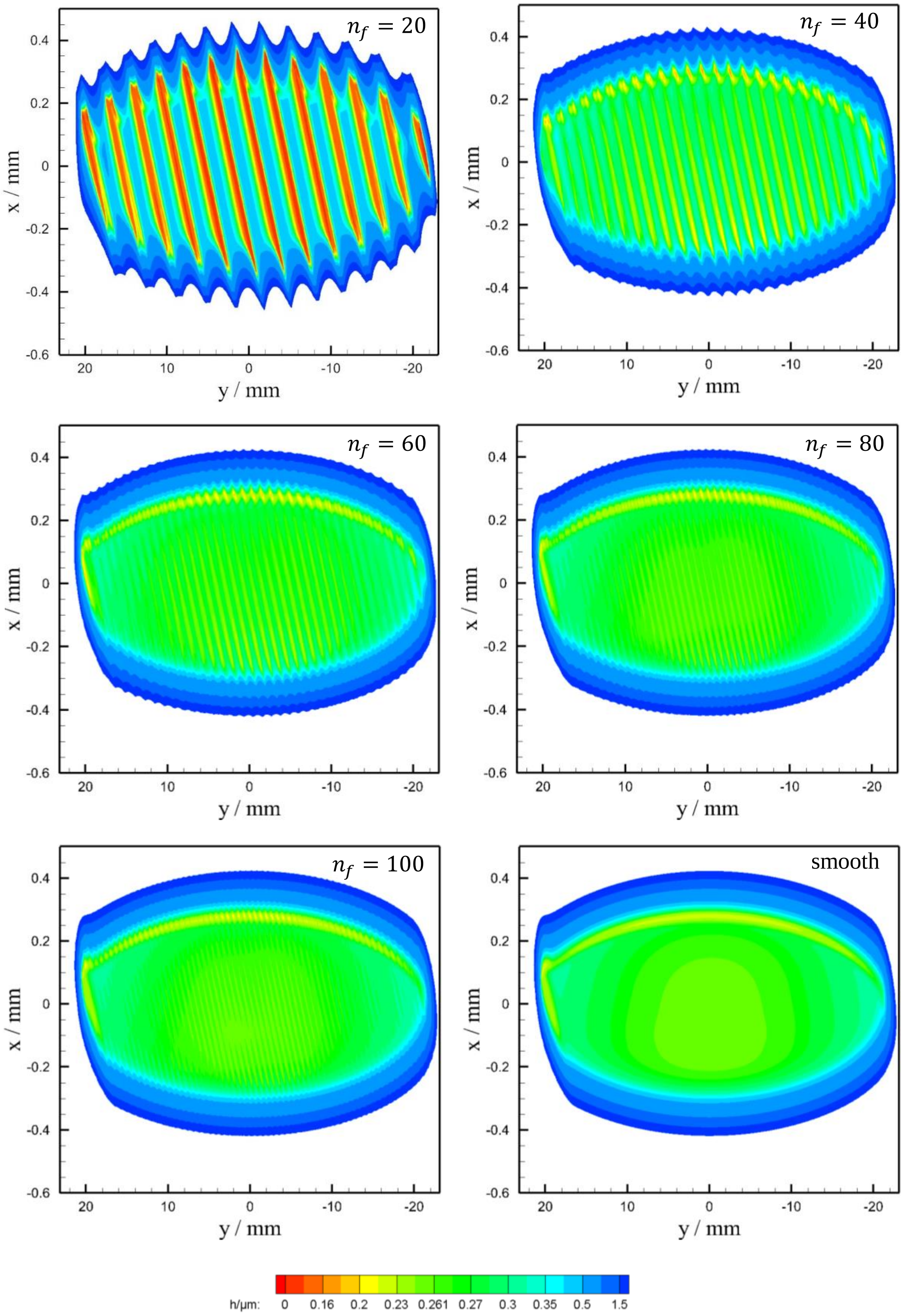

Figure 6.12: Film thickness contours corresponding to six different patterns of tooth profile at time step 300.

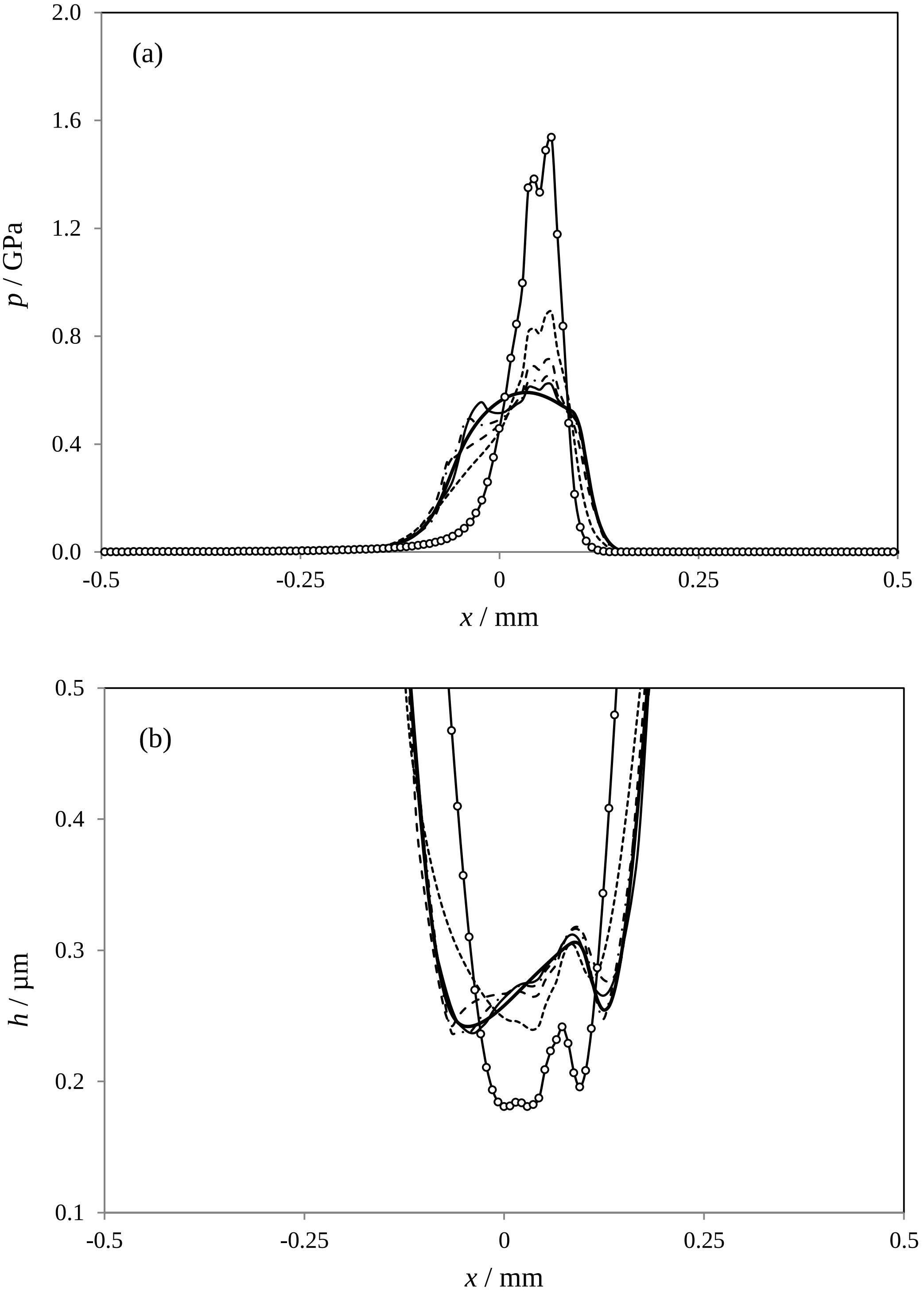

Figure 6.13: Sections at time step 300 of (a) pressure and (b) film thickness at position $y = +19$ mm; ▬▬ smooth profiles, —— $n_f = 100$, -·-· $n_f = 80$, - - - $n_f = 60$, …… $n_f = 40$ and ∘⋯∘⋯ $n_f = 20$

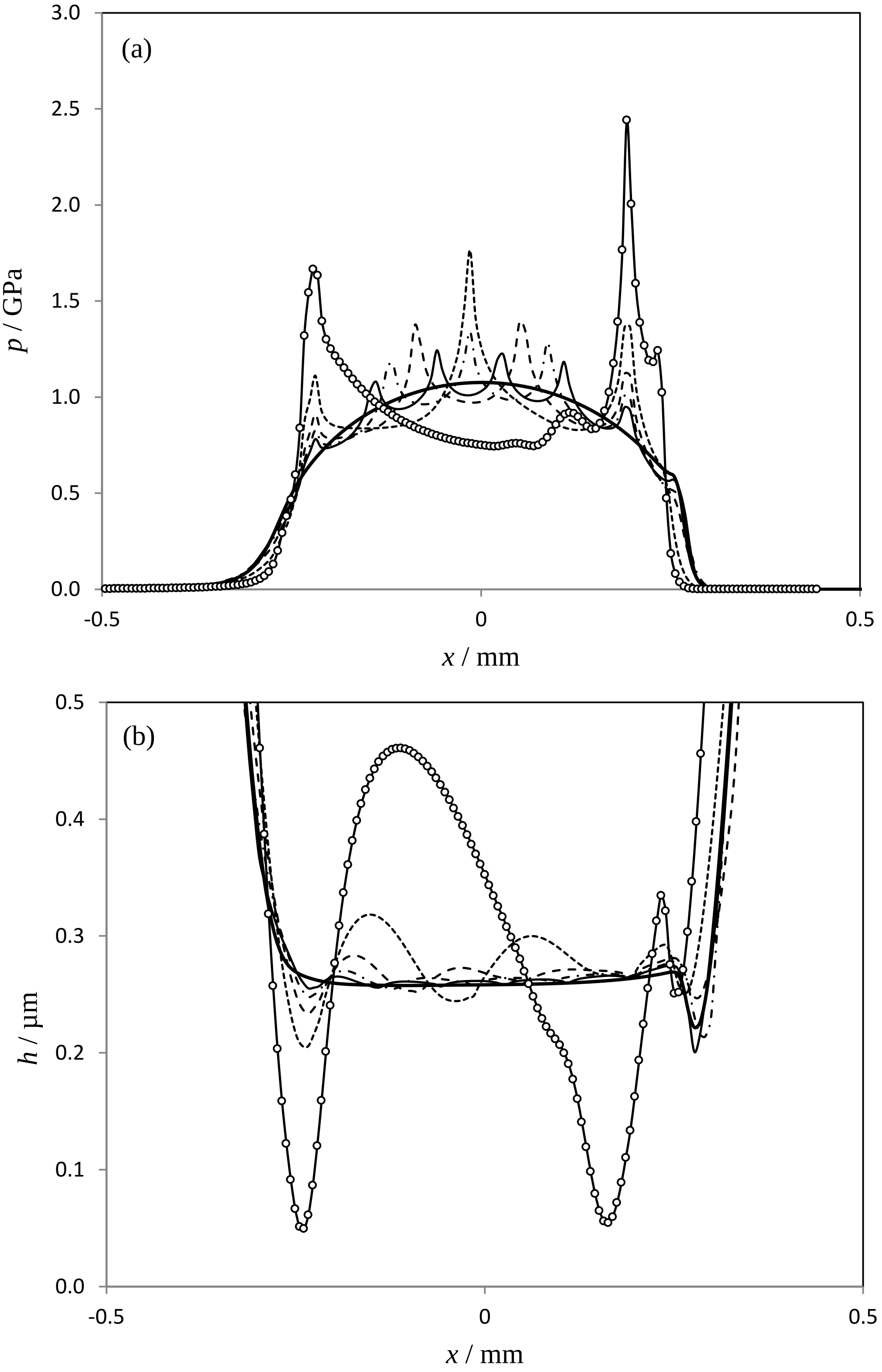

Figure 6.14: Sections at time step 300 of (a) pressure and (b) film thickness at position $y = 0$; ▬▬ smooth profiles, —— $n_f = 100$, -·-· $n_f = 80$, - - - $n_f = 60$, …… $n_f = 40$ and ∘···∘··· $n_f = 20$

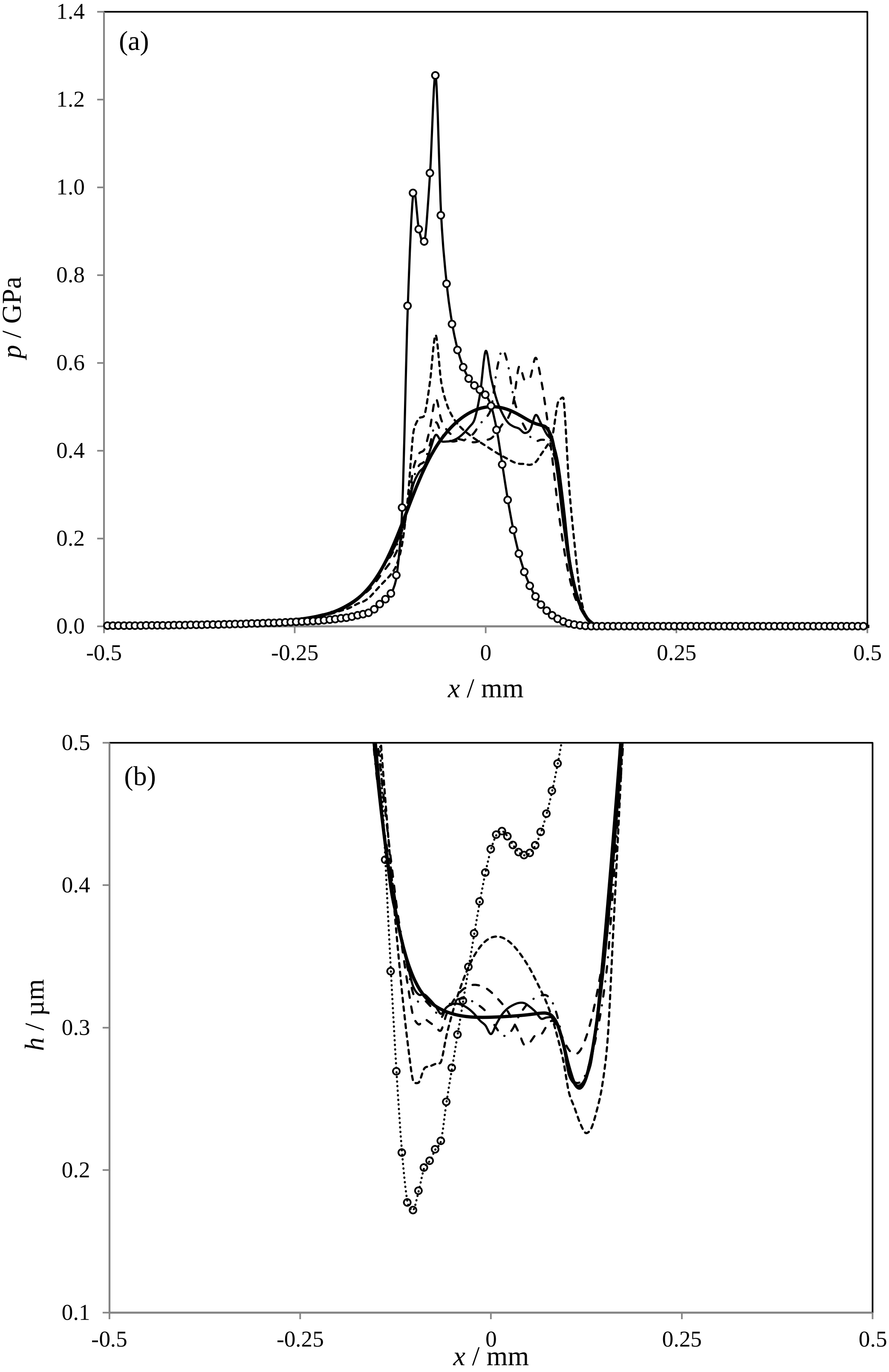

Figure 6.15: Sections at time step 300 of (a) pressure and (b) film thickness at position y = - 19 mm; —— smooth profiles, —— n_f = 100, -·-· n_f = 80, - - - n_f = 60, …… n_f = 40 and ∘··∘·· n_f = 20

Similar comparisons are also made for the results at time step 500. The 3D pressure distribution, film thickness contours and section comparisons at $y = -10$ mm are shown in Figures 6.16, 6.17, and 6.18 respectively. Similar behaviour to the results obtained at time step 75 and 300 are also found at this time step. The case n_f = 20 is the most extreme case for both pressure distribution and film thickness and the results for all the other cases tend towards the smooth results as n_f is increased.

In comparing the results it is clear that faceting modifies the pressure and film thickness response in all of the cases considered. For the finest faceted surface, n_f =100, the modification can be regarded as a mild perturbation of the smooth surface results. As the number of facets is reduced the modifications increased systematically. For the tooth module considered it is clear that the n_f = 20 case causes considerable disturbance and results in extremely thin lubricant films, or metal to metal contact, on the lines corresponds to facet boundaries.

The theoretical analyses indicate that when a facetted surface is being produced the lubrication mechanism may be compromised unless the number of facets is large enough or some further smoothing operations are introduced to the manufacturing process.

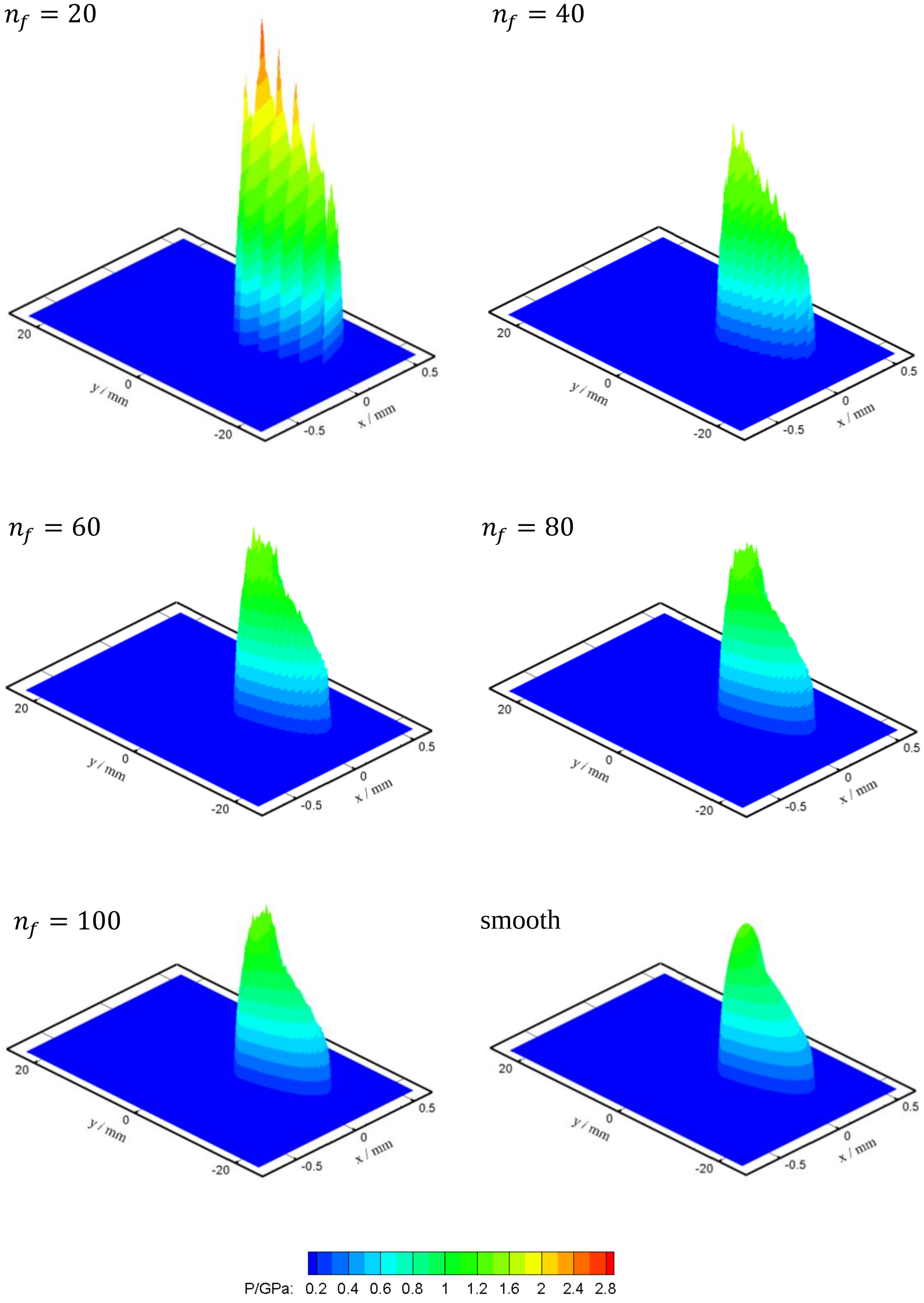

$n_f = 20$

$n_f = 40$

$n_f = 60$

$n_f = 80$

$n_f = 100$

smooth

Figure 6.16: Contact pressure surfaces corresponding to six different patterns of tooth profile at time step 500

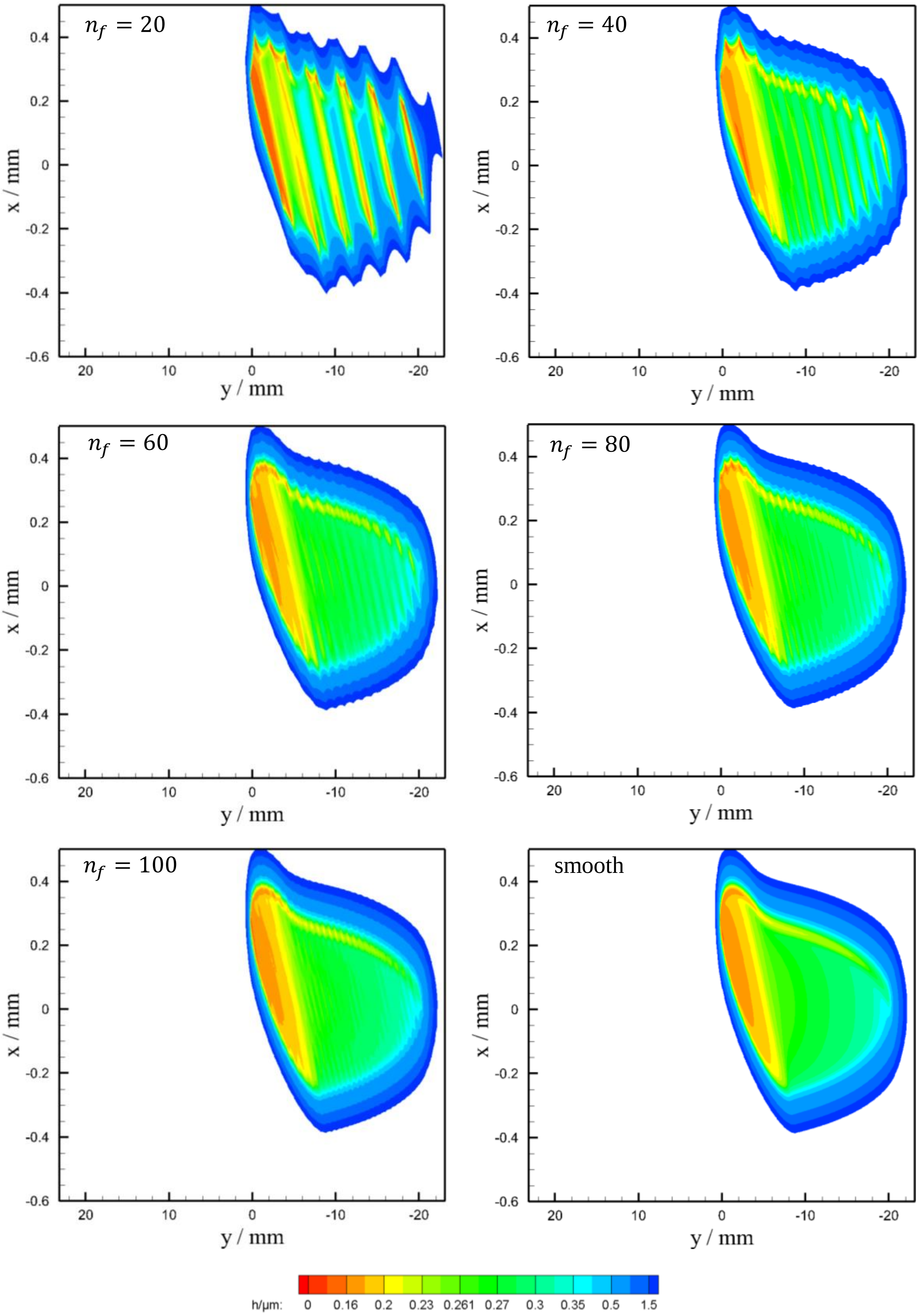

Figure 6.17: Film thickness contours corresponding to six different patterns of tooth profile at time step 500

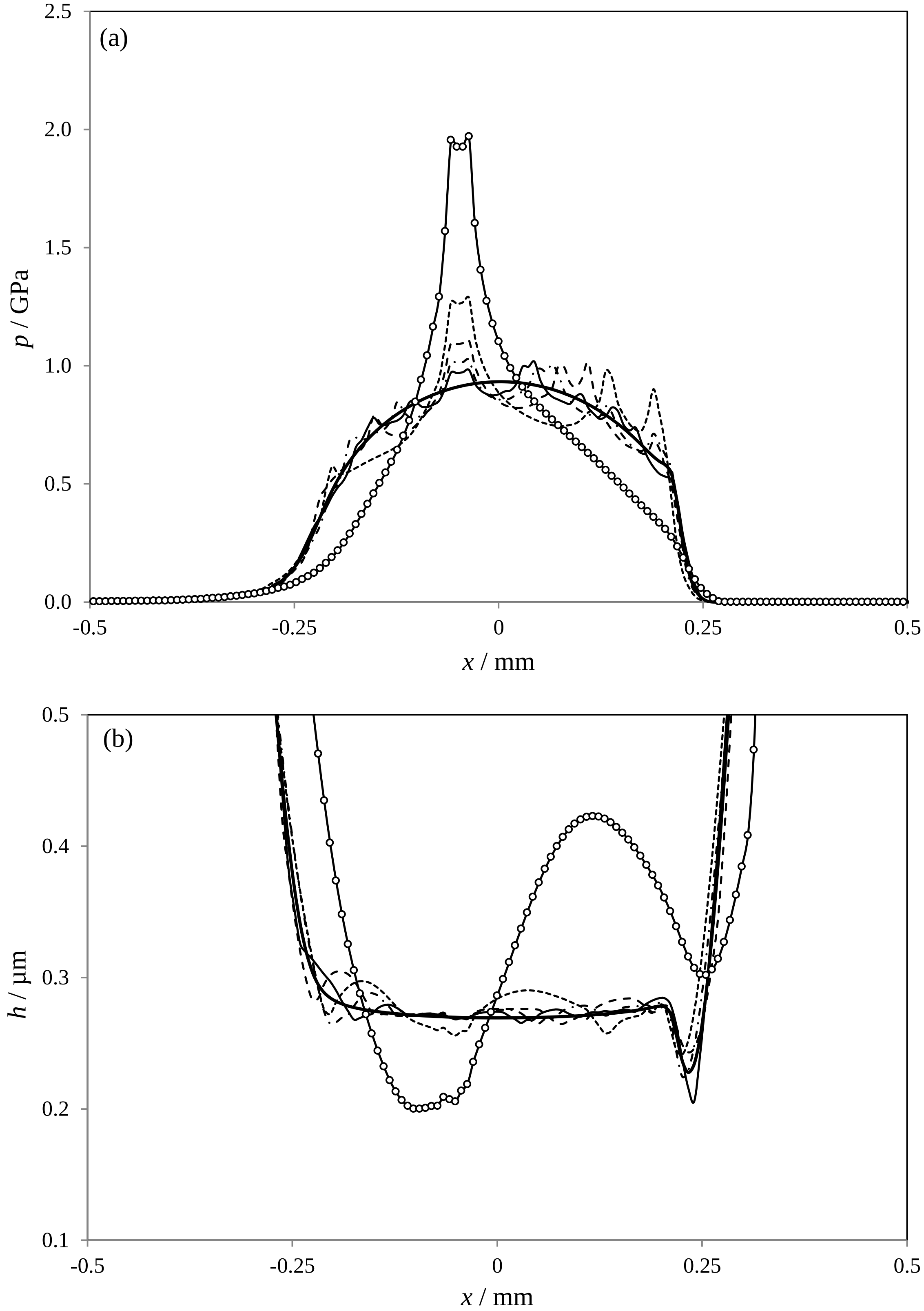

Figure 6.18: Sections at time step 500 of (a) pressure and (b) film thickness at position y = - 10 mm; ▬ smooth profiles, —— n_f = 100, -·-· n_f = 80, - - - n_f = 60, …… n_f = 40 and ∘…∘… n_f = 20

Chapter 7

3D Line Contact Model

7.0 Introduction

The 3D line contact model presented in this chapter is used to investigate the EHL characteristics of the contact between helical gear teeth, and takes the effect of surface roughness into consideration. A special roughness orientation may be found in the helical gears contact and a close form equation is derived to describe its features, as will be shown later. The model is based on the use of the fast Fourier transform (FFT) method to calculate the surface deflection and its differential form where these terms are represented by convolution integrals. This enables a model with limited length along the contact line to be developed in such a way that it allows surface roughness to be incorporated. Figure 7.1 shows an example of a helical gear tooth contact that can be modelled by the method described in this chapter. Figure 7.1 (a) shows a single helical gear tooth together with a typical contact line, and Figure 7.1 (b) illustrates schematically the tangent plane to the tooth surface at the contact line where the length of the contact zone is much bigger than the contact width.

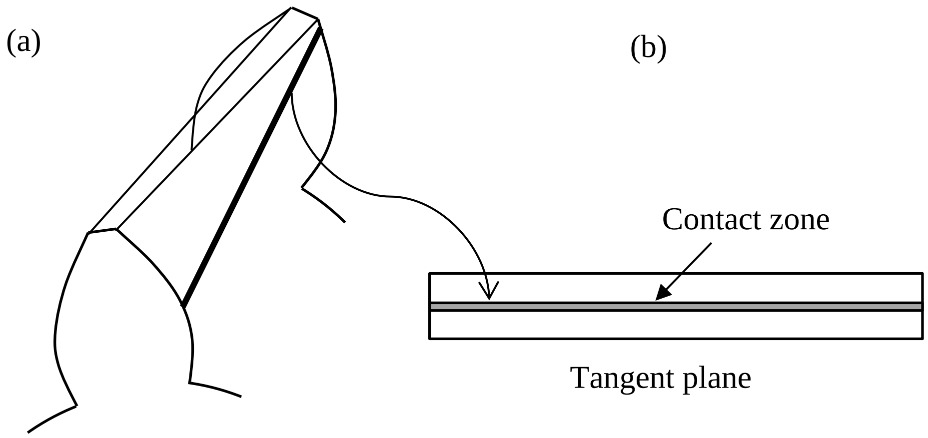

Figure 7.1: Contact of helical gears; (a) contact line on a helical gear tooth and (b) contact zone where its length is much bigger than the width

7.1 Convolution integrals and the FFT method

This section explains that the equations which give the elastic surface deflection and its differential form involve convolution integrals and also clarifies how the FFT method can be used to evaluate them in a 3D line contact model of limited transverse extent.

In solving the EHL problem, the total gap between two smooth surfaces is defined by equation (3.2)

$$h(x,y)=h_u(x,y)+d(x,y)+h_o \tag{3.2}$$

This equation can be modified to take the effect of surface roughness into consideration as

$$h(x,y)=h_u(x,y)+d(x,y)+\Theta_1(x,y)+\Theta_2(x,y)+h_o$$

where $\Theta_1(x,y)$and $\Theta_2(x,y)$are the surface roughness for the two surfaces.

The determination of the elastic deflection in this equation at any point in the solution domain was given by equation (3.3) which is repeated here for clarity

$$d(x_1,y_1)=\frac{2}{\pi E'}\iint_A \frac{p(x,y)}{\sqrt{(x-x_1)^2+(y-y_1)^2}}\,dxdy \tag{3.3}$$

This equation represents a convolution integral. In a continuous system, convolution integrals such as that given by equation (3.3) can be obtained using the convolution theorem where the Fourier transform of a convolution of two functions e.g. g and p is the product of their Fourier transforms.

$$\Psi\{g*p\}=\Psi\{g\}\Psi\{p\}$$

Taking the inverse transform for this equation gives the required convolution integral:

$$g * p = \Psi^{-1}\{\Psi\{g\}\Psi\{p\}\}$$

where Ψ represents the Fourier transform.

Equation (3.3) was written in a discrete form over a finite domain in Chapter 3 as

$$d(x_i, y_j) = \frac{2}{\pi E'} \sum_{k=1}^{N} \sum_{l=1}^{M} g_{k-i,l-j} \; p_{k,l} \tag{3.6}$$

And the differential form of this equation was given by equation (3.7)

$$\nabla^2 d(x_i, y_j) = \sum_{k=1}^{N} \sum_{l=1}^{M} f_{k-i,l-j} \; p_{k,l} \tag{3.7}$$

As with equation (3.3) the right hand terms of equations (3.6) and (3.7) are also convolution integrals of pressure and influence coefficients, but in a discrete form.

There are two types of the discrete convolution which are described as linear (aperiodic) and circular (periodic) convolutions. Distinguishing between the two types is important in adopting the appropriate evaluation method. The fast Fourier transform (FFT) technique has impressive efficiencies in evaluating convolution integrals, but it will produce periodic errors if it is used directly to evaluate the former in contrast with the later type. This can be attributed to the fact that by using the FFT method to evaluate the convolution all input and output functions need to be periodic which is not the case with the linear convolution. Therefore, the use of the FFT method in solving elastic contact problems takes not only the effects of the pressure distribution over the solution domain but also their periodic repeats (Wang et al. 2003). However, in the present problem the contact dimension in the *x* direction is very limited (finite) as previously shown in Figure 7.1, and repeating those values in this direction will produce an additional contribution to the deflection, which is physically unreal. This type of error can be eliminated by using the “zero padding” strategy. In this approach the length of the input function is extended with zeroes in the x and y directions so that the periodic effect becomes negligible due to the localized effect of the influence coefficients g and f in particular. However, in the 3D line contact model the input functions are assumed to be repeated periodically in the y direction. Therefore, a mixed strategy of zero padding in x direction and periodic repetition in the y direction for the input functions is adopted in this model as illustrated in Figure 7.2.

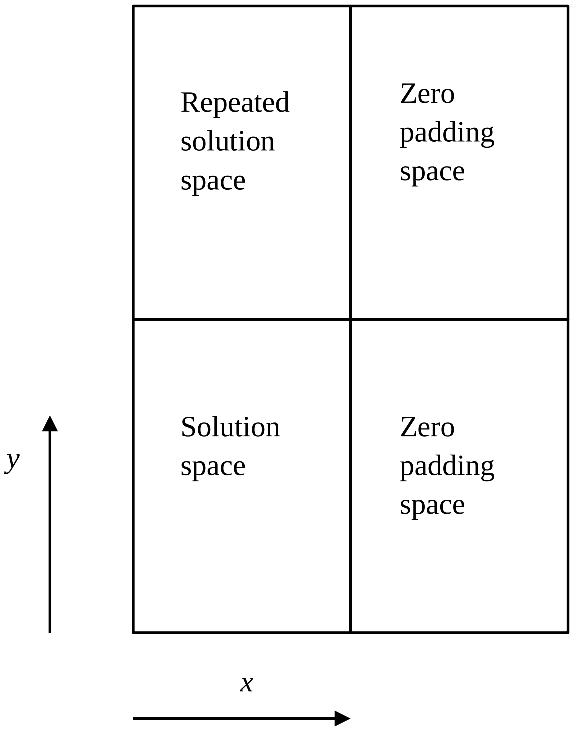

Figure 7.2: Padding strategy for the 3D line contact problem

7.2 Numerical solution

The solution domain for the EHL analysis is defined numerically by:

$$\Omega = [0, N-1] \times [0, M-1]$$

In order to implement the FFT method to calculate the convolution integrals given by equations (3.6) and (3.7), the influence coefficients function in both equations needs to be rewritten in a wrap-around order. This requires a grid size of twice the solution domain size in each direction. A similar grid is also required for the pressure distribution where the same pattern of pressure is repeated in one or both directions as required. As a result the FFT method is performed in a domain defined by a grid size of $2N*2M$.

In the discrete system for a finite length sequence, the discrete Fourier transform for the pressure data in equation (3.6) can be that given by Nussbaumer (1982), for example:

$$\Psi\{p\}_{i,j} = \sum_{k2=0}^{M-1}\sum_{k_1=0}^{N-1} \exp(-2\pi\imath k_2 j/M)\exp(-2\pi\imath k_1 i/N)p(k_1,k_2)$$

where $\imath = \sqrt{-1}$ and the two dimensional grid is defined by

$0 \le i \le N-1$ and $0 \le j \le M-1$

The discrete Fourier transform for the influence coefficient functions *g* and *f* can also be evaluated using the previous equation. Therefore, equation (3.6) can be calculated from:

$$d(x_i, y_j) = \Psi^{-1}\{\Psi\{p\}\Psi\{g\}\}$$

Similarly equation (3.7) can be evaluated as

$$\nabla^2 d(x_i, y_j) = \Psi^{-1}\{\Psi\{p\}\Psi\{f\}\}$$

The procedure (program) for the evaluation of discreet convolution integrals using the FFT method is available widely in the literature and the one given by Press et. al. (1992) is adopted in the current work.

7.3 Angle between contact line and grinding line

The technique described in this section will be used to examine the effects of roughness orientation on the EHL performance of helical gears. This orientation in question is related to the inclination of grinding marks with respect to the line of contact between the gear teeth in the tangent plane as shown in Figure 7.3. Figure 7.3 (a) shows a 3D schematic drawing of a single helical gear tooth (pinion tooth) in contact. The corresponding gear wheel tooth is not shown for the purpose of clarity. Contact of the teeth occurs on the line AC at this specific position in the meshing cycle. Point A is the limit of the contact line on the tooth face which moves along the line of action as the contact progresses between the gear teeth. In spur gears, grinding of the gear teeth usually takes place in the direction of the gear axis which is perpendicular to the tooth face. In this case the grinding marks will be in the same direction as the contact line (both are parallel to the gear axis). In helical gears the helix angle will affect the angle between the contact line and the grinding marks. This can be seen clearly in Figure 7.3 (a) by comparing the direction of lines AC and AD where line AD represents the grinding mark direction. Any point on this line is at a constant radius, r_{A} from the gear axis.

A length AB from the contact line is selected to find the angle θ between the contact line and the projection of the grinding mark line on the tangent plane which is the solution space of the EHL analysis. This projection is represented by line AT where the tangent plane contains the triangle ABT. This angle is given by

$$\theta = \tan^{-1}(\mathrm{BT}/\mathrm{AB}) \tag{7.1}$$

For any given AB distance along the line of contact, equation (7.1) can be used to evaluate the angle θ by calculating the distance BT.

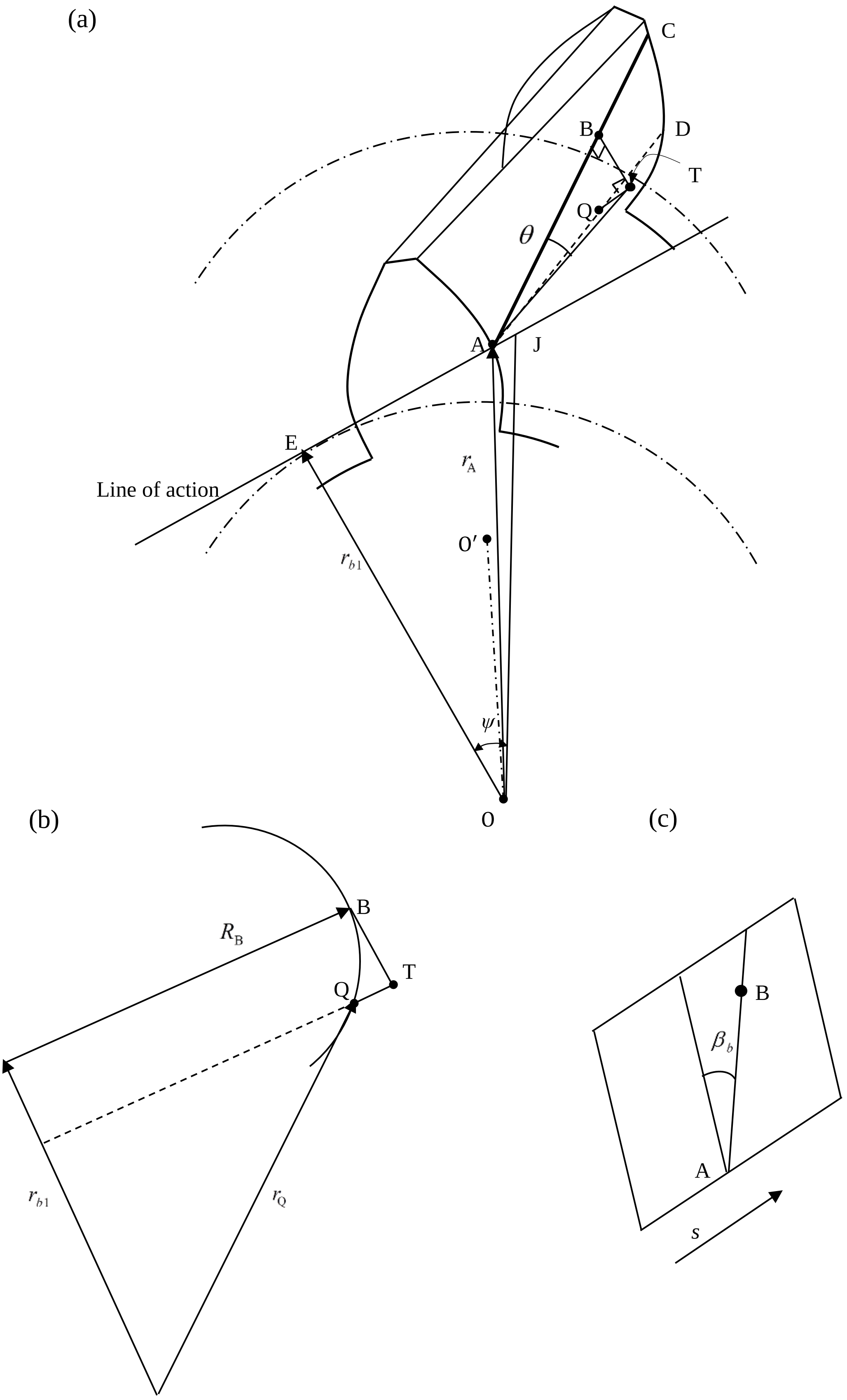

Figure 7.3: Schematic drawing of helical gear tooth contact; (a) 3D drawing for a pinion tooth, (b) parabolic approximation for the contact and (c) *s* positon of point B with respect to point A

Figure 7.3 (b) shows a parabolic approximation of the involute profile at point B in the transverse section. Thus, using this figure the distance QT is given by:

$$\mathrm{QT} = \frac{(\mathrm{BT})^2}{2R_\mathrm{B}} \tag{7.2}$$

where R_B is the tooth radius of curvature at point B which can be determined in terms of the position, s_B of point B relative to the pitch point in the transverse direction:

$$R_\mathrm{B} = r_{b1}\tan\psi + s_\mathrm{B} \tag{7.3}$$

Figure 7.3 (c) shows the contact line AC on the plane of contact. Using this figure, s_B can be determined in terms of the position of point A which is known for all positions in the meshing cycle:

$$s_\mathrm{B} = s_\mathrm{A} + \mathrm{AB}\sin\beta_\mathrm{b} \tag{7.4}$$

Since points A and Q lie on line AD, their distances from the gear axis OO' are:

$$r_\mathrm{A} = r_\mathrm{Q} \tag{7.5}$$

From the triangle OEA in Figure 7.3 (a):

$$r_\mathrm{A} = \sqrt{r_{b1}^2 + (r_{b1}\tan\psi + s_\mathrm{A})^2}$$

The term in the bracket is the tooth radius of curvature at point A, R_A. Therefore this equation can be reduced to

$$r_\mathrm{A} = \sqrt{r_{b1}^2 + R_\mathrm{A}^2} \tag{7.6}$$

Using the schematic drawing of the transverse section at point B that is shown in Figure 7.3 (b), r_Q can be given by:

$$r_\mathrm{Q} = \sqrt{(r_{b1} - \mathrm{BT})^2 + (R_\mathrm{B} - \mathrm{QT})^2}$$

Substituting equation (7.2) into this equation yields:

$$r_{\mathrm{Q}} = \sqrt{(r_{b1} - \mathrm{BT})^2 + (R_{\mathrm{B}} - \frac{(\mathrm{BT})^2}{2R_{\mathrm{B}}})^2} \tag{7.7}$$

Substitution of equations (7.6) and (7.7) in equation (7.5), yields

$$\sqrt{r_{b1}^2 + R_{\mathrm{A}}^2} = \sqrt{(r_{b1} - \mathrm{BT})^2 + (R_{\mathrm{B}} - \frac{(\mathrm{BT})^2}{2R_{\mathrm{B}}})^2}$$

This equation can be written, after some simplification, in the following form

$$\frac{(\mathrm{BT})^4}{4R_{\mathrm{B}}^2} - 2r_{b1}\mathrm{BT} + R_{\mathrm{B}}^2 - R_{\mathrm{A}}^2 = 0 \tag{7.8}$$

Equation (7.8) has four roots and two of them are complex. However, solving this equation at any position along the contact line will only produce one realistic real root. Substituting the solution of equation (7.8) (BT) in equation (7.1) gives the angle between the line of contact and the grinding mark direction at point B for the pinion teeth. Since the tooth radius of curvature increases with *y* along the contact line (for the pinion), the calculated angle with respect to point A also changes and depends on the distance AB. This means that the projection of the grinding line on the tangent plane is not a straight line.

A similar equation can be derived for the contacting wheel tooth using the same procedure taking into account the fact that its radius of curvature decreases with increasing *y* and equation (7.7) needs to be reformulated to the following form:

$$r_{\mathrm{WQ}} = \sqrt{(r_{b2} + \mathrm{BT})^2 + (R_{\mathrm{WB}} - \frac{(\mathrm{BT})^2}{2R_{\mathrm{WB}}})^2}$$

where r_{WQ} is the radial distance from the wheel axis to point Q in the transverse direction and R_{WB} is the wheel tooth radius of curvature at point B. Therefore, the required equation for the wheel tooth is

$$\frac{(\mathrm{BT})^4}{4R_{\mathrm{WB}}^2} + 2r_{b2}\mathrm{BT} + R_{\mathrm{WB}}^2 - R_{\mathrm{WA}}^2 = 0$$

Changing distance AB along the contact line means choosing a different *s* value to calculate the radii of curvature for the two surfaces which correspond to the position of point B. Therefore, the variation of the required angle described in equation (7.1) for both surfaces is actually *s* dependent. Figure 7.4 shows this variation for both surfaces throughout the meshing cycle (variation with *s*) for a distance AB = 1 mm, i.e. close to the gear face at A. It can be seen that angle θ_{P} varies between 4.6$^{\mathrm{o}}$ and 9.5$^{\mathrm{o}}$ and θ_{W} varies between 9.5$^{\mathrm{o}}$ and 4.6$^{\mathrm{o}}$ and both angles are equal at the pitch point $\theta_{\mathrm{W}} = \theta_{\mathrm{P}} = 7.08^{\circ}$. θ_{P} increases and θ_{W} decreases with increasing *s* and the opposite variation of these angles is related to the nature of radii of curvature variation with *s* for the two teeth. For the pinion tooth, the first and last contact points in the meshing cycle (which is defined by *s*) represent the lowest and highest radius of curvature, respectively. For the wheel tooth they represent the highest and lowest radii of curvature, respectively.

The inclination of the contact line with respect to the grinding direction in the tangent plane calculated in this way can also be verified by drawing the gap between the two teeth in contact with a 2 μm height feature added to this gap at a constant distance r_{A} from the gear axis across the whole face width for both gears to represent grinding lines as shown in Figure 7.5. The *y* axis represents the contact line direction. It is clear from this figure that these lines are inclined at different angles with *y* direction and consequently cross each other.

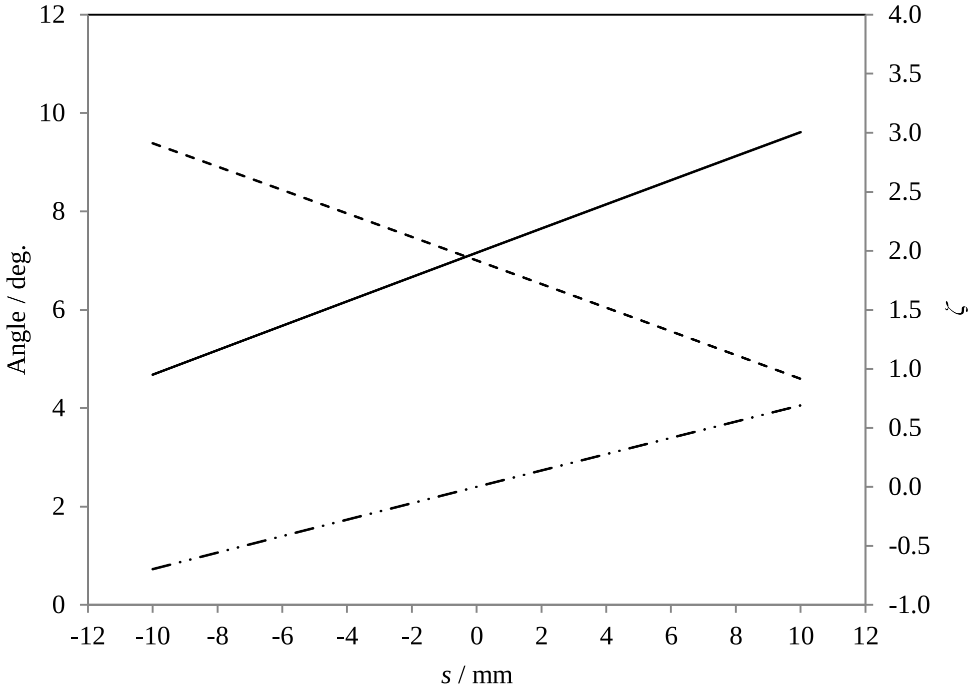

Figure 7.4: Variation of ——— θ_P , - - - - - - θ_W and - · - · - · - ζ with s

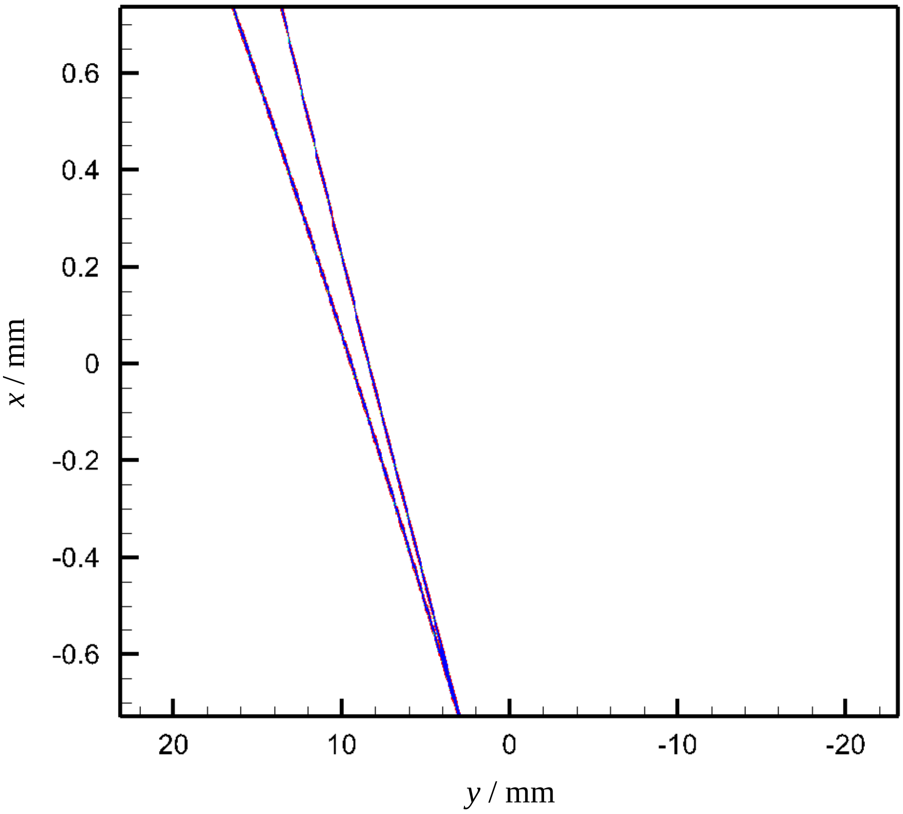

Figure 7.5: Inclination of the contact line with respect to the 2 μm height features added at two radial distances from the gear centre. (Curvatures of the surfaces are removed)

7.4 3D line contact verses line contact results for smooth surfaces.

A comparison between the EHL results for the 3D model and the corresponding line contact analysis is carried out to validate this model for smooth surfaces. For this purpose the solution domain is defined by a selected length in the *y* direction, L_y = 2 mm, and a distance of 4 *a* $(-2.5a \le x \le 1.5a)$ in the *x* direction. The number of elements used in the entrainment direction, *x*, is 800 elements which is then padded with zeros ($p = 0$) to be 1024 (the nearest power of 2 number). These additional 224 points correspond physically to a distance of 1.12 *a*. The number of elements in the *y* direction is 128. The input data for the 3D EHL solution is explained in Table 7.1. The geometry and kinematic characteristics described in this table are also used for the line contact analyses and an input load of 360 kN/m is adopted which is equal to the load/length used in the 3D analyses.

Table 7.1: Input data for the 3D model

R/mm	14.0
Load/N	720
$\bar{u}$ / m/s	6.71
ζ	0.36

The 3D pressure distribution and film thickness for smooth surfaces is shown in Figure 7.6. This figure shows how the pressure and film thickness surfaces are prismatic and perfectly extruded in the *y* direction. Sections at a *y* position (pressure and film thickness results) are compared with the corresponding line contact results as shown in Figure 7.7. It can be seen in this figure that both pressure and film thickness curves coincide almost exactly with the corresponding line contact results.

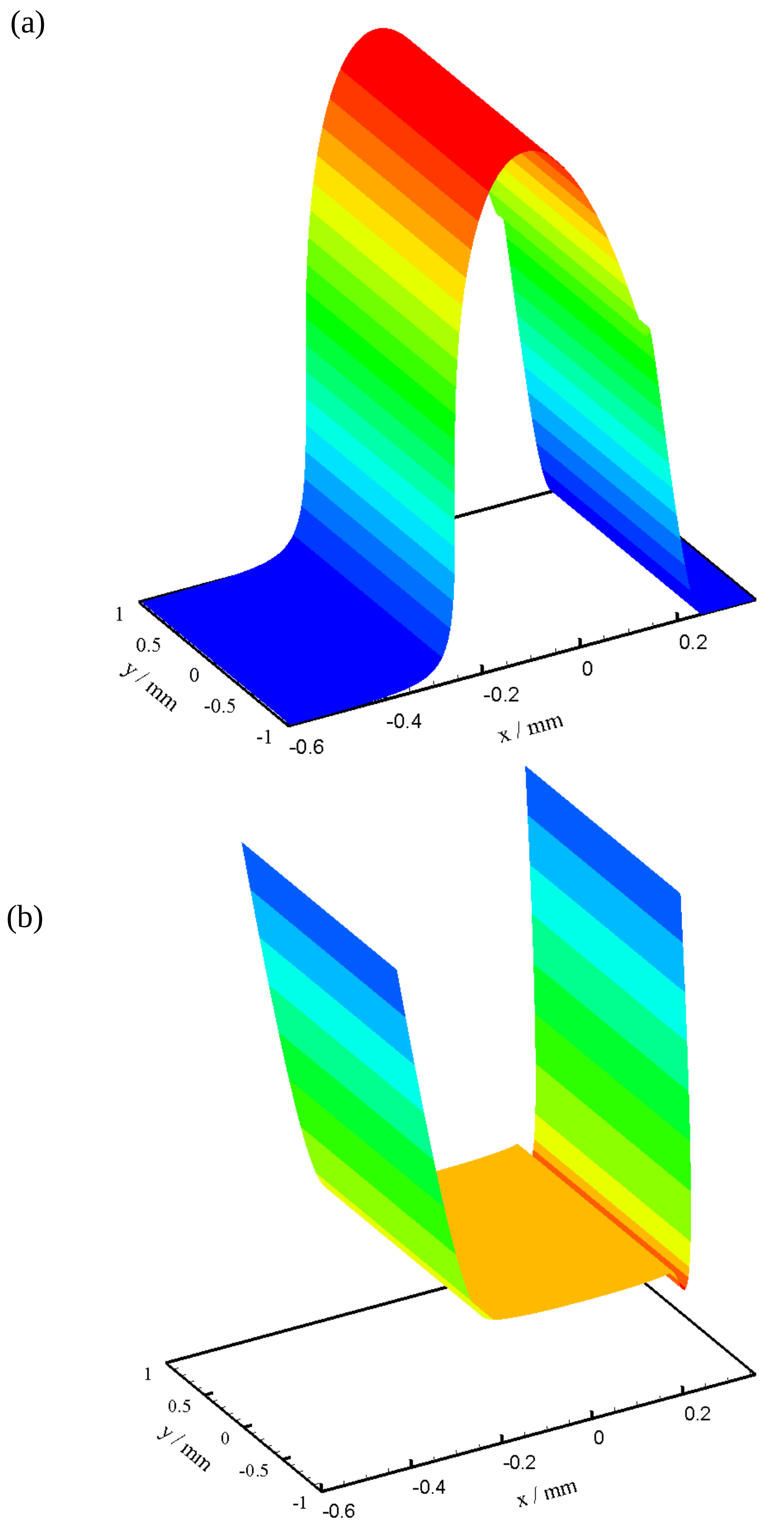

Figure 7.6: 3D smooth surface line contact results, (a) Pressure distribution and (b) Film thickness

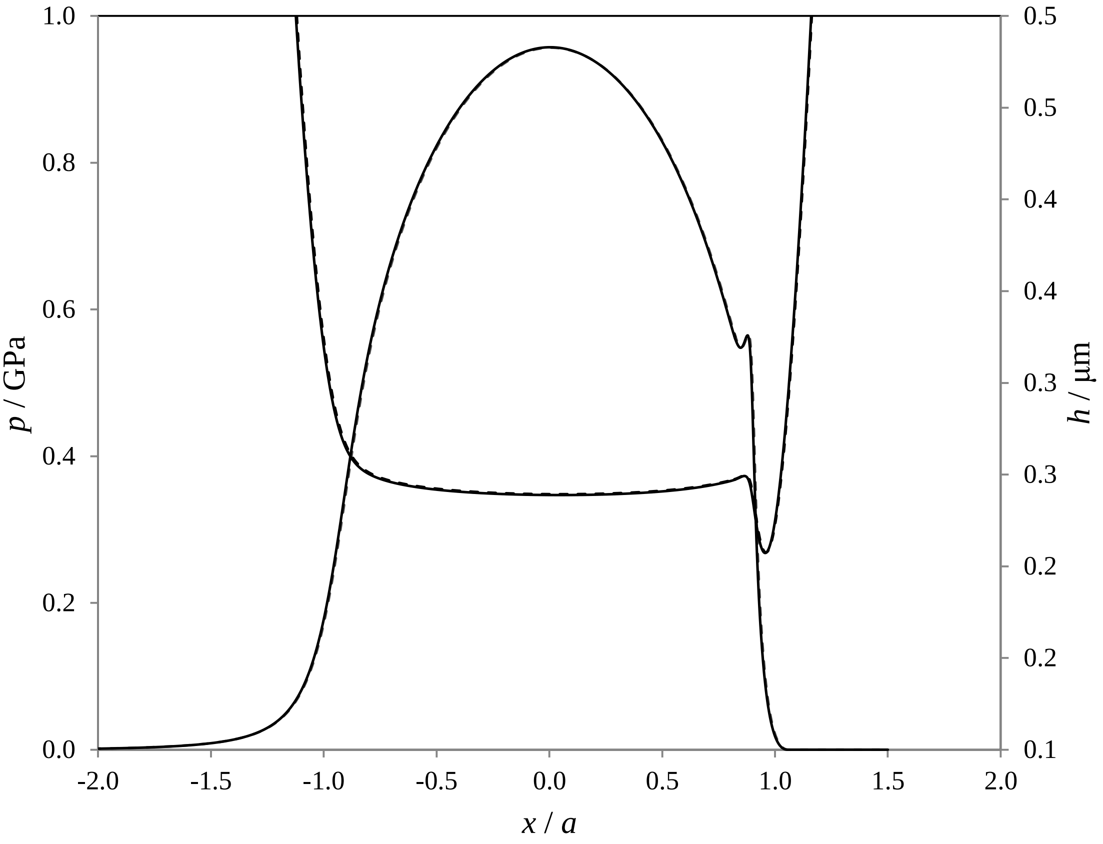

Figure 7.7: Comparison between —— 3D line contact results and corresponding ------ line contact results for smooth surfaces.

7.5 FEM vs FD discretisation

The 3D EHL analysis is performed using both the finite element method (FEM) and finite difference (FD) methods for the purpose of comparison and model development. Figure 7.8 shows the discretisation of the solution domain using both methods. Only one column of elements /nodes is shown in the solution domain for each method which is discretised to four elements (or rows of nodes) for the purpose of clarity. The solution domain is repeated in both transverse directions according to the FFT method and only one repetition is shown in the figure. For the FD method the solution is straightforward. In the central difference case for example, the evaluation of the second derivative of pressure, $\partial^2 p/\partial y^2$, can be done directly at all nodes except the nodes on the first and last rows where this requires the nodal values at the four neighbouring nodes of

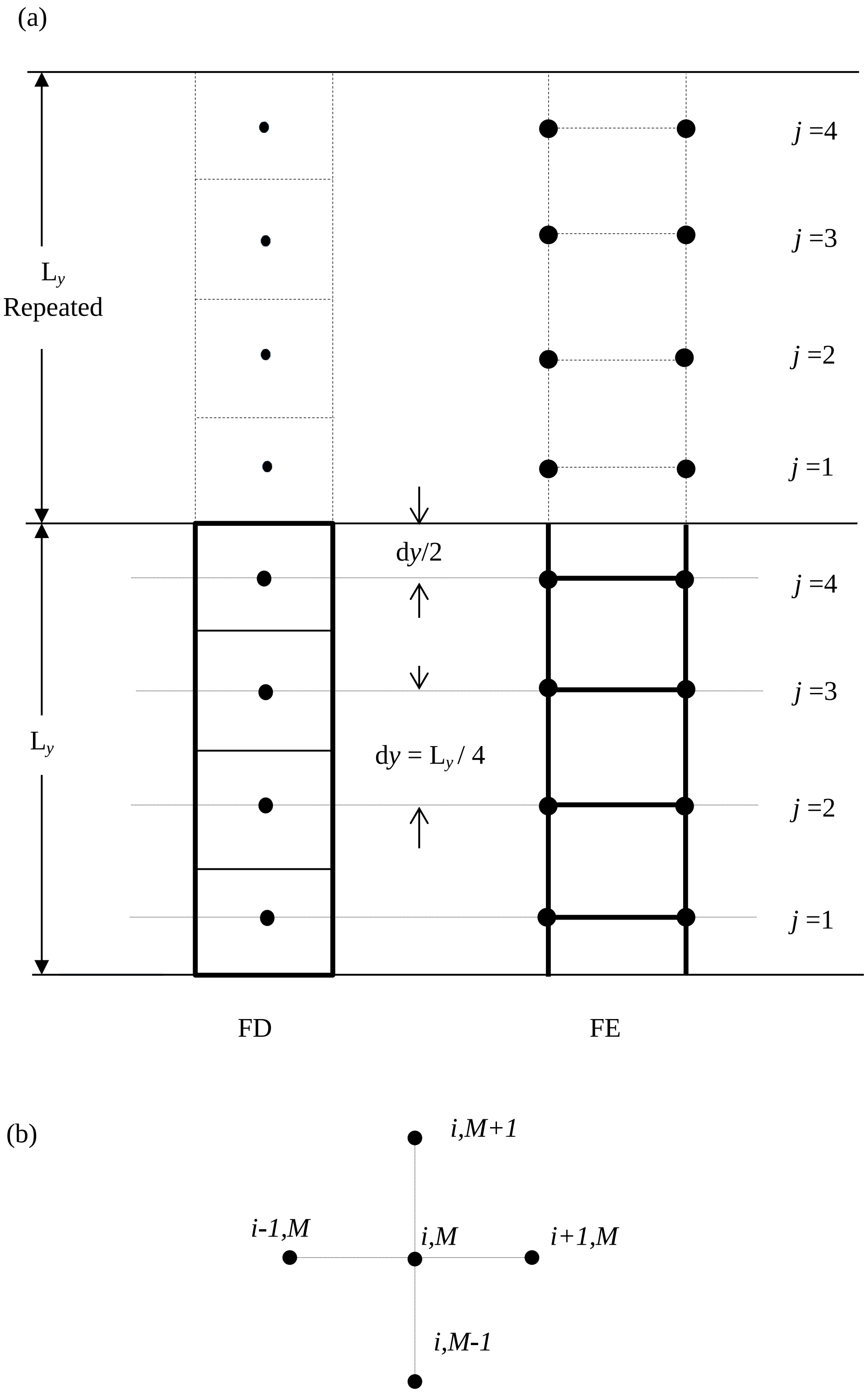

Figure 7.8: Discretization of the solution domain. (a) FEM vs FD (only one column of element/node is shown for each method) and (b) The four neighbour nodes of the general point (*i,M)*.

the node under consideration. This can be achieved by exploiting the nature of repetition of the FFT method where the same solution domain is repeated in both directions as stated above. In the last row ($j = M$) for example the four neighbouring nodes of the general point (i,M) are $(i+1,M)$, $(i-1, M)$, $(i, M+1)$ and $(i,M-1)$ as shown in Figure 7.8 (b) where i indicates the x position of the node and M represents the numbers of node rows in the y direction of the solution domain. The only node outside the solution domain is node $(i, M+1)$ and the nodal value at this node is in fact the value at node $(i,1)$ in the first row of the solution domain which can be used to evaluate the required derivative. Therefore, the second derivative at node (i,M) is now calculable for all i values.

A similar procedure can be used for the nodes that lie on the first row by using the nodal values from the *M*th row. Adopting this cycling method, the nodal values at the boundaries of the solution domain ensures continuity of flow at these boundaries. In the x direction, boundary conditions are applied at the nodes of the first and last columns of the solution domain.

For the FEM method a four node rectangular element is used with element integrations achieved with four Gauss points. The discretisation of this problem using FEM is more complicated in comparison with the FD method. The difficulty is related to the way of dealing with boundaries of the solution domain in the y direction. Each node in the grid has a contribution from four adjacent elements (except the boundary nodes at $i = 1$ and $i = N$). Therefore it is required to add contributions for the first and last rows of nodes in the y direction which come from the elements in the repeated domains. This can be done by adding one row of elements to the solution domain at each side of the boundaries of repetition in the *y* direction. The nodal values for these elements that are outside the solution domain are obtained from the cyclically equivalent nodes that are inside the solution domain. Care is necessary in adding two rows of elements as another contribution will be added not only to the nodes at the boundaries but to the rest of the nodes on the boundary elements and these contributions should be ignored. However, in the assembly procedure adding one row of elements at one of the repetition boundares is sufficient as it will add the contributions for both of the rows of nodes on the boundaries. Figure 7.9 illustrates this method where Figure 7.9 (a) shows the column of elements previously shown in Figure 7.8 (a) which consists of 4 elements only for the purpose of clarity. Regarding this column, the actual rows of elements inside the solution space considered in the EHL calculations are three (M-1) which is shown in Figure 7.9 (b). Each node on the rows j=2 and j=3 have contributions from two elements in this column which is the real case, while the nodes on rows j=1 and j=4 can get contributions from one element in this column. Therefore, it is necessary to add the required missing contributions to the nodes at the rows j=1 and j=4. This can be achieved by adding one row of elements at the upper boundary of the solution space as shown in Figure 7.9 (c). This means there will be an additional row of nodes at $j = 5$ ($j = M+1$), which physically represent the nodes at j=1 as the same nodal values of the solution space are repeated in both directions as explained previously. Now, the new number of elements considered in the EHL analysis is four (M). Adding this row of elements will not only ensure adding the required contributions to the nodes at j=4 but also to the nodes at row j=5 (which is equal to j=1).

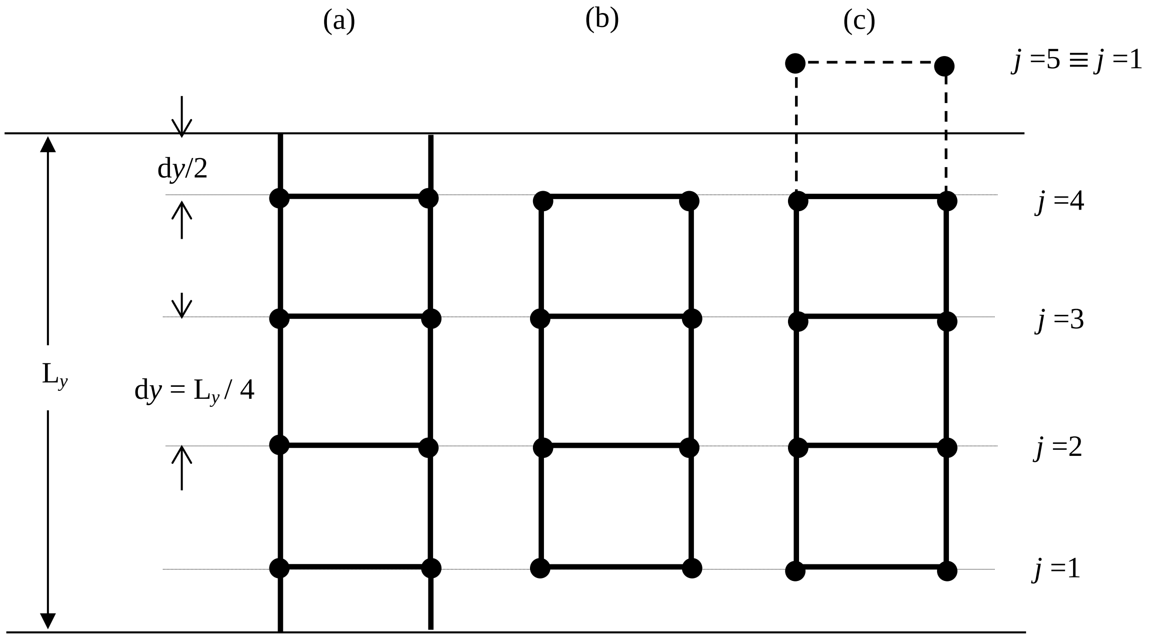

Figure 7.9: Dealing with boundaries in the FEM method**. (**a) Single column of elements in the solution space, (b) The actual number of elements for this column in the solution space and (c) Adding one row of elements (dashed line) at the upper boundary of the solution space

7.6 Selection of the roughness profile

The roughness orientation is taken to be the same as the grinding lines direction with respect to the line of contact as previously shown in Figure 7.4. Figure 7.10 (not to scale) illustrates schematically this orientation in the tangent plane, *xy*, at a position in the meshing cycle. The roughness lines for one tooth surface are shown in this figure for clarity. With the use of the FFT method only a small rectangular area is required to reflect the roughness features on the whole *xy* plane. A sample of this area which is shown by broken lines can be selected for this purpose. The rectangle dimensions are L_x and L_y in the *x* and *y* direction respectively. The required angle of roughness orientation can be obtained by changing the proportion of this rectangle as shown in Figure 7.11 which illustrates the way in which the roughness profile is extruded. Figure 7.11 (a) shows a schematic drawing of a roughness profile. The profile length is L_x and roughness data are illustrated by filled circles at seven positions separated by an equal step, Δ. Figure 7.11 (b) shows how the roughness profile on a single rectangle is extruded and connected to the corresponding profile on the adjacent repeated rectangles. Roughness at the first position (the relatively big circle) in one rectangle is always extruded at an angle θ to the y direction and connected to the same position number on the relevant repeated rectangle and so on for the other positions. Therefore, the angle of extrusion is given by:

$$\theta = \tan^{-1}(L_x + \Delta) / L_y$$

The length of the EHL solution domain in the y direction is L_y while its length in the x direction is not necessarily equal to L_x. Choosing different profile length values, L_x for the two surfaces will produce different extrusion angles. The procedure described above ensures the conservation of lubricant mass as it maintains the equality between the lubricant flows across the boundaries between the repeated domains in both directions. It is worth mentioning that the extruded lines are assumed as perfectly straight lines over the selected rectangular area defined by L_x and L_y as the deviation from a straight line is trivial if L_y is relatively small.

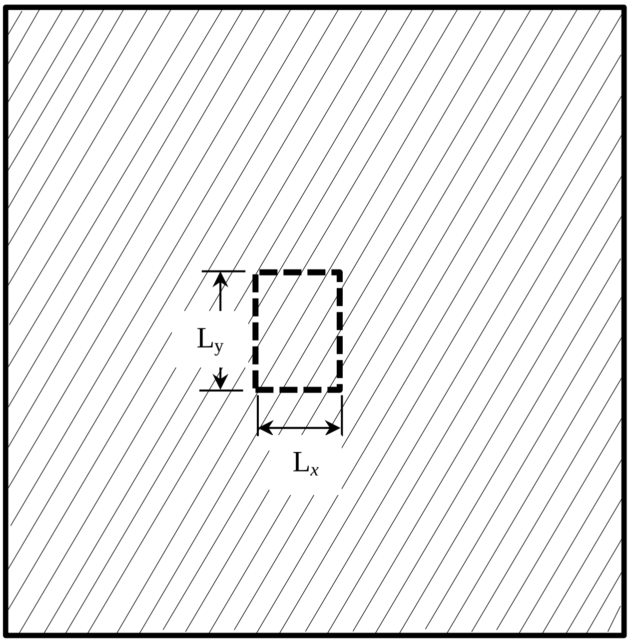

Figure 7.10: Schematic illustration for the roughness orientation in the tangent plane. Broken lines rectangle can be used to reflect the features of the whole plane.

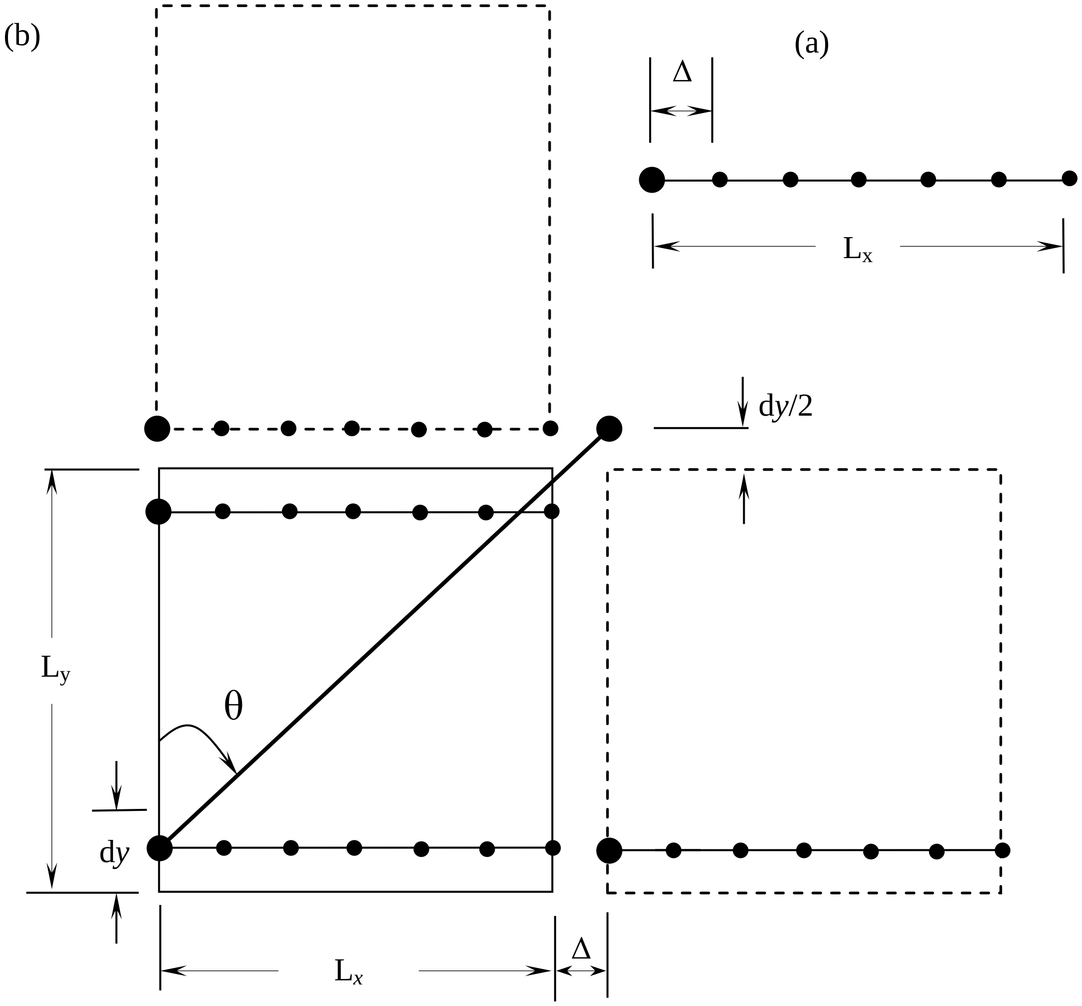

Figure 7.11: Roughness extrusion over the selected domain. (a) A selected profile of length L_x in the x direction and (b) Relation between the roughness features over the solution space and the repeated spaces.

Figure 7.12 shows two surface profiles which represent portions of a real measured profile taken from a tooth surface. The profile in Figure 7.12 (a) has a length of $L_x = 149$ μm while the one in Figure 7.12 (b) has a length of $L_x = 100$ μm. These profiles are repeated to provide long roughness profiles for the extruded analyses for any required length. For example, Figure 7.12(c) shows the profile $L_x = 149$ μm repeated over a distance of 5*a*. Using the method of extrusion described for these profiles over a distance of 1 mm in the *y* direction ($L_y = 1$ mm) will produce angles of extrusion of 8.5^o and 5.7^o for the long and short profiles, respectively. These angle values correspond to a position in the meshing cycle of $s = 5.75$ in Figure 7.4.

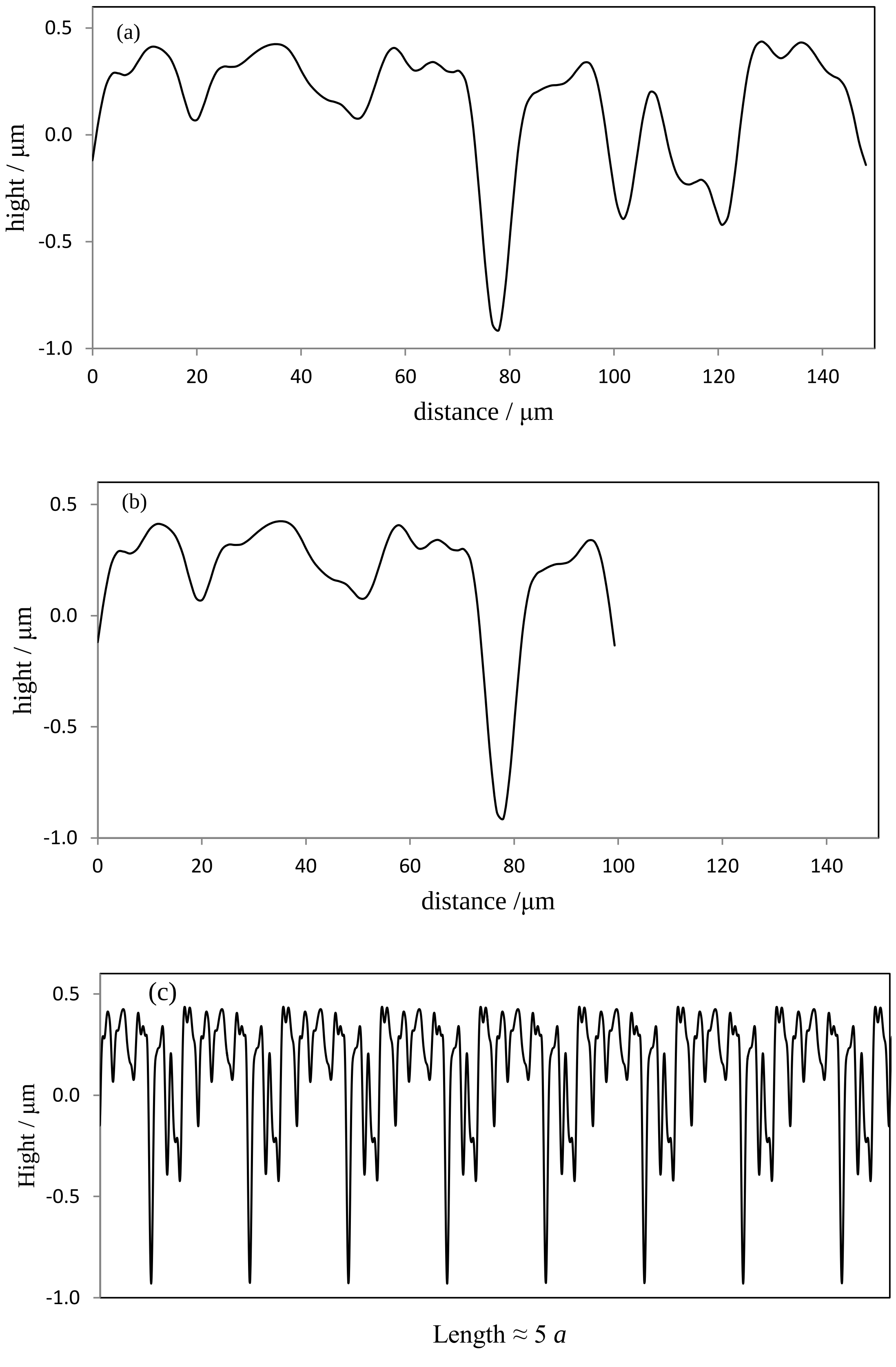

Figure 7.12: Real surface profile. (a) L_x = 149 µm , (b) L_x = 100 µm and (c) repeating of L_x = 149 µm profile over a 5*a* distance.

2D contours for the roughness features are shown in Figure 7.13. Figure 7.13 (a) shows the case for 8.5$^\mathrm{o}$ angle of extrusion and Figure 7.13 (b) shows a perfectly straight extrusion for the same profile (parallel to the *y* direction). The two profile portions shown in Figure 7.12, which can be extruded in *y* direction using any of the forms shown in Figure 7.13, are used in this chapter to investigate the effect of roughness orientation (relative to the entraining direction) on the EHL performance of helical gears.

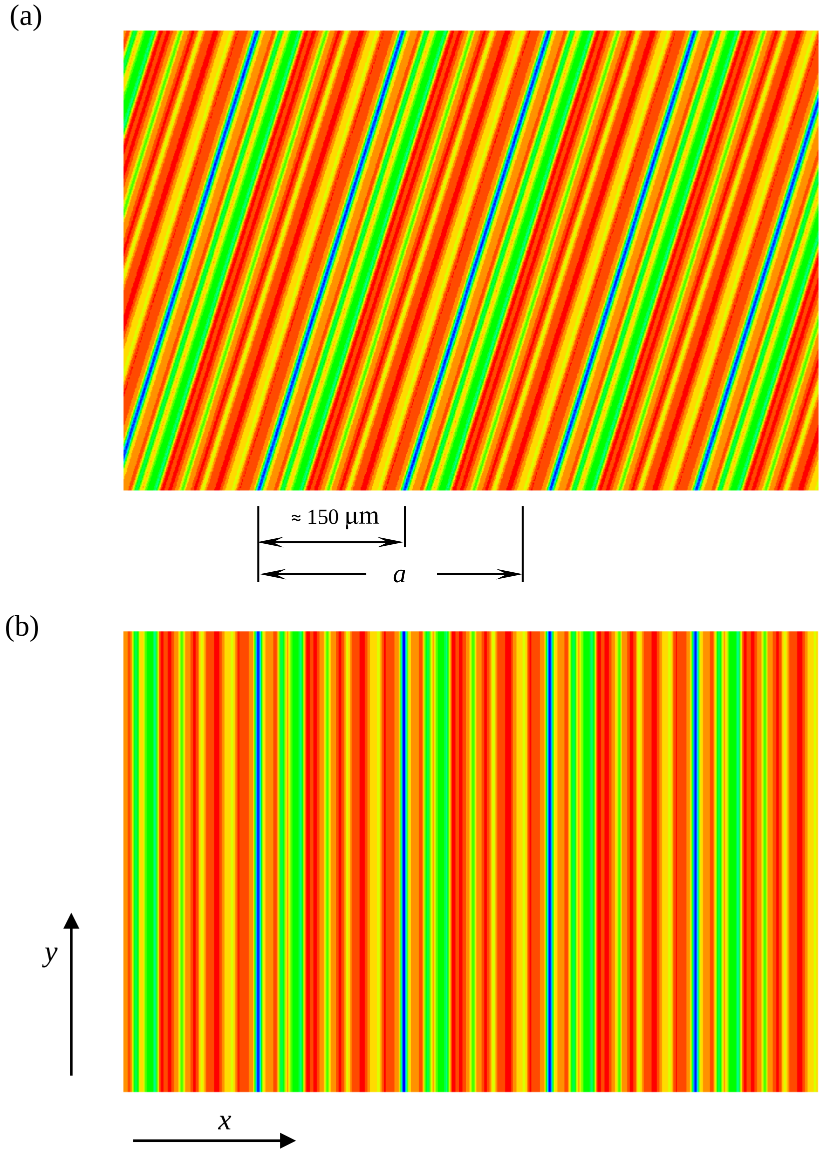

Figure 7.13: Forms of roughness features. (a) $\theta_\mathrm{P} = 8.5^\circ$ and (b) $\theta_\mathrm{P} = 0$.

7.6.1 3D line contact versus line contact results for rough surfaces.

The 3D results were previously validated against the corresponding line contact result for a smooth surface in section 7.4 which showed excellent agreement. In this section a similar comparison is also made using rough surfaces. The profile shown in Figure 7.14 was taken from disk testing carried out by Patching et al. (1995) is used for this comparison and has R_a value of 0.31 µm.

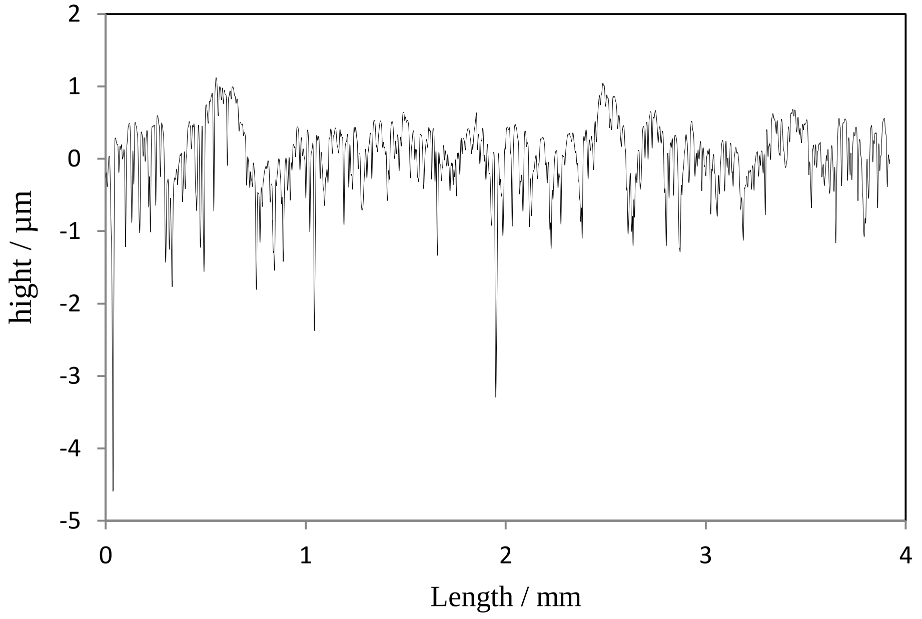

Figure 7.14: Real roughness profile of length 4 mm approximately.

In the 3D case this profile is applied to both surfaces and extruded parallel to the *y* axis over a distance of 1 mm (Load = 360 N). The two surfaces thus have the same roughness profile but they move at different speeds so that the surface asperities on the two surfaces move relative to each other. Figure 7.15 shows transient results for the 3D case at a particular time step. It can be seen in this figure that the calculated pressure distribution and film thickness are both perfectly extruded in the *y* direction. Figure 7.16 shows a section comparison at this time step with the corresponding transient line contact results. It can be seen that both the pressure distribution (Figure 7.16 (a)) and film thickness (Figure 7.16 (b)) coincide almost exactly for the two methods.

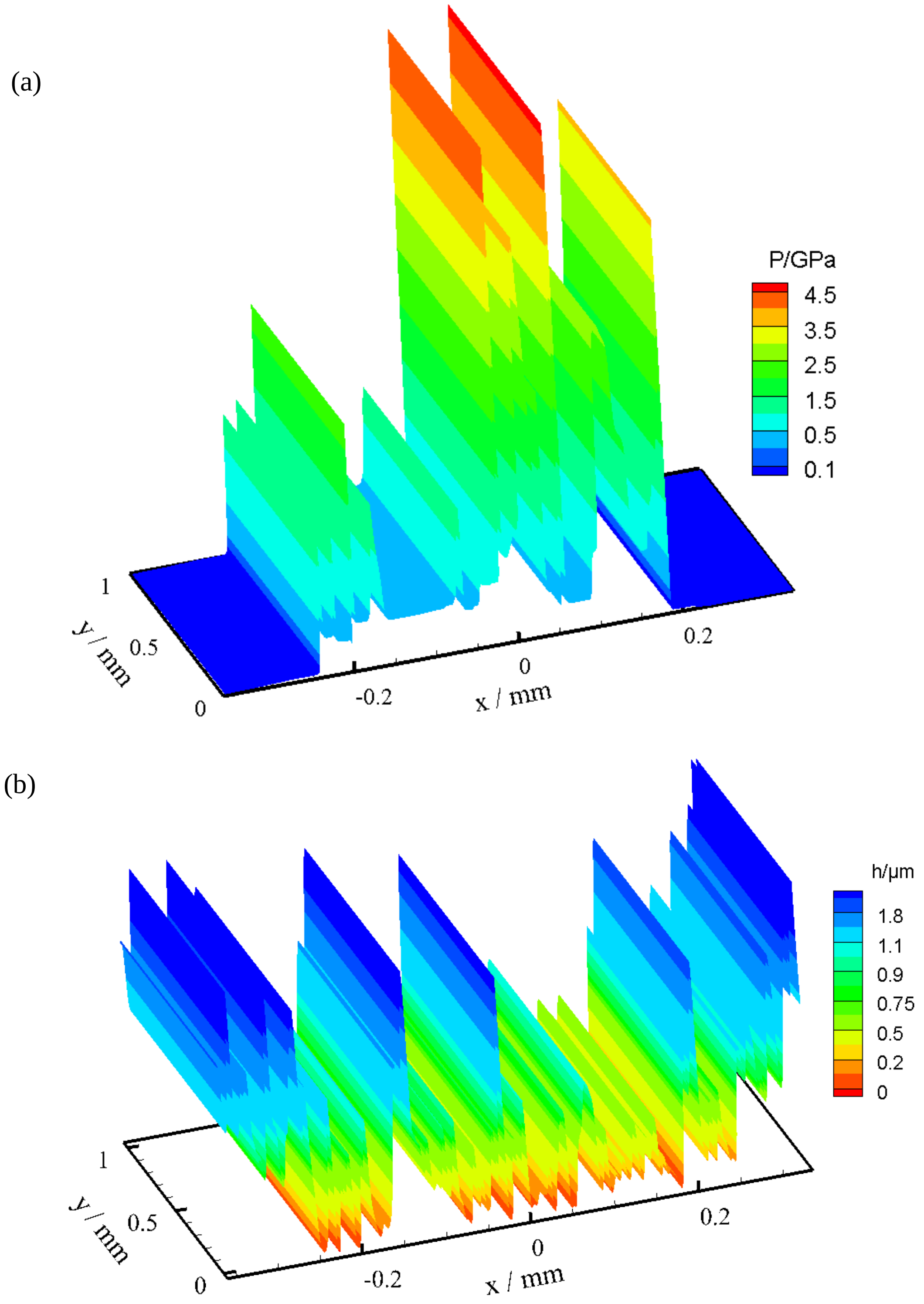

Figure 7.15: Transient results for the 3D line contact model at a particular time step. (a) Pressure and (b) Film thickness

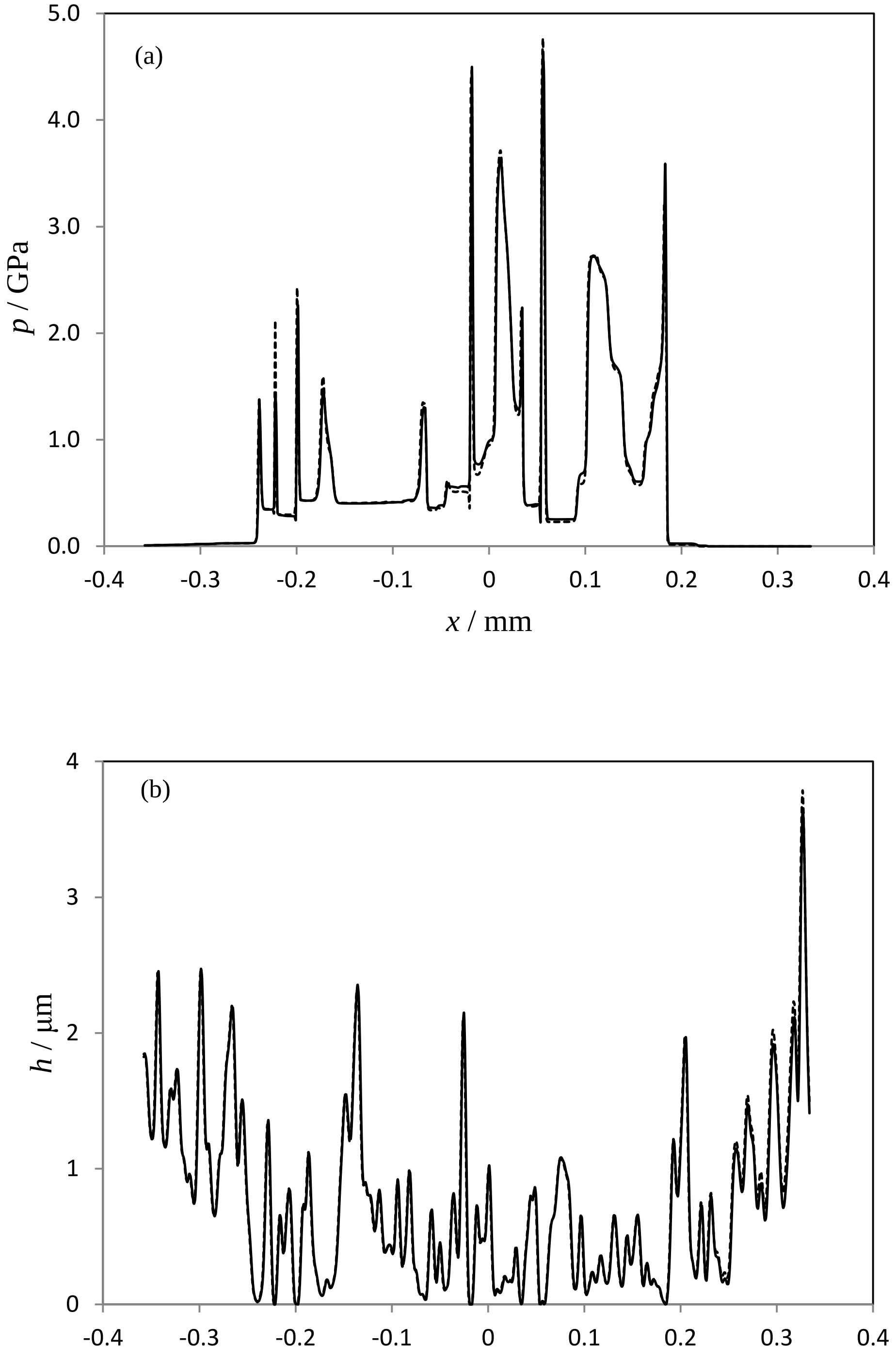

Figure 7.16: Section comparison between line contact (solid) and the 3D model results (dashed) shown in Figure 7.15. (a) Pressure and (b) Film thickness.

7.7 General results for the 3D Line contact model

The transient 3D line contact EHL analysis is carried out using the surface profiles shown previously in Figure 7.12. The extrusion width and length of profile are chosen such that both 3D surfaces repeat exactly over distance L_y. This means that the problem repeats exactly in the *y* direction and that there will be flow continuity at the transverse boundaries of the modelled section. Film thickness and pressure distribution results for a particular time step are shown in Figure 7.17. Due to the difference in the roughness orientation in the two surfaces (8.5^o and 5.7^o), their extruded roughness lines intersect with each other. These intersections initially concentrate the transmitted load on limited areas which produce high pressure spikes at those locations as shown in Figure 7.17 (a). This is not the case when the roughness profile is extruded in the direction parallel to *y* direction. In this situation the intersection between any two asperities acts over the whole L_y distance which increases the area that supports the transmitted load. Figure 7.17 (b) shows the film thickness variation in the solution domain where metal to metal contact ($h = 0$) is predicted at some points.

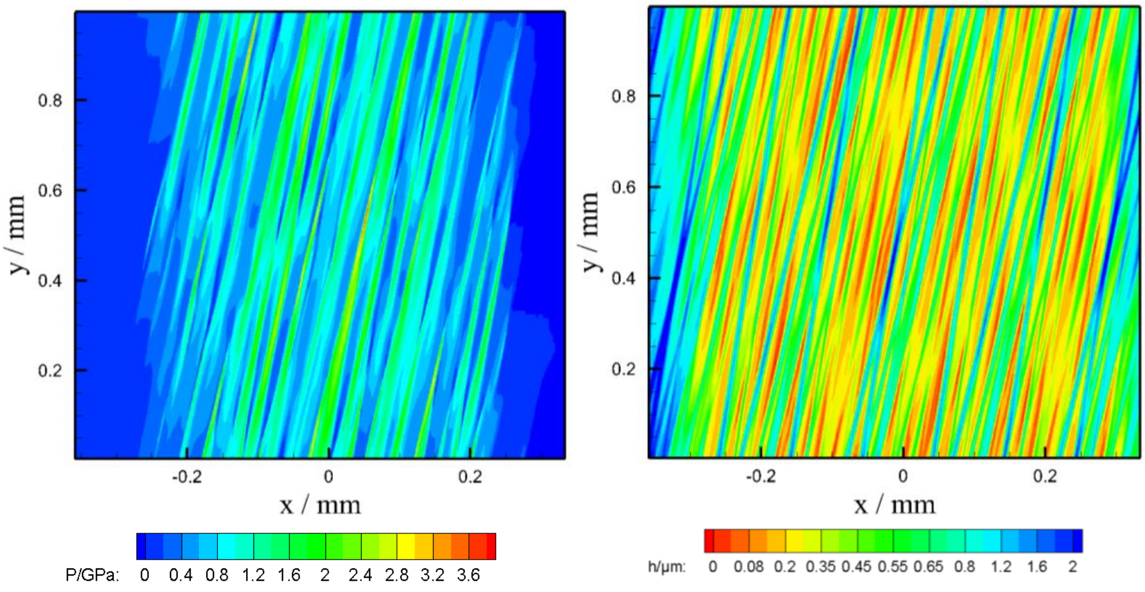

Figure 7.17: EHL results at a time step using the 3D line contact mode, pressure distribution (left) and film thickness (right).

7.7.1 Effect of number of elements in the *y* direction

In this section the effect of mesh density, M, in the y direction is examined. A length of 1 mm in the y direction is discretised to 32, 64, 128 and 256 elements. These numbers coincide with the power of two condition required for the FFT method. The number of nodes in the x direction is fixed to $\mathrm{a}/200$ in all cases as this number gives an element length that corresponds approximately to the spacing at which the roughness data are measured.

The solution starts from the steady state solution for smooth surfaces. The roughness profiles are then fed into the contact zone from the inlet boundary with the moving surfaces. The roughness is attenuated linearly by scaling with a factor that increases linearly from zero to unity over the leading Hertzian dimension of the roughness profile. The analysis becomes “fully rough” at the time when the attenuated parts of the profiles have travelled through the contact zone and reached the exit area where the lubricant film becomes cavitated. The transient analyses is carried out for 4488 time steps which represent the time for the slower surface to move through the calculation zone by a distance of $4a$ from the time at which the analysis becomes fully rough.

This transient problem is computationally demanding. The four different transverse resolution models had grids involving 800 x 32, 800 x 64, 800 x 128 and 800 x 256 nodes / mesh points. The calculations were carried out on an Intel Core i7-2600 CPU @ 3.40 GHz machine using the LINUX operating system with the code written in Fortran 90. The run times for these transient analyses were 1.5, 4, 9 and 21 hours respectively.

Figure 7.18 shows the variation of maximum pressure over this distance when the two roughness profiles are extruded at angles 8.5° and 5.7°. The maximum pressure value is constant at 0.95 GPa in the first 1250 time steps in all cases, which means in effect that M = 32 is sufficiently fine to carry out a 3D smooth EHL analysis. During these time steps the active profiles in the EHL analysis ($-a \le x \le a$) are still smooth. With the progress of roughness through the EHL solution domain, the effect of mesh density becomes more noticeable and the analysis becomes fully rough at time step 2888. It is clear that the M value has an effect on the maximum EHL pressure results when the two surfaces start to be fully rough. For example at time step 2500, the maximum pressure value changes from 3 GPa to 4 GPa when M changes from 32 to 256 elements, respectively. Disregarding the noise in the pressure values in the case of M = 128, it has the same trend as the case M = 256. The variation of the corresponding minimum film thickness values is not shown in this figure as metal to metal contact is always predicted under the operating conditions adopted in this analysis.

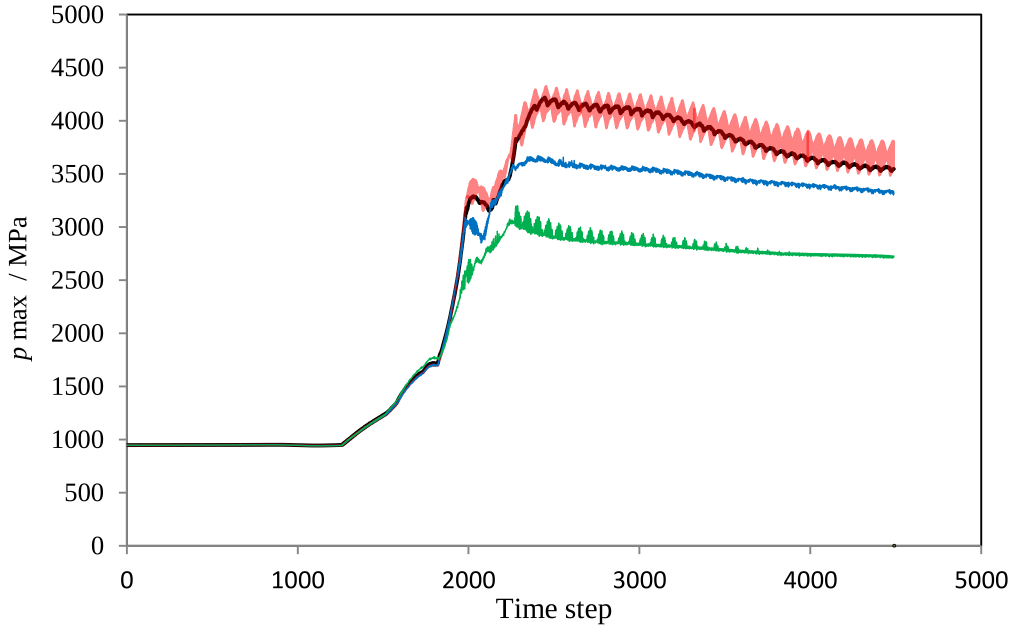

Figure 7.18: Variation of maximum pressure during transient analysis with M.
The two roughness profiles are extruded at angles 8.5° and 5.7°.
Green: M = 32, blue: M = 64, red: M = 128 and black: M =256

Further section comparisons are shown in Figures 7.19, 7.20 and 7.21. Figure 7.19 shows pressure distribution and film thickness at time step 4000. The comparison is made at the centre of the contact ($x = 0$) along the y direction. It can be seen that both film thickness and pressure distribution when $M = 128$ give good agreement with the case of $M = 256$. Figure 7.20 shows similar section comparison at $x = 0.075$ mm at time step 4480. This is the position of the maximum pressure value when $M = 128$ at this time step. Similarly, there is no significant difference between cases $M = 128$ and $M = 256$. The last comparison is carried out in the x direction at time step 4480 which is shown in Figure 7.21. Two cases are compared when $M = 128$ and 256 at the first row of nodes in the y direction. It can be seen that the results of the two cases coincide almost exactly. A similar analysis was also made for the case when the roughness profiles are extruded parallel to the y direction and is shown in Figure 7.22. Three cases were examined where $M = 32$, 64 and 128 elements. It can be seen that changing the M value has no effect on the maximum pressure behaviour. These comparisons lead to the conclusion that 128 elements in the y direction is sufficient to resolve the problem. The resolution in the x direction is 1.1886 μm, and for $M = 128$ the resolution in the y direction is about 8 μm.

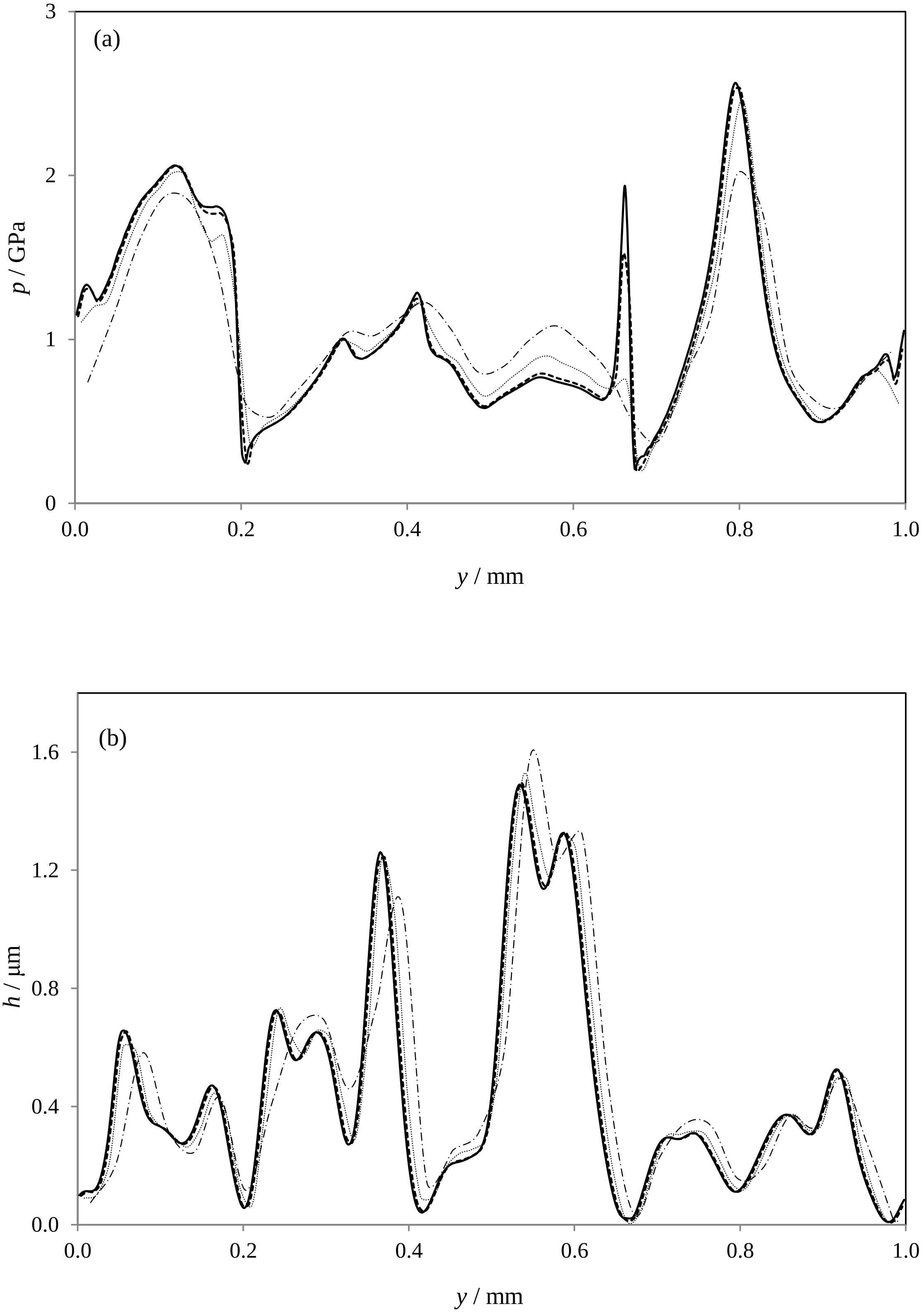

Figure 7.19: Transverse section showing comparison of pressure distribution (a) and film thickness (b) for time step 4000 at the centre of the contact (x = 0); - · - · M = 32 , …… M = 64, ----- M = 128 and —— M =256

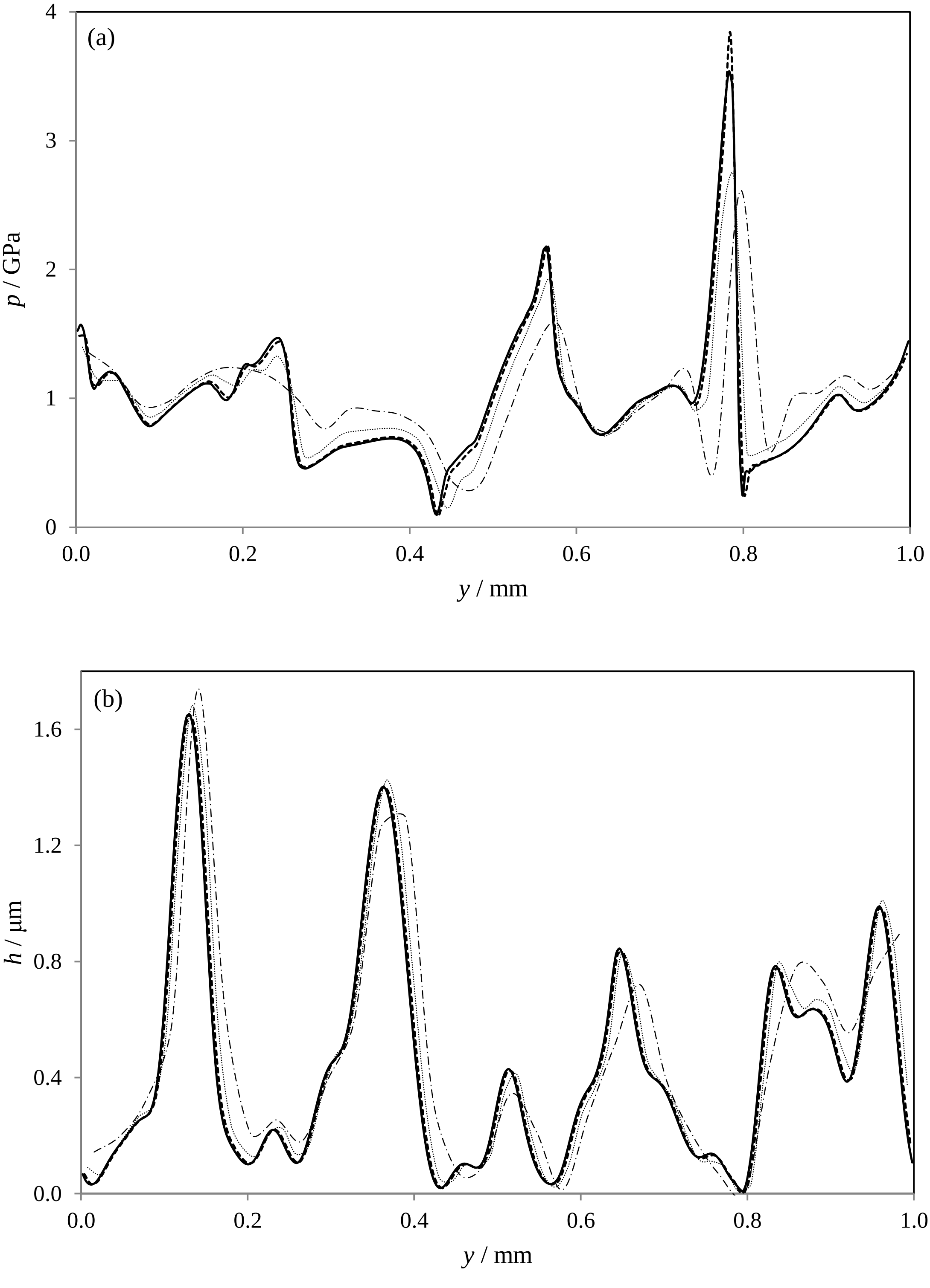

Figure 7.20: Transverse section showing comparison of pressure distribution (a) and film thickness (b) for time step 4480 at x = 0.075 mm; - . - . M = 32 , …… M = 64, ----- M = 128 and —— M =256

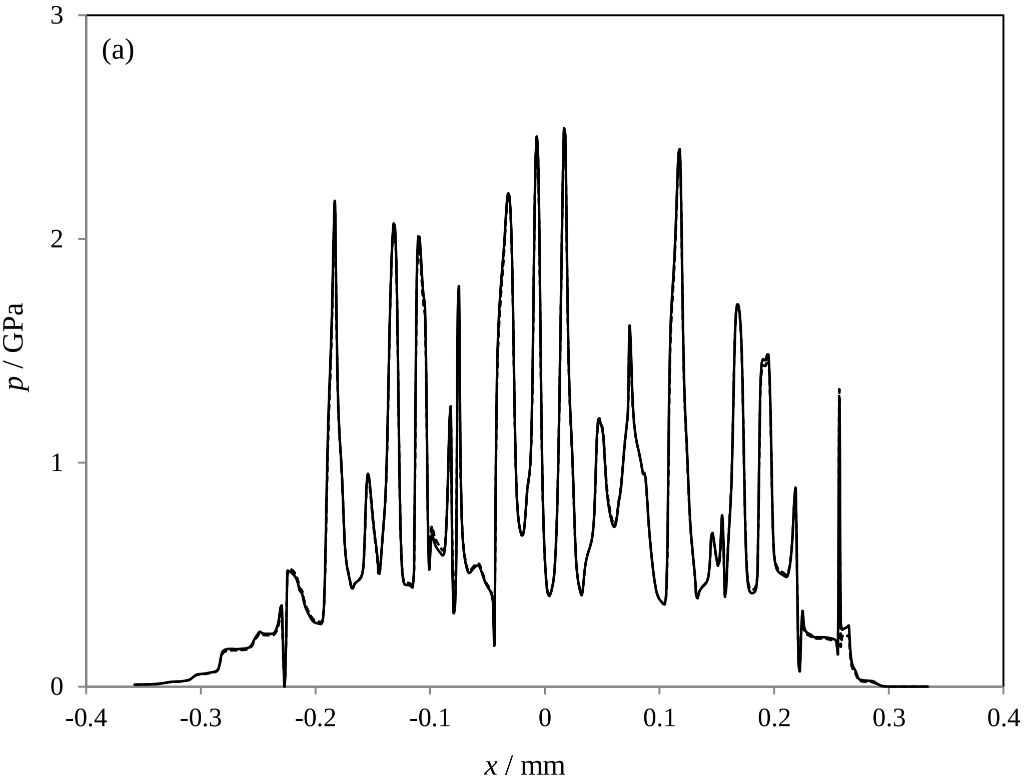

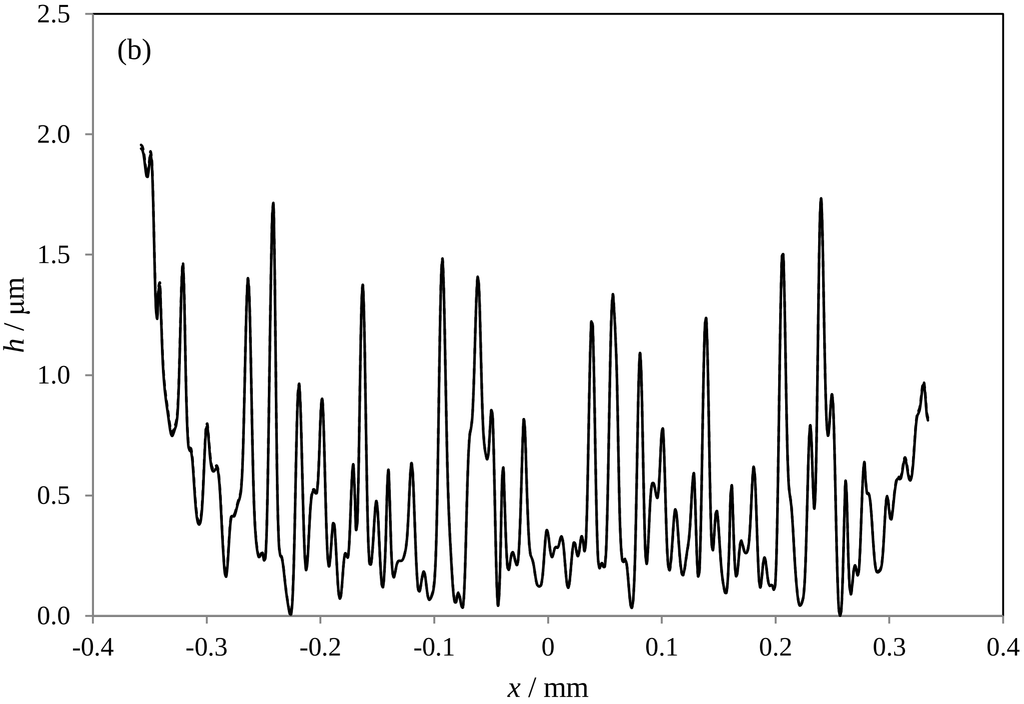

Figure 7.21: Entrainment direction section showing comparison of pressure distribution (a) and film thickness (b). Results for time step 4480 at the first row of nodes (j = 1). ---- M =128 and .... M =256

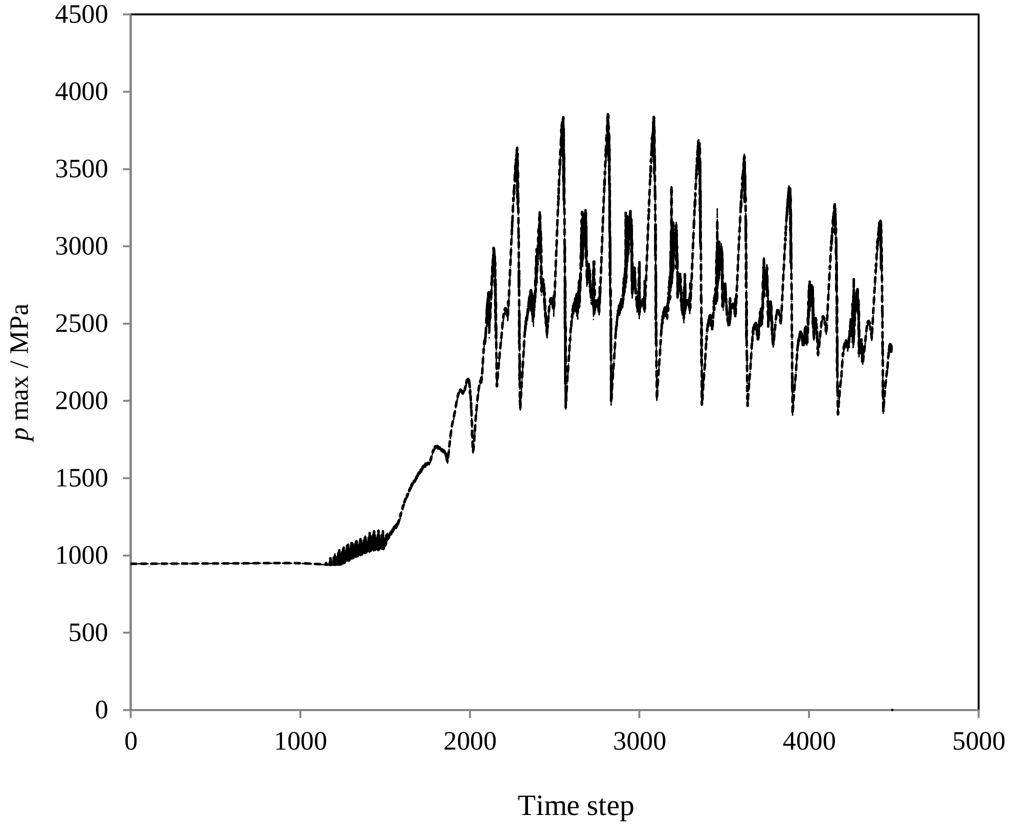

Figure 7.22: Variation of maximum pressure during transient analysis when the two roughness profiles are extruded parallel to the *y*-direction.
. -.-.- $M = 32$, ... $M = 64$, ---- $M = 128$

7.7.2 Comparison between FEM and FD methods.

Figure 7.23 compares the EHL results using the finite element and finite difference methods (central difference). The comparison is carried out at time step 4000 and results at the first row of nodes ($j = 1$) are shown. The roughness profiles are extruded at angles of 8.5^o and 5.7^o for the fast and slow surfaces, respectively. In general the two methods give the same behaviour for the calculated pressure distribution and the FEM gives less aggressive pressure spikes as shown in Figure 7.23 (a). Film thickness variation is illustrated in Figure 7.23 (b) and shows good agreement between the two methods.

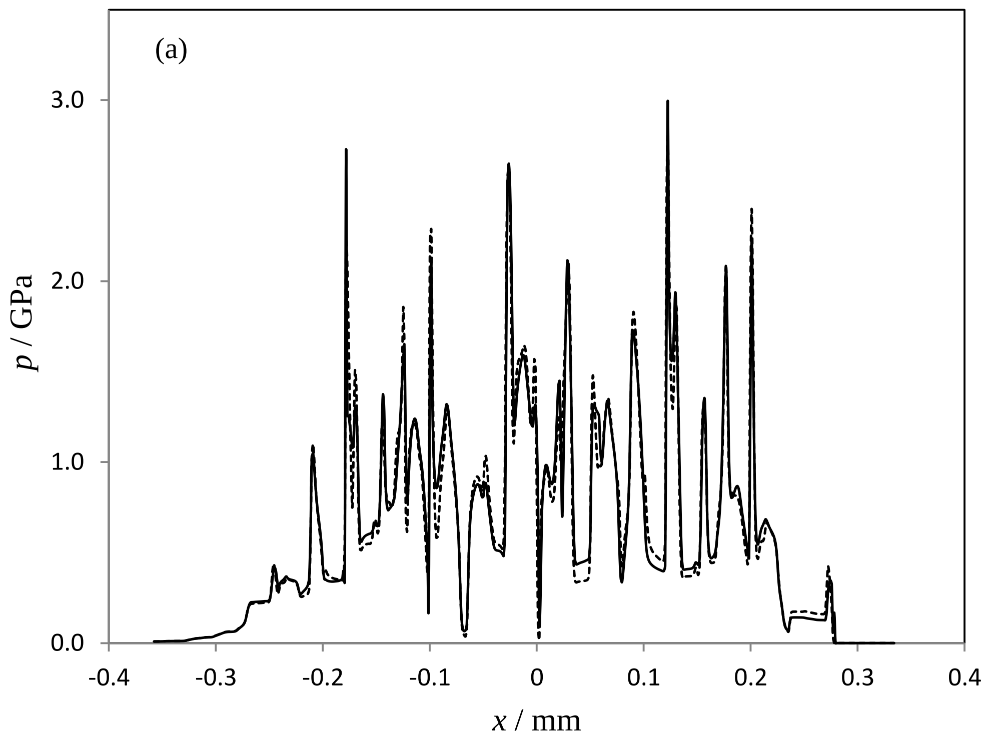

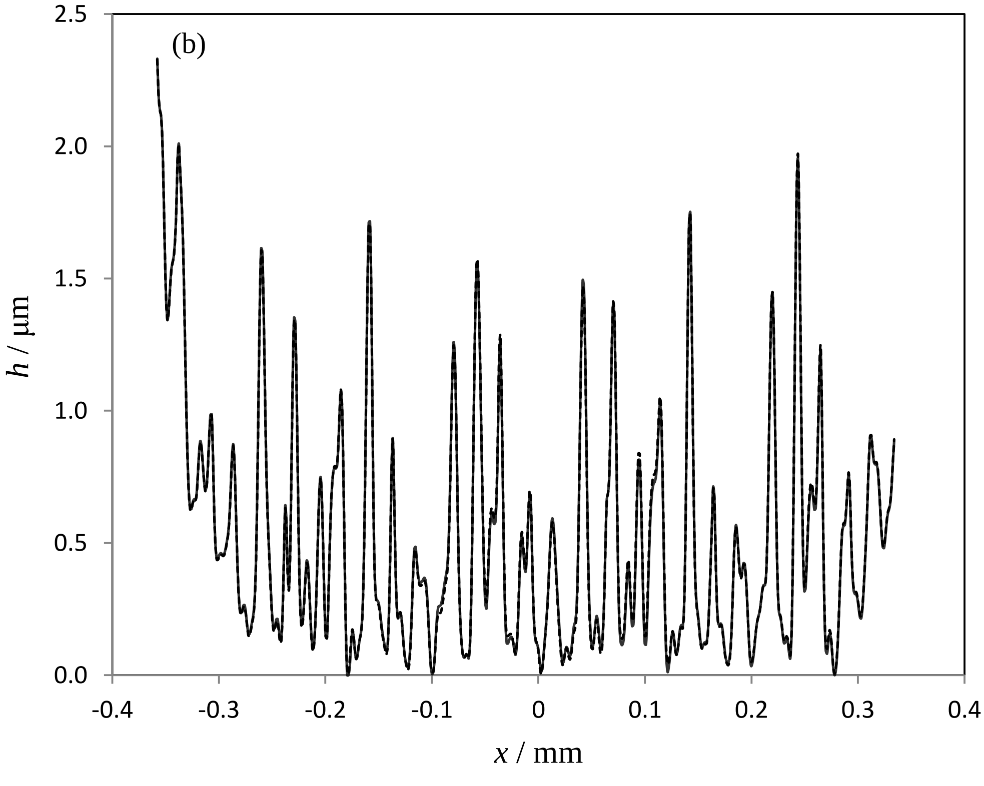

Figure 7.23: Comparison between FEM (solid) and FD (dashed) method at time step 4000. Results are shown at the first row of nodes. The roughness profiles are extruded at angles of 8.5^{o} and 5.7^{o} . (a) Pressure and (b) Film thickness

7.7.3 Effect of roughness orientation on the EHL results

Figure 7.24 compares the transient EHL analysis results for two cases. The roughness profiles in the first case are extruded at angles of 8.5^o and 5.7^o with the *y* direction while the same roughness profiles are extruded parallel to the *y* axis in the second case. The profiles used in these analyses are those shown in Figure 7.12. Figure 7.24 (a) shows that the way in which the roughness profile is extruded significantly affects the maximum pressure value at each time step. The case of “crossing” extrusion produces much higher pressure values, and at some time steps the maximum pressure value for this case reaches twice the value predicted in the straight extrusion case. A similar important difference can also be seen in the comparison of film thickness variation during the transient analyses that are shown in Figure 7.24 (b). For the crossing extrusion case metal to metal contact is predicted in each time step following time step 1772**.** On the other hand, for the straight extrusion case a thin layer of lubricant is generated at a significant number of time steps.

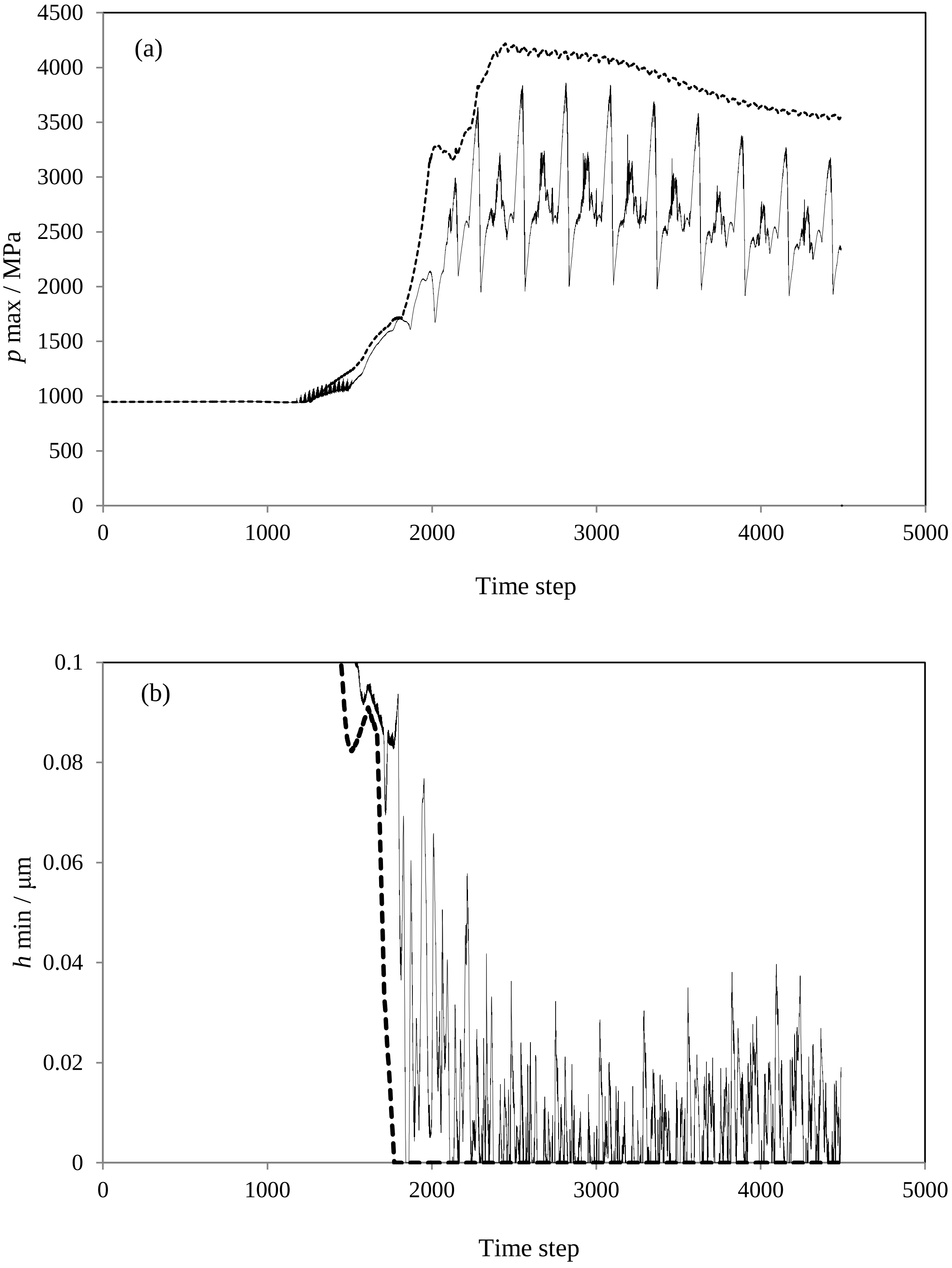

Figure 7.24: Transient EHL comparison between straight (solid) and with angle (dashed) extrusion of the roughness. (a) Pressure and (b) Film thickness

7.8 Effect of surface velocity

The effect of surface velocities on the EHL results is investigated in this section. The profiles shown in Figure 7.12 are used in this analysis which were extruded parallel and at an angle with the *y* direction as previously shown in Figure 7.13. The mean entrainment velocity for the results shown in section 7.7 (where the surface profiles were also those shown in Figure 7.12) was $\bar{u}$ = 6.71 m/s. These results are compared with the corresponding EHL results for the cases when the mean entrainment velocities are $2\bar{u}$ and $5\bar{u}$. The comparison is shown in Figures 7.25 and 7.26. Figure 7.25 shows the maximum pressure variation throughout the transient analysis for the three entrainment velocities for both straight and crossed extrusion of the surface roughness. This figure shows the results after time step 1000 as the surface before this time step (and even after short period of time after this time step) are still smooth as the roughness profiles are attenuated as they enter the contact zone. The crossed extrusion of the roughness always produces higher values of maximum pressure in the three cases compared with the straight extrusion cases. In the crossed extrusion situation, the case when the entrainment velocity is $5\bar{u}$ shows the lowest pressure levels, which are less than 1.5 GPa in comparison with about 2.5 GPa and 4.2 GPa for the $2\bar{u}$ and $\bar{u}$ cases, respectively. The corresponding minimum film thickness variations are shown in Figure 7.26. Straight extrusion of the roughness gives higher minimum film thickness in all compared cases. In the cases when the entrainment velocity is $\bar{u}$ and $2\bar{u}$, metal to metal contact is predicted during the transient analysis, while in the $5\bar{u}$ case, the minimum film thickness is always greater than approximately 0.2 μm.

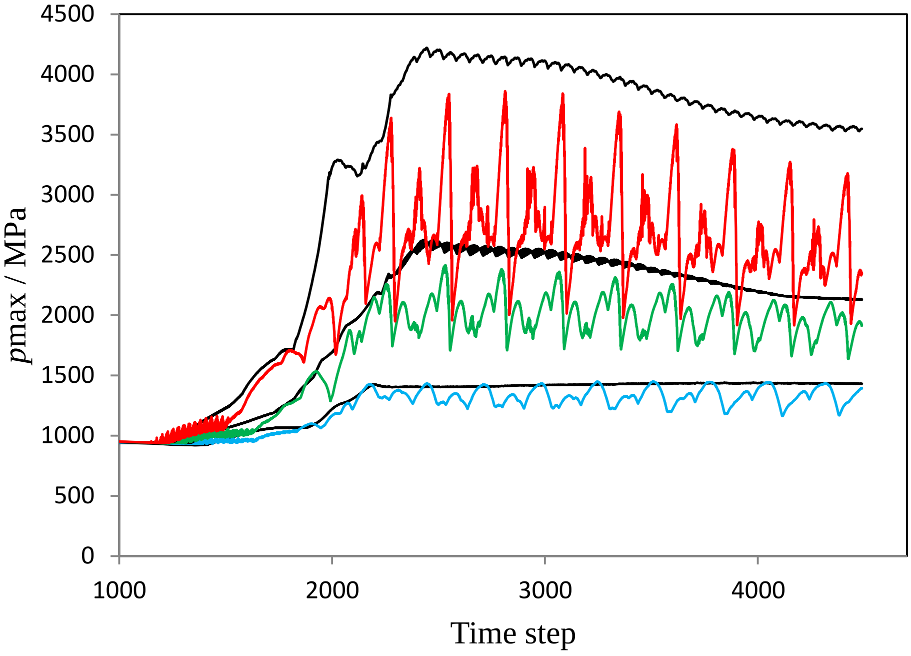

Figure 7.25: Variation of maximum pressure throughout a transient analysis for three entrainment velocities. Crossed extrusion result shown in black curves in ascending order from $5\bar{u}$ (lowest), $2\bar{u}$ to $\bar{u}$ (highest), respectively. The straight extrusion results are: Blue: $5\bar{u}$, Green: $2\bar{u}$ and Red: $\bar{u}$

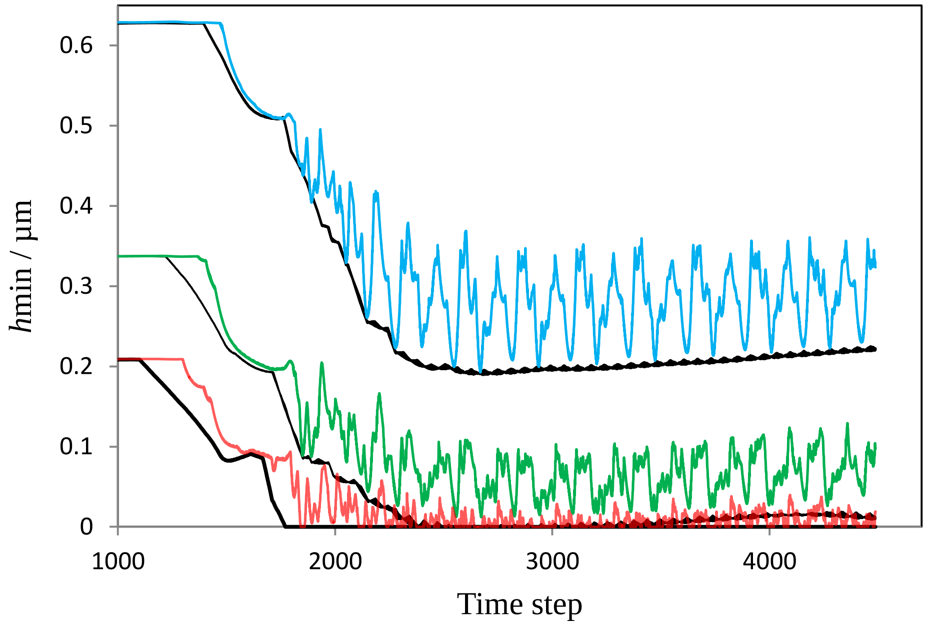

Figure 7.26: Variation of minimum film thickness throughout transient analysis for three entrainment velocities. Crossed extrusion result shown in black curves in ascending order from $\bar{u}$ (lowest), $2\bar{u}$ to $5\bar{u}$ (highest), respectively. The straight extrusion results are: Blue: $5\bar{u}$, Green: $2\bar{u}$ and Red: $\bar{u}$

7.9 Statistical analyses

In this section a statistical analysis is carried out based on EHL results for the straight and crossed extrusion of the roughness profiles. Three different cases of the 3D surface roughness are used in this comparison under same entrainment velocity, slide/roll ratio and input load ($\bar{u}$ = 6.71 m/s , ζ = 0.3632 and load =360 N). The profiles in the first case (case A) are those previously shown in Figure 7.12, and the profiles for the second case (case B) and third case (case C) are shown in Figures 7.27 and 7.28, respectively. For the crossed extrusion, profiles for the fast and slow surfaces in cases A and B are extruded at 8.5^{o} and 5.7^{o} respectively while those in case C are extruded at 6.5^{o} and 7.5^{o}. The profile used for cases A and B are taken from different parts of the full profile shown in Figure 7.14. Comparisons of the results for cases A and B is therefore shows differences due to the roughness features for the same extrusion angles. The profile used for case C are taken from the same part of the full profile, with differing lengths, and can be seen to have shared roughness features. Theses comparisons of the results for cases A and C shows differences that are principally due to differences in the extrusion angles and thus in the *s* value. The slide roll ratio used for case C corresponded to the same *s* value.

The statistical results presented in this section are calculated at mesh points in the corresponding Hertzian zone over the last 1600 time steps of the analysis where both surfaces are fully rough. Figure 7.29 shows comparisons between the cumulative distribution function of film thickness between straight and crossed extrusion for cases A, B and C. It can be seen that the results of the crossed extrusion are, in all cases, relatively skewed to the left. This means that the crossed extrusion of roughness tends to generate lower film thickness levels, as well as the higher levels of contact seen in previous sections.

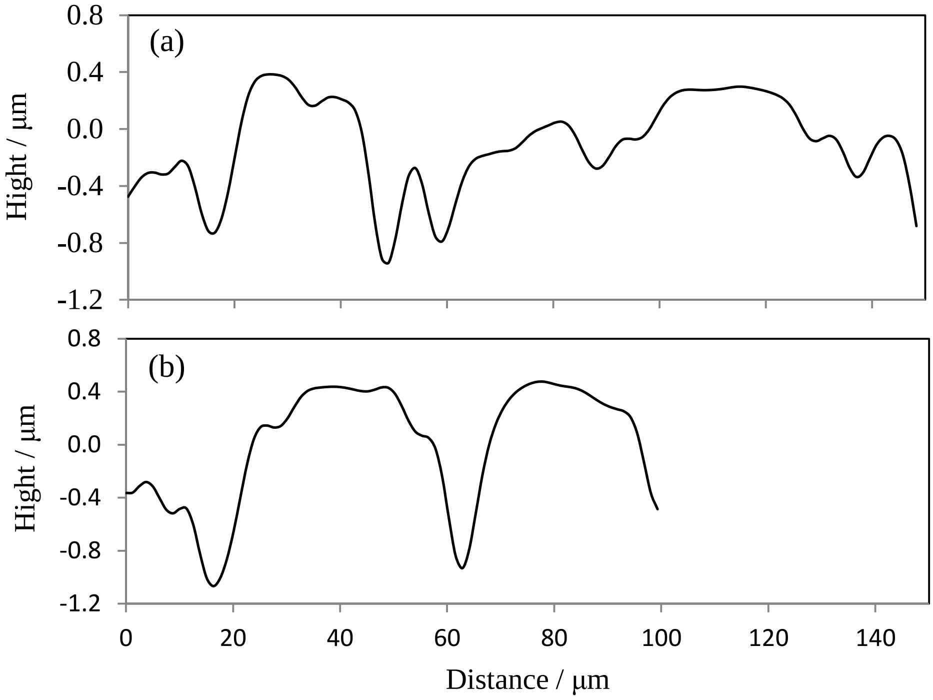

Figure 7.27: Real surface profile of case B. (a) $L_x = 149$ µm and (b) $L_x = 100$ µm

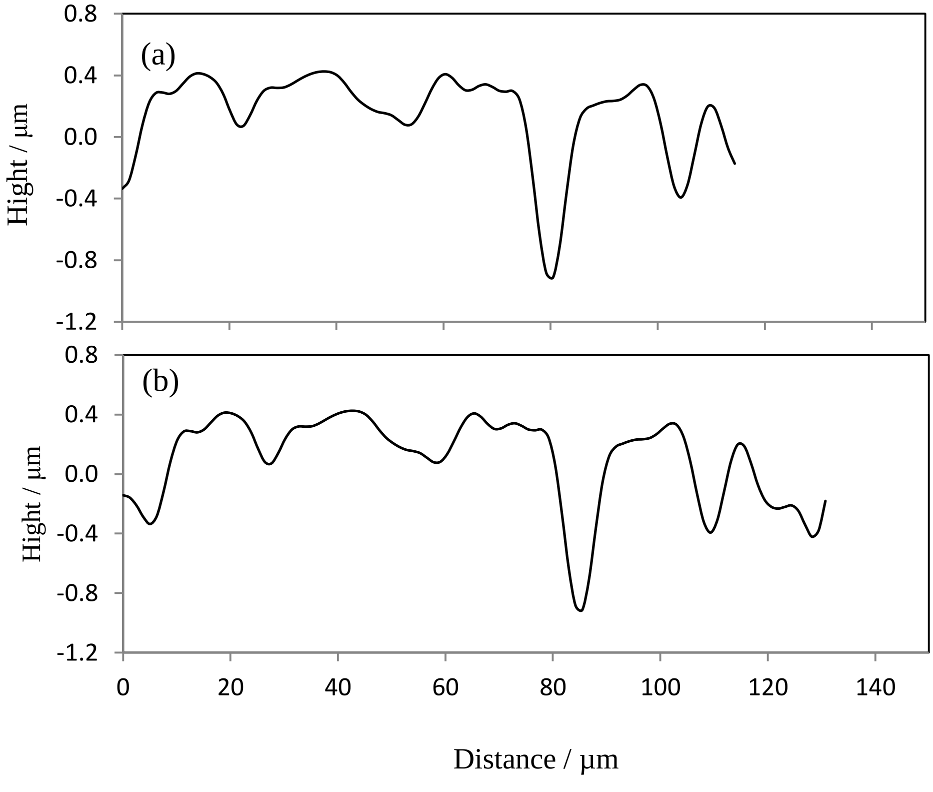

Figure 7.28: Real surface profile of case C. (a) $L_x = 114$ µm and (b) $L_x = 131$ µm

A more detailed film thickness comparison between the two types of extrusion is shown in Figure 7.30 for the three cases. The figure shows frequency distributions (histograms) for the film thickness values that are below 25 nm. It can be seen in Figure 7.30 (a), which shows the results of case A, that metal to metal contact occurs at 128 nodes for the crossing extrusion which represents three times the corresponding result for the straight extrusion. The corresponding results for case B are 318 to 109 contact points (3:1 approximately) which is shown in Figure 7.30 (b). The corresponding results of case C show less difference between the number of contact points between the two methods of extrusion (284/217≈ 1.3:1) as shown in Figure 7.30 (c). This means the angle of extrusion as well as the difference between the angles of extrusion of the two surfaces has an effect on the contact behaviour where $\Delta\theta = 2.8^{o}$ in case A and B while $\Delta\theta = 1.0^{o}$ in case C.

The comparison between the cumulative pressure distribution functions of the two methods of extrusion for the three cases is shown in Figure 7.31. This figure shows that in all cases the crossing extrusion tends to generate higher extreme pressure values.

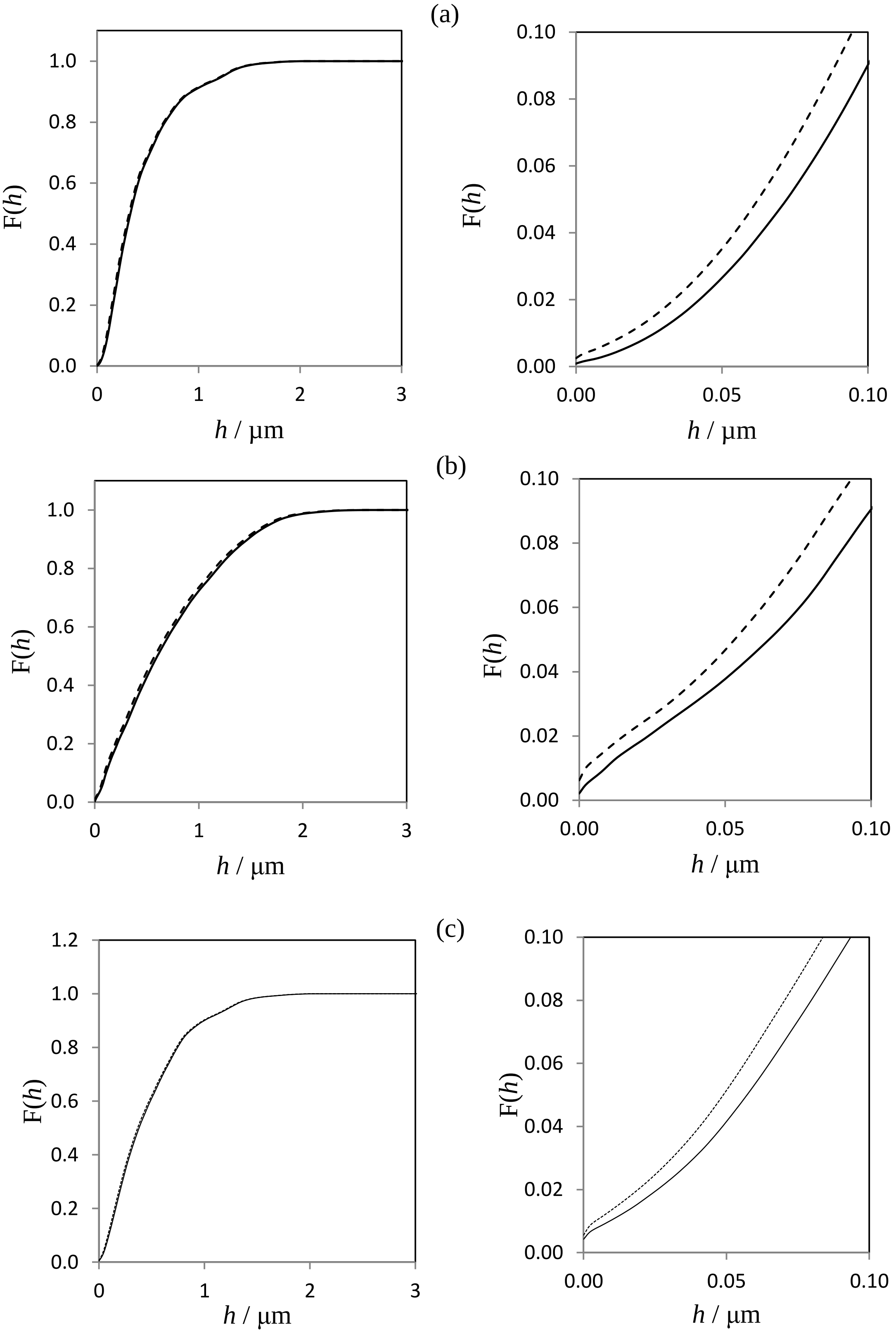

Figure 7.29: Comparison between cumulative film thickness distribution functions (F(*h*)) of straight (solid) and crossed (dashed) extrusion. (a) case A, (b) case B and (c) case C. Left and right figures show the same data but to different scales.

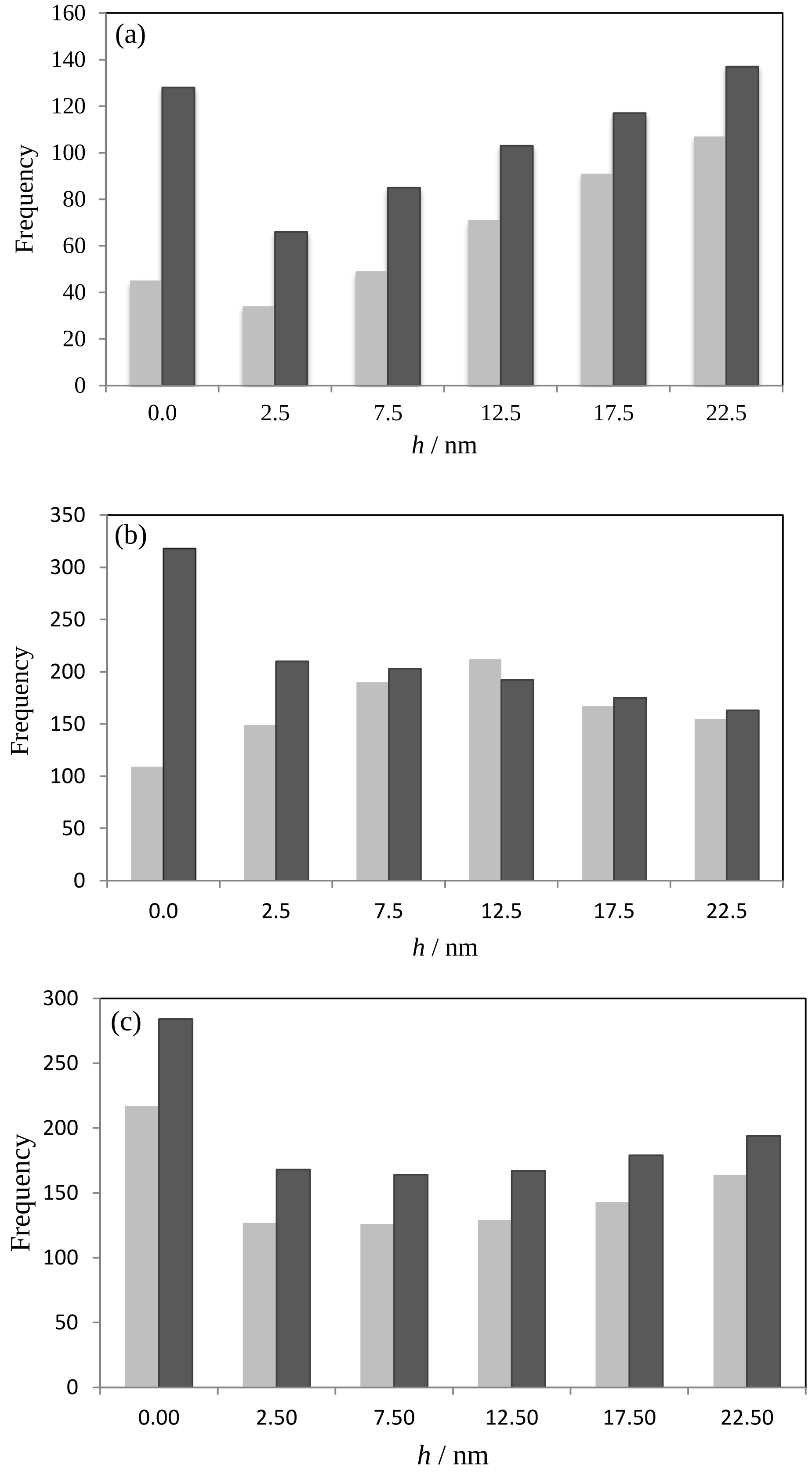

Figure 7.30: Statistical analyses for the transient EHL results. Frequency of film thickness values at 0-25 nm range for straight (light) and crossed (dark) extrusion. (a) case A, (b) case B and (c) case C

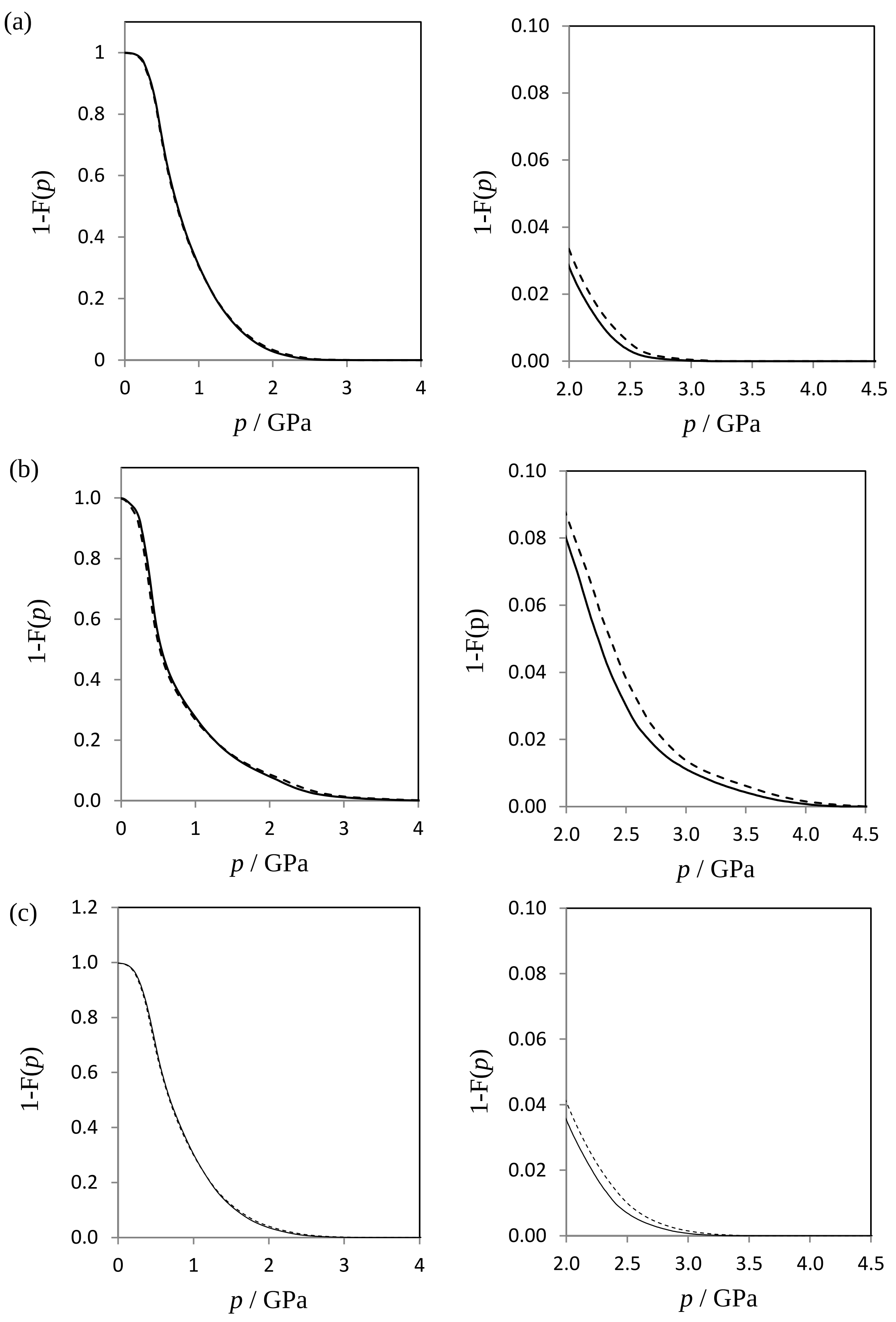

Figure 7.31: Comparison between cumulative pressure distribution function (F(*p*)) of straight (solid) and crossed (dashed) extrusion. (a) case A, (b) case B and (c) case C . Left and right figures show the same data but to different scales.

7.10 Comparison between cyclic and no-flow boundary conditions

The 3D line contact model presented in the current chapter deals with the boundary between the solution space and its repeats in the transverse direction (*y*) on the basis of cyclic boundary conditions. This approach represents the actual physical meaning of the repeated solution space as explained in section 7.6. Ren et al. (2009) also used a 3D line contact model to solve the mixed EHL problem but without using the concept of cycling the boundary conditions. Instead, their model assumes that no flow crosses the boundaries of the solution space in the *y* direction ($\partial p / \partial y = 0$). In this section the terminology used to denote these two methods are '*cyclic*' and '*no-flow*', respectively.

In this section detailed comparisons between these two methods of handling the boundary conditions are made. Three cases of roughness profile (crossed extrusion) are used in the comparisons. These are case A and case B as illustrated in section 7.9, and another further case (case D) which has the same profiles of case A but with an entrainment velocity equal to five times the entrainment velocity used in case A. The comparisons for each case are made at time steps 3600, 4000 and 4400. The 400 time step increment between these selected time steps corresponds to the fast surface moving a distance of 2*a* (a complete Hertzian contact width).

Figure 7.32 shows an example for a comparison between the EHL results using cyclic and no-flow methods for case A at time step 4000. Figure 7.32 (a) shows the pressure contours while Figure 7.32 (b) shows the film thickness contours. This figure does not show significant differences between the compared contours, but sections at the boundaries ($y \approx 0$ and $y \approx 1$ mm) and at the centre of the contact ($x = 0$ and $y = 0.5$ mm) at this time step and at time step 3600 and 4400 give a clear view of the differences between the two methods.

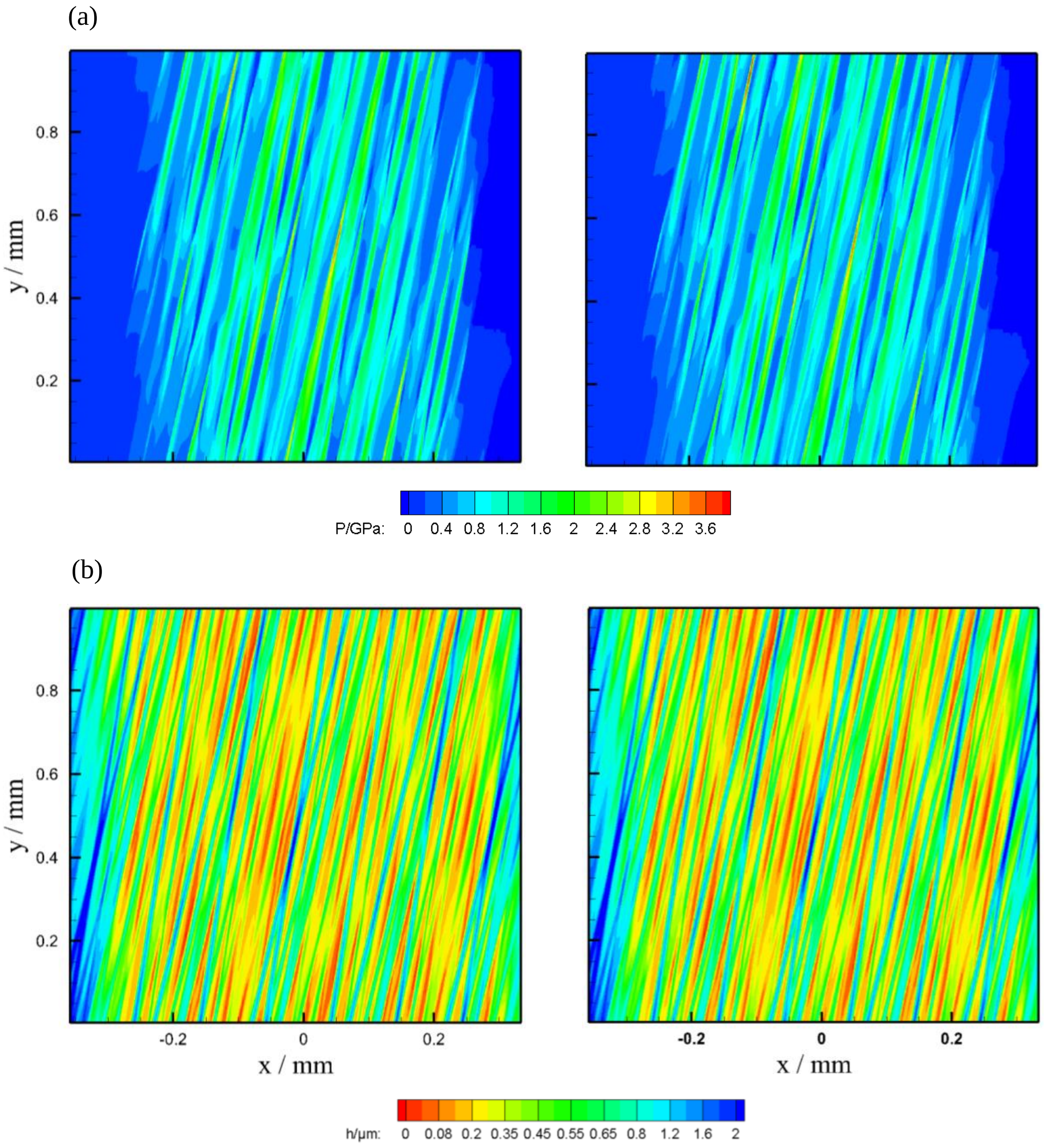

Figure 7.32: Comparison between the EHL results using cyclic (left) and no-flow (right) methods for case A at time step 4000. (a): pressure and (b): film thickness

7.10.1 Case A

Figure 7.33 shows section comparison of pressure and film thickness between the cyclic and no-flow methods at $x = 0$ at the three selected time steps (3600, 4000 and 4400). It can be seen that in all three time steps there are differences between the compared values near the boundaries $y = 0$ and $y = 1$. These differences can be seen over a distance of approximately 10% of L_y from each side while the two methods give approximately similar results over the remaining 80% distance (i.e. far from the two edges). This can be seen clearly in the sectional comparison at y = 0.5 mm which is shown in Figure 7.34 at the three time steps. The results of the two methods coincide with each other in this comparison.

An example of the difference between the results of the two methods at the boundary $y \approx 1$ mm of case A at time step 4000 is shown in Figure 7.35. Figure 7.35 (a) compares the pressure distributions and Figures 7.35 (b) and (c) show film thickness comparison at different scales for clarity. The difference between the two methods at the boundaries ($y \approx 0$ and $y \approx 1$) is further investigated at the three time steps as shown in Figure 7.36. In this figure the differences $\Delta p = p_{\text{cyclic}} - p_{\text{no-flow}}$ and $\Delta h = h_{\text{cyclic}} - h_{\text{no-flow}}$ are shown at these boundaries for the three time steps. This figure shows how the difference in the pressure can exceed 1.0 GPa at some positions. This difference represents about 25% of the maximum pressure value calculated in the transient analyses of case A. Also the film thickness differences reach a relatively high value of about 0.14 µm at some positions.

These comparisons illustrate the effect of allowing transverse flow at the boundary in that where significant differences occur they are opposite in sign at the $y \approx 0$ and $y \approx 1$ boundaries. This indicates that when cross-boundary flow is correctly incorporated in the analysis, significant transverse pressure gradients develop at the boundary. These are associated with transverse flows that clearly influence the results. This can be deduced from the anticorrelation between the pressure and film thickness differences in each trace. As far as elastic deflection is concerned an increase in pressure generally results in an increase in film thickness, but in these comparisons the opposite occurs.

This indicates that significant cross boundary flow is occurring driven by the transverse pressure gradient.

7.10.2 Cases B and D

The corresponding comparisons for the results of case B are shown in Figures 7.37, 7.38, 7.39 and 7.40, and for case D are shown in Figures 7.41, 7.42, 7.43 and 7.44. In general similar behaviours to those found in the results of case A are found in these two cases. The differences between the two methods are also found at and near the boundary, and the two methods give almost the same results at positions well away from the boundaries. It is worth mentioning that, for the results of case D shown in Figure 7.44, although the difference between the pressure distribution at the boundaries does not exceed 0.2 GPa, this value represents more than 10% of the transient maximum pressure value calculated in this case which was previously shown in Figure 7.25 (case $5\bar{u}$ in this figure).

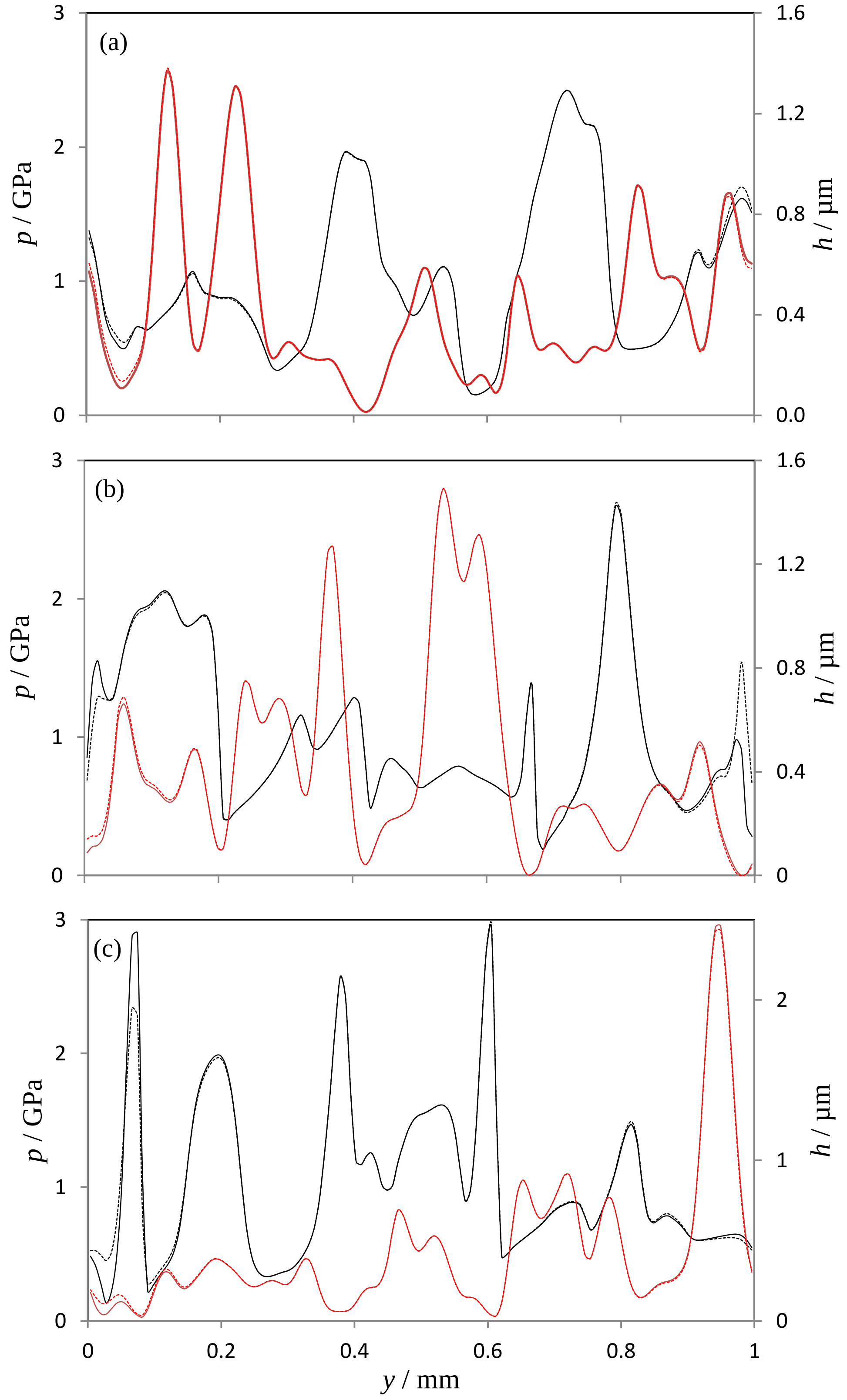

Figure 7.33: Section comparison of pressure (black) and film thickness (red) of case A between the cyclic (solid) and no-flow (dashed) methods at $x = 0$, (a) time step 3600, (b) time step 4000 and(c) time step 4400.

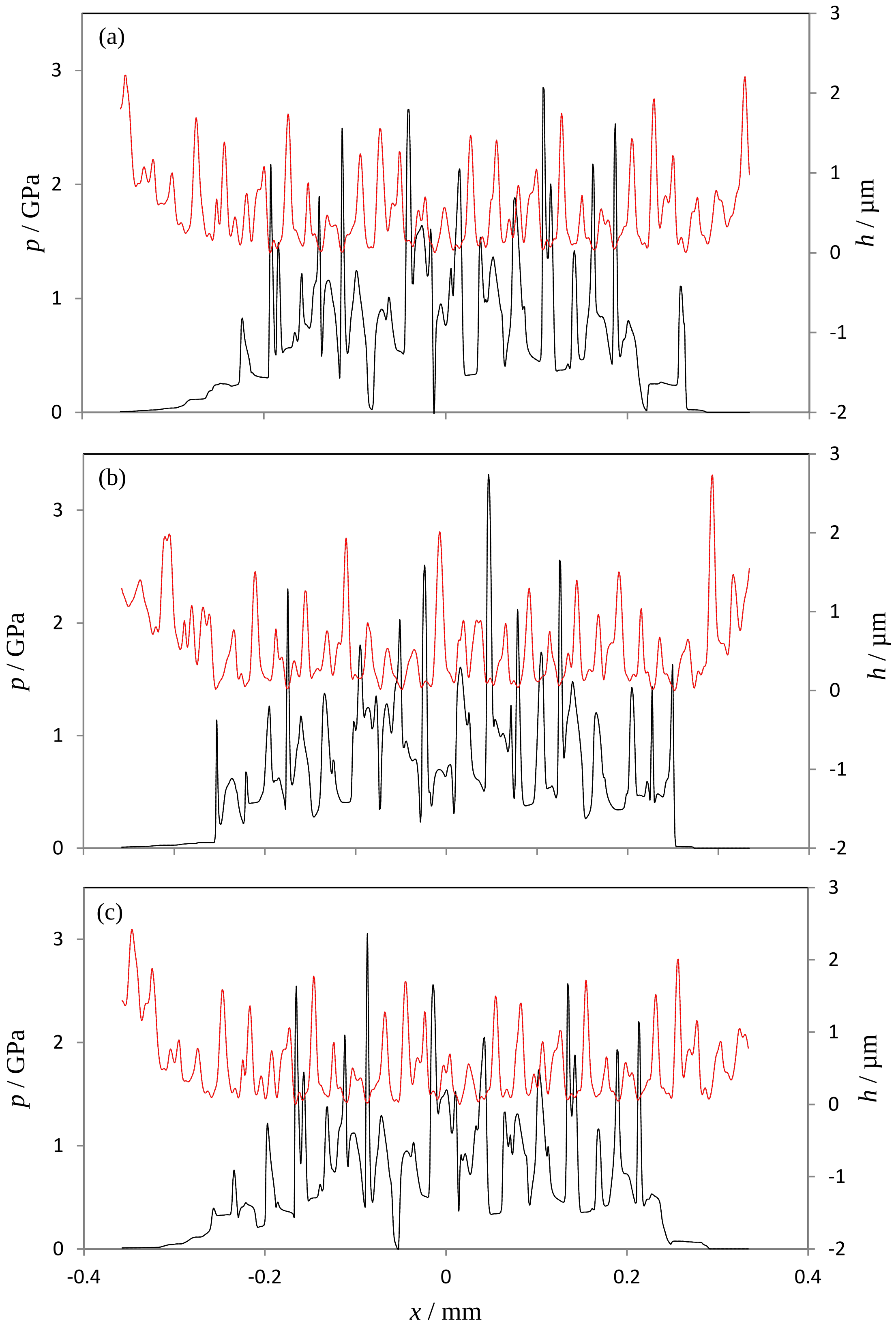

Figure 7.34: Section comparison of pressure (black) and film thickness (red) of case A between the cyclic (solid) and no-flow (dashed) methods at $y = 0.5$ mm, (a) time step 3600, (b) time step 4000 and (c) time step 4400.

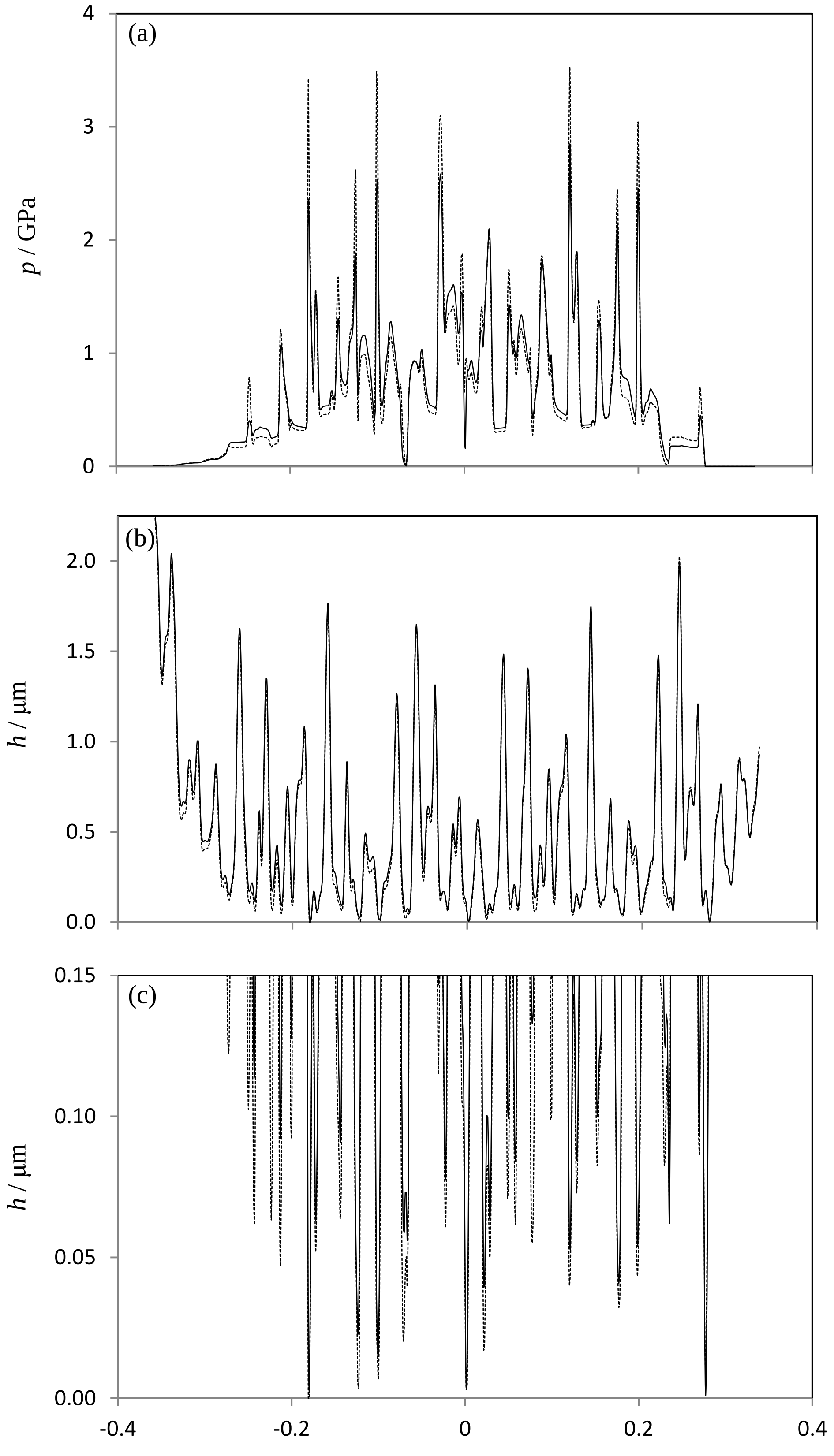

Figure 7.35: Section comparison between the results of the cyclic (solid) and no-flow (dashed) methods at the boundary $y \approx 1$ mm of case A at time step 4000, (a) pressure, (b) and (c) film thickness at different scale.

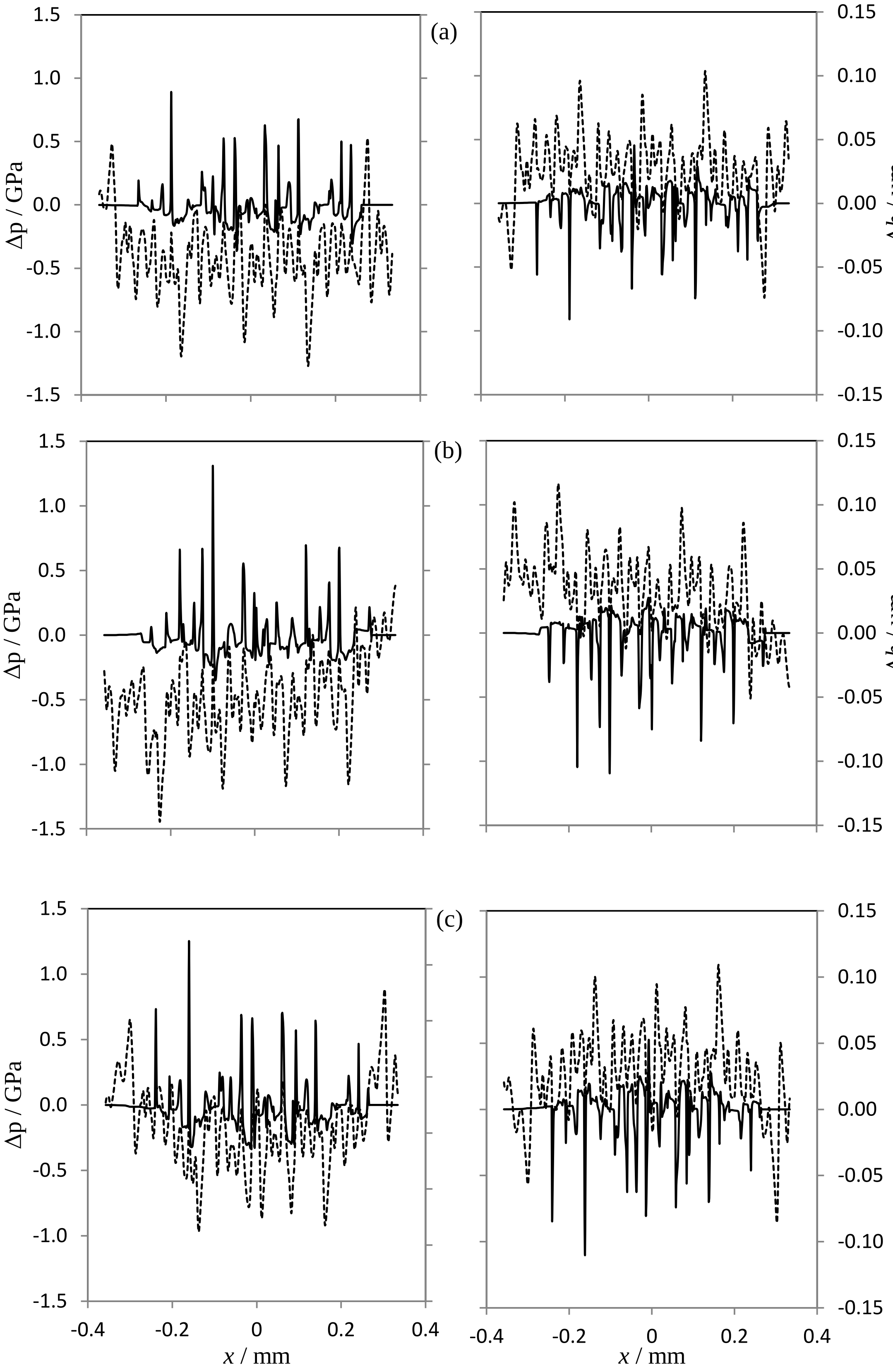

Figure 7.36: Difference between results of the cyclic and no flow methods for case A at the boundaries $y \approx 0$ (left) and $y \approx 1$ (right), $\Delta p = p_{\mathrm{cyclic}} - p_{\mathrm{no\ flow}}$ (solid) and $\Delta h = h_{\mathrm{cyclic}} - h_{\mathrm{no\ flow}}$ (dashed), (a) time step 3600, (b) time step 4000 and (c) time step 4400.

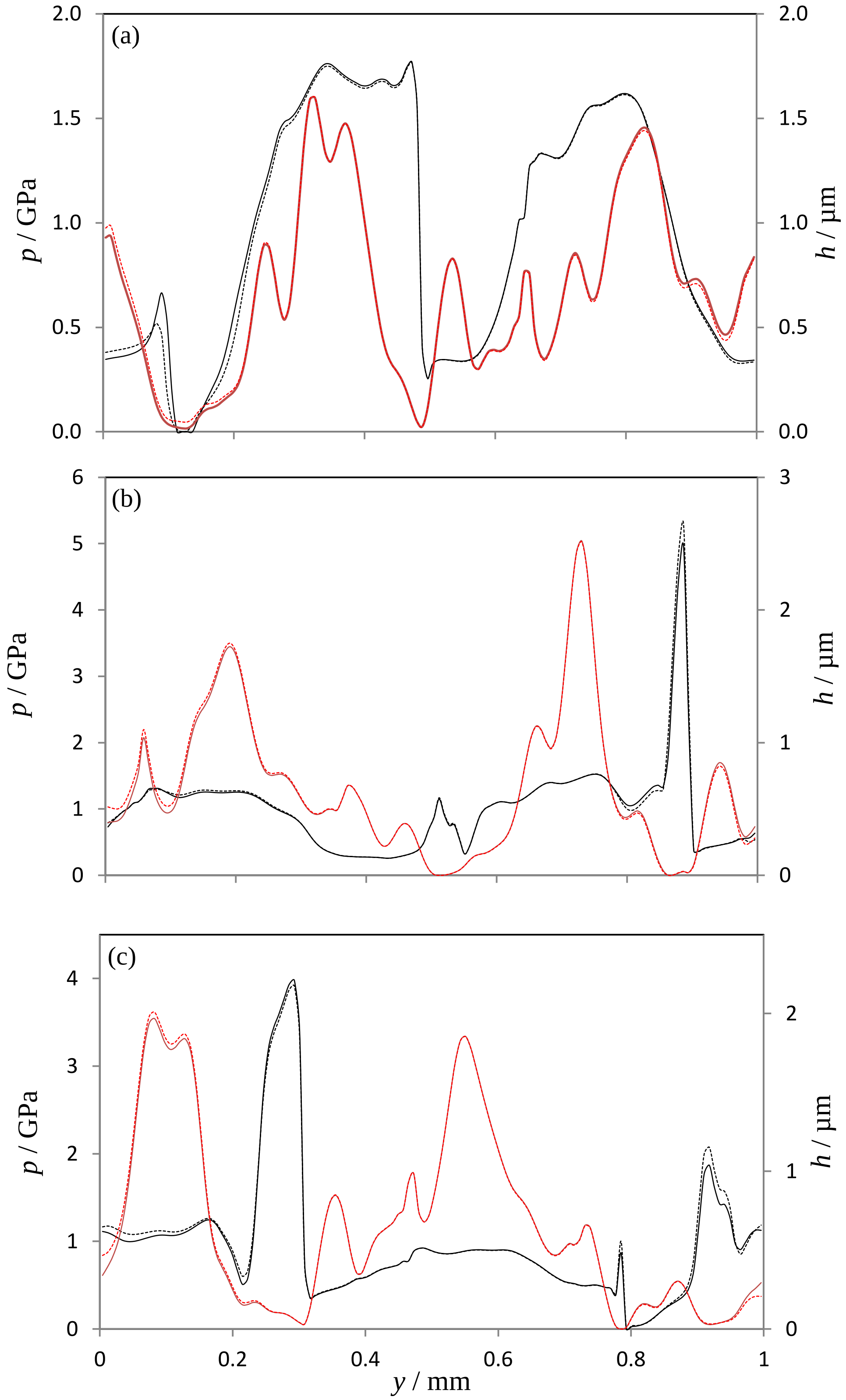

Figure 7.37: Section comparison of pressure (black) and film thickness (red) of case B between the cyclic (solid) and no-flow (dashed) methods at $x = 0$, (a) time step 3600, (b) time step 4000 and(c) time step 4400.

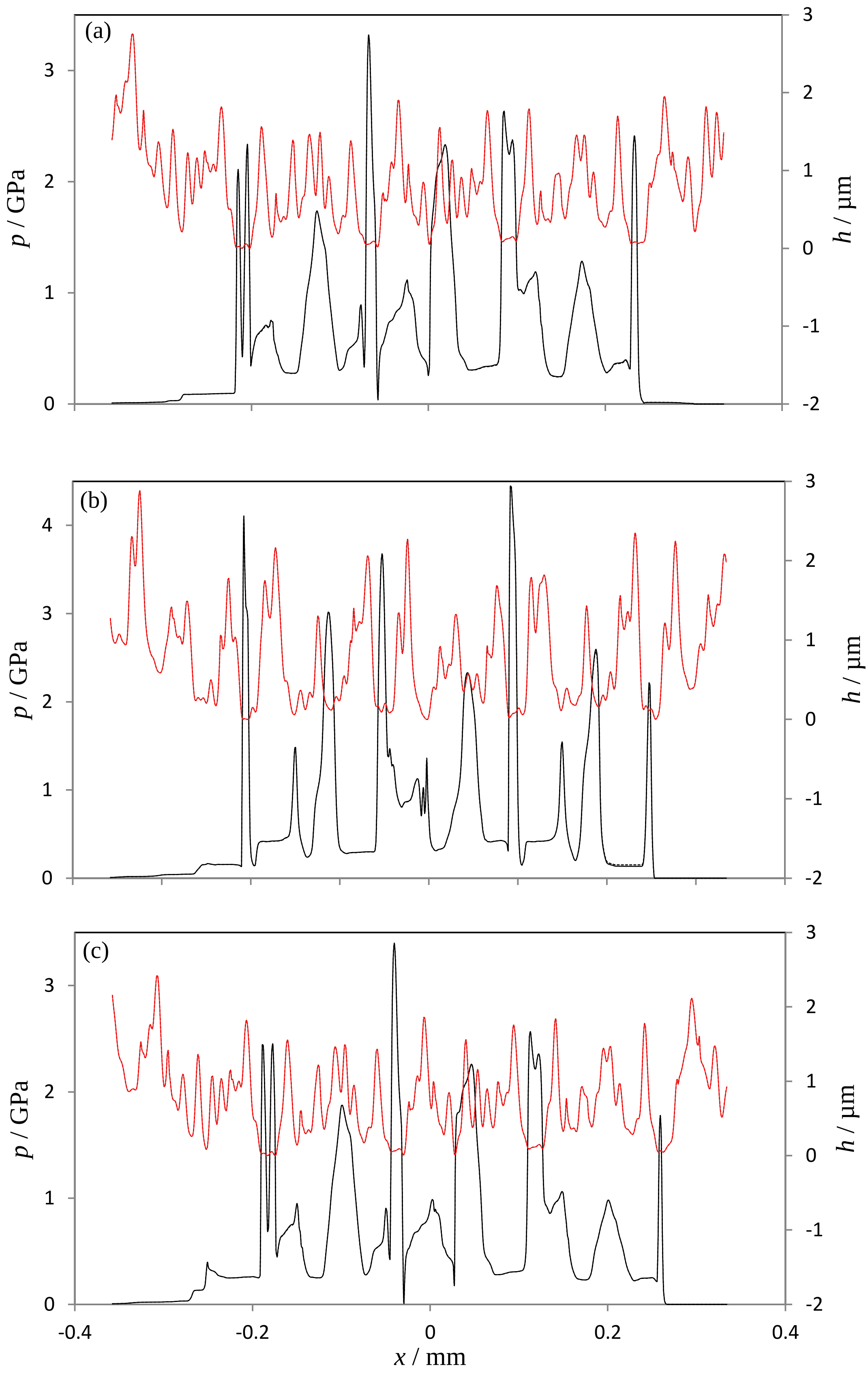

Figure 7.38: Section comparison of pressure (black) and film thickness (red) of case B between the cyclic (solid) and no-flow (dashed) methods at y = 0.5 mm, (a) time step 3600, (b) time step 4000 and (c) time step 4400.

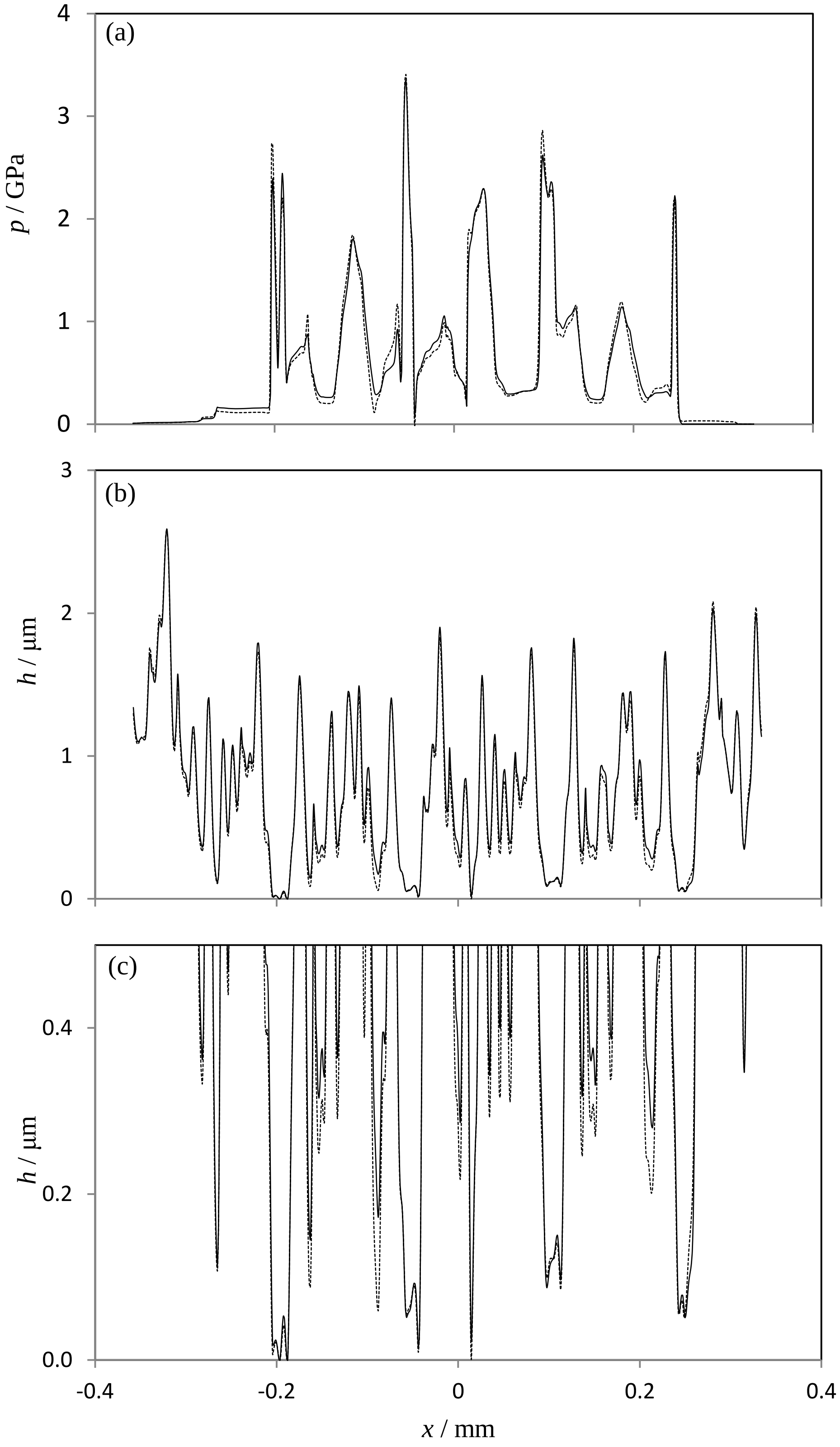

Figure 7.39: Section comparison between the results of the cyclic (solid) and no-flow (dashed) methods at the boundary $y \approx 1$ mm of case B at time step 4000, (a) pressure, (b) and (c) film thickness at different scale.

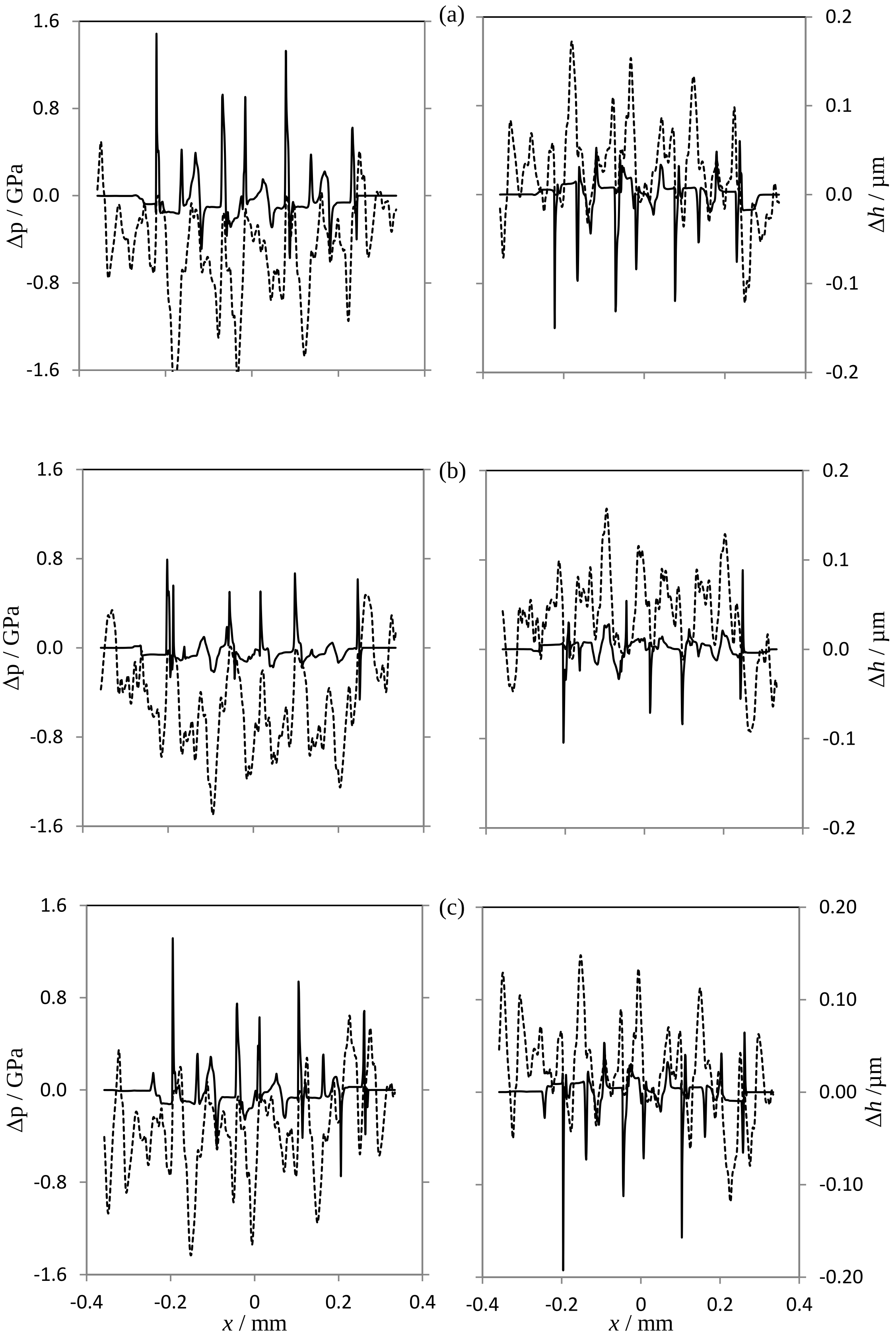

Figure 7.40: Difference between results of the cyclic and no-flow methods for case B at the boundaries $y \approx 0$ (left) and $y \approx 1$ (right), $\Delta p = p_{\text{cyclic}} - p_{\text{no flow}}$ (solid) and $\Delta h = h_{\text{cyclic}} - h_{\text{no flow}}$ (dashed), (a) time step 3600, (b) time step 4000 and (c) time step 4400

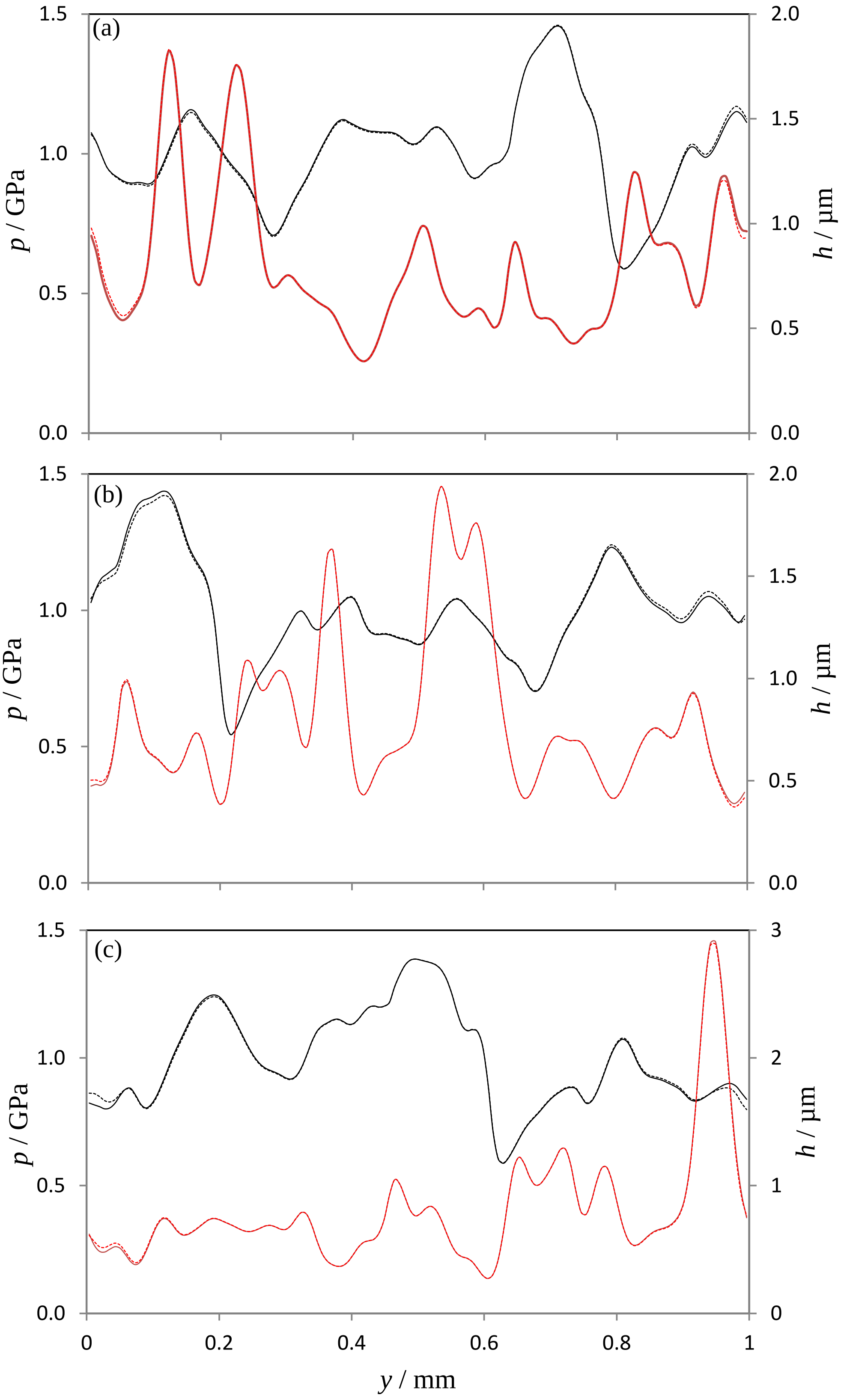

Figure 7.41: Section comparison of pressure (black) and film thickness (red) of case D between the cyclic (solid) and no-flow (dashed) methods at $x = 0$, (a) time step 3600, (b) time step 4000 and (c) time step 4400.

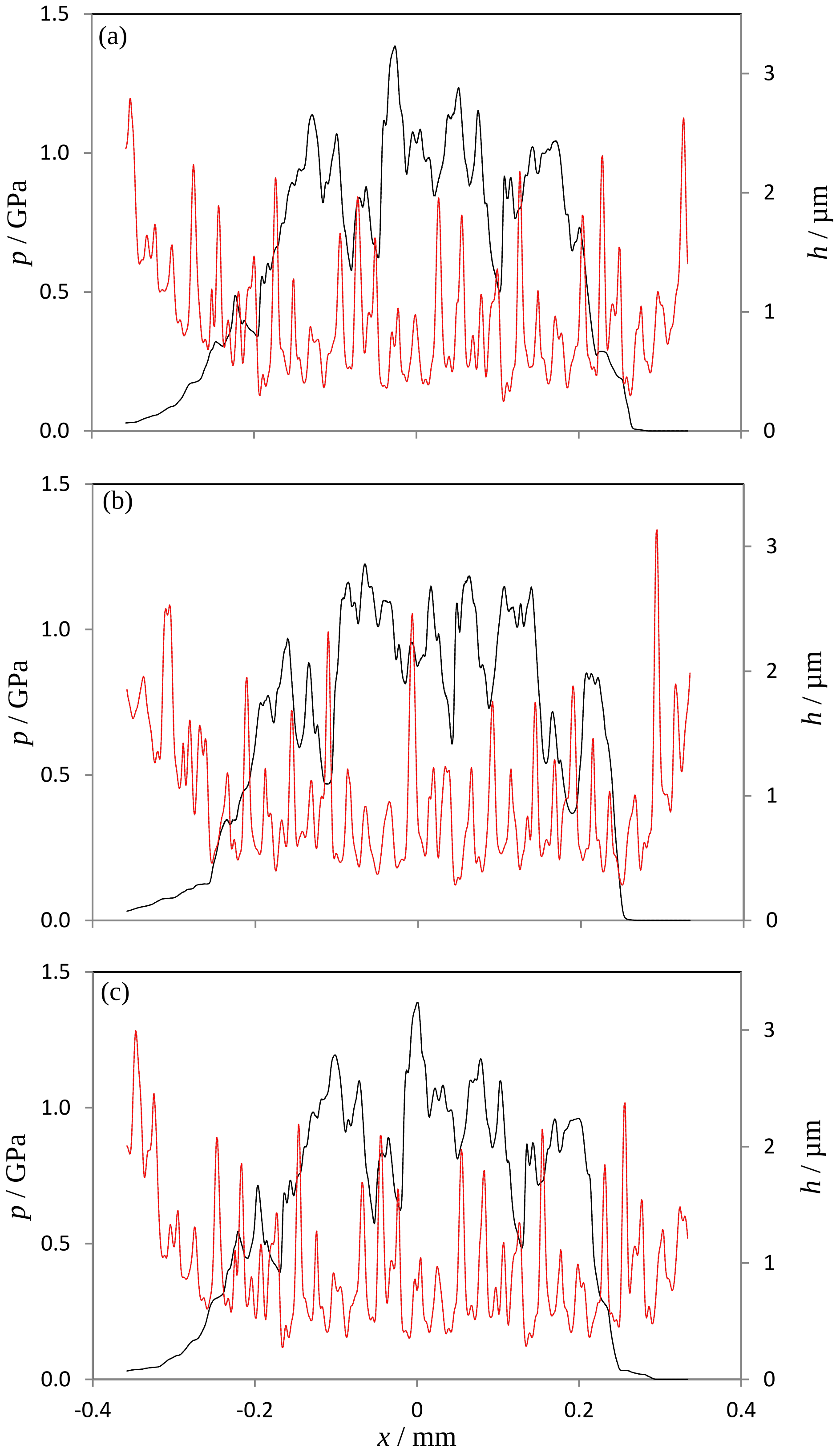

Figure 7.42: Section comparison of pressure (black) and film thickness (red) of case D between the cyclic (solid) and no-flow (dashed) methods at y = 0.5 mm, (a) time step 3600, (b) time step 4000 and (c) time step 4400.

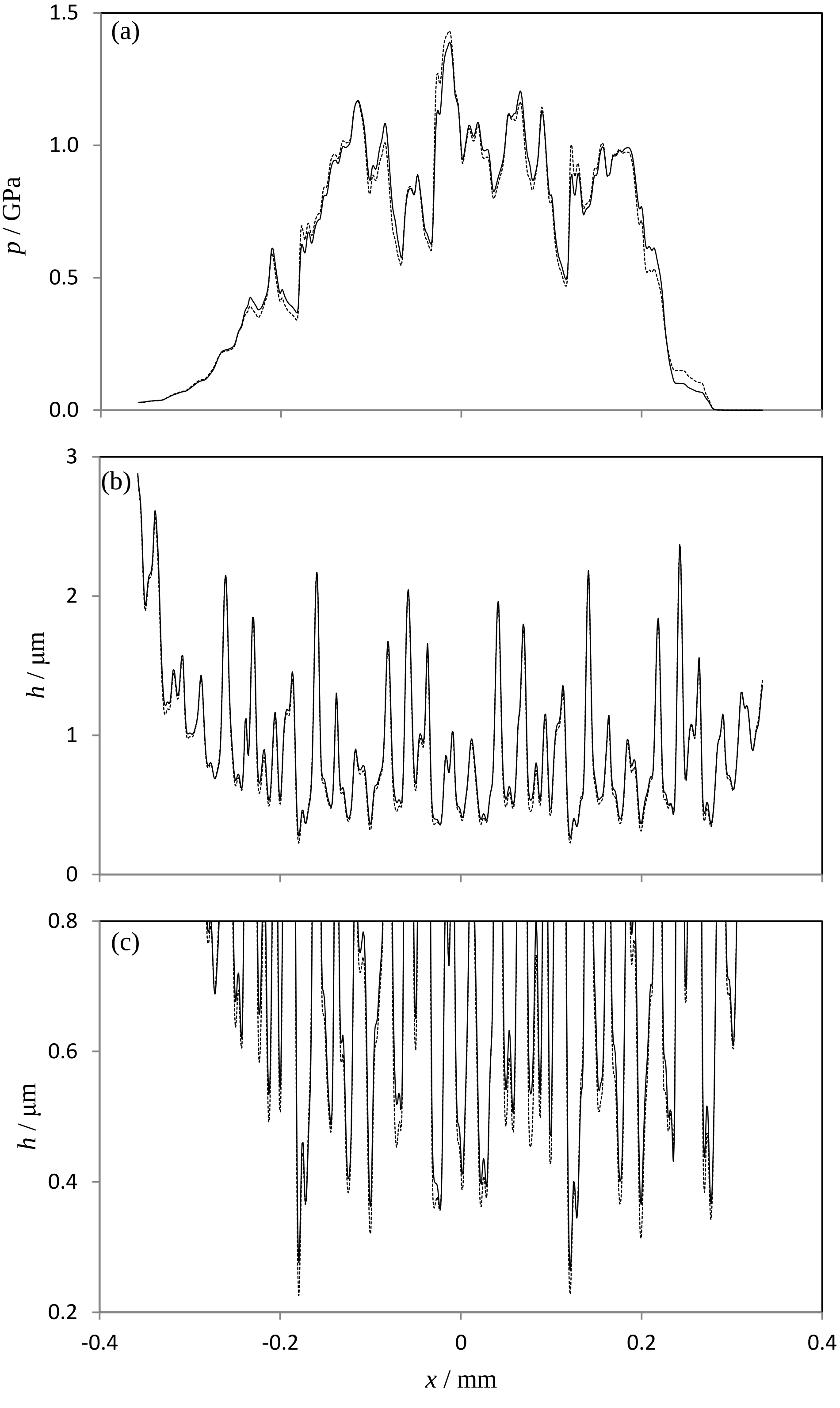

Figure 7.43: Section comparison between the results of the cyclic (solid) and no-flow (dashed) methods at the boundary $y \approx 1$ mm of case D at time step 4000, (a) pressure, (b) and (c) film thickness at different scale.

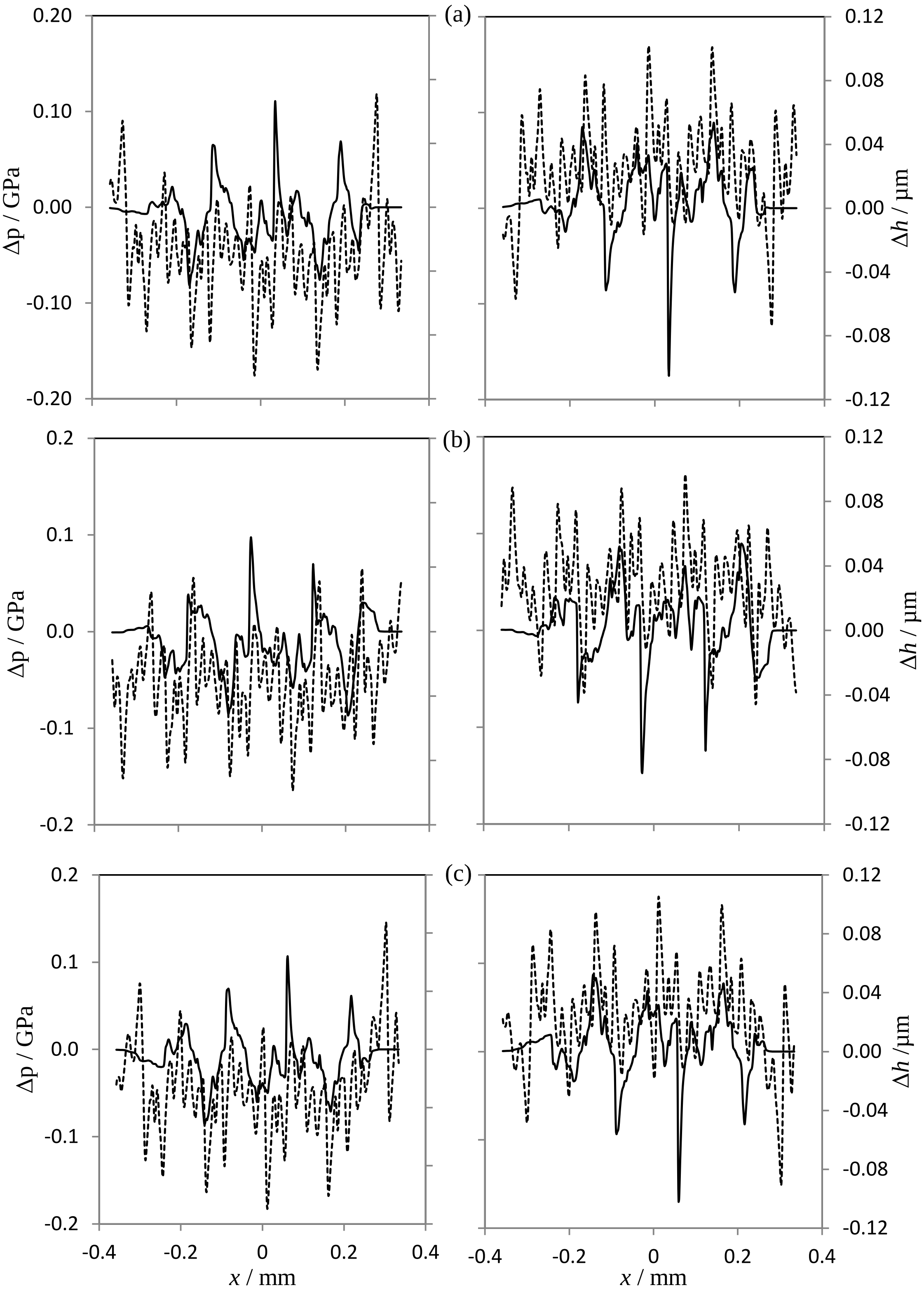

Figure 7.44: Difference between results of the cyclic and no-flow methods for case D at the boundaries $y \approx 0$ (left) and $y \approx 1$ (right) , $\Delta p = p_{\text{cyclic}} - p_{\text{no flow}}$ (solid) and $\Delta h = h_{\text{cyclic}} - h_{\text{no flow}}$ (dashed), (a) time step 3600, (b) time step 4000 and (c) time step 4400

The above comparisons give an indication of the difference between the results of adopting cyclic and no-flow boundary conditions at the boundaries and at the centre of the contact. A comparison between the results of the two concepts at other positions in the solution space also needs to be investigated.

The maximum differences between the two methods in both film thickness and pressure distribution is found in case B at time step 3600 as previously shown in Figure 7.40 (a). Therefore the results at this time step are further investigated by making more sectional comparisons between the two methods. Figure 7.45 shows the difference between the results of the two methods at thirteen y positions. The first and last comparisons ($y \approx 0$ and $y \approx 1$ mm) in this figure are those previously shown in Figure 7.40 (a) which are repeated here to give a complete picture of the comparisons over the whole solution space. It is clear that as the distance from the boundaries is increased, both Δp and Δh decay significantly. For example, between $y \approx 0.2$ mm and $y \approx 0.8$ mm results of the two methods are very similar, and at $y \approx 0.5$ mm (centre of the solution space) the differences are almost zero.

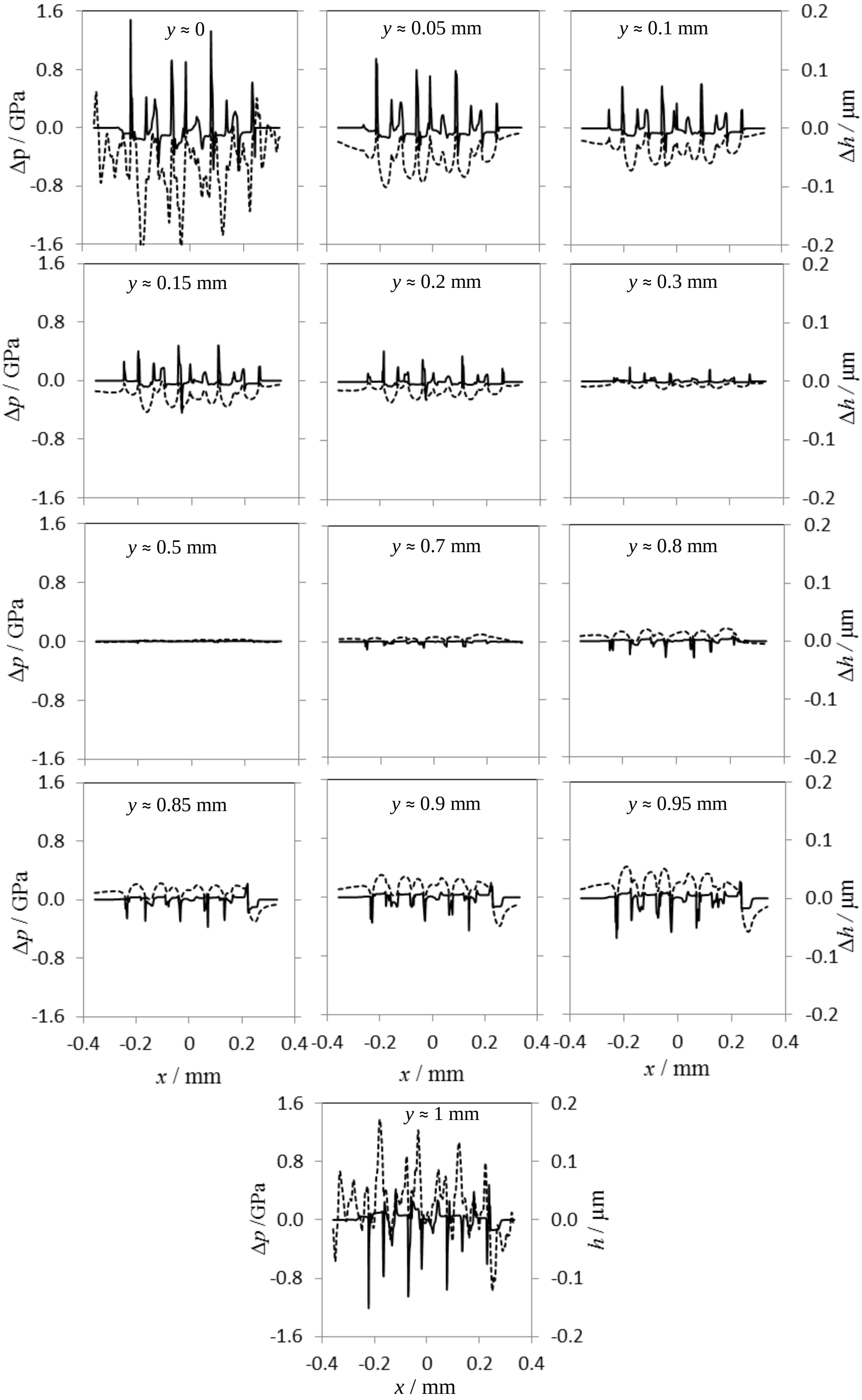

Figure 7.45: Difference between results of the cyclic and no-flow methods for case B at time step 3600 at 13 y positions, $\Delta p = p_{\text{cyclic}} - p_{\text{no flow}}$(solid) and $\Delta h = h_{\text{cyclic}} - h_{\text{no flow}}$(dashed)

Chapter 8

Conclusions and future work

8.1 Conclusions

The thesis has been concerned with the EHL analysis of helical gears where both smooth and rough surface profiles are considered, and the effect of profile modifications (such as tip relief and axial crowning) is also investigated

A full transient point contact numerical analysis procedure for predicting the pressure and film thickness over the full the meshing cycle of helical gear teeth is developed and presented in this thesis. Various aspects of the numerical analyses are described in detail in the thesis and the differential deflection technique is used in the formulation of the fundamental EHL problem. The point contact solver was available as a starting point for the work and this was developed to be able to solve the helical gear contact problem.

A range of subroutines were developed to specify all aspects of the kinematics and the 3D shape of the tooth flanks as contact proceeded through the meshing cycle. The EHL action takes place in the common tangent plane at the contact of the tooth flanks. The geometry specification in this plane requires the calculation of the contact characteristics due to the variation in the radius of relative curvature in the plane normal to the contact line, which changes continually as the contact moves from root to tip. This fundamental geometry of the involute gears is modified due to profile modification effects in the transverse and axial directions (tip relief and axial crowning).

Results of EHL analysis were obtained for two examples of helical gear contacts. The 4.5 mm module pinion was the same for both gear pairs with 33 teeth and a 44 mm face width. The meshing gears gave gear ratios of 1.03 and 3.0, and were chosen to allow the effect of gear ratio to be assessed as the higher ratio gives a greater variation of entrainment velocity during the meshing cycle.

Tip relief modification is used to prevent premature tooth engagement under load due to flexure of the loaded teeth. This can cause a local stress-raising discontinuity in the curvature of the tooth profile according to the form of tip relief profile adopted. In addition, axial profile relief is used to prevent edge contact at the side faces of the gears under misalignment conditions due to mounting errors or shaft deflections. Both of these microgeometry modifications were included in the analysis and their effects were considered by variation of the form adopted.

The basic form of tip relief adopted was parabolic so that the slope of the gear profile was maintained at the transition to the tip relief zone. Using the basic tip relief, a series of different axial form modifications was introduced with the same edge clearance at the face edges. Full transient analyses for these cases allowed the effect of the axial form modifications to be assessed and compared.

A simple axial crown radius was used for evaluations of a number of different tip relief profiles with each providing the same amount of relief at the tip of the gear. Two forms of tip relief profile were adopted for the tests. The first was a combination of a parabolic transition curve to a linear relief profile, with slope continuity throughout. These profiles varied according to the length of the parabolic section and the subsequent slope of the linear section. The case of a linear profile was used as an asymptotic limit for the combined profile. The other profile form adopted was a power law for which a number of powers were adopted including power 2 to give the parabolic profile. The effect of the tip relief profile adopted was found to be significant in terms of the peak stresses and the lubricant film thickness at the location of the transition to tip relief.

A further geometrical modification of the involute form was examined in the form of axial faceting that results from the generation grinding process. This was found to lead to significant changes in the EHL results, particularly so for the case of the smallest number of facets considered (20) which corresponds to facets that are approximately 1 mm long for the gear considered.

Incorporating surface roughness in the EHL analysis of helical gears is a very significant numerical challenge. This is due to the relatively large size of the contact area which requires very high resolution to make the model sensitive to the surface roughness. The transient analyses of the helical tooth contacts led to the conclusion that most of the contact line behaved as if it was a quasi-steady state line contact. This observation was developed to provide a means of investigating 3D roughness effects in the gear contact. A 3D line contact model was developed to solve the EHL problem over a representative length of the contact line with cyclic transverse boundary conditions. The elastic deflection analysis was carried out using a Fast Fourier Transform approach to exploit the periodicity properties in such a way as to obtain an effective 3D line contact analysis. The advantage of developing such an EHL model is to have the ability to model a selected area of the contact region and include the real 3D surface roughness features without sacrificing the accuracy of the analysis.

The conclusions from the work can be categorised into three main parts:

8.1.1 Transient solution of the helical gear meshing cycle including the effect of tip relief and axial crown modifications (smooth surfaces):

- Comparison of transient and quasi-steady EHL analyses shows the important influence of time-varying behaviour in helical gears, particularly in its effect on the detailed distribution of film thickness at the tooth contacts brought about by tip geometry modifications. This work clearly demonstrates the necessity for inclusion of the transient terms in the hydrodynamic equation when analysing gear tooth contacts. Over most of the contact between the meshing teeth an effective EHL film is predicted, but significant thinning of the film occurs where the contact reaches the tip relief zone, where transient squeeze film effects become significant.
- Severe thinning of the film where the lubricated line of contact would otherwise reach the side faces of the gears is substantially alleviated by the introduction of appropriate crowning. This is most effective in preventing edge contact for contact lines that cross the centre plane of the teeth but has a diminished effect at the beginning and end of contact. (It is suggested that this is not the case for spur gears where crowning can be expected to prevent side edge contact throughout the meshing cycle).

- It is shown that the detailed geometry of the tip relief feature can have a profound effect on the local contact pressure distribution. For the gear pairs considered, application of a simple “linear” tip relief introduces a more than three-fold increase in the nominal contact pressure at the profile modification start-point compared to that for a gradually blended parabolic relief geometry. This aggressive stress concentration is accompanied by poor local film forming capability.
- Comparison between the results of different power law modifications illustrates that the parabolic curve is the ideal form of those considered and the other higher power law modifications do not lead to significant improvement in the results. This demonstrates that the continuous change of slope is the important requirement.

8.1.2 Transient EHL Analysis of Helical Gears Having Faceted Tooth Surfaces

- Closed form equations were derived for the resulting gap between faceted profiles during the engagement between gear teeth.
- The presence of axial facets on the tooth surfaces, which can be the result of the intermittent nature of the finishing process, have been found to have a significant effect on the predicted transient EHL behaviour of helical gears. Small numbers of facets such as $n_f = 20$, lead to high stress concentrations producing maximum pressures of more than three times the corresponding smooth surface values. This is associated with a breakdown in the film thickness throughout the meshing cycle. The predictions are considerably improved by

increasing the number of facets, and the case $n_f = 100$, for example, shows very similar results to those found in the smooth surface case.

8.1.3 3D line contact model (rough surfaces)

- A 3D line contact EHL model has been developed to predict the effect of surface roughness on the EHL analysis over a finite length in the transverse direction of the tooth. This model is based on the use of the FFT method to reflect the repetition of the solution space along the nominal contact line between the helical teeth, and is applied to repeating roughness profiles so that transverse flow at the model boundaries is correctly calculated.
- Unlike the case of spur gears, in helical gears the lay of tooth roughness is generally inclined to the direction in which rolling (entrainment) and sliding take place. In order to include this feature in the EHL model a closed form equation has been derived, for the case where the roughness is inclined at an angle with respect to the nominal contact line. The concept of cyclic boundary conditions at the boundary of the solution space has been used for the first time in order to correctly model the behaviour of a short, representative section of the total contact line.
- Cases in which the roughness lay on the two surfaces is either aligned or “crossed” have been modelled. In general, the crossed extrusion of the roughness profile produces about three times as many predicted metal to metal contact points in comparison with aligned extrusion, with a tendency to produce much higher local pressure values.
- A comparison between the concepts of a cyclic boundary condition as presented in this thesis with the no-flow boundary approach adopted by other workers,

shows that significant transverse pressure gradients develop at the boundary which are wrongly neglected by imposing the no-flow condition. These pressure gradients are associated with transverse flows that significantly influence the results.

8.2 Suggestions for future work

The transient EHL solution of helical gears based on the point contact approach with the consideration of profile modifications effects is a complex problem. As stated above this thesis introduces a numerical analysis of all these aspects in addition to developing the 3D line contact model in order to consider the surface roughness and due to time constraints there are still other important aspects not considered in this work. Therefore, it is recommended that further research be undertaken in the following areas:

- Inclusion of the thermal effect in the EHL solution of the helical gear meshing cycle.

  The thermal effects can be considered in the EHL analyses by solving the energy equation for the lubricant film and for the gear flanks. Knowing the temperature distribution is important due to the lubricant viscosity dependency on the temperature and the consequence effects on the film thickness. This will also have to be developed for the case where the lubricant film breaks down and direct contact occurs between the gears over limited areas.

- Considering of the plastic deformation of the roughness asperities in the EHL analyses.

  The interaction between the surfaces asperities during the gear meshing cycle produces high level of pressure which may lead to a plastic deformation. The work in this thesis only considers the elastic deformation of the surface which represents an approximation to the real contact problem. In reality plastic deflection occurs as new, more extreme, operating conditions are encountered and the gear pair operates elastically after some shakedown as plastic deformation occurs.

- Development of a contact model for helical gears to calculate the real load sharing between simultaneous pairs of teeth in contact due to elastic deformation (predominantly bending) of the teeth under load. This will require a detailed FEM analysis of the tooth contacts to establish the way in which the load is distributed in along the contact lines. It may then be possible to use this information in the EHL analysis to provide solutions which have the same contact line load distribution characteristics. A way of attempting this would be to introduce a misalignment of the contact lines of the tooth surfaces in the EHL analysis and to adjust it so that the resulting contact line load distribution corresponds to the FEM result.

- Development of the current 3D line contact model to consider the effect of roughness orientation on the predicted fatigue life of the helical gears.

  It has been shown in this thesis how the transient pressure distribution resulting from the EHL analysis of rough surfaces deviates significantly from the corresponding smooth surface results. As the surface asperities in the two surfaces interact with each other, a kind of cycling pressure variation over the contact area occurs. Such loading condition may produce micropitting at the roughness asperities particularly for low Λ ratio where the pressure deviations are particularly large. This form of surface failure is considered as a fatigue failure. Researchers tend to solve the EHL problem related to this form of fatigue failure in gears based on a line contact EHL approach. This may introduce significant approximations to the solution of the contact problem from a fatigue failure consideration. Therefore, extending the 3D line contact model developed in this thesis to incorporate fatigue analyses may have an impact on predicting the life of gears.

References

Ai, X. and Cheng, H. 1994. A transient EHL analysis for line contacts with measured surface roughness using multigrid technique. *Journal of tribology* 116, pp. 549–556.

Akbarzadeh, S. and Khonsari, M.M. 2008. Thermoelastohydrodynamic Analysis of Spur Gears with Consideration of Surface Roughness. *Tribology Letters* 32, pp. 129–141.

Alban, L. 1985. *Systematic Analysis of Gear Failures*. American Society for Metals

B. K. Gears Pvt. Ltd. Available at: http://www.bkgears.com/gears.html#demo2 (Accessed: 2 December 2014).

Bahk, C. and Parker, R.G. 2013. Analytical investigation of tooth profile modification effects on planetary gear dynamics. *Mechanism and Machine Theory* 70, pp. 298–319.

Bonori, G., Barbieri, M. and Pellicano, F. 2008. Optimum profile modifications of spur gears by means of genetic algorithms. *Journal of Sound and Vibration* 313, pp. 603–616

Chapra, S.C. and Canale, R. P. 2006. *Numerical methods for engineers*. 5th ed. McGraw-Hill.

Chen, W. Liu, S. and Wang, Q. 2008. Fast Fourier Transform Based Numerical Methods for Elasto-Plastic Contacts of Nominally Flat Surfaces. *Journal of Applied Mechanics* 75, pp. 011022(1–11).

Chittenden, R., Dowson, D., Dunn, J. F. and Taylor, C. M. 1985. A theoretical analysis of the isothermal elastohydrodynamic lubrication of concentrated contacts. II. General Case, with lubricant entrainment along either principal axis of the Hertzian contact ellipse or at some intermediate angle. *Proc. R. Soc. London*, pp. 271-294.

Chittenden, R., Dowson, D., Dunn, J. F. and Taylor, C. M. 1985. A Theoretical Analysis of the Isothermal Elastohydrodynamic Lubrication of Concentrated Contacts. I. Direction of Lubricant Entrainment Coincident with the Major Axis of the Hertzian Contact Ellipse. *Proc. R. Soc. London*, pp. 245–269.

Clarke, A. Sharif, K., Evans, H.P., Snidle, R.W. 2006. Heat partition in rolling/sliding elastohydrodynamic contacts. *Journal of Tribology* 128, pp. 67-78.

Cooly, J. and Tukey, J. 1965. An algorithm for the machine calculation of complex Fourier series. *Mathmatics Computation* 19, pp. 297–301.

Dowson, D. and Higginson, G.R. 1959. A Numerical Solution to the Elasto-Hydrodynamic Problem. *Journal of Mechanical Engineering Science* 1, pp. 6–15.

Dowson, D. and Higginson, G.R. 1966. *Elastohydrodynamic Lubrication*. Pergamon, Oxford.

Dowson, D. 1979. *History of tribology*. Longman Ltd

Drago, R.J. 1988. *Fundamentals of gear design*. Butterworths.

Dudley, D.W. 1969. *The evolution of the gear art*. American Gear Manufacturers Association.

Dudley, D.W. 1984. *Handbook of practical gear design*. McGraw-Hill

Ebrahimi, A. and Akbarzadeh, S. 2013. Mixed-elastohydrodynamic analysis of helical gears using load-sharing concept. *Proceedings of the Institution of Mechanical Engineers, Part J: Journal of Engineering Tribology* 228, pp. 320–331.

Elcoate, C. D. 1996. Coupled solution methods for the elasto- hydrodynamic problem. PhD thesis, University of Wales, Cardiff.

Elcoate, C.D. , Evans, H.P. and Hughes, T.G. 1998. On the coupling of the elastohydrodynamic problem. *Proceedings of the Institution of Mechanical Engineers, Part C: Journal of Mechanical Engineering Science* 212, pp. 307–318.

Elcoate, C.D. Evans, H.P., Hughes, T.G. and Snidle, R.W. 2001. Transient elastohydrodynamic analysis of rough surfaces using a novel coupled differential deflection method. *Proceedings of the Institution of Mechanical Engineers, Part J: Journal of Engineering Tribology* 215, pp. 319–337.

Evans, H.P. 2015, *Private Communication*.

Evans, H.P. and Snidle, R.W. 1981. The isothermal elastohydrodynamic lubrication of spheres. *Journal of Lubrication Technology* 103, pp. 547-557.

Evans, H. P. and Snidle, R.W. 1982. The elastohydrodynamic lubrication of point contacts at heavy loads. *Proc. R. Soc. London*, A 382, pp. 183-199.

Evans, H.P. and Hughes, T.G. 2000. Evaluation of deflection in semi-infinite bodies by a differential method. *Proceedings of the Institution of Mechanical Engineers, Part C: Journal of Mechanical Engineering Science* 214, pp. 563–584.

Evans, H.P., Snidle, R.W., Sharif , K.J. and Bryant, M. J. 2012. Predictive modelling of fatigue failure in concentrated lubricated contacts. *Faraday Discussions* 156, pp. 105-121.

Evans, H.P. Snidle, R.W., Sharif, K., Shaw, B. and Zhang, J. 2013. Analysis of micro-EHL and prediction of surface fatigue damage in micropitting tests on helical gears. *Journal of Tribology* 135, p. 011501(1-9).

Fish, J. and Belytschko, T. 2012. *A First Cource in Finite Elements*. John Wiley & Sons Ltd.

Hamrock, B.J. and Dowson, D. 1976. Isothermal Elastohydrodynamic Lubrication of Point Contacts. Part II—Ellipticity Parameter Results. *Journal of Lubrication Technology*, pp. 375–381.

Hamrock, B.J. and Dowson, D. 1977. Isothermal elastohydrodynamic lubrication of point contacts. Part III—Fully flooded results. *Journal of Lubrication Technology*, pp. 264–275.

Han, L. Zhang, D. and Wang, F. 2013. Predicting Film Parameter and Friction Coefficient for Helical Gears Considering Surface Roughness and Load Variation. *Tribology Transactions* 56, pp. 49–57.

Holmes, M. 2002. Transient analysis of the point contact elastohydrodynamic lubrication problem using coupled solution methods. PhD thesis, Cardiff University, UK.

Holmes, M., Evans, H.P., Hughes, T.G., and Snidle, R.W. 2003a. Transient elastohydrodynamic point contact analysis using a new coupled differential deflection method, Part 1: Theory and validation. *Proceedings of the Institution of Mechanical Engineers, Part J: Journal of Engineering Tribology* 217, pp. 289–304.

Holmes, M., Evans, H.P., Hughes, T.G., and Snidle, R.W. 2003b. Transient elastohydrodynamic point contact analysis using a new coupled differential deflection method Part 2: results. *Proceedings of the Institution of Mechanical Engineers, Part J: Journal of Engineering Tribology* 217, pp. 305–321.

Houghton, P.S. 1961. *Gears: Spur, Helical, Bevel and Worms*. The Technical Press LTD, London .

Houpert, L. and Hamrock, B. 1986. Fast approach for calculating film thicknesses and pressures in elastohydrodynamically lubricated contacts at high loads. *Journal of Tribology* 108, pp. 411–419.

Hu, Y. and Zhu, D. 2000. A full numerical solution to the mixed lubrication in point contacts. *Journal of Tribology* 122, pp. 1–9.

Hughes, T.G. Elcoate, C.D., and Evans, H.P. 2000. Coupled solution of the elastohydrodynamic line contact problem using a differential deflection method. *Proceedings of the Institution of Mechanical Engineers, Part C: Journal of Mechanical Engineering Science* 214, pp. 585–598.

Johnson, K. Greenwood, J. and Poon, S. 1972. A simple theory of asperity contact in elastohydro-dynamic lubrication. *Wear* 19, pp. 91–108.

Johnson, K.L. and Tevaarwerk, J.L. 1977. Shear Behaviour of Elastohydrodynamic Oil Films. *Proc. R. Soc. London*, A.356, pp. 215–236

Jost, P.H. 1966. *Lubrication (Tribology) Education and Research. A Report on the Present Position and Industry Needs*. London.

Kahraman, A. and Blankenship, G. 1999. Effect of involute tip relief on dynamic response of spur gear pairs. *Journal of Mechanical Design* 121, pp. 313-315.

Kahraman, A., Bajpai, P., and Anderson, N. 2005. Influence of Tooth Profile Deviations on Helical Gear Wear. *Journal of Mechanical Design* 127, pp. 656-663.

Kong, S. 2001. Contact, kinematics and film formation in worm gears. PhD thesis, University of Wales, UK.

Kreyszig, E. 1999. *Advanced engineering mathematics*. 8th edition. John Wiley & Son, Inc.

Kugimiya, H. 1966. Profile Modification of Helical Gear Teeth. *The Japan Society of Mechanical Engineers* 9, pp. 829–841.

Kweh, C.C., Evans, H.P., and Snidle, R.W. 1989. Micro-elastohydrodynamic lubrication of an elliptical contact with transverse and three-dimensional sinusoidal roughness. *Journal of Tribology* 111, pp. 577–584.

Kweh, C.C., Patching, M.J., Evans, H.P. and Snidle, R.W. 1992. Simulation of elastohydrodynamic contacts between rough surfaces. *Journal of Tribology* 114, pp. 412–419.

Larsson, R. 1997. Transient non-Newtonian elastohydrodynamic lubrication analysis of an involute spur gear. *Wear* 207, pp. 67–73.

Lee, K., and Cheng, H.S. 1973. Effect of surface asperity on elastohydrodynamic lubrication. *NASA CR-2195*.

Li, S., Vaidyanathan, A., Harianto, J. and Kahraman, A. 2009. Influence of Design Parameters on Mechanical Power Losses of Helical Gear Pairs. *Journal of Advanced Mechanical Design, Systems, and Manufacturing* 3, pp. 146–158.

Li, S. and Kahraman, a. 2010. A Transient Mixed Elastohydrodynamic Lubrication Model for Spur Gear Pairs. *Journal of Tribology* 132, pp. 011501(1-9).

Li, S. and Kahraman, A. 2010. Prediction of Spur Gear Mechanical Power Losses Using a Transient Elastohydrodynamic Lubrication Model. *Tribology Transactions* 53, pp. 554–563.

Li, S. 2013. Influence of Surface Roughness Lay Directionality on Scuffing Failure of Lubricated Point Contacts. *Journal of Tribology* 135, pp. 041502(1-9).

Li, S., Kahraman, A., Anderson, N. and Wedeven, L. 2013. A model to predict scuffing failures of a ball-on-disk contact. *Journal of Tribology International* 60, pp. 233–245.

Litvin, F. and Fuentes, A. 2004. *Gear Geometry and Applied Theory*. Cambridge University Press.

Litvin, F., Gonzalez, I., Fuentes, A., Hayasaka, K. and Yukishima, K. 2005. Topology of modified surfaces of involute helical gears with line contact developed for improvement of bearing contact, reduction of transmission errors, and stress analysis. *Journal of Mathematical and Computer Modelling* 42, pp. 1063–1078.

Liu, H., Mao, K., Zhu, C., Chen, S., Xu, X. and Liu, M. 2013. Spur Gear Lubrication Analysis with Dynamic Loads. *Tribology Transactions* 56, pp. 41–48.

Liu, S. Wang, Q. And Liu, G. 2000. A versatile method of discrete convolution and FFT (DC-FFT) for contact analyses. *Wear* 243, pp. 101–111.

Lubrecht, A. Napel, W. and Bosma, R. 1986. Multigrid, an alternative method for calculating film thickness and pressure profiles in elastohydrodynamically lubricated line contacts. *Journal of Tribology* 108. pp. 551-556

Lubrecht, A., Ten, W. And Bosma, R. 1988. The influence of longitudinal and transverse roughness on the elastohydrodynamic lubrication of circular contacts. *Journal of Tribology* 110, pp. 421–426.

Maitra, G.M. 1994. *Handbook of Gear Design*. Tata McGraw-Hill Education.

Mobil Oil Corporation, 1979, “Mobil EHL Guide Book”, Products Department, 150 East 42nd Street, New York.

Morales-Espejel, G.E. 2013. Surface roughness effects in elastohydrodynamic lubrication: A review with contributions. *Proceedings of the Institution of Mechanical Engineers, Part J: Journal of Engineering Tribology* 0, pp. 1-26

Morris, S.J. 2000.*Traction in elliptical point contacts*, PhD thesis, University of Wales, UK.

Nijenbanning, G., Venner, C. and Moes, H. 1994. Film thickness in elastohydrodynamically lubricated elliptic contacts. *Wear* 176, pp. 217-229

Nussbaumer, H.J. 1982. *Fast Fourier transform and convolution algorithms*. 2nd ed. Springer-Verlag.

Park, S. and Yoo, W. 2004. Deformation overlap in the design of spur and helical gear pair. *Finite Elements in Analysis and Design* 40, pp. 1361–1378.

Patir, N. and Cheng, H. 1978. An average flow model for determining effects of three-dimensional roughness on partial hydrodynamic lubrication. *Journal of lubrication Technology* 100, pp. 12–17.

Patching, M.J., Kweh, C.C., Evans, H.P., & Snidle, R.W., 1995, “Conditions for scuffing failure of ground and superfinished steel disks at high sliding speeds using a gas turbine engine oil”, *Trans. ASME Journal of Tribology*, v.117, pp. 482-489.

Polonsky, I. and Keer, L. 2000. Fast Methods for Solving Rough Contact Problems: A Comparative Study. *Journal of Tribology* 122, pp. 36–41.

Poon, C. and Sayles, R. 1994. Numerical Contact Model of a Smooth Ball on an Anisotropic Rough Surface. *Journal of Tribology* 116, pp. 194-201

Press, W., Teukolsky, S., Vetterling, W., and Flannery, B. 1992. *Numerical recipes in FORTRAN, The art of scientific computing*. Cambridge University Press.

Ranger, A., Ettles, C. and Cameron, A. 1975. The Solution of the Point Contact Elasto-Hydrodynamic Problem. *Proc. R. Soc. London*, A.346, pp. 227–244

Ren, N., Dong, Z., Chen, W., Liu, Y. And Wang, Q. 2009. A Three-Dimensional Deterministic Model for Rough Surface Line-Contact EHL Problems. *Journal of Tribology* 131, pp. 011501(1–9).

Roelands, C. 1966. Correlational aspects of the viscosity-temperature-pressure relationships of lubricating oils. PhD thesis, Technical University Delft, The Netherlands

Sankar, S. and Nataraj, M. 2010. Prevention of helical gear tooth damage in wind turbine generator: A case study. *Proceedings of the Institution of Mechanical Engineers, Part A: Journal of Power and Energy* 224, pp. 1117–1125.

Sharif, K.J. Kong, S., Evans, H.P. and Snidle, R.W. 2001. Contact and elastohydrodynamic analysis of worm gears Part 1: theoretical formulation. *Proceedings of the Institution of Mechanical Engineers, Part C: Journal of Mechanical Engineering Science* 215, pp. 817–830

Sharif, K.J. Evans, H. P., Snidle, R. W. and Newall, J. P. 2004. Modeling of Film Thickness and Traction in a Variable Ratio Traction Drive Rig. *Journal of Tribology* 126, 92-104

Simon, V. 1988. Thermo-EHD analysis of lubrication of helical gears. *Journal of Mechanisms, Transmissions, and Automation in Design* 110, pp.330-336

Simon, V. 1989. Optimal tooth modifications for spur and helical gears. *Journal of Mechanisms, Transmissions, and Automation in Design* 111, pp. 611–615.

Snidle, R.W. and Evans, H.P. 2009. Some aspects of gear tribology. *Proceedings of the Institution of Mechanical Engineers, Part C: Journal of Mechanical Engineering Science* 223, pp. 103–141.

Stanley, H. and Kato, T. 1997. An FFT-based method for rough surface contact. *Journal of tribology* 119, pp. 481–485.

Tao, J., Hughes, T.G., Evans, H.P., Snidle, R.W., Hopkinson, N.A., Talks, M., and Starbuck, J.M. 2003. Elastohydrodynamic Lubrication Analysis of Gear Tooth Surfaces From Micropitting Tests. *Journal of Tribology* 125, pp. 267-274.

Timoshenko, S.P. and Goodier, J.N. 1951. *Theory of elasticity*. 2nd ed. McGraw-Hill.

Tuplin, W.A. 1962. *Involute gear geometry*. Chatto and Windus, London.

Venner, C. and Lubrecht, A. 1994. Numerical simulation of a transverse ridge in a circular EHL contact under rolling/sliding. *Journal of Tribology* 116. pp. 751-761

Wagaj, P. and Kahraman, A. 2002. Influence of Tooth Profile Modification on Helical Gear Durability. *Journal of Mechanical Design* 124, pp. 501-510.

Walker, H. 1940. Gear tooth deflection and profile modification. *The Engineer* 166. pp. 102-104.

Wang, W, Wang, H., Liu, Y., Hu, Y., and Zhu, D. 2003. A comparative study of the methods for calculation of surface elastic deformation. *Proceedings of the Institution of Mechanical Engineers, Part J: Journal of Engineering Tribology* 217, pp. 145–153.

Wang, Y. Li, H., Tong, J., Yang, P. 2004. Transient thermoelastohydrodynamic lubrication analysis of an involute spur gear. *Tribology International* 37, pp. 773–782.

Wang, Y.Q. He, Z. and Su, W. 2012. Effect of Impact Load on Transient Elastohydrodynamic Lubrication of Involute Spur Gears. *Tribology Transactions* 55, pp. 155–162.

Zhang, J. and Shaw, B.A. 2011. The Effect of Superfinishing on the Contact Fatigue of Case Carburised Gears. *Journal of Applied Mechanics and Materials* 86, pp. 348–351.

Zhu, D. 2007. On some aspects of numerical solutions of thin-film and mixed elastohydrodynamic lubrication. *Proceedings of the Institution of Mechanical Engineers, Part J: Journal of Engineering Tribology* 221, pp. 561–579.

Zhu, D., Ren, N. and Wang, Q. 2009. Pitting Life Prediction Based on a 3D Line Contact Mixed EHL Analysis and Subsurface von Mises Stress Calculation. *Journal of Tribology* 131(4), pp. 041501(1–8).

Zhu, D. and Wang, Q. 2013. Effect of Roughness Orientation on the Elastohydrodynamic Lubrication Film Thickness. *Journal of Tribology* 135, p. 031501(1-9).

Appendix

List of Publications Arising from this Study

1- Jamali, H.U., Sharif, K., Evans, H.P. and Snidle, R.W. 2014. The transient effects of profile modification on elastohydrodynamic oil films in helical gears. *Tribology Transactions* 58 (1), pp. 119-130.

2- Jamali, H.U., Sharif, K., Evans, H.P. and Snidle, R.W. 2014. Transient EHL analysis of helical gears. Presented at: *International Gear Conference 2014*, Lyon Villeurbanne, France, 26-28 August 2014. *International Gear Conference 2014 - Conference Proceedings.* Cambridge: Woodhead Publishing, pp. 721-730.

3- Clarke, A., Jamali, H.U., Weeks, I., Sharif, K., Evans, H.P. and Snidle, R.W. 2014. The influence of macro and micro geometry on the generation of adverse contact conditions associated with micropitting in gear tooth contacts. Presented at: *Gears 2014 technical awareness seminar*, Newcastle, England, 20 November 2014.

4- Jamali, H.U., Sharif, K., Evans, H.P. and Snidle, R.W. 2013. Analysis of elastohydrodynamic lubrication of helical gear tooth contacts including the effects of crowning and the form of tip relief. Presented at: *International Conference on Gears 2013*, Dusseldorf, Germany, 7-9 October 2013.

5- Snidle, R.W., Sharif, K., Evans, H.P. and Jamali, H.U. 2013. Transient elastohydrodynamic analysis of helical gear tooth contacts. Presented at: *68th STLE Annual Meeting & Exhibition*, Detroit Marriott at the Renaissance Center Detroit, MI, USA, 5-9 May 2013.